

REPORT DOCUMENTATION PAGE

AFRL-SR-BL-TR-01-

0584

Public reporting burden for this collection of information is estimated to average 1 hour per response, including the time for reviewing the data needed, and completing and reviewing this collection of information. Send comments regarding this burden estimate or any reducing this burden to Washington Headquarters Services, Directorate for Information Operations and Reports, 1215 Jefferson Dav Management and Budget, Paperwork Reduction Project (0704-0188), Washington, DC 20503

1. AGENCY USE ONLY (Leave blank)		2. REPORT DATE August 23, 2001	3. REPORT TYPE AND DATES COVERED Final Technical Report: 01 July 97 - 30 Sep 99 31 Dec 99	
4. TITLE AND SUBTITLE Shock Propagation and Supersonic Drag in Low Temperature Plasmas			5. FUNDING NUMBERS AFOSR Grant #F49620-97-1-0497	
6. AUTHOR(S) Professor Richard B. Miles				
7. PERFORMING ORGANIZATION NAME(S) AND ADDRESS(ES) Princeton University Dept. Mechanical & Aerospace Engrg. Olden St. Princeton, NJ 08544			8. PERFORMING ORGANIZATION REPORT NUMBER	
9. SPONSORING / MONITORING AGENCY NAME(S) AND ADDRESS(ES) AFOSR/NA 801 North Randolph St. Room 732 Arlington, VA 22203-1977			10. SPONSORING / MONITORING AGENCY REPORT NUMBER	
11. SUPPLEMENTARY NOTES				
12a. DISTRIBUTION / AVAILABILITY STATEMENT Approved for public release; distribution is unlimited.				
13. ABSTRACT (Maximum 200 Words) This work supported the development of new diagnostic techniques, modeling, and a series of experiments designed to study the propagation of shock waves through weakly ionized plasmas. It also supported the design and construction of a small-scale, supersonic, microwave-coupled wind tunnel to determine the effects of weakly ionized plasmas on supersonic flow properties and shock stand-off distances around blunt bodies. The motivation of the work was to establish whether the ions and electrons in the weakly ionized plasma affected the shock propagation, as has been claimed by some research groups. The work conducted under this grant has had four principal outcomes: <ol style="list-style-type: none"> 1. The determination that effects associated with shock propagation through weakly ionized plasmas can be fully described by spatially non-uniform temperature fields rather than charge particle interactions. 2. The development of a capability to measure neutral gas temperature profiles by ultraviolet filtered Rayleigh scattering. 3. The design, construction, and demonstration of a Mach 3 wind tunnel integrated into a tapered microwave wave guide for the study of microwave discharges and supersonic flow. 4. The further development of new diagnostic techniques, including the use of atomic, fluorescence, and dispersive filters for rotational raman detection, a MHz pulse-burst laser for the visualization of shock wave/boundary layer interactions, and the use of group velocity dispersion in an atomic vapor filter to characterize the performance of laser seeding devices. 				
14. SUBJECT TERMS Diagnostic Techniques, Weakly Ionized Plasmas, Shock Wave/Boundary Layer Interactions			15. NUMBER OF PAGES 4 plus 4 Appendices	
			16. PRICE CODE	
17. SECURITY CLASSIFICATION OF REPORT Unclassified	18. SECURITY CLASSIFICATION OF THIS PAGE Unclassified	19. SECURITY CLASSIFICATION OF ABSTRACT Unclassified	20. LIMITATION OF ABSTRACT UL	

20011126 099

FINAL TECHNICAL REPORT

AFOSR GRANT #F49620-97-1-0497

SHOCK PROPAGATION AND SUPERSONIC DRAG IN LOW TEMPERATURE PLASMAS (150-6745)

Richard B. Miles
Department of Mechanical & Aerospace Engineering
Princeton University
Princeton, NJ 08544

August 23, 2001

ABSTRACT

This work supported the development of new diagnostic techniques, modeling, and a series of experiments designed to study the propagation of shock waves through weakly ionized plasmas. It also supported the design and construction of a small-scale, supersonic, microwave-coupled wind tunnel to determine the effects of weakly ionized plasmas on supersonic flow properties and shock stand-off distances around blunt bodies. The motivation of the work was to establish whether the ions and electrons in the weakly ionized plasma affected the shock propagation, as has been claimed by some research groups. The work conducted under this grant has had four principal outcomes:

1. The determination that effects associated with shock propagation through weakly ionized plasmas can be fully described by spatially non-uniform temperature fields rather than charge particle interactions.
2. The development of a capability to measure neutral gas temperature profiles by ultraviolet filtered Rayleigh scattering.
3. The design, construction, and demonstration of a Mach 3 wind tunnel integrated into a tapered microwave wave guide for the study of microwave discharges and supersonic flow.
4. The further development of new diagnostic techniques, including the use of atomic, refluorescence, and dispersive filters for rotational Raman detection, a MHz pulse-burst laser for the visualization of shock wave/boundary layer interactions, and the use of group velocity dispersion in an atomic vapor filter to characterize the performance of laser seeding devices.

DISCUSSION

The major results of this research effort are included in papers which are appended to this report. The most significant outcome is reported in an AIAA paper (AIAA-2000-0714), "Shock Wave Propagation Through Flow Discharge Plasmas: Evidence of Thermal Mechanism of Shock Dispersion," and in the Physics Letters A paper, "Direct Evidence for Thermal Mechanism of

Plasma Influence on Shock Wave Propagation." A more complete paper is pending publication at the Physics of Fluids, "Shock Wave Propagation in Dispersion in Glow Discharge Plasmas." These three papers are included as Appendix A in this report. These papers describe a series of experiments conducted in our laboratory on the propagation of shock waves through weakly ionized plasmas under various conditions. The plasmas were well characterized, particularly by using the new ultraviolet filtered Rayleigh scattering measurement of the neutral gas temperature to establish the temperature profile across the discharge tube. That actual profile was used together with computational modeling of shock propagation to predict signals that would be measured, assuming only thermal effects were important. The signals that were, in fact, measured closely match the predicted signals, strongly suggesting that shock propagation in weakly ionized plasmas was dominated by thermal processes. In order to confirm that prediction, a controller was added to the electronics so the plasma could be turned on or off quickly. These experiments showed that the observed "anomalous" shock propagation characteristics did not occur immediately after turning on the plasma, but only were observed when thermal equilibrium was reached. Similarly, after the discharge was terminated, the "anomalous" propagation effects persisted until the thermal non-uniformity dissipated. It is our view that these experiments unequivocally demonstrate that there is no anomalous behavior associated with shock propagation through weakly ionized plasmas.

Closely associated with the effort to measure shock propagation through plasmas is the need for an accurate measurement of the neutral gas temperature profile. Much of the controversy associated with "anomalous" shock propagation arises from the uncertainty in the temperature profile across the plasma. Clearly, at equilibrium, the plasma deposits energy to the neutral gas creating a high temperature region in the center of the discharge compared to the lower temperature region near the walls. The magnitude of this temperature difference and the shape of the curve dramatically affect shock propagation phenomenon. The higher temperature in the core leads to a higher speed-of-sound, and the shock wave propagating through such a plasma becomes curved. The shock interaction at the wall depends on the character of the temperature profile and can be rather complex. This need to measure the temperature profile motivated us to develop a robust method of measuring temperature in the presence of background scattering from the walls of the plasma containment vessel. Appendix B includes several papers describing that measurement process. To accomplish it, we used an injection-locked, frequency-tunable Ti:Sapphire laser that was frequency up-converted to the ultraviolet to overlap the atomic mercury vapor absorption lines near 253.7 nm. An optically thick mercury vapor filter was placed in front of the camera, so when the laser was tuned to one of the mercury vapor absorption lines, all the light that was scattered from the walls of the discharge tube was eliminated by absorption in the mercury vapor. Light scattered from the hot neutral molecules in the electric discharge was broadened by the thermal motion of those molecules and a portion of that light passed through the mercury filter to the camera. By calibration, that light level could be directly associated with the temperature of the gas, assuming the pressure in the tube was known. For these experiments the pressure was held constant and measured using a separate pressure gauge. This provided a robust method of measuring temperature with uncertainties less than 4%.

The "anomalous" effects associated with shock waves and plasmas have also been observed in ballistic range experiments where projectiles have been passed through plasmas at supersonic

speeds. In order to understand these processes, a supersonic plasma-coupled wind tunnel was designed and built. The design of this wind tunnel was significantly aided through collaboration with the Princeton Plasma Physics Laboratory (Dr. Philip Efthimion) and the use of their microwave modeling capabilities. This tunnel is described in Appendix C and some preliminary experiments are included. The important feature of this tunnel is that the microwaves enter in the plenum and propagate through a dielectric nozzle and into the supersonic test region. The dielectric nozzle is placed inside a microwave wave guide which is tapered so that, at the nozzle exit, the cross section is below the cut-off frequency. The taper concentrates the microwaves, creating a high field region just downstream of the nozzle. The taper makes the waveguide section into a waveguide resonator so that high strength fields are created and very little microwave energy leaks out. The discharge is stabilized by using small pins protruding from the wall (in more recent work, the discharge is stabilized and controlled by electron beams). The microwaves are provided either in pulsed form at 50 kW for 1 millisecond, or continuously at 6 kW. The wind tunnel is connected to an ejector system and operates from room air with a static pressure in the test section of 20 torr. The paper in Appendix C shows the change in Mach number of the flow that occurs when the discharge is on. This facility can also be used to study plasma drag reduction and plasma steering.

Also partially funded by this program was the continued development of a variety of new optical diagnostic techniques that provide information for flow field imaging, combustion processes, and for characterization of laser performance. Papers related to these topics are included in Appendix D. The first of these papers is a publication from the Journal of Raman Spectroscopy on the use of atomic fluorescent and dispersive filters for high signal-to-noise detection of rotational Raman scattering. Rotational Raman scattering is an alternative method of measuring temperature in diatomic and polyatomic gases, such as air, for combustion environments (it will not work for atomic gases such as argon). Raman scattering also has the capability of measuring species concentrations and thermal nonequilibrium. Generally speaking, vibrational Raman scattering is observed, although it is approximately 1,000 times weaker than Rayleigh scattering. For this reason, Raman scattering has not been a particularly useful tool for flow field or combustion diagnostics. Rotational Raman scattering is more than one order of magnitude stronger than vibrational, but has usually not been studied because of very strong background interference associated with Rayleigh scattering, and scattering from windows and walls. With the new atomic filters, however, this background scattering can be removed and rotational Raman becomes a more promising diagnostic approach. The paper outlines several methods of using atomic filters to both remove background scattering and simultaneously observe the rotational Raman signal.

The second paper in Appendix D discusses the use of atomic filters for the characterization of laser pulse frequency. For diagnostic approaches that rely on the use of atomic or molecular filters, it is important to have very good control of the laser frequency. This is usually done through an injection-locking process, where a low power, controllable laser is introduced into the high power laser cavity in such a manner as to lock that high power laser cavity output to the low power frequency. The problem is that this locking process is highly dependent on alignment as well as on the precise length of the high power laser cavity. In many cases it is not apparent that the locking is not operating properly, and much time can be wasted taking data which later proves to be worthless because of poor laser locking performance. The second paper in

Appendix D is from Optics Letters entitled, "Characterization of Laser Seeding by Use of Group-Velocity Dispersion in an Atomic-Vapor Filter." In this case, the laser is tuned so the output is just off the atomic resonance, but close enough so that the index-of-refraction is highly dispersive. Since the index-of-refraction controls the group velocity of the laser pulse propagating through the atomic cell, the time at which the pulse exits the cell is a function of the frequency of the laser. If the laser is operating with single frequency, then a single pulse exits the cell. If, on the other hand, the laser is operating multi-mode, then several pulses in time are seen exiting the cell. Since time is an easy measurement to make as compared to very closely spaced frequencies, this method provides a convenient tool for monitoring laser performance. With proper injection-locking, only a single pulse exits the cell.

The third paper in Appendix D discusses the MHz-rate, pulse-burst laser system that has been developed at Princeton and applied to the study of shock wave/boundary layer interactions. The construction of the laser was supported through an AFOSR DURIP grant with the Princeton Electric Propulsion group. The laser is capable of operating at repetition rates of up to 1 M pulses per second, with a pulse burst lasting approximately 100 microseconds. Generally speaking, we operate the laser with 30 pulses at a 500 kHz rate. This laser is matched together with a high-speed framing camera which has been developed by Princeton Scientific Instruments, Inc., to capture time-evolving flow structure in a supersonic wind tunnel facility. In order to better highlight flow properties, the air was seeded with approximately 1% CO₂ upstream of the plenum. That CO₂ vapor condensed into 10 nm scale particles, forming a particle fog in the core or cold section of the supersonic flow. In the warm section near the walls, condensation did not occur, so the structure of the upper portion of the boundary layer is clearly visible in the images. Studies of boundary layer effects on shock waves have been made by placing a 14° angle wedge along the wall and observing the variations in this shock structure that are forced by the boundary layer. These images are shown in the paper.

PERSONNEL

Personnel supported under this grant were Prof. Richard Miles, Principal Investigator, Dr. Walter Lempert, Dr. Sergey Macheret, Philip Howard, and graduate students, Azer Yalin, Pingfan Wu, Brendan McAndrew, and Xingguo Pan.

APPENDIX A

1. Yu.Z. Ionikh, N.V. Chernysheva, **A.P. Yalin**, **S.O. Macheret**, L. Martinelli, and **R.B. Miles**, "Shock Wave Propagation Through Glow Discharge Plasmas: Evidence of Thermal Mechanism of Shock Dispersion," AIAA 2000-0714, 38th Aerospace Sciences Meeting & Exhibit, Jan. 10-13, 2000, Reno, NV.
2. Y.Z. Ionikh, N.V. Chernysheva, A.V. Meshchanov, **A.P. Yalin**, and **R.B. Miles**, "Direct Evidence for Thermal Mechanism of Plasma Influence on Shock Wave Propagation," Physics Letters A, 259 (1999) pp. 387-392.
3. **S. O. Macheret**, Y.Z. Ionikh, N.V. Chernysheva, **A.P. Yalin**, L. Martinelli, and **R.B. Miles**, "Shock Wave Propagation and Dispersion in Glow Discharge Plasmas," Submitted to Physics of Fluids, 7/25/00.



AIAA 2000-0714

**SHOCK WAVE PROPAGATION
THROUGH GLOW DISCHARGE
PLASMAS:
EVIDENCE OF THERMAL MECHANISM
OF SHOCK DISPERSION**

**Yu.Z.Ionikh, N.V.Chernysheva, A.P. Yalin,
S.O.Macheret, L.Martinelli, and R.B. Miles**

Princeton University

**38th Aerospace Sciences
Meeting & Exhibit
10-13 January 2000 / Reno, NV**

SHOCK WAVE PROPAGATION THROUGH GLOW DISCHARGE PLASMAS: EVIDENCE OF THERMAL MECHANISM OF SHOCK DISPERSION

Yuri Z. Ionikh,* Naira V. Chernysheva,* Azer P. Yalin,**
Sergey O. Macheret,[#] Luigi Martinelli,^{##} and Richard B. Miles[&]

*Department of Mechanical and Aerospace Engineering
Princeton University
D-414 Engineering Quadrangle
Princeton, NJ 08544
Phone: (609) 258-5130; E-mail: macheret@princeton.edu*

Abstract

The paper examines, experimentally and computationally, propagation of shock waves in weakly ionized plasmas. Spark-generated shocks were studied in glow discharges in argon and argon-nitrogen mixtures. UV Filtered Rayleigh Scattering was used to measure radial profiles of gas temperature, and laser Schlieren (laser beam deflection) method was used to measure shock arrival times and axial density gradients across the shock. Highly accurate inviscid axisymmetric CFD computations were run and compared with the experiments. Comparison of experimental and computational results show that experimentally observed changes in shock structure and velocity in weakly ionized gases are explained by conventional gas dynamics, with thermal effects and non-one-dimensionality (transverse gradients, shock curvature, etc.) playing a critical role. A direct experimental proof of the thermal mechanism was provided by pulsing a glow discharge. With several hundred microseconds time delay between starting the discharge and shock launch, electric current, field, and the discharge luminosity reach their steady-state values, while the temperature is still cold. In this regime, laser Schlieren signals are virtually identical to those without the discharge, differing dramatically from the signals in discharges with fully established temperature profiles.

I. Introduction

Weakly ionized gases (plasmas) could potentially have an impact on high-speed aerodynamics. Using plasmas for shock wave control, drag reduction, vehicle steering, sonic boom attenuation, ignition of combustion in engines, and MHD power extraction and enthalpy by-pass is being actively discussed. Of course, fundamental issues have to be resolved prior to any practical applications.

Propagation of shock waves in weakly ionized plasmas was studied in Russia,^{1-11, 15, 16} and, later, in the U.S.¹²⁻¹⁴ Shock acceleration, broadening, and "splitting" was observed in various d.c., RF, and pulsed discharges, in inert as well as molecular gases. Some researchers^{1-11, 12-14} attributed experimental observations to various plasma-specific phenomena, from electric double layers to ion-acoustic waves to new long-range interactions or microscopic structure formed in gas discharges. However, other Russian researchers^{15, 16} found that their data can be adequately explained by conventional thermal phenomena.

* Visiting Scholar, on leave from Institute of Physics, St.Petersburg State University, Russia

* Visiting Scholar, on leave from Institute of Physics, St.Petersburg State University, Russia

** Graduate Student, Student Member AIAA

[#] Research Scientist, Senior Member AIAA

^{##} Assistant Professor, Associate Fellow AIAA

[&] Professor, Fellow AIAA

In Refs. 17 and 18, analysis of various physical mechanisms resulted in a conclusion that the "broadening", "splitting", and acceleration of shocks in gas discharges could hardly be explained by plasma-specific effects. This is due ultimately to the very low ionization fraction in the discharges, which leads to small fraction of the total gas energy stored in ionized and excited states, to very inefficient energy and momentum transfer from electrons and ions to the bulk neutral gas, and to very long times of these transfer processes.

Our CFD modeling¹⁹ demonstrated that transverse temperature and density gradients present in gas discharges due to Joule heating could be responsible for the observed "anomalous" phenomena. The transverse gradients result in non-one-dimensional nature of shock propagation, and attempts to interpret the phenomena in one-dimensional terms could be misleading. For example, shock curvature could be misinterpreted as a "broadened" or "split" 1D structure.

In the present paper, we describe a combined experimental and computational effort to clarify mechanisms of shock propagation in weakly ionized plasmas. Experiments were done in well-characterized positive column of glow discharge in Ar and Ar-N₂ mixtures. Shock velocity and structure was measured using laser Schlieren method, similar to experiments of Refs. 12-14. Since temperature and its gradients could play a critical role in shock propagation, radial temperature profiles in our experiments were measured with Filtered Rayleigh Scattering. Axisymmetric CFD modeling gives a very good agreement with experimental data, thus proving that it is conventional, but non-one-dimensional, gas dynamics that is responsible for the "anomalous" effects.

In order to study shock propagation in weakly ionized plasma with very small or absent temperature gradients, pulsed discharge experiments were done. Those experiments prove again the thermal nature of shock propagation in gas discharges.

II. Experiments on shock propagation in steady-state glow discharges

II.1. Experimental setup and procedures

The experimental setup at Princeton University^{20, 21} was basically similar to that of Refs. 12-14. The plasmas studied were created by longitudinal continuous or pulsed glow discharge. The discharge tube, 3.8 cm i.d. and 120 cm full length, was made of quartz. Shock waves were generated by a spark discharge at the one end of the tube. The spark circuit parameters are: capacitor 0.2 μ F, voltage 15 – 20 kV. The capacitor discharge was controlled by a triggering spark gap. The shock wave entered the discharge through a narrow (2 mm) ring electrode made of stainless steel foil mounted adjacent to the wall. The electrode nearest to the spark was always the anode, in order to prevent the incoming shock wave from passing by the hot cathode and through the cathode fall of the discharge. Both the cathode and anode could be placed at different location in the tube, so that the distance between the spark and the anode could be 20 or 40 cm, and the length of discharge could be 20, 40, or 60 cm. The flexibility in changing the discharge length was used for measuring the electric field in the plasma (see below).

Similar to Refs. 12-14, we used a laser Schlieren method²² for detecting the shock wave front (Fig.1). A He-Ne laser beam crossed the discharge horizontally along the diameter and was then focused onto the plane of a knife by a lens ($f=50$ cm). The beam 1/e diameter was about 0.3 mm. A photodiode with a response time of 20 ns measured the light intensity after the knife edge. The signal was recorded by a digital oscilloscope with 1 k Ω resistor at the input, and a time resolution $\approx 0.1 \mu$ s. In some measurements a miniature pressure sensor was also used.

To measure the instantaneous shock wave velocity we used an approach similar to that proposed in Ref. 22. After the laser beam crossed the discharge it was retro-reflected from a small 90° prism and passed through the discharge once more with the spatial offset and then focused onto the knife edge. This produced two closely separated Schlieren signals of opposite signs. Shock wave velocity was found by dividing the distance between the two beam passages (12 to 21 mm) by the time gap between Schlieren signals. This method provided an accuracy of absolute velocity near 3 per cent (≈ 10 m/s) and that of relative velocity about 0.5 per cent (2 m/s).

Experiments were performed in an Ar-N₂ mixture (1% of N₂). Addition of nitrogen substantially improved the radial uniformity of the discharge. A pure argon discharge contracted at currents $i > 30 - 40$ mA (for pressures $p \geq 30$ Torr). With nitrogen the discharge was not contracted at all conditions studied ($p \leq 100$ Torr, $i \leq 100$ mA). To prevent electrophoresis and accumulation of impurities, the gas mixture was pumped through the discharge with a rate of 300 sccm, which corresponded to 5 – 10 cm/s linear speed in the tube.

As was already mentioned, the flexibility in changing the discharge length allowed us to measure an electric field E in a positive column of the discharge (cathode voltage drop V_c could also be found in these measurements). For $p = 30 - 50$ Torr, $i = 30 - 100$ mA the E value was from 8 to 14 V/cm. Assuming a Bessel radial profile for gas temperature, we calculated the reduced electric field E/N (N is gas number density) and electron number density n_e . Averaged over the tube cross section, these values are $E/N = 1.2 - 1.4$ Td, $n_e = (1.2 - 4) \cdot 10^{10} \text{ cm}^{-3}$ for the condition range mentioned above.

II.2. Measurements of temperature profiles

We have used Ultraviolet Filtered Rayleigh Scattering (UV FRS)^{24, 25} to measure temperature profiles of the discharges studied. A summary of these measurements is presented here. A narrow linewidth laser is used to illuminate the sample gas and the scattered light is imaged through a narrow band absorption filter onto a detector, as shown schematically in Fig.2. The laser should be tunable so that it may be tuned within an absorption notch, and narrow linewidth so that the elastic background (due to windows, particulates etc.) is narrow compared to the spectral width of the absorption notch. The amount of scattered light measured by the detector depends on the spectral overlap of the scattered light and the filter absorption profile. The filter offers very nearly 100% transmission in its passband, yet is extremely optical thick (suppression modeled as 10^5 and higher) within the absorption notches. The light scattered by the atoms and/or molecules in the flow is thermally and collisionally broadened, and is therefore spectrally wider than the laser and background. The filter serves to suppress the background while transmitting a large fraction of the light scattered from the flow. By appropriate selection of filter conditions, and laser frequency, one may obtain very strong background suppression (greater than 10^5) while transmitting close to half of the scattered light.

Depending on the conditions of a specific measurement, slightly different approaches may be used. In cases of constant (known) pressure we use a method which precludes the need for background subtraction. The approach is to ratio the FRS signal at a temperature to be measured, T_M , to the signal at a known temperature, T_{ref} . Both measurements are taken at the same frequency within an absorption notch so that any background is strongly suppressed in both cases. At constant pressure there is a one-to-one correspondence of temperature and density so that the measured ratio uniquely defines the unknown temperature T_M . The signal ratio is primarily determined by the density ratio, with a smaller opposing contribution from lineshape effects.

Modeling results for the present measurements are shown in Figs.3 and 4. Fig. 3 shows the modeled filter transmission profile and FRS signal levels as functions of frequency. The filter has a length of 5 cm, a mercury vapor pressure of 0.0030 torr, and a temperature of 315K. In this spectral region, mercury has six absorption notches due to hyperfine splitting and different isotopic contributions. Fig. 3 is a closer view of the highest frequency absorption notch – the one used in the current work. The nominal location of the lines is at 253.7 nm. The modeled FRS signal levels are for a scatterer of 50 torr of argon at various temperatures. The Rayleigh scattering cross-section is not affected by the weak ionization and so the curves describe both argon gases and the plasmas used in these experiments. The signals are normalized to 300K (by the ideal gas law) so that their relative magnitude scale as would be measured by a detector. In the absence of the filter the signal is linear with density (or $1/T$), while within the absorption features there is also a weaker effect from the variation of scattering linewidth with temperature. From such modeling one may find the relationship between the experimentally measured FRS signal ratio

$$\text{Ratio} = \text{FRS signal } (T=T_M) / \text{FRS signal } (T=T_{ref})$$

and the unknown temperature T_M . Fig. 4 is such a curve. In this case the unknown temperature, T_M , corresponds to the "plasma On" temperature while the reference temperature, T_{ref} , corresponds to the "plasma OFF" temperature -- in this case $T_{ref}=308$ K.

The experimental configuration for FRS temperature measurements is illustrated in Fig. 2. A high power, tunable, narrow linewidth Titanium Sapphire laser²⁶ was used as the excitation source. The frequency-tripled output was delivered to the plasma tube through several anti-reflection coated beam-shaping optics. For these experiments pulse energies of ~ 10 mJ in the ultraviolet (254 nm) were used. The beam passed through a quarter wave plate to ensure the correct orientation of the linearly polarized beam, and through a half-wave plate to correct for the slight elliptical polarization introduced at the tube windows. Several irises were used to reduce stray light carried with beam. A long focal length lens (~ 90 cm) was used to weakly focus the beam to a waist of ~ 200 microns at the sample volume. The sample volume was within the discharge tube and was defined by the laser beam waist and an iris located between the discharge tube and imaging lens ($f\# = 2.4$). The geometry was such that the sample volume had a length of about 1 mm. The scattered light was collected at a scattering angle of 90 degrees with the imaging lens and imaged through the mercury vapor filter. The filter had length 5 cm and had two temperature controllers yielding a vapor pressure of 0.003 Torr, and a filter temperature of 315 K. After the mercury filter, the light passed through a monochromator, which acted as a broad passband filter, while rejecting plasma luminosity and other colors of light from the laser. Finally, the scattered light signal was collected with a Hamamatsu R960 photomultiplier tube. After propagation through the discharge tube a quartz flat was used to pick off a fraction of the beam for power normalization as well as a frequency reference. The picked off beam illuminated a diffuser, and the elastically scattered light was detected through a second mercury filter (frequency reference), as well as measured by a photodiode (power reference). The latter two measurements used thin film interference filters (CORION G25-254-F) for spectral filtering. The three signals were collected with a Stanford Research System boxcar onto a computer.

In plasma temperature profile measurements, a thermocouple was used to measure the wall temperature. Two 1-D translation stages were used to translate the discharge tube horizontally relative to the laser beam. Radial profiles along the horizontal axis were found by translating the discharge tube. Profiles were obtained in the argon plasma as well as the argon plus 1% nitrogen mixture, both at a pressure of 50 Torr, at several different values of electric current.

For the range of experimental conditions studied, $p=30 - 50$ Torr, $i=30 - 100$ mA, the steady-state centerline temperature range was found to be from 440 ± 30 K to 830 ± 70 K. Fig. 5 shows the experimental profile of an argon plasma at pressure 50 Torr and current 20 mA. Figures 6 and 7 are experimental profiles of an argon + 1% nitrogen mixture at a pressure of 50 Torr, and currents of 10 and 40 mA respectively. The experimental points are in good agreement with computation.²⁵ We have plotted them here with fitted Gaussian curves:

$$\frac{T(r)}{T_w} = \frac{T_c}{T_w} \exp \left[- \ln \frac{T_c}{T_w} \cdot \left(\frac{r}{R} \right)^2 \right], \quad (1)$$

where T_c and T_w are the centerline and wall temperature, respectively; r is the radial variable; and R is the tube radius.

III. Results of shock propagation studies in steady-state discharges and comparison with CFD axisymmetric modeling

In our earlier work,¹⁹ we performed a 2D inviscid modeling of shock propagation through a discharge-heated gas and concluded that transverse gradient and non-one-dimensionality play a crucial role in shock propagation in glow discharges, and that multi-peak laser Schlieren signals are simply due to the shock curvature. For better comparison with experiments, in this work the code was modified from 2D into axisymmetric. The solver was still that developed earlier in Ref. 27.

As found in the earlier work,¹⁹ to model shock structure on a 10-microsecond time scale, simple computations of a "piston-driven", or "step" shock would suffice. This simplification, while being quite

accurate, would save us from running extremely CPU-intensive full computations of the spark-generated pulse shocks. The plasma region between the infinitely thin electrodes was considered uniform along the tube axis (x), and to have a symmetric radial temperature profile described by the analytical fit (1) to the experimentally measured profile. Both wall temperature and the gas temperature outside the discharge were put equal to room temperature. Mach number of the incident shock was selected so as to give the shock velocity in the uniform room-temperature gas at a given location close to that measured experimentally with the discharge off.

For comparison with laser Schlieren measurements, the density gradient integrated in x direction across the "laser beam" and averaged in the radial direction across the tube was computed. The "laser beam" width in the computations was adjusted once to match the experimentally determined width of the Schlieren signal with the discharge off. The result of this calibration is shown in Fig.8. As seen in the Figure, computations reproduce the shape of the experimental peak very well.

Figures 9 – 11 show measured and computed Schlieren signals in pure argon (Fig.9) and Ar+1%N₂ (Figs.10 and 11). In each figure, upper plots correspond to the discharge-off case, while lower plots correspond to the discharge current of 20 mA (Fig.9), and 10 and 40 mA in Figs.10 and 11. Figs. 10 and 11 differ in that the Schlieren measurement point in Fig.11 is about 11 cm downstream of that in Fig.10. Measured and computed velocities of shock waves are shown near all the signals in Figs.9 – 11.

As seen in the figures, agreement between the computations and experiments, in both shock velocities and the two-peak signal shapes, is excellent. As discussed in Ref.19, the two-peak structure of the laser Schlieren signals is due to the curvature of the shock front in a region with transverse temperature gradient. This is illustrated in Fig.12 (a-d), where lines of constant density are shown in 4 moments of time, as the shock propagated from the room-temperature gas into the plasma. The first peak in the Schlieren signal comes from the portion of the shock that propagates through the hot centerline region. The high temperature and low density in this region result in both higher speed of the shock and lower intensity of the peak compared with those corresponding to colder near-wall regions. The portion of the shock moving through the cold near-wall region lags behind and produces a strong peak in the signal due to the high density near the wall.

For further quantitative comparison between computational and experimental results, Figures 13 and 14 show the width of Schlieren signals versus centerline temperature (Fig.13) and the shock velocity versus average temperature in the discharge (Fig.14). The average temperature was determined in a standard way:

$$T_{av} = \frac{\int_0^R T(r) \cdot 2\pi r dr}{\pi R^2} \quad (2)$$

Again, Figure 13 and 14 show excellent agreement between computations and experimental data. This provides a strong evidence of conventional, thermal mechanism of shock propagation in weakly ionized plasmas.

IV. Experiments on shock propagation in pulsed discharges

To distinguish between thermal and plasma-specific mechanisms of shock propagation, it would be desirable to eliminate temperature effects while maintaining plasma with the same density of charged particles, electric field, etc. Unfortunately, conventional steady-state discharge is a system where thermal effects are coupled with electric fields and electron density. However, in pulsed discharges, a relatively long time interval can exist when electron, ion, and excited molecule densities are quite high while the temperature is low. Indeed, gas heating and cooling occurs on time scale orders of magnitude longer than the time scale for ionization/recombination/excitation processes.²⁸

In this work, the pulsed mode of the discharge was produced by using a transistor switch in series with the discharge. The rise time for the current pulse was 20 μ s, and the pulse duration was about 0.5 ms. It was found that this time was insufficient to get a uniform discharge. In fact, when the discharge was turned on, undesirable transitional processes (for example, discharges on the wall of the tube) were observed. Therefore a weak pilot discharge with 1 mA current was maintained between pulses, which resulted in a fairly uniform volume pulsed discharge. Fig.15 shows the discharge pulse shape and the time dependence of discharge integral emission (with no shock wave). Clearly, at times near to the middle of the pulse the emission reaches its steady-state value, similar to that of the continuous discharge. The initial peak of intensity is a result of the higher electric field arising in the discharge immediately after the transistor switch is opened (see below).

As shown in Figs. 16 and 17, for the pilot discharge a small acceleration, accompanied by some widening and weakening of the signal can be noticed, but the changes are very small compared to the higher-current continuous discharge. This is no surprise since the electron number density in the pilot discharge is $\approx 10^8$ cm⁻³ only and the measured axial gas temperature is less than 320 K.

Much more important is that Schlieren signal obtained from the pulsed discharge, as seen in Figs. 16 and 17, closely matches both no-discharge and pilot-discharge curves, and is very unlike the signal from the continuous discharge. After the transistor switch is turned on, the discharge current reaches its new steady-state value in ≈ 20 μ s. This value is almost the same as in continuous discharge. The electric field strength E in the pulse could be found by subtracting cathode drop V_c and voltage drop across the ballast resistor from the power supply voltage. The E values were found to be somewhat larger than in the continuous discharge, but the E/N values are almost identical. Thus, the electron number densities and mean electron energies (electron temperatures) should be very close to those in the continuous discharge. This is confirmed by the behavior of the discharge emission (Fig.15). It reaches its steady-state value that is very close to that of the continuous discharge. An initial overshoot is related to the overvoltage applied to the discharge in the transition period (~ 20 μ s) from small to large current. Higher E/N values in this interval result in efficient excitation of atoms and molecules, including those with radiative lifetime ~ 1 – 10 μ s (e.g., intensive bands of the 1st positive system of the N_2 molecule).

The increase in gas temperature, ΔT , during the pulse for the pulse duration τ_p may be calculated from the simple balance equation $iE\tau_p = c_p m_1 \Delta T$, where c_p is the specific heat, and m_1 is a mass of gas per unit length. Here we ignore heat losses because the pulse duration is a factor of 100 less than the characteristic time for thermal conductivity. For the conditions of Fig.16, this equation gives $\Delta T = 0.4$ K – 0.6 K. Thus, the pulsed discharge has electron component parameters (E/N , n_e , T_e) the same as in the continuous discharge, but the gas temperature is the same as in the pilot discharge, that is, close to room temperature. Comparing the three Schlieren curves of Fig.16 (and, similarly, those of Fig.17) definitely shows that changing the electron density by two orders of magnitude does not affect shock wave propagation, while changing gas temperature from $T_g \approx 320$ K to $T_g \approx 500$ – 600 K (from the pilot or pulsed discharge to the continuous discharge) affects the shock dramatically. This result may be considered as a strong evidence of thermal mechanism of shock wave – plasma interaction.

To further illustrate the role of heating in shock dynamics, Fig. 18 shows Schlieren signals taken with time delay between turning the discharge on and launching the shock ranging from 1 ms to 200 ms. The 1-ms-delay signal is very close to that in the pilot discharge, while the 200-ms-delay signal is close to that in the continuous discharge. It takes tens and hundreds of milliseconds of the discharge existence for the signal to get close to its steady-state shape. The same point is also illustrated in Fig.19, showing measured shock speed and Schlieren signal width approaching their d.c. discharge values as the discharge is allowed to exist longer. Only gas heating in the discharge takes that long; ionization and excitation processes are many orders of magnitude faster.

As the discharge is turned off, one would expect thermal effects to persist for a long time, tens or even hundreds of milliseconds, when recombination of charged species and quenching of excited states will be long since complete. Indeed, this persistence is clearly seen in Figs. 20 and 21, again supporting the thermal mechanism of shock-plasma interaction.

It should be noted that vibrational temperature, or populations of vibrational states, of nitrogen molecules, could be another parameter (apart from the gas temperature) that is quite different in pulsed and continuous discharges. The vibrational relaxation characteristic time is 1 – 2 orders of magnitude longer than the pulse duration, so the vibrational temperature in the pulsed discharge must be almost the same as in the pilot (1 mA) discharge.

To clarify the role of vibrational relaxation, shock wave propagation through pure argon discharge was also studied at low currents where contraction did not occur. In Fig.22 Schlieren signals for the two gases (Ar and Ar-N₂) are compared. The main features of Schlieren signals for both cases are similar. For a more detailed comparison, one has to take into account that addition of nitrogen changes the electron drift velocity²⁹ and also can affect ionization and recombination processes.²⁸ As a result, plasma parameters such as E/N, electron number density, and gas temperature are different for Ar and Ar-N₂ plasmas even if the gas pressure and discharge current are similar. Data presented in Fig.22 for Ar-N₂ mixture are shown at $i=20$ mA (the same as for pure argon), at 40 mA, where gas temperatures are equal for both discharges, and at 60 mA, where electron densities are equal. It is evident that for the condition of equal gas temperatures (40 mA) similarity of the patterns is the best. This eliminates unambiguously the vibrational relaxation effect and supplies one more evidence of the thermal mechanism of shock dispersion.

V. Conclusions

Extensive experimental data on shock propagation in steady-state glow discharges in argon and argon-nitrogen mixtures were found to be in excellent agreement with high-accuracy axisymmetric CFD modeling. This provides compelling evidence that shock acceleration, attenuation, and "broadening" in weakly ionized plasmas can be explained by conventional gas dynamics, with non-one-dimensionality (due to transverse temperature gradients) playing a critical role.

Experiments with pulsed discharges allowed us to separate thermal effects from those due to electric fields and charged particles. It turned out that gas heating is necessary for shock velocity and Schlieren signal parameters to attain their steady-state values. This provides a direct proof of thermal mechanism of weakly ionized plasma effects on shock propagation.

Acknowledgements

This work was sponsored by the Air Force Office of Scientific Research whose support is gratefully acknowledged. We also express our special thanks to M.N.Shneider for his help.

References

- ¹ G.I.Mishin, A.P.Bedin, N.I.Yushchenkova, G.E.Skvortsov, A.P.Ryazin, "Anomalous Relaxation and Instability of Shock Waves in Plasmas," *Sov. Phys. Tech. Phys.*, Vol. 26, 1981, p.1363.
- ² A.I.Klimov, A.N.Koblov, G.I.Mishin, Yu.L.Serov, and I.P.Yavor, "Shock Wave Propagation in a Glow Discharge," *Sov. Tech. Phys. Lett.*, Vol. 8, 1982, p. 192.
- ³ A.I.Klimov, A.N.Koblov, G.I.Mishin, Yu.L.Serov, K.V.Khodataev, and I.P.Yavor, "Shock Wave Propagation in a Decaying Plasma," *Sov. Tech. Phys. Lett.*, Vol. 8, 1982, pp. 240-241.
- ⁴ I.V.Basargin and G.I.Mishin, "Probe Studies of Shock Waves in the Plasma of a Transverse Glow Discharge," *Sov. Tech. Phys. Lett.*, Vol. 11, No. 11, 1985, pp. 535-538.
- ⁵ V.A.Gorshkov, A.I.Klimov, G.I.Mishin, A.B.Fedotov, and I.P.Yavor, "Behavior of Electron Density in a Weakly Ionized Nonequilibrium Plasma with a Propagating Shock Wave," *Sov. Phys. Tech. Phys.*, Vol. 32, No. 10, 1987, pp. 1138-1141.
- ⁶ A.P.Ershov, S.V.Klishin, A.A.Kuzovnikov, S.E.Ponomareva, and Y.P.Pyt'ev, "Application of the Reduction Method to the Microwave Interferometry of Shock Waves in Weakly Ionized Plasma," *Sov. Phys. Tech. Phys.*, Vol. 34, No. 8, 1989, pp.936-937.
- ⁷ I.V.Basargin and G.I.Mishin, "Precursor of Shock Wave in Glow Discharge Plasma," *Sov. Tech. Phys. Lett.*, Vol. 15, No. 4, 1989, p. 311-313.
- ⁸ S.A.Bystrov, I.S.Zaslanko, Y.K.Mukoseev, and P.V.Shugaev, "Precursor Ahead of a Shock Front in an RF Discharge Plasma," *Sov. Phys. - Doklady*, Vol. 35, No. 1, 1990, pp. 39-40.

- ⁹ G.I.Mishin, A.I.Klimov, and A.Y.Gridin, "Measurements of the Pressure and Density in Shock Waves in a Gas Discharge Plasma," *Sov. Tech. Phys. Lett.*, Vol. 17, No. 8, 1992, pp. 602-604.
- ¹⁰ A.Y.Gridin, A.I.Klimov, and K.V.Khodataev, "Propagation of Shock Waves in a Nonuniform Transverse Pulsed Discharge," *High Temperature*, Vol. 32, No. 4, 1994, pp. 454-457.
- ¹¹ A.Y.Gridin, A.I.Klimov, K.V.Khodataev, N.B.Shcherbak, and S.B.Shcherbak, "Two-Dimensional Simulation of Shock Wave Propagation in a Transverse Pulse Glow Discharge with a Heated Cathode layer," *High Temperature*, Vol. 32, No. 6, 1994, pp. 755-758.
- ¹² B.N.Ganguly, P.Bletzinger, and A.Garscadden, "Shock Wave Damping and Dispersion in Nonequilibrium Low Pressure Argon Plasmas," *Phys. Lett. A*, Vol. 230, 1997, pp. 218 - 222.
- ¹³ B.N.Ganguly and P.Bletzinger, "Shock Wave Dispersion in Nonequilibrium Plasmas," Paper AIAA-96-4607.
- ¹⁴ A.Garscadden, P.Bletzinger, and B.N.Ganguly, "Acoustic Shock Interaction in a Positive Column Plasma," Paper AIAA-99-4973.
- ¹⁵ N.V.Evtyukhin, A.D.Margolin, and V.M.Shmelev, *Sov. J. Chem. Phys.*, Vol. 3, 1986, p. 2080.
- ¹⁶ P.A.Voinovich, A.P.Ershov, S.E.Ponomareva, and V.M.Shibkov, *High Temp.*, Vol. 29, 1991, p. 468.
- ¹⁷ I.V.Adamovich, V.V.Subramaniam, J.W.Rich, and S.O.Macheret, "Shock Wave Propagation in Weakly Ionized Plasmas," Paper AIAA-97-2499.
- ¹⁸ I.V.Adamovich, V.V.Subramaniam, J.W.Rich, and S.O.Macheret, "Phenomenological Analysis of Shock-Wave Propagation in Weakly Ionized Plasmas," *AIAA Journal*, Vol. 36, No. 5, 1998, pp. 816-822.
- ¹⁹ S.O.Macheret, L.Martinelli, and R.B.Miles, "Shock Propagation and Structure in Non-Uniform Gases and Plasmas," Paper AIAA-99-0598
- ²⁰ Y.Z.Ionikh, N.V.Chernysheva, A.V.Meshchanov, A.P.Yalin, and R.B.Miles, "Direct Evidence for Thermal Mechanism of Plasma Influence on Shock Wave Propagation," *Phys. Lett. A*, Vol. 259, 1999, pp. 387 - 392.
- ²¹ S.O.Macheret, Y.Z.Ionikh, L.Martinelli, P.F.Barker, and R.B.Miles, "External Control of Plasmas for High-Speed Aerodynamics," paper AIAA-99-4853.
- ²² J.H.Kiefer and R.W.Lutz, *Phys. Fluids*, Vol. 8, 1965, p. 1393.
- ²³ J.A.Bander and G.Sanzone, *Rev. Sci. Instrum.*, Vol. 45, 1974, p. 949.
- ²⁴ A.P.Yalin and R.B.Miles, "Ultraviolet Filtered Rayleigh Scattering Temperature Measurements with a Mercury Filter," *Optics Lett.*, Vol. 24, No. 9, 1999, pp. 590 - 592.
- ²⁵ A.P.Yalin, Y.Ionikh, and R.B.Miles, "Temperature Measurements in Glow Discharges with Ultraviolet Filtered Rayleigh Scattering," Paper AIAA-99-3431.
- ²⁶ N.D.Finkelstein, W.R.Lempert, and R.B.Miles, "Mercury Vapor Filter Technology and Ultraviolet Laser Source for Flowfield Imaging," Paper AIAA-97-0157.
- ²⁷ C.A.Kim, A.Jameson, L.Martinelli, and K.Xu, "An Accurate LED-BGK Solver in Unstructured Adaptive Meshes," Paper AIAA 97-0328.
- ²⁸ Yu.P.Raizer, *Gas Discharge Physics*, Springer, 1991.
- ²⁹ S.C.Brown, *Basic Data of Plasma Physics*. M.I.T. Press, Cambridge, MA and London, 1966.

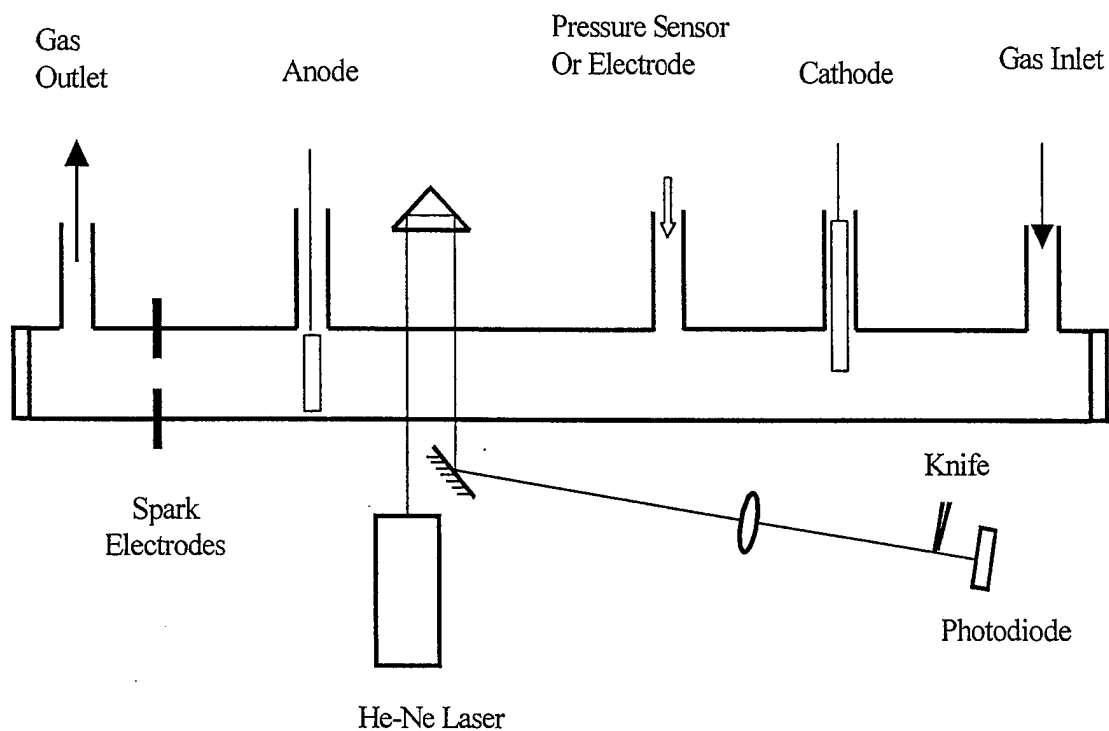


Fig.1. Schematic of the experimental setup for studies of shock propagation in glow discharges.

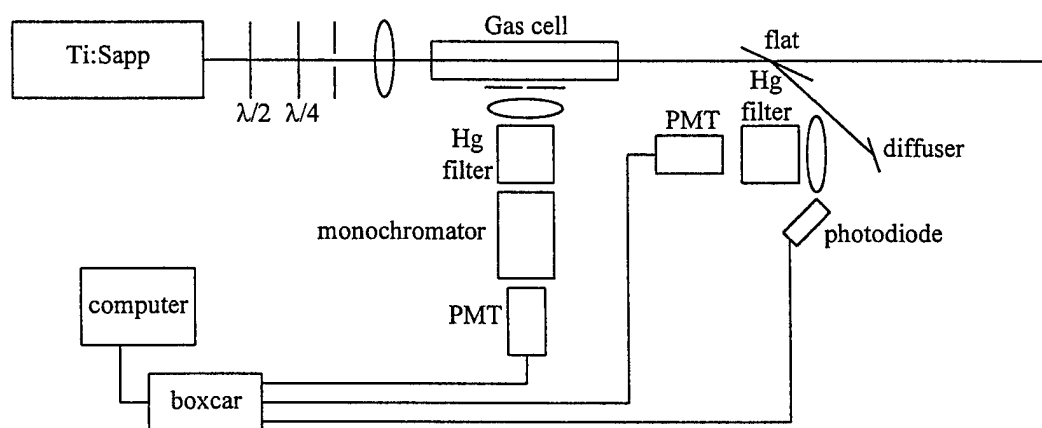


Fig.2. Schematic diagram of experimental setup for UV FRS measurements of temperature profiles.

Modeled UV FRS signal levels for Argon, T=300,...,750 K

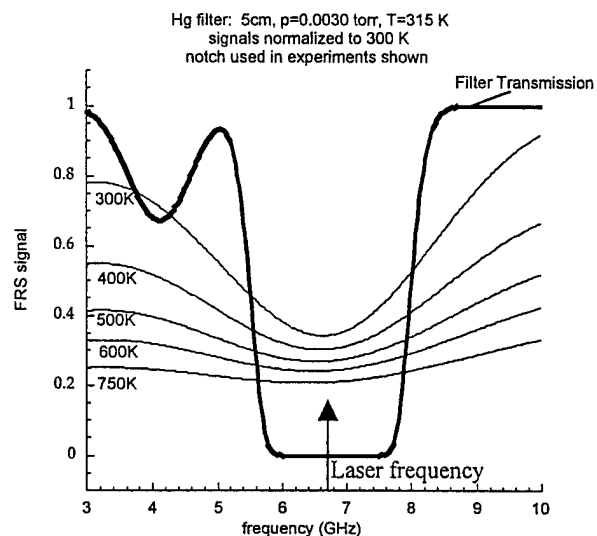


Fig. 3. Modeled FRS signal levels for Argon at a range of temperatures. Mercury has several absorption notches in the 253.7 nm vicinity, however Fig.3 shows the experimentally used (high-frequency) notch.

Conversion Graph: Signal Ratio - Temperature

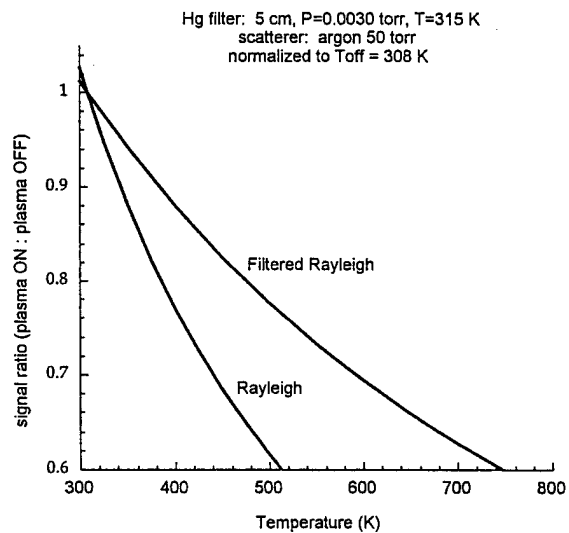


Fig.4. Look-up graph used to convert signal ratio found with discharge ON/OFF to plasma temperature.

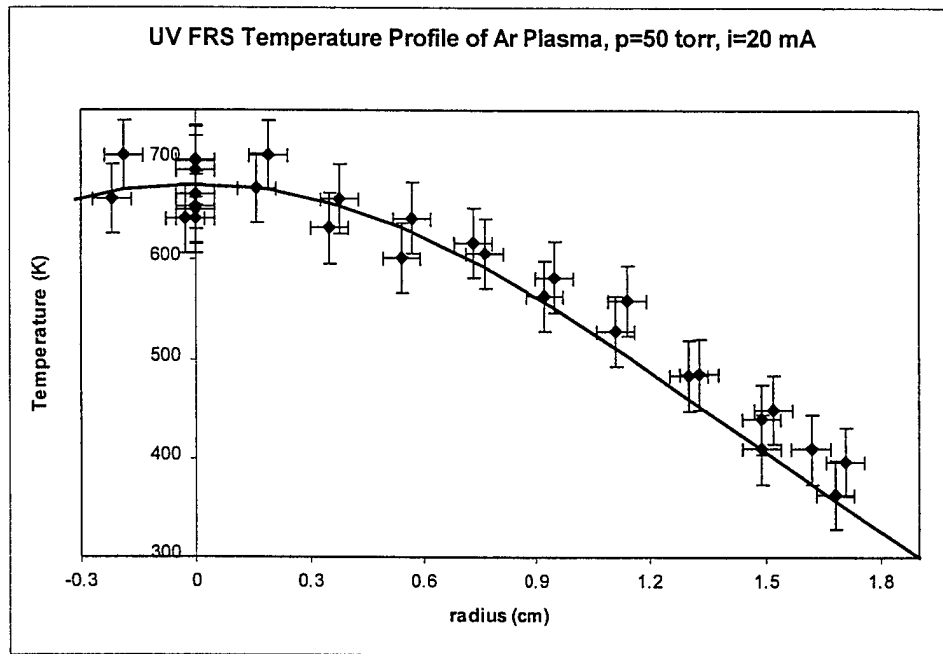


Fig.5. Radial temperature profile in Ar glow discharge tube measured by UV Filtered Rayleigh Scattering. Pressure and electric current are indicated on the plot. Fitting curve – see Eqn. (1).

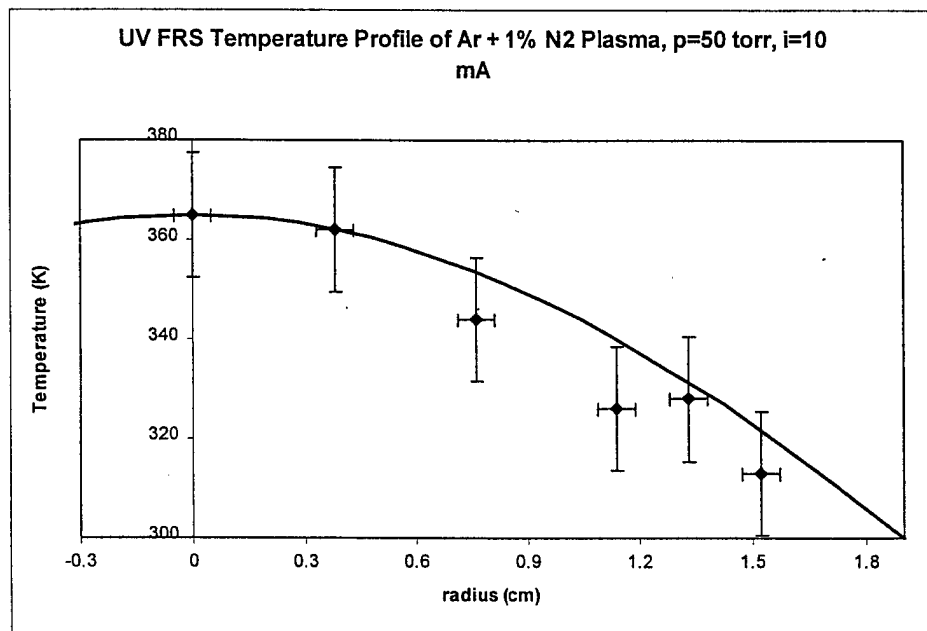


Fig.6. Radial temperature profile in Ar+1%N₂ glow discharge tube measured by UV Filtered Rayleigh Scattering. Pressure and electric current are indicated on the plot. Fitting curve – see Eqn. (1).

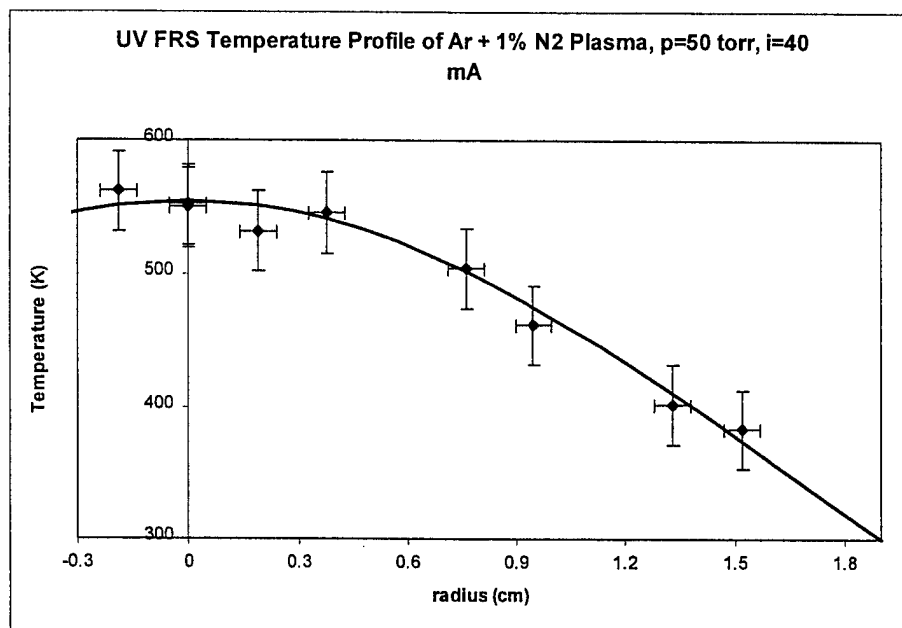


Fig.7. Radial temperature profile in Ar+1%N₂ glow discharge tube measured by UV Filtered Rayleigh Scattering. Pressure and electric current are indicated on the plot. Fitting curve – see Eqn. (1).

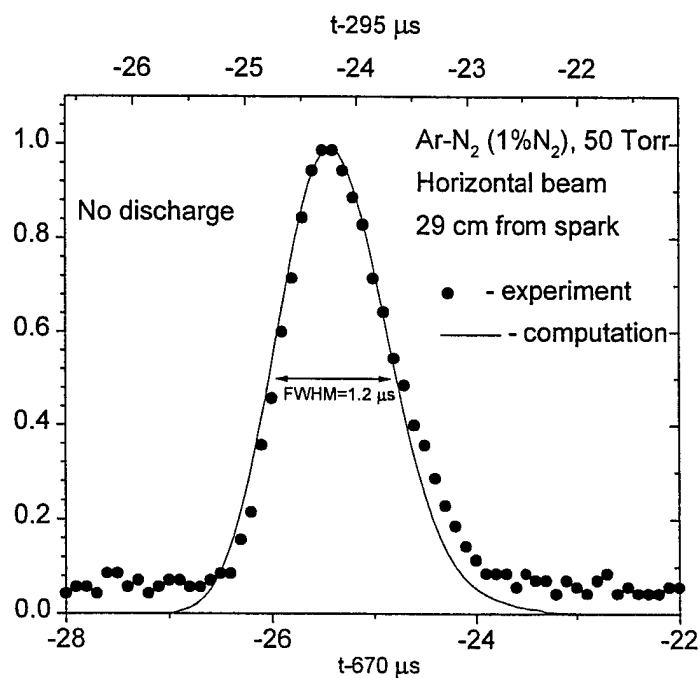


Fig.8. Calibration of the "laser beam width" for CFD modeling against laser Schlieren signal with the discharge off.

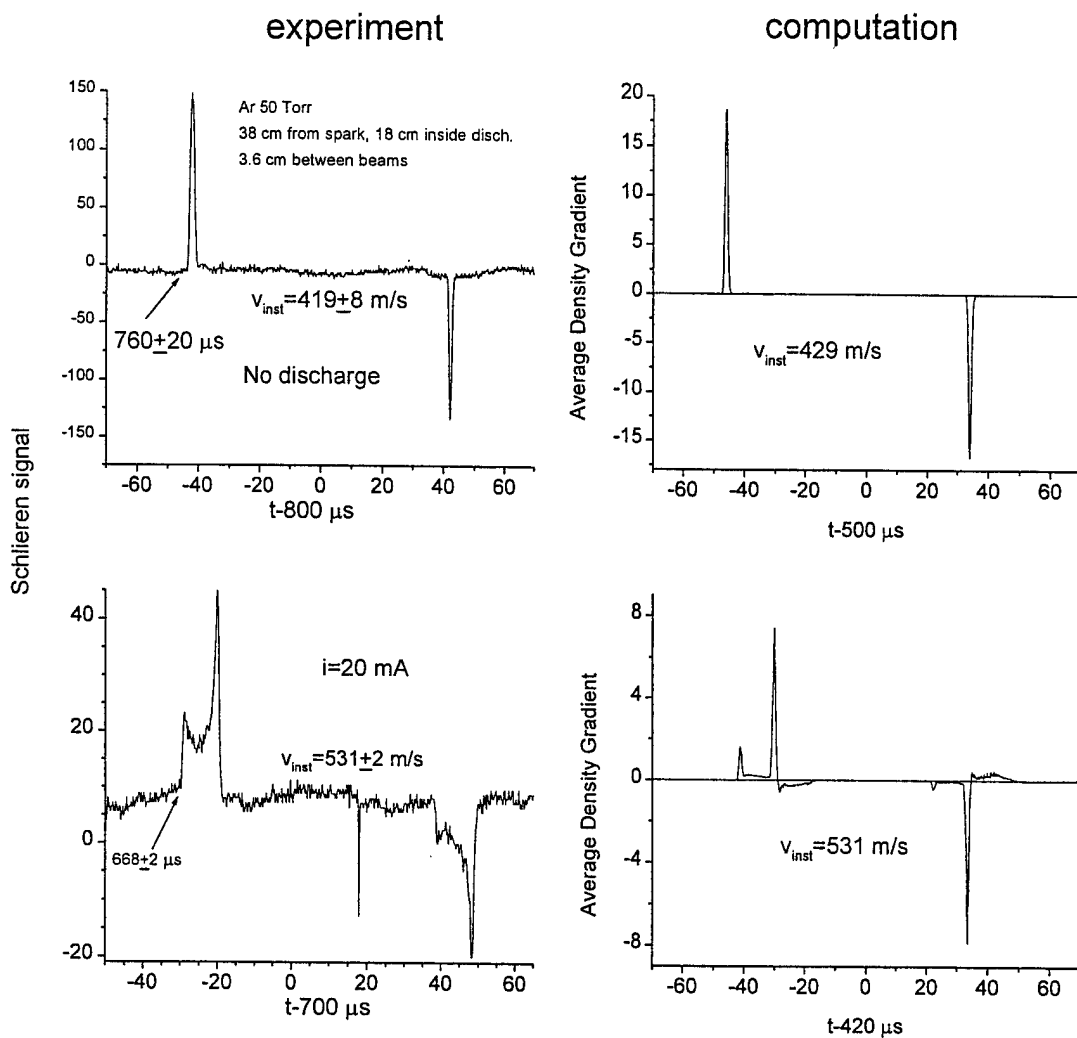


Fig.9. Experimentally measured and simulated laser Schlieren signals for shocks propagating in glow discharge in pure Ar at 50 Torr. The discharge current is 20 mA. The first of the two laser beams is located 18 cm from the entrance to the discharge, and the spacing between the two beams is 3.6 cm. The experimentally measured and computed shock velocities are indicated on the figure.

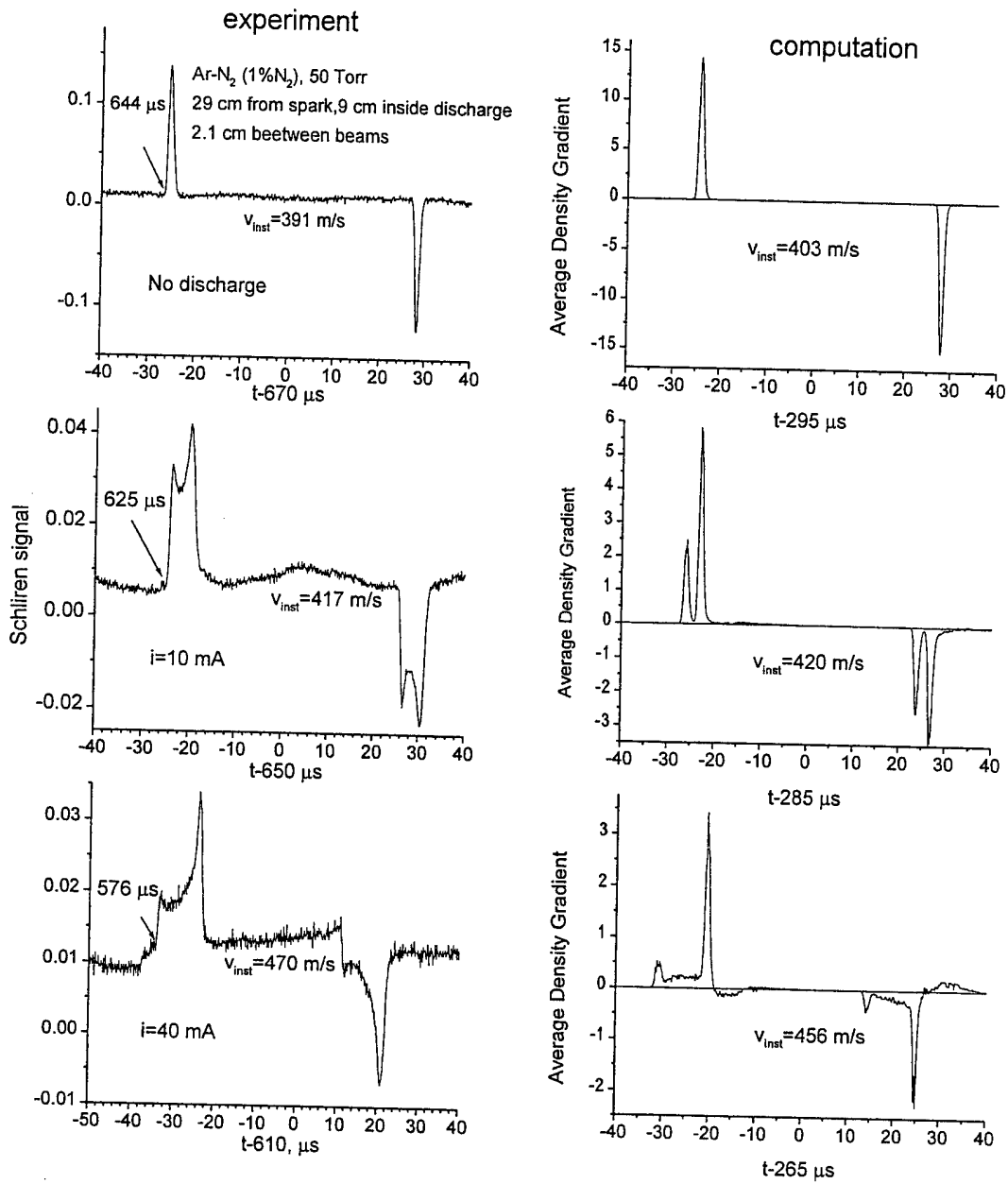


Fig.10. Experimentally measured and simulated laser Schlieren signals for shocks propagating in glow discharge in Ar+1%N₂ at 50 Torr. The discharge current values are 10 mA and 40 mA. The first of the two laser beams is located 9 cm from the entrance to the discharge, and the spacing between the two beams is 2.1 cm. The experimentally measured and computed shock velocities are indicated on the figure.

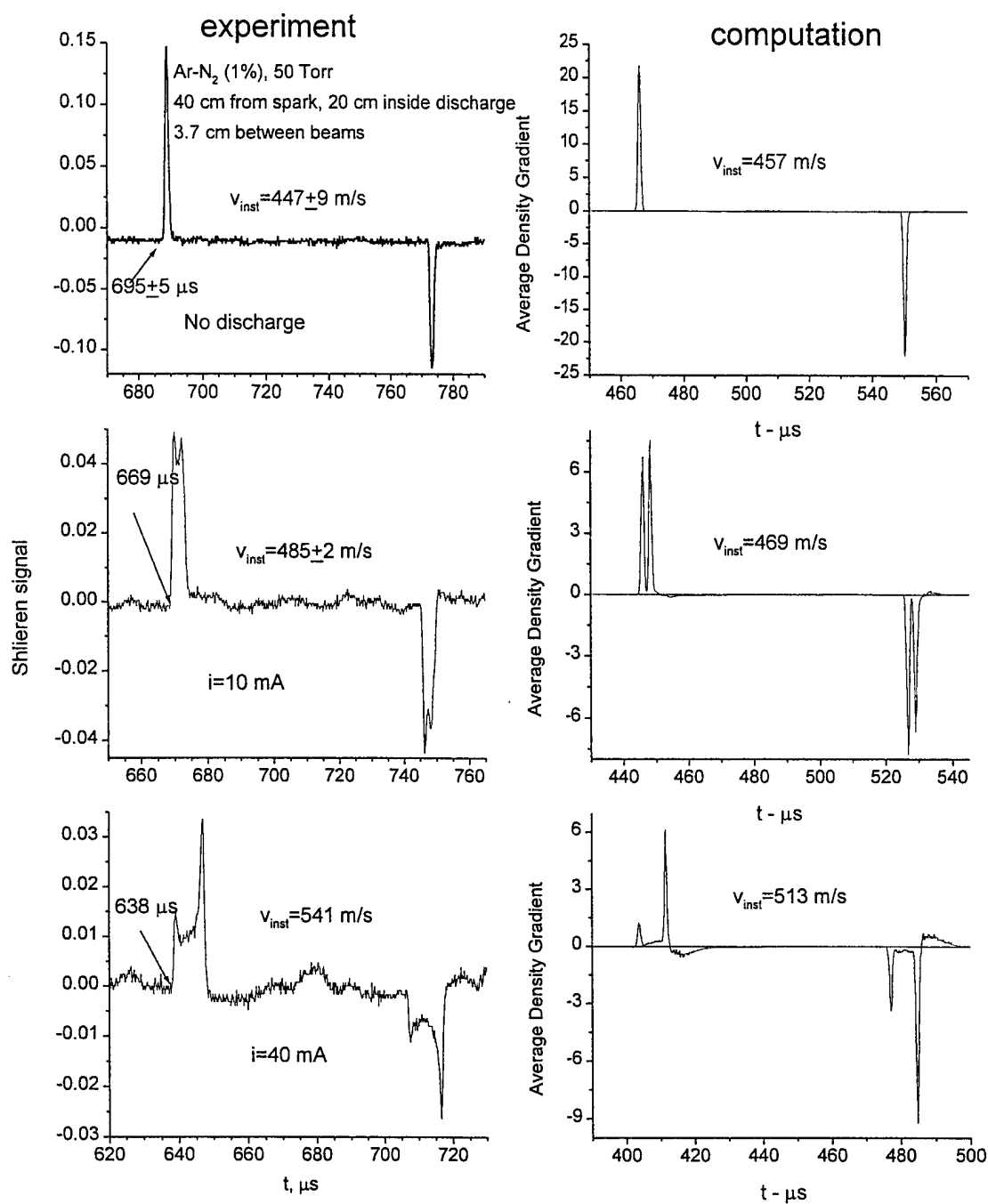
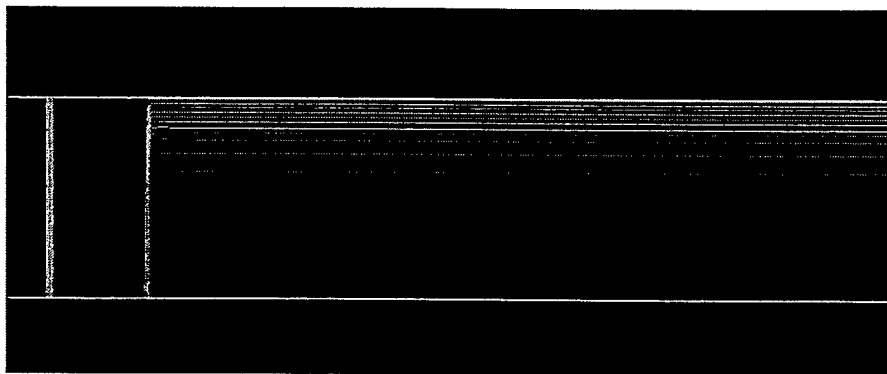
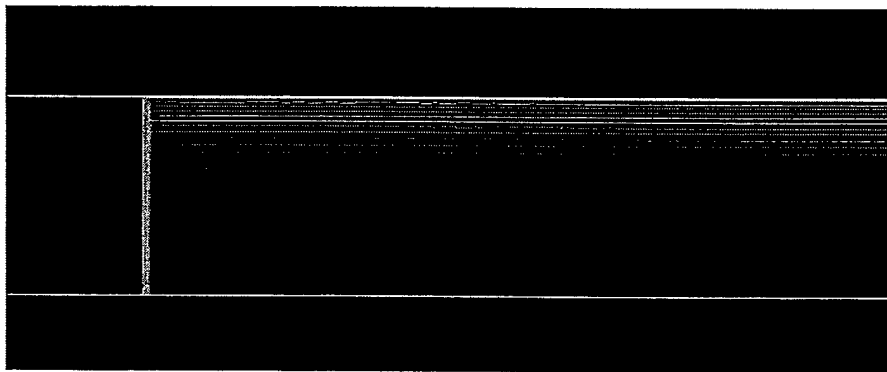


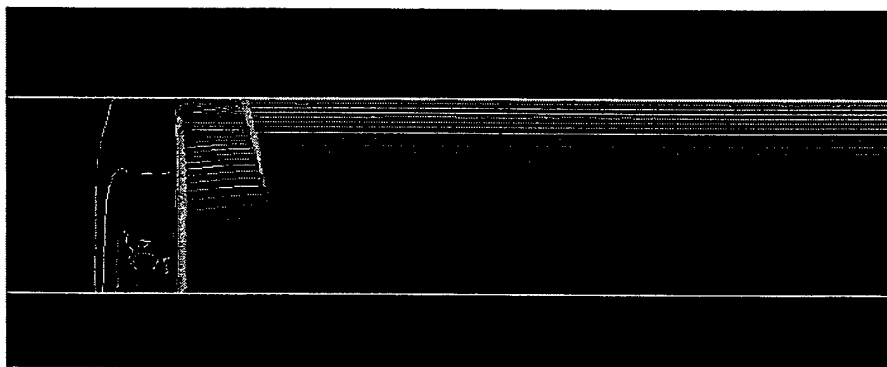
Fig.11. Experimentally measured and simulated laser Schlieren signals for shocks propagating in glow discharge in Ar+1%N₂ at 50 Torr. The discharge current values are 10 mA and 40 mA. The first of the two laser beams is located 20 cm from the entrance to the discharge, and the spacing between the two beams is 3.7 cm. The experimentally measured and computed shock velocities are indicated on the figure.



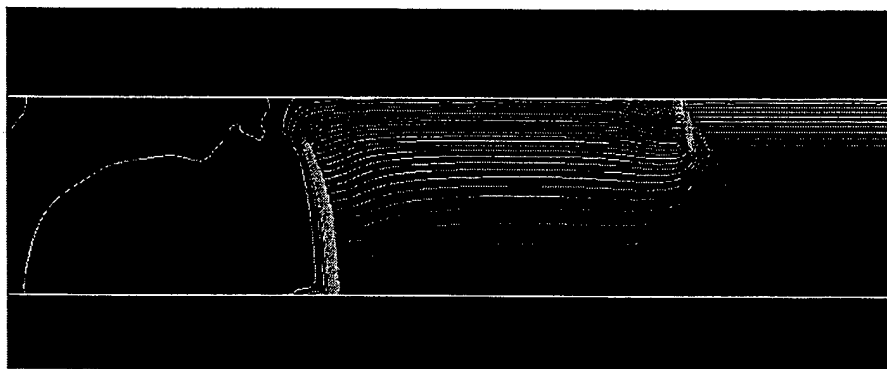
a



b



c



d

Fig.12. Computed constant-density lines during shock propagation in glow discharge tube (pure Ar, 50 Torr, 20 mA): a – prior to shock entry into the discharge; b – shock entering the discharge; c – shortly after the shock entered the discharge; d – shock has penetrated deep inside the discharge.

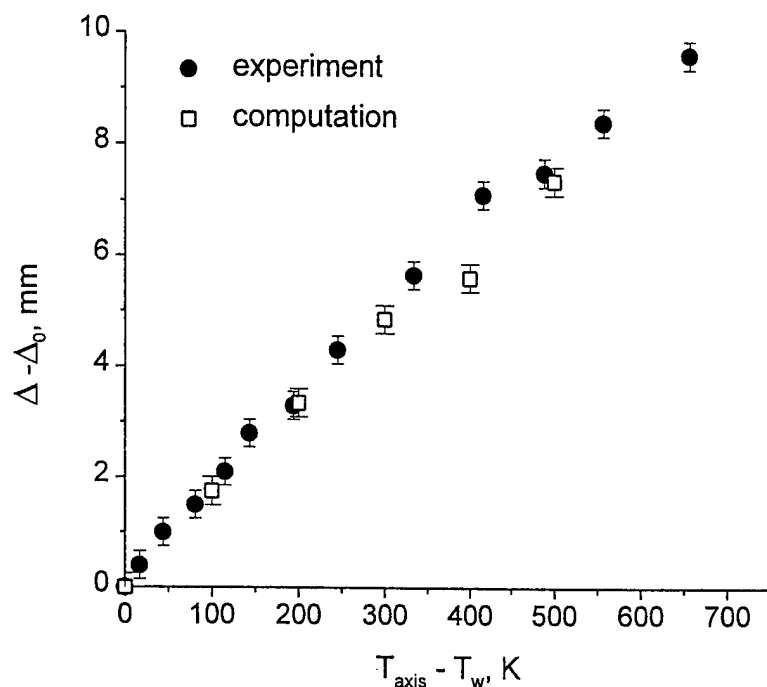


Fig.13. Width of the Schlieren signal in the discharge (Δ) minus the signal width with the discharge off (Δ_0) versus temperature difference between the axis and the wall, $T_{axis}-T_w$. Gas mixture Ar+0.16%N₂, pressure 50 Torr; 3 cm spark gap, 15 kV spark voltage; first laser beam is 24.8 cm inside the discharge; spacing between the two beams is 2.9 cm.

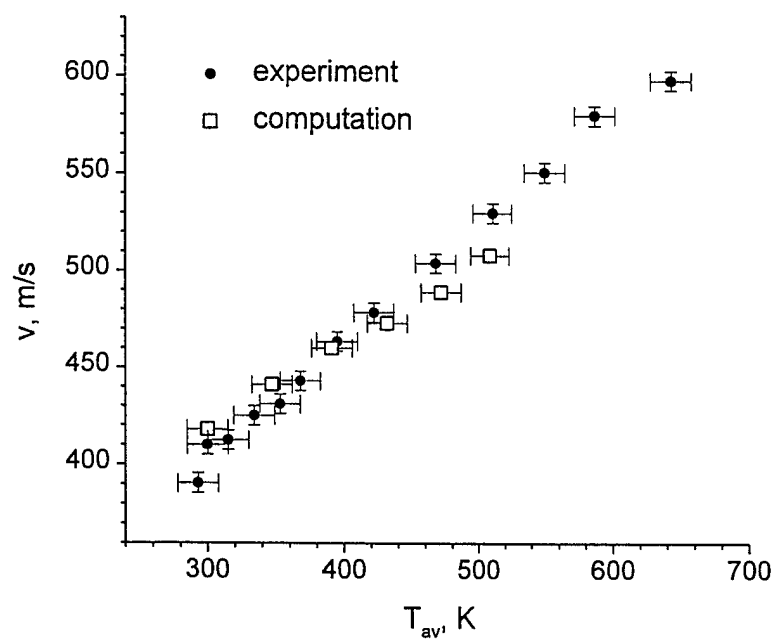


Fig.14. Shock wave velocity versus average temperature [definition – see Eqn. (2)] in the discharge. Gas mixture Ar+0.16%N₂, pressure 50 Torr; 3 cm spark gap, 15 kV spark voltage; first laser beam is 24.8 cm inside the discharge; spacing between the two beams is 2.9 cm.

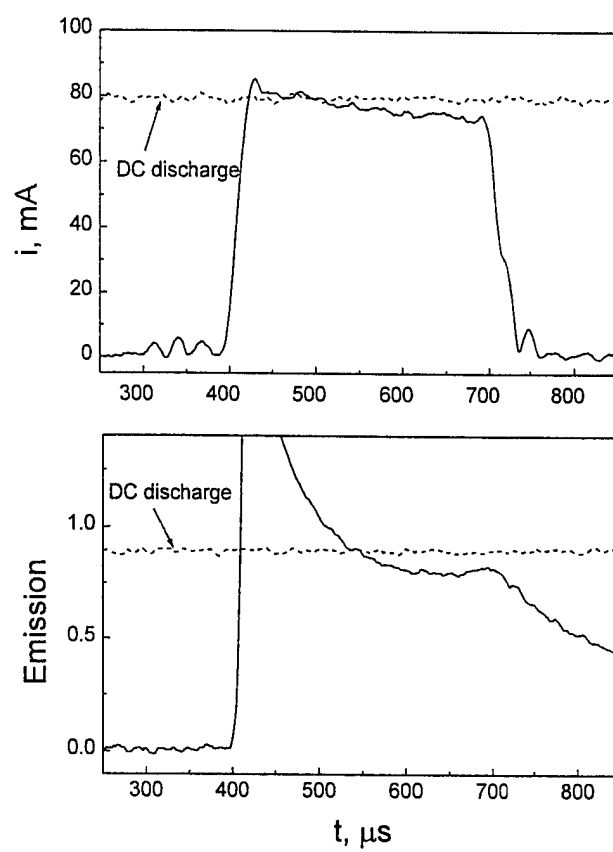


Fig.15. Discharge current and integrated spectral emission versus time during the pulse.

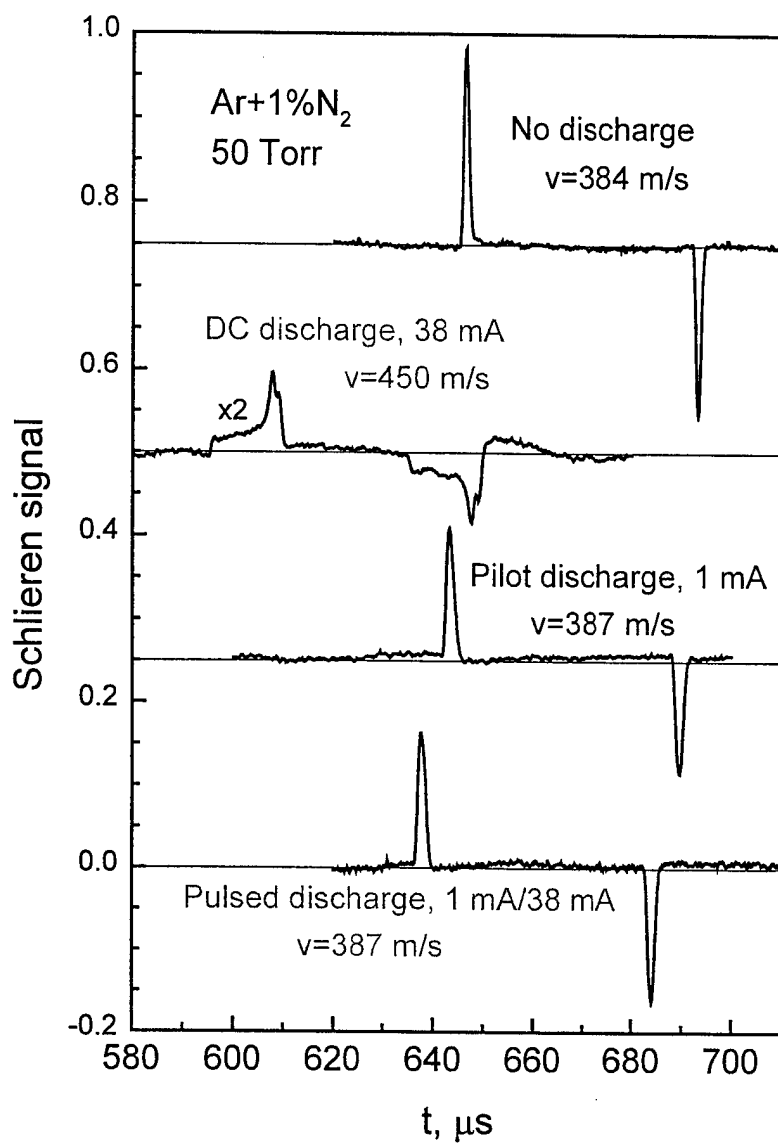


Fig.16. Schlieren signals and shock velocities in glow discharge in Ar+1%N₂ at 50 Torr: the discharge off, 38-mA continuous d.c. discharge, weak (1 mA) pilot discharge, and a pulsed discharge.

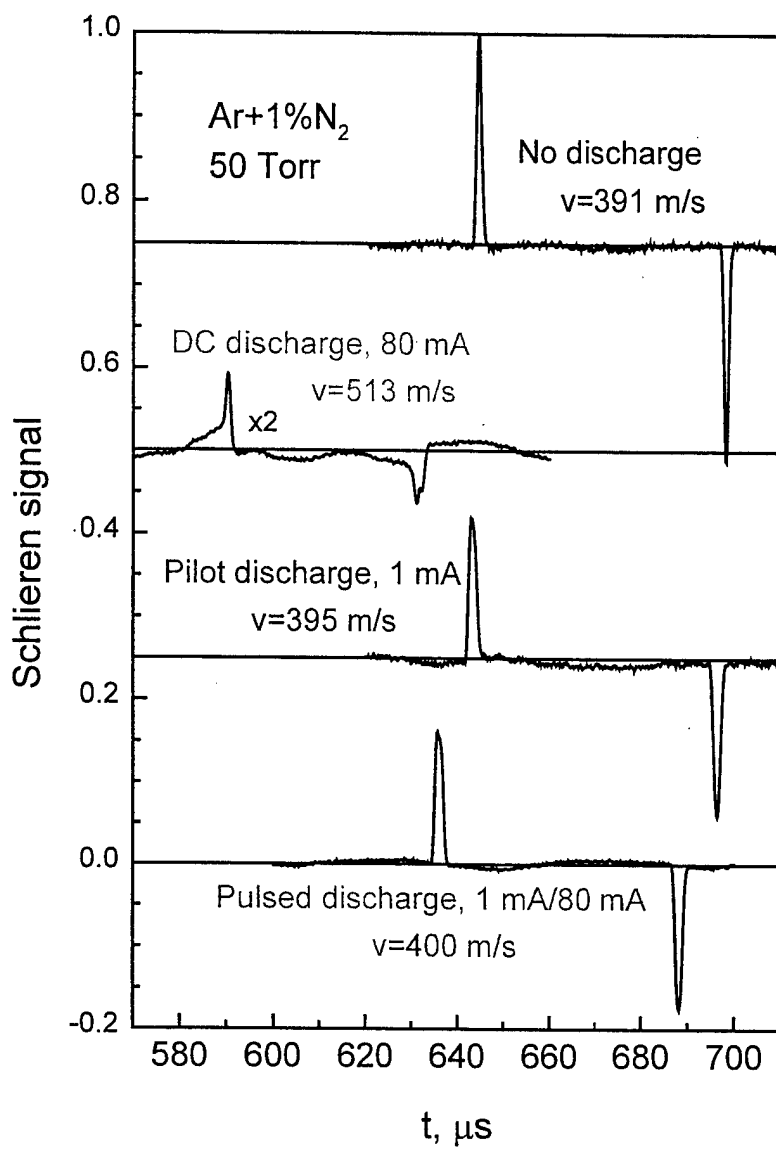


Fig.17. Schlieren signals and shock velocities in glow discharge in $\text{Ar}+1\%\text{N}_2$ at 50 Torr: the discharge off, 80-mA continuous d.c. discharge, weak (1 mA) pilot discharge, and a pulsed discharge.

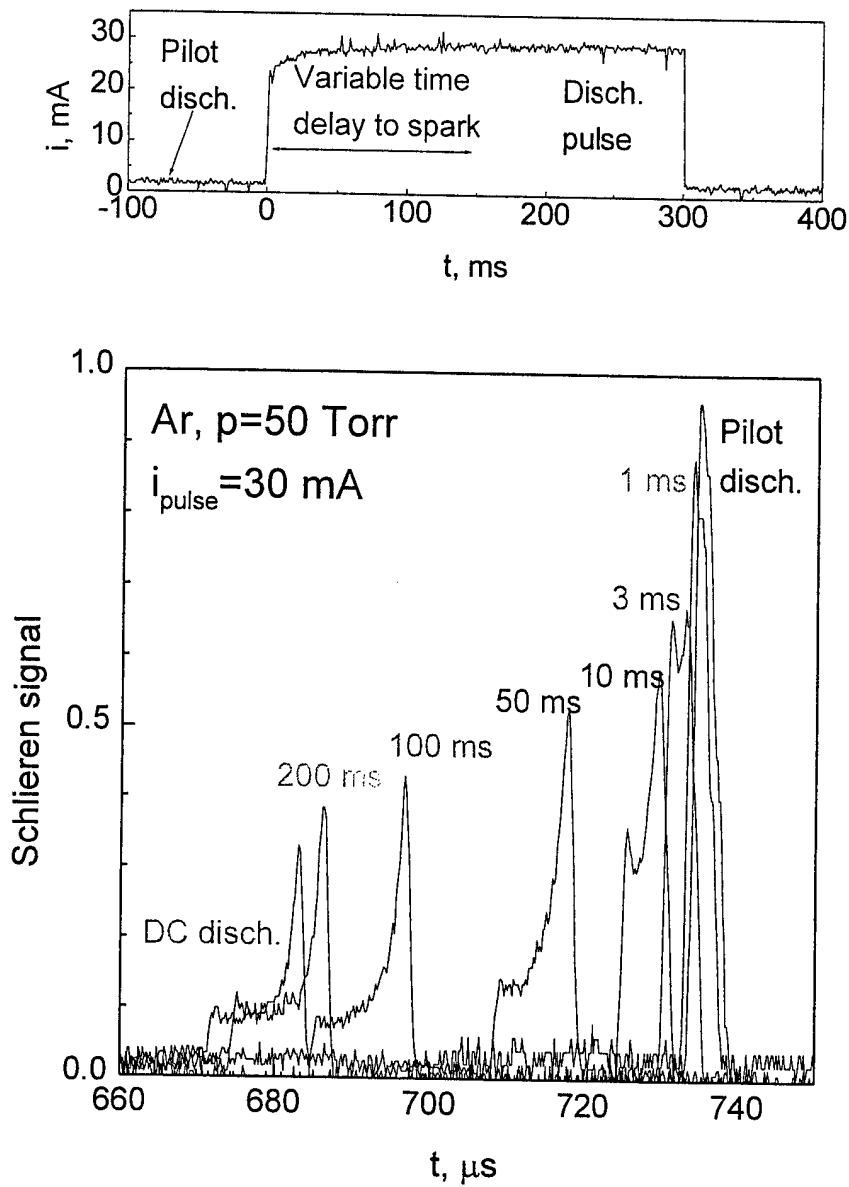


Fig.18. Evolution of the Schlieren signal at a fixed location inside the discharge with time delay between the beginning of the discharge and the shock launch

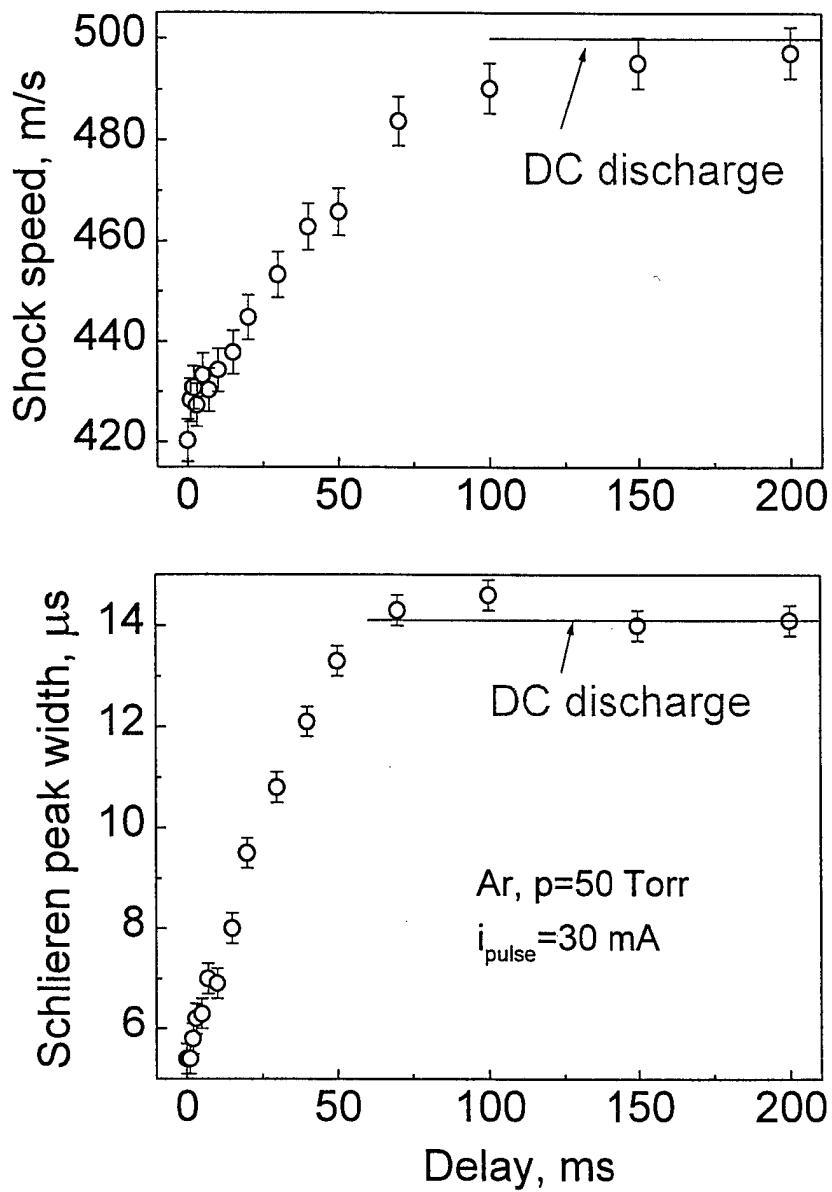


Fig.19. Evolution of shock velocity and the width of the Schlieren signal at a fixed location inside the discharge with time delay between the beginning of the discharge and the shock launch

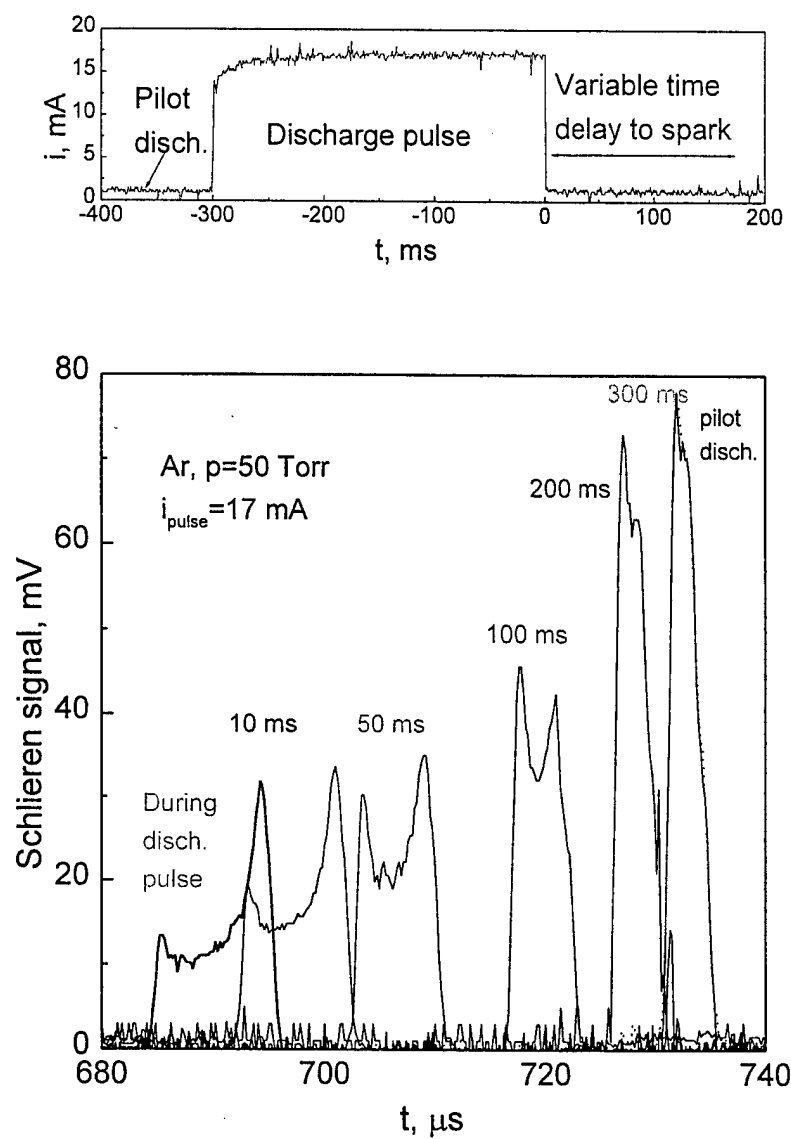


Fig.20. Evolution of the Schlieren signal at a fixed location inside the discharge with time delay between the end of the discharge pulse and the shock launch.

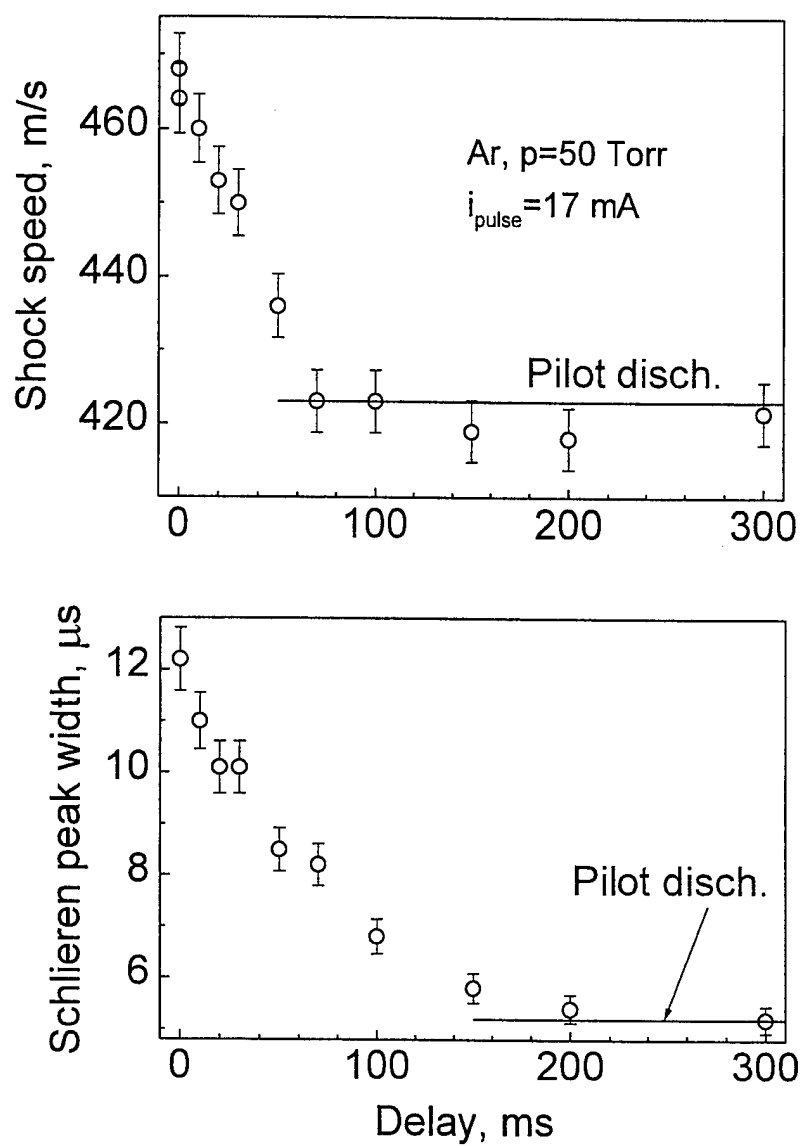


Fig.21. Evolution of shock velocity and the width of the Schlieren signal at a fixed location inside the discharge with time delay between the end of the discharge pulse and the shock launch

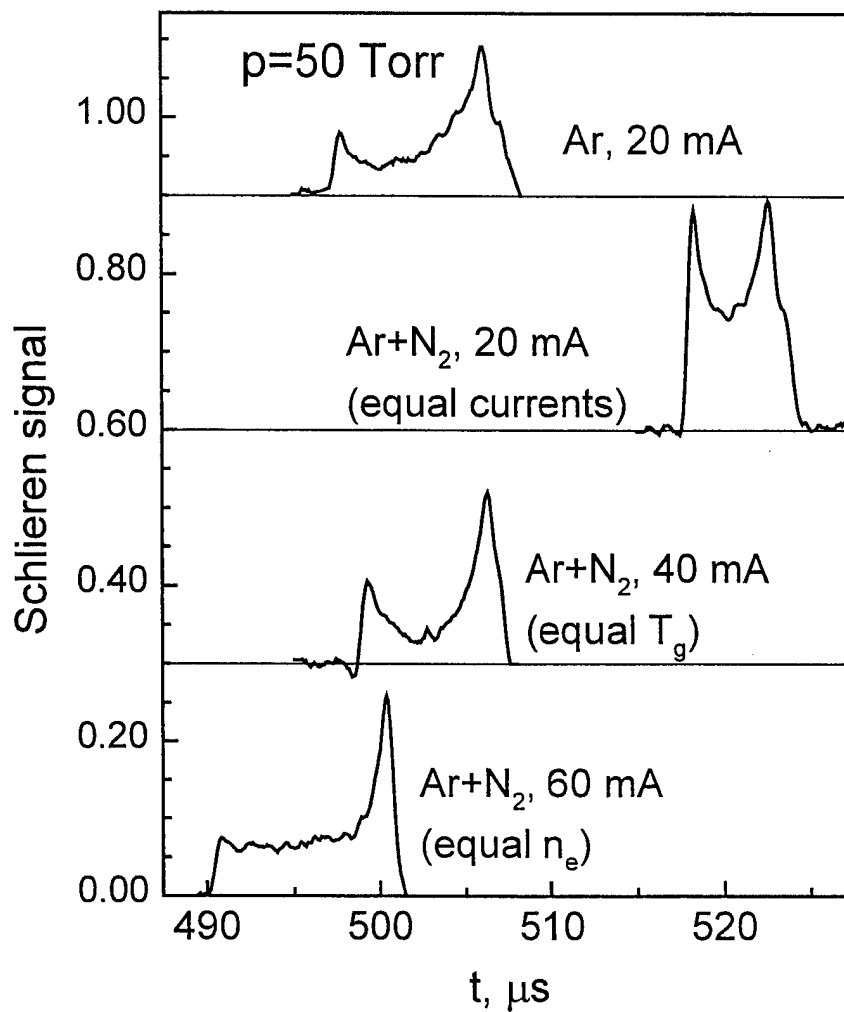


Fig.22. Comparison of shock Schlieren signals at a fixed location in Ar and Ar+N₂ discharges at 50 Torr and various values of electric current.



ELSEVIER

23 August 1999

PHYSICS LETTERS A

Physics Letters A 259 (1999) 387–392

www.elsevier.nl/locate/physleta

Direct evidence for thermal mechanism of plasma influence on shock wave propagation

Y.Z. Ionikh¹, N.V. Chernysheva¹, A.V. Meshchanov¹, A.P. Yalin, R.B. Miles^{*}

Department of Mechanical and Aerospace Engineering, Princeton University, Princeton, NJ 08544, USA

Received 14 June 1999; accepted 27 June 1999

Communicated by M. Porkolab

Abstract

Shock wave propagation through a glow discharge is studied by a double beam laser Schlieren method. A pulsed discharge is used to separate electron and other plasma related phenomena from thermal effects. The results prove the pure thermal nature of the influence of a plasma on a shock wave. © 1999 Published by Elsevier Science B.V. All rights reserved.

PACS: 52.35T; 52.80; 52.70; 42.60.K

Keywords: Shock waves; Nonequilibrium plasmas; Glow discharges

1. Introduction

During the last two decades a number of experiments were performed (see Refs. [1–8] and references therein) to study the influence of gas discharge plasmas on the properties of shock waves propagating through them. In spite of the variety of kinds of discharge studied, of gases and of experimental conditions, the main features of this influence are similar. They are accelerating of the shock, its spreading and/or splitting, and weakening. The effects are rather pronounced and are reproduced in studies of different authors. However, there is no consensus of

opinion as to reasons for these phenomena. Some authors [3,4,6] propose the most evident explanation, attributing all the effects to the heating action of the discharge and the resulting increase and non-uniformity of gas temperature. These authors showed that their results could be well described by this model. The same model is supported in theoretical works [9,10]. An opposite point of view is advocated by the authors of Refs. [1,2,5,7,8]. They claim that gas heating is not sufficient to produce the observed effects and alternative mechanisms have to be invoked. A number of mechanisms have been proposed, sometimes rather exotic. They are reviewed by the authors of Ref. [11], who conclude that none of them can provide satisfactory quantitative description of the phenomena observed.

It is clear that gas heating is produced by any kind of discharge. Further, all of the observed phenomena

^{*} Corresponding author. E-mail: miles@princeton.edu

¹ Permanent address: Institute of Physics, St. Petersburg University, St. Petersburg 198904, Russia.

can, in principle, be explained by this heating. To conclude that heating does not provide quantitative agreement with experiment, one needs to have reliable data on gas temperature in the discharge and on its spatial distribution. Such data are difficult to acquire and are usually not available. In rejecting the thermal model, the authors of [5] claim that they pass the shock wave through a cold (unheated) pulsed discharge, but simple estimation shows that for conditions where splitting and broadening of shock wave are observed (Fig. 3 of Ref. [5]), their average temperature could easily have reached 520 K. Some of the studies seem to confirm thermal mechanisms, though the authors proclaim the opposite. For example, Fig. 3 of Ref. [7] shows almost identical dependencies of pressure versus time for a shock wave propagating through a discharge and through gas heated by a special warmer, but the authors argue against a thermal mechanism.

On the other hand, solid evidence of the thermal mechanism also requires detailed information about the spatial distribution of the gas temperature in the discharge. This is a challenging measurement problem for studies of shock wave propagation. It is performed in only Ref. [6] by emission spectroscopy. Unfortunately velocity is the only shock wave parameter that is measured by the authors of [6], and the detection method is indirect. They used microwave interferometry for observing a change in electron number density induced by the shock wave. The measurements therefore have rather poor spatial resolution (~ 15 mm). Calculation of gas temperature in a plasma [3,4] requires data on spatial distribution of energy input (of current density in a longitudinal discharge). The lack of such data casts some doubt on the results of these studies.

In order to determine whether gas heating is a governing factor or not, some definitive experiment is needed. Two kinds of experiments can be proposed, both of them based on the slow gas temperature time dependence as compared to that of electron parameters. The first one uses the far discharge afterglow stage, when there are no charged or excited species but gas the temperature is still similar to the temperature under discharge conditions. Estimations show, that for the conditions of recent study [8] (Ar discharge at pressure 30–50 Torr, current about 50 mA) electron and ion densities drop by two

orders of magnitude during the first 10 ms of afterglow. The excited level populations drop still more. Meanwhile, the gas temperature and its spatial distribution have a characteristic decay time of ~ 100 ms. An afterglow study was performed in [2] but without any clear treatment of the results.

The second approach is to study an initial stage of a discharge pulse (or a short discharge pulse), when the densities of charged and excited species are close to their steady-state value, while the gas is still cold. Similar experiments were performed in [4,5], but in [5] gas heating may have actually occurred (see above). In [4], it is impossible to understand from the presented plot how close to cold gas conditions the authors could come.

In this study we utilized the second approach. Its advantage is that one can follow the discharge current as a simple way to monitor reaching the steady-state electron density. Another very important advantage is that if a sufficiently high overvoltage across the discharge is used, it is possible to reach steady state for the electron component very quickly, many orders of magnitude faster than that for gas temperature. This almost completely prevents the gas from heating.

2. Experimental

The experimental set-up was basically similar to that of [8]. The plasmas studied were created by longitudinal continuous or pulsed glow discharge. The discharge tube, 3.8 cm i.d. and 120 cm full length, was made of quartz. Shock waves were generated by a spark discharge at the one end of the tube. The spark circuit parameters are: capacitor 0.2 μ F, voltage 15–20 kV. The capacitor discharge was controlled by a triggering spark gap. The shock wave entered the discharge through a narrow (2 mm) ring electrode made of stainless steel foil mounted adjacent to the wall. The electrode nearest to the spark was always the anode, in order to prevent the incoming shock wave from passing by the hot cathode and through the cathode fall of the discharge. Both the cathode and anode could be placed at different location in the tube, so that the distance between the spark and the anode could be 20 or 40 cm, and the length of discharge could be 20, 40, or 60 cm. The

flexibility in changing the discharge length was used for measuring the electric field in the plasma (see below).

Similar to [8], we used a laser Schlieren method [12] for detecting the shock wave front (Fig. 1). A He–Ne laser beam crossed the discharge horizontally along the diameter and was then focused onto the plane of a knife by a lens ($f = 50$ cm). The beam $1/e$ diameter was about 0.3 mm. A photodiode with a response time of 20 ns measured the light intensity after the knife edge. The signal was recorded by a digital oscilloscope with $1\text{ k}\Omega$ resistor at the input, and a time resolution $\approx 0.1\text{ }\mu\text{s}$. In some measurements a miniature pressure sensor was also used.

To measure the instantaneous shock wave velocity we used an approach similar to that proposed in [13]. After the laser beam crossed the discharge it was retro-reflected from a small 90° prism and passed through the discharge once more with the spatial offset and then focused onto the knife edge. This produced two closely separated Schlieren signals of opposite signs. Shock wave velocity was found by dividing the distance between the two beam passages (12 to 21 mm) by the time gap between Schlieren signals. This method provided an accuracy of absolute velocity near 3% ($\approx 10\text{ m/s}$) and that of relative velocity about 0.5% (2 m/s).

Experiments were performed in an Ar–N₂ mixture (1% of N₂). Addition of nitrogen essentially improved the radial uniformity of the discharge. A pure argon discharge contracted at current $i > 30\text{--}40\text{ mA}$ (for pressure $p \geq 30\text{ Torr}$). With nitrogen the discharge was not contracted at all conditions studied ($p \leq 100\text{ Torr}$, $i \leq 100\text{ mA}$). To prevent elec-

trophoresis and accumulation of impurities, the gas mixture was pumped through the discharge with a rate of 300 sccm, which corresponded to 5–10 cm/s linear speed in the tube.

Axial gas temperatures in the discharge were measured by ultraviolet Rayleigh scattering [14]. A frequency tripled, pulsed, Ti:Sapphire laser system was used as the illumination source for measurements. Pulse energies of 5–10 mJ were delivered along the axis of the discharge tube and the Rayleigh signal was collected with a photomultiplier tube. The discharge temperatures were inferred by measuring the ratio of the Rayleigh scattering signal with the discharge on, to the Rayleigh scattering signal with the discharge off (room temperature). For the range of experimental conditions studied, $p = 30\text{--}50\text{ Torr}$, $i = 30\text{--}100\text{ mA}$, the steady-state centerline temperature range was found to be from $440 \pm 30\text{ K}$ to $830 \pm 70\text{ K}$.

As was already mentioned, the flexibility in changing the discharge length allowed us to measure an electric field E in a positive column of the discharge (cathode voltage drop V_c could also be found at these measurements). For $p = 30\text{--}50\text{ Torr}$, $i = 30\text{--}100\text{ mA}$ the E value was from 8 to 14 V/cm. Assuming a Bessel radial profile for gas temperature, we calculated the reduced electric field E/N (N is gas number density) and electron number density n_e . Averaged over the tube cross section, these values are $E/N = 1.2\text{--}1.4\text{ Td}$, $n_e = (1.2\text{--}4) \times 10^{10}\text{ cm}^{-3}$ for the condition range mentioned above. We emphasize that these values are not used for any analysis of the results of this study. (Notice that electric field values given in [8] are evidently erroneous (see, e.g. [15]). For such a field the gas temperature at the discharge axis must reach the unlikely value of 1800 K).

The pulsed mode of the discharge was produced by using a transistor switch in series with the discharge. The rise time for the current pulse was 20 μs , and the pulse duration was about 0.5 ms. It was found that this time was insufficient to get a uniform discharge. Therefore a weak pilot discharge with 1 mA current was maintained between pulses, which resulted in a fairly uniform volume pulsed discharge. Fig. 2 shows the discharge pulse shape and the position of Schlieren signals inside the pulse. The time dependence of discharge integral emission is

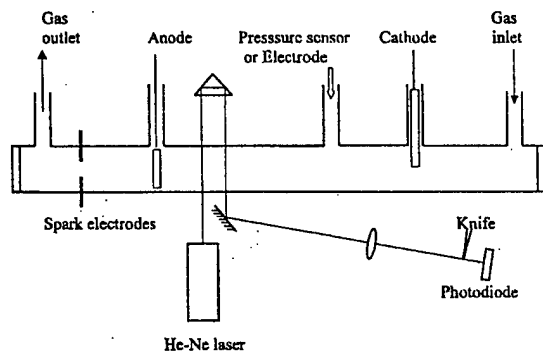


Fig. 1. Schematic of the experimental set-up.

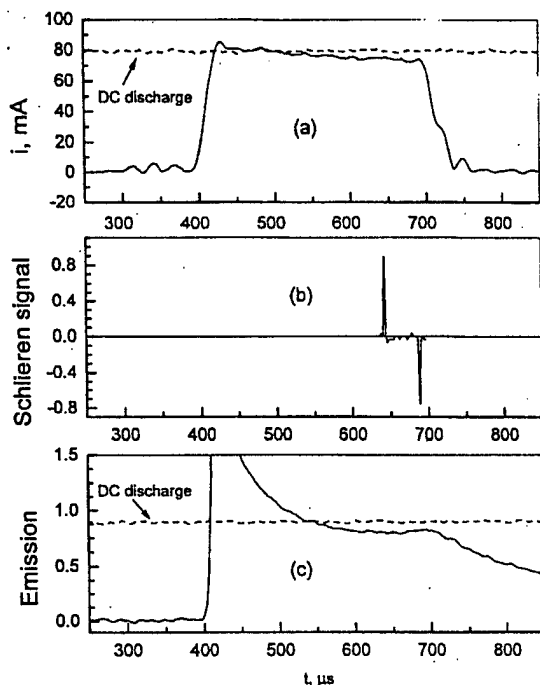


Fig. 2. Time dependence of discharge current (a), Schlieren signal (b), and discharge emission intensity (c). Time $t = 0$ corresponds to the spark shot.

also plotted (with no shock wave). It shows that at times near to the middle of the pulse the emission reaches a steady-state value, similar to that of the continuous discharge. The initial peak of intensity is a result of the higher electric field arising in the discharge immediately after the transistor switch is opened (see below).

3. Results and discussion

Data from our Schlieren measurements in a steady glow discharge are in general agreement with results of previous studies [1–8]. Some of them are presented in Figs. 3 and 4 for $p = 50$ Torr, 29 cm distance of the laser from the spark (9 cm from the anode), and for two different discharge currents (38 and 80 mA). Time for all of the curves is measured from the spark. Curves (a) of these Figures correspond to Mach 1.2 in cold (with no discharge) gas. Curves (b) (continuous discharge) demonstrate all the main features described in the Introduction. The

shock wave is accelerated, the effect being more pronounced at larger current. Further, the signal (which is proportional to gas density gradient) is attenuated by the plasma, and it is split and spread out.

For the pilot discharge [curves (c)] a small acceleration, accompanied by some widening and weakening of the signal can also be noticed, but they are very weak compared to the higher current discharge. This is no surprise since the electron number density in the pilot discharge is $\approx 10^8 \text{ cm}^{-3}$ only and the measured axial gas temperature $T_g < 320 \text{ K}$.

Much more important is that Schlieren signal obtained from the pulsed discharge [curves (d)] closely matches both (a) and (c) curves, and is very unlike the signal from the continuous discharge, curves (b). After the transistor switch turns on, the discharge current reaches its new steady-state value in $\approx 20 \mu\text{s}$. This value is almost the same as in continuous discharge [curves (b)]. The electric field strength E in the pulse could be found by subtracting cathode drop V_c and voltage drop across the ballast resistor from the power supply voltage. The

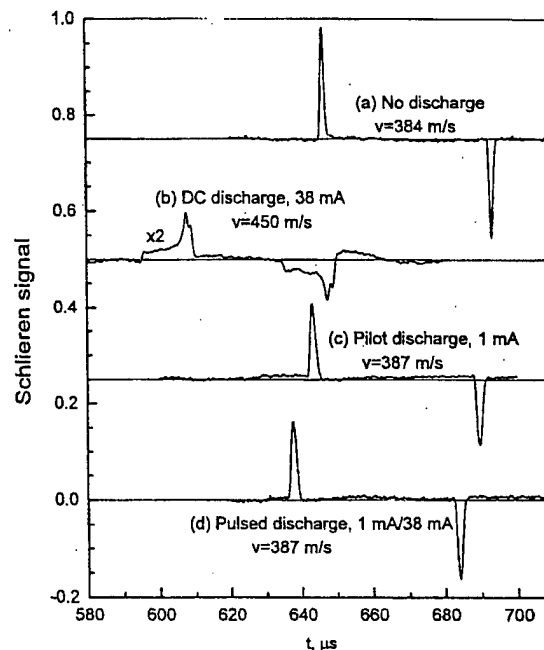


Fig. 3. Schlieren signals for Ar-N₂ mixture (1% of N₂). Pressure 50 Torr, 29 cm from the spark, 9 cm inside the discharge, 1.8 cm between the two laser beam passages.

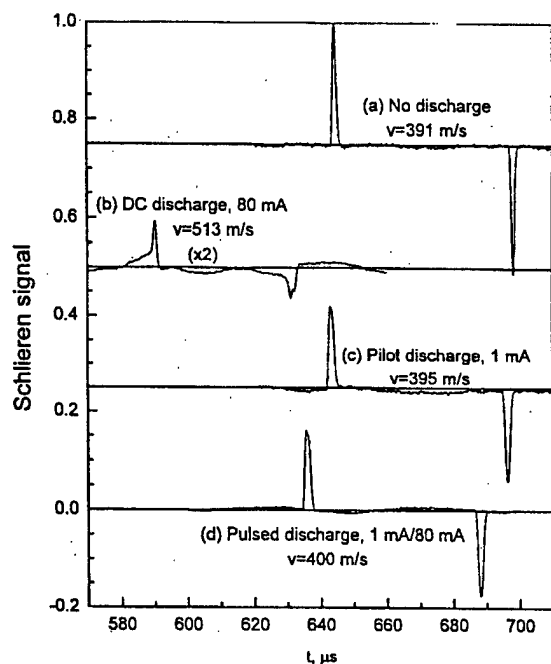


Fig. 4. The same as Fig. 3 (2.1 cm between the two laser beam passages).

E values were found to be somewhat larger than in the continuous discharge, but the E/N values are almost equal. So the same is valid for the electron number densities and mean electron energies (electron temperatures). This is confirmed by the behavior of the discharge emission (Fig. 2). It reaches a steady-state value that is very close to that of the continuous discharge. An initial peak is related to the overvoltage applied to the discharge in the transition period from small to large current ($\sim 20 \mu\text{s}$). Higher E/N values in this interval result in efficient excitation of atoms and molecules, including those with radiative lifetime $\sim 1\text{--}10 \mu\text{s}$ (e.g., intensive bands of the 1st positive system of the N_2 molecule).

The rise in gas temperature ΔT during the pulse for the pulse duration τ_p may be calculated from the equation

$$iE\tau_p = c_p m_1 \Delta T,$$

where c_p is specific heat capacity and m_1 is a mass of gas per unit length. Here we ignore heat losses because the pulse duration is a factor of 100 less than the characteristic time for thermal conductivity. For the conditions of Figs. 3 and 4 this equation

gives $\Delta T = 0.4 \text{ K}$ and 0.6 K . So, the pulsed discharge has electron component parameters (E/N , n_e , T_e) the same as in the continuous discharge, but a gas temperature is the same as in pilot discharge, that is close to room temperature. Comparing the three Schlieren curves (b), (c), and (d) of Figs. 3 and 4 definitely shows that changing the electron density by two orders of magnitude [(c) \rightarrow (d)] does not influence shock wave propagation, while changing gas temperature from $T_g \approx 320 \text{ K}$ to $T_g \approx 500\text{--}600 \text{ K}$ [(d) \rightarrow (b)] affects it drastically. This result may be considered as strong evidence of thermal mechanism effecting a shock-wave-plasma interaction.

It should be noted that apart from the gas temperature one more parameter is quite different for a pulsed and continuous discharge. This is nitrogen vibrational populations, or vibrational temperature T_v . The vibrational relaxation characteristic time is 1–2 orders of magnitude longer than the pulse duration, so T_v in the pulsed discharge must be almost the same as in the pilot (1 mA) discharge. Therefore this study can not argue against the vibrational mechanism to explain the effect [7].

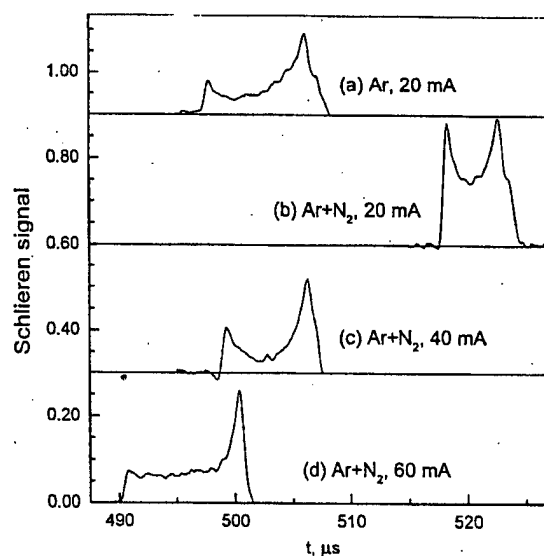


Fig. 5. Comparison of the Schlieren signals from the discharge in Ar and in Ar- N_2 mixture at equal currents [(a) and (b)], equal gas temperatures [(a) and (c)], and equal electron densities [(a) and (d)]. Pressure 50 Torr, the same point as in Figs. 3 and 4 (larger shock wave velocity is due to larger spark electrode gap).

In order to clear up its role, shock wave propagation through pure argon discharge was also studied at low currents where contraction did not occur. In Fig. 5, Schlieren signals for the two gas media (Ar and Ar–N₂) are compared. We can see that the main features of the pattern for both cases are similar. For a more detailed comparison, one has to take into account that addition of nitrogen changes the electron drift velocity [16] and also can influence ionization and recombination processes. As a result, plasma parameters such as electron field E/N , electron number density and gas temperature are different for Ar and Ar–N₂ plasmas even if the gas pressure and discharge current are similar. Data presented in Fig. 5 for Ar–N₂ mixture are shown at $i = 20$ mA (the same as for pure argon), at 40 mA, where gas temperatures are equal for both discharges, and at 60 mA, where electron densities are equal. It is evident, that for the condition of equal T_e (40 mA) similarity of the patterns is the best. This eliminates unambiguously the vibrational mechanism and supplies one more confirmation of the validity of the thermal one.

Acknowledgements

The work was supported by the AFOSR New World Vistas Program.

References

- [1] A.I. Klimov, A.N. Koblov, G.I. Mishin, Yu.L. Serov, I.P. Yavor, *Sov. Tech. Phys. Lett.* 8 (1982) 192.
- [2] A.I. Klimov, A.N. Koblov, G.I. Mishin, Yu.L. Serov, K.V. Khodataev, I.P. Yavor, *Sov. Tech. Phys. Lett.* 8 (1982) 240.
- [3] N.V. Evtyuhin, A.D. Margolin, V.M. Shmelev, *Sov. J. Chem. Phys.* 3 (1986) 2080.
- [4] A.P. Ershov, A.A. Kuzovnikov, S.E. Ponomareva, A.I. Shcherbakov, in: *Fundamental problems of shock wave physics, Proc. Conf. 1987, Chernogolovka. V.1. Pt.2. P.183* (in Russian).
- [5] A.I. Klimov, G.I. Mishin, *Sov. Tech. Phys. Lett.* 16 (1990) 960.
- [6] P.A. Voinovich, A.P. Ershov, S.E. Ponomareva, V.M. Shibkov, *High Temp.* 29 (1991) 468.
- [7] A.Yu. Gridin, A.I. Klimov, N.E. Molevich, *Tech. Phys.* 38 (1993) 238.
- [8] B.N. Ganguly, P.B. Bletzinger, A. Garscadden, *Phys. Lett. A* 230 (1997) 218.
- [9] A.Kh. Mnatsakanyan, G.V. Naidis, S.V. Rumyantsev, *Proc. 16th Int. Symp. on Shock Tubes and Waves, Aachen, 1987*, p.201.
- [10] S.O. Macheret, L. Martinelli, R.B. Miles, *AIAA Paper* 99-0598.
- [11] I.O. Adamovich, V.V. Subramaniam, J.W. Rich, S.O. Macheret, *AIAA J.* 36 (1998) 816.
- [12] J.H. Kiefer, R.W. Lutz, *Phys. Fluids* 8 (1965) 1393.
- [13] J.A. Bander, G. Sanzone, *Rev. Sci. Instrum.* 45 (1974) 949.
- [14] A. von Engel, *Ionized Gases*, Clarendon Press, Oxford, 1955.
- [15] A.P. Yalin, Y. Ionikh, R.B. Miles, *AIAA Paper* 99-0642.
- [16] S.C. Brown, *Basic Data of Plasma Physics*, M.I.T. Press, Cambridge, MA and London, 1966.

SHOCK WAVE PROPAGATION AND DISPERSION IN GLOW DISCHARGE PLASMAS

**Sergey O. Macheret,^{a)} Yuri Z. Ionikh,^{b)} Naira V. Chernysheva,^{b)} Azer P. Yalin,
Luigi Martinelli, and Richard B. Miles**

Department of Mechanical and Aerospace Engineering, Princeton University

D-414 Engineering Quadrangle, Princeton, NJ 08544

ABSTRACT

Spark-generated shock waves were studied in glow discharges in argon and argon-nitrogen mixtures. UV Filtered Rayleigh Scattering was used to measure radial profiles of gas temperature, and laser schlieren method was used to measure shock arrival times and axial density gradients. Time accurate, inviscid, axisymmetric CFD computations were run and results compared with the experiments. Our simulation show that changes in shock structure and velocity in weakly ionized gases are explained by classical gas dynamics, with critical role of thermal and multi-dimensional effects (transverse gradients, shock curvature, etc.). A direct proof of the thermal mechanism was obtained by pulsing the discharge. With sub-millisecond delay between starting the discharge and shock launch, plasma parameters reach their steady-state values, but the temperature is still low, laser schlieren signals are virtually identical to those without the discharge,

differing dramatically from the signals in discharges with fully established temperature profiles.

I. INTRODUCTION

Weakly ionized gases (plasmas) could potentially have an impact on high-speed aerodynamics. Using plasmas for shock wave control, drag reduction, vehicle steering, sonic boom attenuation, ignition of combustion in engines, and MHD power extraction and enthalpy by-pass is being actively discussed. Of course, fundamental issues have to be resolved prior to any practical applications.

Propagation of shock waves in weakly ionized plasmas was studied in Russia,^{1-11, 15, 16} and, later, in the U.S.¹²⁻¹⁴ Shock acceleration, broadening, and "splitting" was observed in various d.c., RF, and pulsed discharges, in inert as well as molecular gases. Some researchers^{1-11, 12-14} attributed experimental observations to various plasma-specific phenomena, from electric double layers to ion-acoustic waves to new long-range interactions or microscopic structure formed in gas discharges. However, other Russian researchers^{15, 16} found that their data can be adequately explained by conventional thermal phenomena. Gas heating, temperature inhomogeneity, and vibrational relaxation were theoretically shown to result in "anomalous" behavior of shocks in gas discharges.¹⁷⁻¹⁹

In Refs. 20 and 21, analysis of various physical mechanisms resulted in a conclusion that the "broadening", "splitting", and acceleration of shocks in gas discharges could hardly be explained by plasma-specific effects. This is due ultimately to the very low

ionization fraction in the discharges, which leads to small fraction of the total gas energy stored in ionized and excited states, to very inefficient energy and momentum transfer from electrons and ions to the bulk neutral gas, and to very long times of these transfer processes.

In 1997, two research groups simultaneously and independently showed, based on inviscid CFD modeling,^{22, 23} that transverse and longitudinal temperature and density gradients present in gas discharges due to Joule heating can be responsible for the observed “anomalous” shock profiles. The inviscid modeling of Ref. 22, extended in Ref. 24, emphasized that transverse gradients result in multi-dimensional nature of shock propagation, and that attempts to interpret the phenomena in one-dimensional terms can be misleading. For example, shock curvature could be misinterpreted as a “broadened” or “split” 1D structure. The inviscid results were confirmed in Navier-Stokes computations.²⁵ Additionally, as demonstrated in Ref. 25, in the case of very weak shocks (with Mach number very close to 1) or very long propagation distances (many meters) wall shear could also result in an apparent “splitting” of laser schlieren signals even in a cold gas.

In the present paper, we describe a combined experimental and computational effort to clarify mechanisms of shock propagation in weakly ionized plasmas. Experiments were done in well-characterized positive column of glow discharge in Ar and Ar-N₂ mixtures. Shock velocity and structure was measured using laser schlieren method, similar to experiments of Refs. 12-14. Since temperature and its gradients could play a critical role in shock propagation, radial temperature profiles in our experiments were measured with Filtered Rayleigh Scattering. Axisymmetric CFD modeling gives a very

good agreement with experimental data, thus proving that it is classical, but multi-dimensional, gas dynamics can explain for the "anomalous" effects.

In order to study shock propagation in weakly ionized plasma with very small or absent temperature gradients, pulsed discharge experiments were carried out. Those experiments prove again the thermal nature of shock propagation in gas discharges.

II. EXPERIMENTS ON SHOCK PROPAGATION IN STEADY-STATE GLOW DISCHARGES

II.1. Experimental setup and procedures

The experimental setup at Princeton University^{26, 27} is basically similar to that of Refs. 12-14. The plasmas studied were created by longitudinal continuous or pulsed glow discharge. The discharge tube, 3.8 cm i.d. and 120 cm full length, was made of quartz. Shock waves were generated by a spark discharge at the one end of the tube. The spark circuit parameters are: capacitor 0.2 μ F, voltage 15 – 20 kV. The capacitor discharge was controlled by a triggering spark gap. The shock wave entered the discharge through a narrow (2 mm wide and 0.1 mm thick) ring electrode made of stainless steel foil mounted adjacent to (almost flush with) the wall. The electrode nearest to the spark was always the anode, in order to prevent the incoming shock wave from passing by the hot cathode and through the cathode fall of the discharge. The cathode in all pulse and most steady-state experiments was identical in size and material to the anode. In some experimental runs, where shock profiles deep inside the plasma, far from the cathode, were studied, another

cathode was used: a 25 mm diameter hollow cylinder with the axis perpendicular to the tube axis. This cathode was used only when it was far enough downstream of the shock and could not affect shock propagation. Both the cathode and anode could be placed at different location in the tube, so that the distance between the spark and the anode could be 20 or 40 cm, and the length of discharge could be 20, 40, or 60 cm. The flexibility in changing the discharge length was used for measuring the electric field in the plasma (see below).

Similarly to Refs. 12-14, we used a laser schlieren method²⁸ for detecting the shock wave front (Fig.1). A He-Ne laser beam crossed the discharge horizontally along the diameter and was then focused onto the plane of a knife by a lens ($f=50$ cm). The beam $1/e$ diameter was about 0.3 mm. A photodiode with a response time of 20 ns measured the light intensity after the knife edge. The signal was recorded by a digital oscilloscope with 1 k Ω resistor at the input, and a time resolution $\approx 0.1 \mu\text{s}$. In some measurements a miniature pressure sensor was also used.

To measure the instantaneous shock wave velocity we used an approach similar to that proposed in Ref. 29. After the laser beam crossed the discharge it was retro-reflected from a small 90° prism and passed through the discharge once more with the spatial offset and then focused onto the knife edge. This produced two closely separated schlieren signals of opposite signs. Shock wave velocity was found by dividing the distance between the two beam passages (12 to 21 mm) by the time gap between the schlieren signals. This method provided an accuracy of absolute velocity near 3 per cent (≈ 10 m/s) and that of relative velocity about 0.5 per cent (2 m/s).

Experiments were performed in an Ar-N₂ mixture (1% of N₂). Addition of nitrogen substantially improved the radial uniformity of the discharge. A pure argon discharge contracted at currents $i > 30 - 40$ mA (for pressures $p \geq 30$ Torr). With nitrogen the discharge was not contracted at all conditions studied ($p \leq 100$ Torr, $i \leq 100$ mA). To prevent electrophoresis and accumulation of impurities, the gas mixture was pumped through the discharge with a rate of 300 sccm, which corresponded to 5 – 10 cm/s linear speed in the tube. Control measurements with the gas flow turned off for a short time gave shock velocities and schlieren profiles identical to those with the flow on.

As was already mentioned, the flexibility in changing the discharge length allowed us to measure an electric field E in a positive column of the discharge (cathode voltage drop V_c could also be found in these measurements). For $p = 30 - 50$ Torr, $i = 30 - 100$ mA the E value was from 8 to 14 V/cm. Assuming a Bessel radial profile for gas temperature, we calculated the reduced electric field E/N (N is the gas number density) and electron number density n_e . Averaged over the tube cross section, these values are $E/N = 1.2 - 1.4$ Td, $n_e = (1.2 - 4) \cdot 10^{10} \text{ cm}^{-3}$ for the condition range mentioned above.

II.2. Measurements of temperature profiles

We have used Ultraviolet Filtered Rayleigh Scattering (UV FRS)^{30,31} to measure temperature profiles of the discharges studied. A summary of these measurements is presented here. A narrow linewidth laser is used to illuminate the sample gas and the scattered light is imaged through a narrow band absorption filter onto a detector, as shown schematically in Fig.2. The laser should be tunable so that it may be tuned within

an absorption notch, and narrow linewidth so that the elastic background (due to windows, particulates etc.) is narrow compared to the spectral width of an absorption notch. The amount of scattered light measured by the detector depends on the spectral overlap of the scattered light and the filter absorption profile. The filter offers very nearly 100% transmission outside of the absorption notches, yet is extremely optically thick (suppression modeled as 10^5 and higher) within the absorption notches. The light scattered by the atoms and/or molecules in the flow is thermally and collisionally broadened, and is therefore spectrally wider than the laser and background. When the laser is tuned to overlap an absorption notch, the filter serves to suppress the background while transmitting a large fraction of the light scattered from the flow. By appropriate selection of filter conditions, and laser frequency, one may obtain very strong background suppression (greater than 10^5) while transmitting close to half of the scattered light.

Depending on the conditions of a specific measurement, slightly different approaches may be used. In cases of constant (known) pressure we use a method which precludes the need for background subtraction. The approach is to ratio the FRS signal at a temperature to be measured, T_M , to the signal at a known temperature, T_{ref} . Both measurements are taken at the same frequency within an absorption notch so that any background is strongly suppressed in both cases. At constant pressure there is a one-to-one correspondence of temperature and density so that the measured ratio uniquely defines the unknown temperature T_M . The signal ratio is primarily determined by the density ratio, with a smaller opposing contribution from lineshape effects.

Modeling results for the present measurements are shown in Figs.3 and 4. Fig. 3 shows the modeled filter transmission profile and FRS signal levels as functions of

frequency. The filter has a length of 5 cm, a mercury vapor pressure of 0.0030 torr, and a temperature of 315K. In this spectral region, mercury has six absorption notches due to hyperfine splitting and different isotopic contributions. Fig. 3 is a closer view of the highest frequency absorption notch – the one used in the current work. The nominal location of the lines is at 253.7 nm. The modeled FRS signal levels are for a scatterer of 50 Torr of argon at various temperatures. The Rayleigh scattering cross-section is not affected by the weak ionization and so the curves describe both argon gases and the plasmas used in these experiments. The signals are normalized to 300 K (by the ideal gas law) so that their relative magnitude scales as would be measured by a detector. In the absence of the filter the signal is linear with density (or $1/T$), while within the absorption features there is also a weaker effect from the variation of scattering linewidth with temperature. From such modeling one may find the relationship between the experimentally measured FRS signal ratio,

$$\text{Ratio} = \text{FRS signal } (T=T_M) / \text{FRS signal } (T=T_{\text{ref}}),$$

and the unknown temperature T_M . Fig. 4 is such a curve. In this case the unknown temperature, T_M , corresponds to the “plasma on” temperature while the reference temperature, T_{ref} , corresponds to the “plasma off” temperature – in this case $T_{\text{ref}}=308$ K.

The experimental configuration for FRS temperature measurements is illustrated in Fig.2. A high power, tunable, narrow linewidth Titanium Sapphire laser³² was used as the excitation source. The frequency-tripled output was delivered to the plasma tube through several anti-reflection coated beam-shaping optics. For these experiments pulse energies of ~ 10 mJ in the ultraviolet (254 nm) were used. The beam passed through a quarter wave plate to ensure the correct orientation of the linearly polarized beam, and

through a half-wave plate to correct for the slight elliptical polarization introduced at the tube windows. Several irises were used to reduce stray light carried with beam. A long focal length lens (~ 90 cm) was used to weakly focus the beam to a waist of ~ 200 microns at the sample volume. The sample volume was within the discharge tube and was defined by the laser beam waist and an iris located between the discharge tube and imaging lens ($f\# = 2.4$). The geometry was such that the sample volume had a length of about 1mm. The scattered light was collected at a scattering angle of 90 degrees with the imaging lens and imaged through the mercury vapor filter. The filter had length 5 cm and had two temperature controllers yielding a vapor pressure of 0.003 Torr, and a filter temperature of 315 K. After the mercury filter, the light passed through a monochromator, which acted as a broad passband filter, while rejecting plasma luminosity and other colors of light from the laser. Finally, the scattered light signal was collected with a Hamamatsu R960 photomultiplier tube. After propagation through the discharge tube a quartz flat was used to pick off a fraction of the beam for power normalization as well as a frequency reference. The picked off beam illuminated a diffuser, and the elastically scattered light was detected through a second mercury filter (frequency reference), as well as measured by a photodiode (power reference). The latter two measurements used thin film interference filters (CORION G25-254-F) for spectral filtering. The three signals were collected with a Stanford Research System boxcar onto a computer.

In plasma temperature profile measurements, a thermocouple was used to the measure the wall temperature. Two 1-D translation stages were used to translate the discharge tube horizontally relative to the laser beam. Radial profiles along the horizontal

axis were found by translating the discharge tube. Profiles were obtained in the argon plasma as well as the argon plus 1% nitrogen mixture, both at a pressure of 50 Torr, at several different values of electric current.

For the range of experimental conditions studied, $p=30 - 50$ Torr, $i=30 - 100$ mA, the steady-state centerline temperature range was found to be from 440 ± 30 K to 830 ± 70 K. Fig. 5 shows the experimental profile of an argon plasma at pressure 50 Torr and current 20 mA. Figures 6 and 7 are experimental profiles of an argon + 1% nitrogen mixture at a pressure of 50 Torr, and currents of 10 and 40 mA respectively. The experimental points are in good agreement with computation.³¹ We have plotted them here with fitted Gaussian curves:

$$\frac{T(r)}{T_w} = \frac{T_c}{T_w} \exp\left[-\ln\frac{T_c}{T_w} \cdot \left(\frac{r}{R}\right)^2\right], \quad (1)$$

where T_c and T_w are the centerline and wall temperature, respectively; r is the radial variable; and R is the tube radius.

III. RESULTS OF SHOCK PROPAGATION STUDIES IN STEADY-STATE DISCHARGES AND COMPARISON WITH CFD AXISYMMETRIC MODELING

In our earlier work^{22, 24}, we performed a 2D inviscid modeling of shock propagation through a discharge-heated gas and concluded that transverse gradient and multi-dimensionality play a crucial role in shock propagation in glow discharges, and that multi-peak laser schlieren signals are simply due to the shock curvature. For better comparison with experiments, in this work we developed an axisymmetric version of our code. The code solves the axisymmetric conservative form of the Euler equations on

unstructured, triangular, adaptive meshes. The flux balance and shock capturing were carried out by extending the BGK solver developed and validated in Ref 33 to axisymmetric problems. The grid adaption technique was identical to the one used for the two-dimensional code. The "driven" gas was initially at rest, and a shock wave of prescribed strength separated initially the "driven" gas from the "driver". The state of the "driver" gas was specified according to the Rankine-Hugoniot conditions.

The subsequent development of the flow field was computed by solving time-dependent Euler equations in conservation form. Thus, no additional care was required to satisfy the Rankine-Hugoniot conditions, and the correct shock propagation and jump conditions across shocks and other discontinuities were captured by the solution.

As found in the earlier work,²⁴ to model shock structure on a 10-microsecond time scale, simple computations of a "piston-driven", or "step" shock would suffice. This is due to the fact that the initial spark-generated shock broadens so much in its 20-40 cm path to the discharge entrance or a measurement point that on the 5-mm distance (or 10 μ s time interval) from the shock front the shock is very close to a "step" shock.²⁴ This simplification, while being quite accurate, saved us from running extremely CPU-intensive full computations of the spark-generated pulse shocks. The plasma region between the infinitely thin electrodes was considered uniform along the tube axis (x), and to have a symmetric radial temperature profile described by the analytical fit (1) to the experimentally measured profile. Both wall temperature and the gas temperature outside the discharge were set equal to room temperature. Thus, there was a sharp thermal diaphragm between the cold and hot regions. In absence of diffusion (both physical and numerical) this diaphragm will remain fixed with respect to a quiescent gas until the

incident shock impinges upon it. The initial position of the incident shock in the calculations reported here was one tube radius to the left from the boundary between the cold and the discharge-heated gases. Mach numbers of the incident shock were selected so as to give the shock velocity in the uniform room-temperature gas at a given location close to that measured experimentally with the discharge off.

For comparison with laser schlieren measurements, the density gradient integrated in x direction across the narrow "laser beam" and averaged in the radial direction across the tube was computed. The "laser beam" width in the computations was adjusted once to match the experimentally determined width of the schlieren signal with the discharge off. The result of this calibration is shown in Fig.8. As seen in the Figure, computations reproduce the shape of the experimental peak very well.

Note that in the experiments time was measured from the moment of spark firing, while the computations started with the shock located at a distance of one tube radius to the left of the discharge region. Thus, computational time is shifted with respect to the experimental one by a constant. This is reflected in Figs. 8 – 11. For example, in Fig. 9, the experimental signals are plotted versus $(t - 700 \mu s)$, where t is the time from the spark firing, and the computational results are plotted against $(t - 420 \mu s)$, with the computational time t counted from the moment when the shock was located at a distance of one tube radius to the left of the discharge region. The constant shift of t obviously does not affect differential measurements or computations of shock velocity.

Figures 9 – 11 show measured and computed schlieren signals in pure argon (Fig.9) and Ar+1%N₂ (Figs. 10 and 11). In each figure, upper plots correspond to the discharge-off case, while lower plots correspond to the discharge current of 20 mA (Fig.

9), and 10 and 40 mA in Figs. 10 and 11. Figs. 10 and 11 differ in that the schlieren measurement point in Fig. 11 is about 11 cm downstream of that in Fig. 10. Measured and computed velocities of shock waves are shown near all the signals in Figs. 9 – 11.

As seen in the figures, agreement between the computations and experiments, in both shock velocities and the two-peak signal shapes, is excellent. As discussed in Ref. 24, the two-peak structure of the laser schlieren signals is due to the curvature of the shock front in a region with transverse temperature gradient. This is illustrated in Fig. 12 (a-d), where lines of constant density are shown in 4 moments of time, as the shock propagated from the room-temperature gas into the plasma. Note that flow perturbations upstream of the moving shock, such as the distortion of the boundary between hot and cold regions seen in Figs. 12 (c) and (d), do not affect shock propagation. The first peak in the schlieren signal comes from the portion of the shock that propagates through the hot centerline region. The high temperature and low density in this region result in both higher shock speed and lower intensity of the peak compared with those corresponding to colder near-wall regions. The portion of the shock moving through the cold near-wall region lags behind and produces a strong peak in the signal due to the high density near the wall. (Note that in Fig. 12d, a well-resolved Mach stem is discernible near the wall). The decrease in the schlieren signal following the first peak is due to the curvature of the shock. Indeed, the signal is proportional to the axial component of the density gradient. Therefore, with the decrease of the shock angle with the tube axis from 90° to lower values (Fig. 12d), the signal weakens substantially.

Although in Figs. 9 – 11 the agreement between computed and experimentally measured parameters is excellent, it is not perfect. Specifically, computed shock

velocities and distances between two peaks in schlieren signals agree very well with experimental values. On the other hand, computed height of both peaks in the signals relative to the signal strength between the peaks is higher than that in experiments. One of the principal uncertainties in computations is due to the use of Gaussian fit (1) to the experimentally measured temperature profile, especially since temperature measurements have their own errors. Next, neither experimental nor computational (the latter – due to the mesh size) resolution is perfect. Still another factor is the use of inviscid model that disregards viscosity and heat conduction. According to the data of Ref. 34, kinematic viscosity of Ar at 50 Torr, 300 K, is $\nu=2.1 \text{ cm}^2/\text{s}$, and at 50 Torr, 600 K, it is $\nu=7.1 \text{ cm}^2/\text{s}$. Thermal diffusivity values are, of course, comparable with those of viscosity.³⁴ The total width of the signal (that is, the distance between the peaks) in Figs. 9 – 11 is about $t=10 \text{ }\mu\text{s}$. During this time, viscosity and heat conduction can smear velocity and density profiles on a length scale of $\delta \approx \sqrt{6\nu t} = 0.1 - 0.2 \text{ mm}$. Since the width of each peak, converted into the length scale, is about 0.5 mm, and the distance between the peaks – about 5 mm, viscosity and heat conduction cannot change the overall structure of the schlieren signals, which reaffirms the validity of inviscid modeling; however, some smearing of the signals can occur, helping to fill the “trough” between the peaks.

Note that since the linear velocity of the gas downstream of the shock is extremely low, 5-10 cm/s, boundary layer is virtually nonexistent prior to the shock arrival. Behind the shock, boundary layer thickness growth with distance x can be estimated, similar to the previous paragraph, as $\delta \approx \sqrt{6\nu t}$, where $t = x/u$, and u is the gas velocity behind the shock. On the time scale of 1-10 μs after the shock passage, the boundary layer will grow to only $\delta = 0.03\text{-}0.09 \text{ mm}$ in our experimental conditions.

Thus, the boundary layer is very thin in the vicinity of the shock and does not affect schlieren signals. As to the boundary layer farther upstream, it has no effect on the shock propagation.

For further quantitative comparison between computational and experimental results, Figures 13 and 14 show the width of schlieren signals versus centerline temperature (Fig.13) and the shock velocity versus average temperature in the discharge (Fig.14), using the same set of shock propagation data. The average temperature was determined in a standard way:

$$T_{av} = \frac{\int_0^R T(r) \cdot 2\pi r dr}{\pi R^2} \quad (2)$$

Again, Figure 13 and 14 show excellent agreement between computations and experimental data. This provides a strong evidence of conventional, thermal mechanism of shock propagation in weakly ionized plasmas.

IV. EXPERIMENTS ON SHOCK PROPAGATION IN PULSED DISCHARGES

To distinguish between thermal and plasma-specific mechanisms of shock propagation, it would be desirable to eliminate temperature effects while maintaining plasma with the same density of charged particles, electric field, etc. Unfortunately, conventional steady-state discharge is a system where thermal effects are coupled with electric fields and electron density. However, in pulsed discharges, a relatively long time interval can exist when electron, ion, and excited molecule densities are quite high while

the temperature is low. Indeed, gas heating and cooling occurs on time scale orders of magnitude longer than the time scale for ionization/recombination/excitation processes.³⁵

In this work, the pulsed mode of the discharge was produced by using a transistor switch in series with the discharge. The rise time for the current pulse was 20 μ s, and the pulse duration was about 0.5 ms. It was found that this time was insufficient to get a uniform discharge. In fact, when the discharge was turned on, undesirable transitional processes (for example, discharges on the wall of the tube) were observed. Therefore a weak pilot discharge with 1 mA current was maintained between pulses, which resulted in a fairly uniform volume pulsed discharge. Fig.15 shows the discharge pulse shape and the time dependence of discharge integral emission (with no shock wave). Clearly, at times near to the middle of the pulse the emission reaches its steady-state value, similar to that of the continuous discharge. The initial peak of intensity is a result of the higher electric field arising in the discharge immediately after the transistor switch is opened (see below).

As shown in Figs. 16 and 17, for the pilot discharge a small acceleration, accompanied by some widening and weakening of the signal can be noticed, but the changes are very small compared to the higher-current continuous discharge. This is no surprise since the electron number density in the pilot discharge is $\approx 10^8 \text{ cm}^{-3}$ only and the measured axial gas temperature is less than 320 K.

Much more important is that schlieren signal obtained from the pulsed discharge, as seen in Figs. 16 and 17, closely matches both no-discharge and pilot-discharge curves, and is very unlike the signal from the continuous discharge. After the transistor switch is turned on, the discharge current reaches its new steady-state value in $\approx 20 \mu$ s. This value

is almost the same as in continuous discharge. The electric field strength E in the pulse could be found by subtracting cathode drop V_c and voltage drop across the ballast resistor from the power supply voltage. The E values were found to be somewhat larger than in the continuous discharge, but the E/N values are almost identical. Thus, the electron number densities and mean electron energies (electron temperatures) should be very close to those in the continuous discharge. This is confirmed by the behavior of the discharge emission (Fig.15). It reaches its steady-state value that is very close to that of the continuous discharge. An initial overshoot is related to the over voltage applied to the discharge in the transition period ($\sim 20 \mu s$) from small to large current. Higher E/N values in this interval result in efficient excitation of atoms and molecules, including those with radiative lifetime $\sim 1-10 \mu s$ (e.g., intensive bands of the 1st positive system of the N_2 molecule).

The increase in gas temperature, ΔT , during the pulse for the pulse duration τ_p may be calculated from the simple balance equation $iE\tau_p = c_p m_1 \Delta T$, where c_p is the specific heat, and m_1 is a mass of gas per unit length. Here we ignore heat losses because the pulse duration is a factor of 100 less than the characteristic time for thermal conductivity. For the conditions of Fig.16, this equation gives $\Delta T = 0.4 \text{ K} - 0.6 \text{ K}$. Thus, the pulsed discharge has electron component parameters (E/N , n_e , T_e) the same as in the continuous discharge, but the gas temperature is the same as in the pilot discharge, that is, close to room temperature. Comparing the three schlieren curves of Fig.16 (and, similarly, those of Fig.17) definitely shows that changing the electron density by two orders of magnitude does not affect shock wave propagation, while changing gas temperature from $T_g \approx 320 \text{ K}$ to $T_g \approx 500-600 \text{ K}$ (from the pilot or pulsed discharge to the

continuous discharge) affects the shock dramatically. This result may be considered as a strong evidence of thermal mechanism of shock wave – plasma interaction.

To further illustrate the role of heating in shock dynamics, Fig. 18 shows schlieren signals taken with time delay between turning the discharge on and launching the shock ranging from 1 ms to 200 ms. The 1-ms-delay signal is very close to that in the pilot discharge, while the 200-ms-delay signal is close to that in the continuous discharge. It takes tens and hundreds of milliseconds of the discharge existence for the signal to get close to its steady-state shape. The same point is also illustrated in Fig. 19, showing measured shock speed and schlieren signal width approaching their d.c. discharge values as the discharge is allowed to exist longer. Only gas heating in the discharge takes that long; ionization and excitation processes are many orders of magnitude faster.

As the discharge is turned off, one would expect thermal effects to persist for a long time, tens or even hundreds of milliseconds, when recombination of charged species and quenching of excited states will be long since complete. Indeed, this persistence is clearly seen in Figs. 20 and 21, again supporting the thermal mechanism of shock-plasma interaction.

It should be noted that vibrational temperature, or populations of vibrational states, of nitrogen molecules, could be another parameter (apart from the gas temperature) that is quite different in pulsed and continuous discharges. The vibrational relaxation characteristic time is 1 – 2 orders of magnitude longer than the pulse duration, so the vibrational temperature in the pulsed discharge must be almost the same as in the pilot (1 mA) discharge.

To clarify the role of vibrational relaxation, shock wave propagation through pure argon discharge was also studied at low currents where contraction did not occur. In Fig.22 schlieren signals for the two gases (Ar and Ar+1%N₂) are compared. The main features of schlieren signals for both cases are similar. For a more detailed comparison, one has to take into account that addition of even 0.1-1% of nitrogen to argon dramatically changes the electron drift velocity for the same E/N.³⁶ Another important factor found in our experiments is that the values of E/N in Ar+1%N₂ are substantially lower than those in pure Ar. Since E/N in the positive column is determined by the local ionization balance,³⁵ ionization and/or recombination rates must be affected by the addition of nitrogen. The exact mechanism of the decrease in E/N with nitrogen addition is not clear at this time, and, being outside the immediate goal of this work, can be investigated in the future. One possible explanation is that metastables, such as N₂(³Σ), and vibrationally excited nitrogen molecules enhance the ionization. In any case, the reduction in E/N is an experimental fact, and it results in lower gas temperature in Ar+1%N₂ even at the same current as in pure Ar. (See, for example, Figs. 5 and 7). For a meaningful comparison of shock propagation data in Ar and Ar+N₂ mixtures, at least one of the parameters – electric current, electron number density, or gas temperature – should be the same in both cases. Data presented in Fig. 22 for Ar+1%N₂ mixture are shown at i=20 mA (the same as for pure argon), at 40 mA, where gas temperatures are close for both discharges, and at 60 mA, where electron densities are almost equal. It is evident that for the condition of almost-equal gas temperatures (40 mA) similarity of the patterns is the best. This eliminates unambiguously the vibrational relaxation effect and supplies one more evidence of the thermal mechanism of shock dispersion.

V. CONCLUSIONS

Extensive experimental data on shock propagation in steady-state glow discharges in argon and argon-nitrogen mixtures were found to be in excellent agreement with high-accuracy axisymmetric CFD modeling. This provides compelling evidence that shock acceleration, attenuation, and “broadening” in weakly ionized plasmas can be explained by conventional gas dynamics, with multi-dimensionality (due to transverse temperature gradients) playing a critical role.

Experiments with pulsed discharges allowed us to separate thermal effects from those due to electric fields and charged particles. It turned out that gas heating is necessary for shock velocity and schlieren signal parameters to attain their steady-state values. This provides a direct proof of thermal mechanism of weakly ionized plasma effects on shock propagation.

ACKNOWLEDGEMENTS

This work was sponsored by the Air Force Office of Scientific Research.

REFERENCES

^{a)} The author to whom the correspondence should be addressed. E-mail address: macheret@princeton.edu.

^{b)} Permanent address: Institute of Physics, St.-Petersburg State University, St.-Petersburg, Russia.

¹ G.I.Mishin, A.P.Bedin, N.I.Yushchenkova, G.E.Skvortsov, A.P.Ryazin, "Anomalous Relaxation and Instability of Shock Waves in Plasmas," Sov. Phys. Tech. Phys. **26**, 1363 (1981).

² A.I.Klimov, A.N.Koblov, G.I.Mishin, Yu.L.Serov, and I.P.Yavor, "Shock Wave Propagation in a Glow Discharge," Sov. Tech. Phys. Lett. **8**, 192 (1982).

³ A.I.Klimov, A.N.Koblov, G.I.Mishin, Yu.L.Serov, K.V.Khodataev, and I.P.Yavor, "Shock Wave Propagation in a Decaying Plasma," Sov. Tech. Phys. Lett. **8**, 240 (1982).

⁴ I.V.Basargin and G.I.Mishin, "Probe Studies of Shock Waves in the Plasma of a Transverse Glow Discharge," Sov. Tech. Phys. Lett. **11**, 535 (1985).

⁵ V.A.Gorshkov, A.I.Klimov, G.I.Mishin, A.B.Fedotov, and I.P.Yavor, "Behavior of Electron Density in a Weakly Ionized Nonequilibrium Plasma with a Propagating Shock Wave," Sov. Phys. Tech. Phys. **32**, 1138 (1987).

⁶ A.P.Ershov, S.V.Klishin, A.A.Kuzovnikov, S.E.Ponomareva, and Y.P.Pyt'ev, "Application of the Reduction Method to the Microwave Interferometry of Shock Waves in Weakly Ionized Plasma," Sov. Phys. Tech. Phys. **34**, 936 (1989).

⁷ I.V.Basargin and G.I.Mishin, "Precursor of Shock Wave in Glow Discharge Plasma," Sov. Tech. Phys. Lett. **15**, 311 (1989).

⁸ S.A.Bystrov, I.S.Zaslanko, Y.K.Mukoseev, and P.V.Shugaev, "Precursor Ahead of a Shock Front in an RF Discharge Plasma," Sov. Phys. – Doklady **35**, 39 (1990).

⁹ G.I.Mishin, A.I.Klimov, and A.Y.Gridin, "Measurements of the Pressure and Density in Shock Waves in a Gas Discharge Plasma," Sov. Tech. Phys. Lett. **17**, 602 (1992).

- ¹⁰ A.Y.Gridin, A.I.Klimov, and K.V.Khodataev, "Propagation of Shock Waves in a Nonuniform Transverse Pulsed Discharge," *High Temperature* **32**, 454 (1994).
- ¹¹ A.Y.Gridin, A.I.Klimov, K.V.Khodataev, N.B.Shcherbak, and S.B.Shcherbak, "Two-Dimensional Simulation of Shock Wave Propagation in a Transverse Pulse Glow Discharge with a Heated Cathode layer," *High Temperature* **32**, 755 (1994).
- ¹² B.N.Ganguly, P.Bletzinger, and A.Garscadden, "Shock Wave Damping and Dispersion in Nonequilibrium Low Pressure Argon Plasmas," *Phys. Lett. A* **230**, 218 (1997).
- ¹³ B.N.Ganguly and P.Bletzinger, "Shock Wave Dispersion in Nonequilibrium Plasmas," Paper AIAA-96-4607, 1996.
- ¹⁴ A.Garscadden, P.Bletzinger, and B.N.Ganguly, "Acoustic Shock Interaction in a Positive Column Plasma," Paper AIAA-99-4973, 1999.
- ¹⁵ N.V.Evtyukhin, A.D.Margolin, and V.M.Shmelev, "On the Nature of Shock Wave Acceleration in Glow Discharge Plasma," *Sov. J. Chem. Phys.* **3**(9), 2080 (1986).
- ¹⁶ P.A.Voinovich, A.P.Ershov, S.E.Ponomareva, and V.M.Shibkov, "Propagation of Weak Shock Waves in Plasma of Longitudinal Glow Discharge in Air," *High Temperature* **29**(3), 468 (1991).
- ¹⁷ N.Babaeva, "On the Structure of Shock and Blast Waves in Nonequilibrium Plasma of Gas Discharge," *Russian Journal of Chemical Physics* **12**, 357 (1993) [in Russian].
- ¹⁸ N.Babaeva, A.Mnatsakanyan, and G.Naidis, "Simulation of Shock Wave Propagation in a Gas Discharge Developing in Nitrogen," *High Temperature* **31**, 617 (1993).
- ¹⁹ N.Babaeva and G.Naidis, "Simulation of Shock Wave Propagation in Gas Discharge Plasma Regions," in: *Proceedings of the Workshop "Perspectives of MHD and Plasma Technologies in Aerospace Applications,"* Moscow, March 24-25, 1999, p. 108.

- ²⁰ I.V.Adamovich, V.V.Subramaniam, J.W.Rich, and S.O.Macheret, "Shock Wave Propagation in Weakly Ionized Plasmas," Paper AIAA-97-2499, 1997.
- ²¹ I.V.Adamovich, V.V.Subramaniam, J.W.Rich, and S.O.Macheret, "Phenomenological Analysis of Shock-Wave Propagation in Weakly Ionized Plasmas," AIAA Journal **36**, 816 (1998).
- ²² S.O.Macheret, L.Martinelli, and R.B.Miles, "Shock Propagation in Weakly Ionized Plasmas: Mechanisms and Key Problems," Proceedings of the 1st Weakly Ionized Gases Workshop, pp. X-11 – X-33, U.S. Air Force Academy, June 9-13, 1997.
- ²³ W.F.Bailey and W.M.Hilbun, "Baseline of Thermal Effects on Shock Propagation in Glow Discharge," Proceedings of the 1st Weakly Ionized Gases Workshop, pp. GG3 – GG18, U.S. Air Force Academy, June 9-13, 1997.
- ²⁴ S.O.Macheret, L.Martinelli, and R.B.Miles, "Shock Propagation and Structure in Non-Uniform Gases and Plasmas," Paper AIAA-99-0598, 1999.
- ²⁵ S.M.Aithal and V.V.Subramaniam, "On the Characteristics of a Spark Generated Shock Wave," Phys. Fluids **12**, 924 (2000)
- ²⁶ Y.Z.Ionikh, N.V.Chernysheva, A.V.Meshchanov, A.P.Yalin, and R.B.Miles, "Direct Evidence for Thermal Mechanism of Plasma Influence on Shock Wave Propagation," Phys. Lett. A **259**, 387 (1999).
- ²⁷ S.O.Macheret, Y.Z.Ionikh, L.Martinelli, P.F.Barker, and R.B.Miles, "External Control of Plasmas for High-Speed Aerodynamics," Paper AIAA-99-4853, 1999.
- ²⁸ J.H.Kiefer and R.W.Lutz, "Simple Quantitative Schlieren Technique of the High Sensitivity for Shock Tube Densitometry," Phys. Fluids **8**, 1393 (1965).

- ²⁹ J.A.Bander and G.Sanzone, "An Improved Laser-Schlieren System for the Measurement of Shock-Wave Velocity," *Rev. Sci. Instrum.* **45**, 949 (1974).
- ³⁰ A.P.Yalin and R.B.Miles, "Ultraviolet Filtered Rayleigh Scattering Temperature Measurements with a Mercury Filter," *Optics Lett.* **24**, 590 (1999).
- ³¹ A.P.Yalin, Y.Ionikh, and R.B.Miles, "Temperature Measurements in Glow Discharges with Ultraviolet Filtered Rayleigh Scattering," Paper AIAA-99-3431, 1999.
- ³² N.D.Finkelstein, W.R.Lempert, and R.B.Miles, "Mercury Vapor Filter Technology and Ultraviolet Laser Source for Flowfield Imaging," Paper AIAA-97-0157, 1997.
- ³³ C.A.Kim, A.Jameson, L.Martinelli, and K.Xu, "An Accurate LED-BGK Solver in Unstructured Adaptive Meshes," Paper AIAA 97-0328, 1997.
- ³⁴ *Handbook of Physical Quantities*, Ed. by I.S.Grigoriev and E.Z.Meilikhov, CRC Press, Boca Raton, Florida, 1997, Chapters 15 and 16.
- ³⁵ Yu.P.Raizer, *Gas Discharge Physics*, Springer, 1991, Chapters 4, 10, and 14.
- ³⁶ S.C.Brown, *Basic Data of Plasma Physics*, M.I.T. Press, Cambridge, MA and London, 1966, p. 94.

FIGURE CAPTIONS

Fig.1. Schematic of the experimental setup for studies of shock propagation in glow discharges

Fig.2. Schematic diagram of experimental setup for UV FRS measurements of temperature profiles.

Fig. 3. Modeled FRS signal levels for Argon at a range of temperatures. Mercury has several absorption notches in the 253.7 nm vicinity, however Fig.3 shows the experimentally used (high-frequency) notch.

Fig.4. Look-up graph used to convert signal ratio found with discharge ON/OFF to plasma temperature.

Fig.5. Radial temperature profile in Ar glow discharge tube measured by UV Filtered Rayleigh Scattering. Pressure and electric current are indicated on the plot. Fitting curve – see Eqn. (1).

Fig.6. Radial temperature profile in Ar+1%N₂ glow discharge tube measured by UV Filtered Rayleigh Scattering. Pressure and electric current are indicated on the plot. Fitting curve – see Eqn. (1).

Fig.7. Radial temperature profile in Ar+1%N₂ glow discharge tube measured by UV Filtered Rayleigh Scattering. Pressure and electric current are indicated on the plot. Fitting curve – see Eqn. (1).

Fig.8. Calibration of the “laser beam width” for CFD modeling against laser schlieren signal with the discharge off. Note: experimental time t was measured from the moment of spark firing, while the computational time t was counted from the moment when the shock was located at a distance of one tube radius to the left of the discharge.

Fig.9. Experimentally measured and simulated laser schlieren signals for shocks propagating in glow discharge in pure Ar at 50 Torr. The discharge current is 20 mA. The first of the two laser beams is located 18 cm from the entrance to the discharge, and the spacing between the two beams is 3.6 cm. The experimentally measured and computed shock velocities are indicated on the figure. Note: experimental time t was measured from the moment of spark firing, while the computational time t was counted from the moment when the shock was located at a distance of one tube radius to the left of the discharge.

Fig.10. Experimentally measured and simulated laser schlieren signals for shocks propagating in glow discharge in Ar+1%N₂ at 50 Torr. The discharge current values are 10 mA and 40 mA. The first of the two laser beams is located 9 cm from the entrance to the discharge, and the spacing between the two beams is 2.1 cm. The experimentally measured and computed shock velocities are indicated on the figure. Note: experimental

time t was measured from the moment of spark firing, while the computational time t was counted from the moment when the shock was located at a distance of one tube radius to the left of the discharge.

Fig.11. Experimentally measured and simulated laser schlieren signals for shocks propagating in glow discharge in Ar+1%N₂ at 50 Torr. The discharge current values are 10 mA and 40 mA. The first of the two laser beams is located 20 cm from the entrance to the discharge, and the spacing between the two beams is 3.7 cm. The experimentally measured and computed shock velocities are indicated on the figure. Note: experimental time t was measured from the moment of spark firing, while the computational time t was counted from the moment when the shock was located at a distance of one tube radius to the left of the discharge.

Fig.12. Computed constant-density lines during shock propagation in glow discharge tube (pure Ar, 50 Torr, 20 mA): (a) – $t=21 \mu\text{s}$, prior to shock entry into the discharge; (b) – $t=43 \mu\text{s}$, shock entering the discharge; (c) – $t=60 \mu\text{s}$, shortly after the shock entered the discharge; (d) – $t=123 \mu\text{s}$, shock has penetrated deep inside the discharge. The computational time t was counted from the moment when the shock was located at a distance of one tube radius to the left of the discharge.

Fig.13. The width of the schlieren signal in the discharge (Δ) minus the signal width with the discharge off (Δ_0) versus temperature difference between the axis and the wall, $T_{\text{axis}} - T_w$. Gas mixture Ar+0.16%N₂, pressure 50 Torr; 3 cm spark gap, 15 kV spark voltage;

first laser beam is 24.8 cm inside the discharge; spacing between the two beams is 2.9 cm.

Fig.14. Shock wave velocity versus average temperature [definition – see Eqn. (2)] in the discharge. Gas mixture Ar+0.16%N₂, pressure 50 Torr; 3 cm spark gap, 15 kV spark voltage; first laser beam is 24.8 cm inside the discharge; spacing between the two beams is 2.9 cm.

Fig.15. Discharge current and integrated spectral emission versus time during the pulse.

Fig.16. Schlieren signals and shock velocities in glow discharge in Ar+1%N₂ at 50 Torr: the discharge off; 38-mA continuous d.c. discharge, weak (1 mA) pilot discharge, and a pulsed discharge.

Fig.17. Schlieren signals and shock velocities in glow discharge in Ar+1%N₂ at 50 Torr: the discharge off; 80-mA continuous d.c. discharge, weak (1 mA) pilot discharge, and a pulsed discharge.

Fig.18. Evolution of the schlieren signal at a fixed location inside the discharge with time delay between the beginning of the discharge and the shock launch

Fig.19. Evolution of shock velocity and the width of the schlieren signal at a fixed location inside the discharge with time delay between the beginning of the discharge and the shock launch

Fig.20. Evolution of the schlieren signal at a fixed location inside the discharge with time delay between the end of the discharge pulse and the shock launch.

Fig.21. Evolution of shock velocity and the width of the schlieren signal at a fixed location inside the discharge with time delay between the end of the discharge pulse and the shock launch.

Fig.22. Comparison of shock schlieren signals at a fixed location in Ar and Ar+1%N₂ discharges at 50 Torr and various values of electric current.

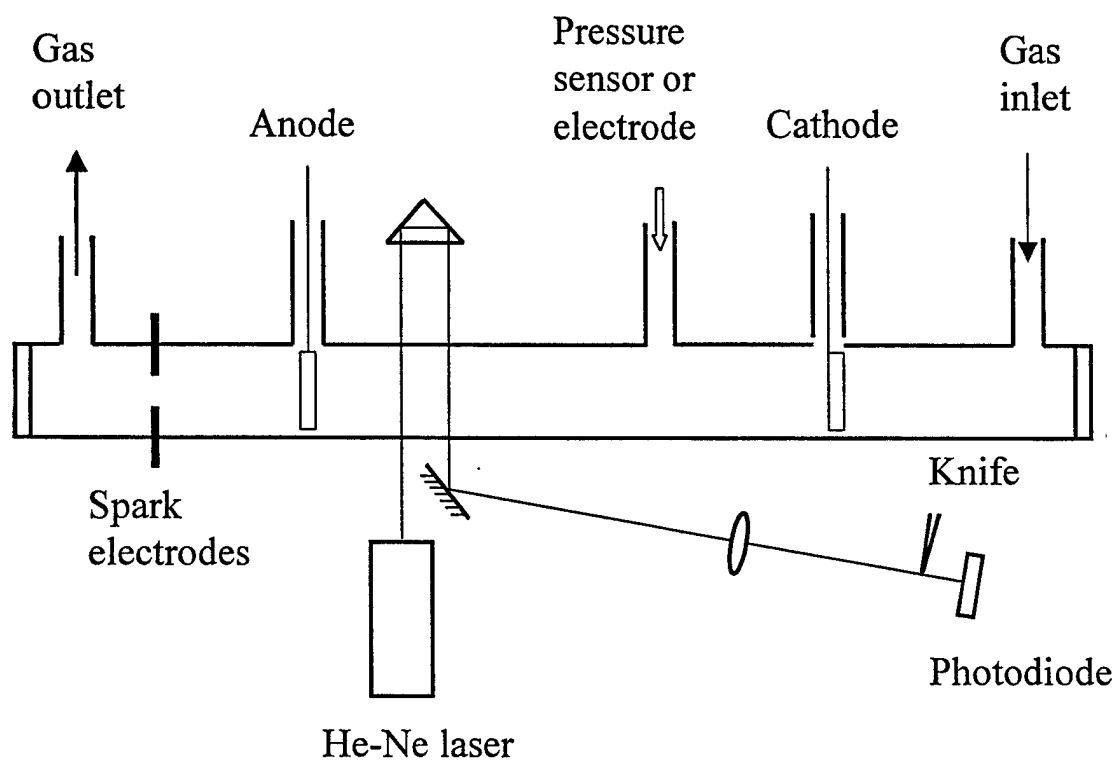


Fig. 1.
Macheret et. al., *Phys. Fluids*

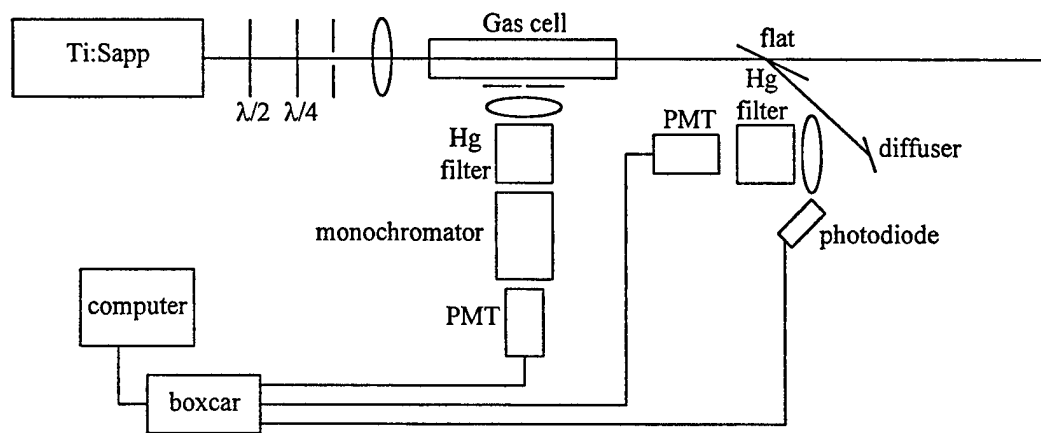


Fig. 2.
Macheret et. al., *Phys. Fluids*

Modeled UV FRS signal levels for Argon, $T=300, \dots, 750$ K

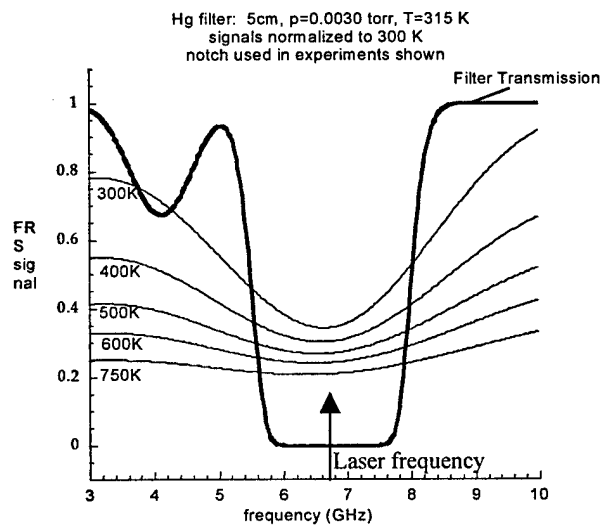


Fig. 3.
 Macheret et. al., *Phys. Fluids*

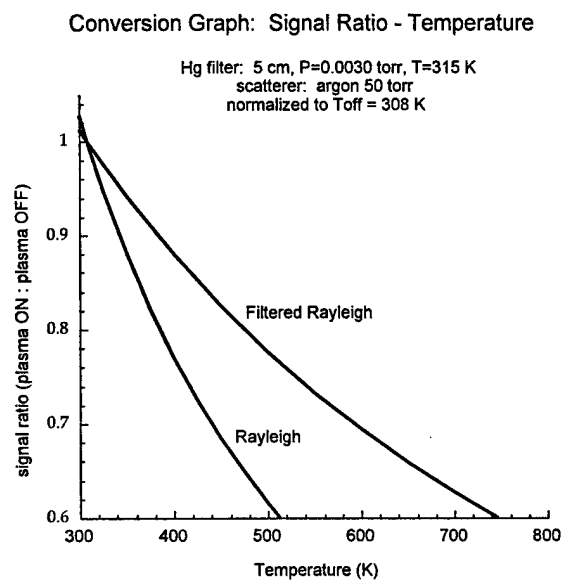


Fig. 4.
Macheret et. al., *Phys. Fluids*

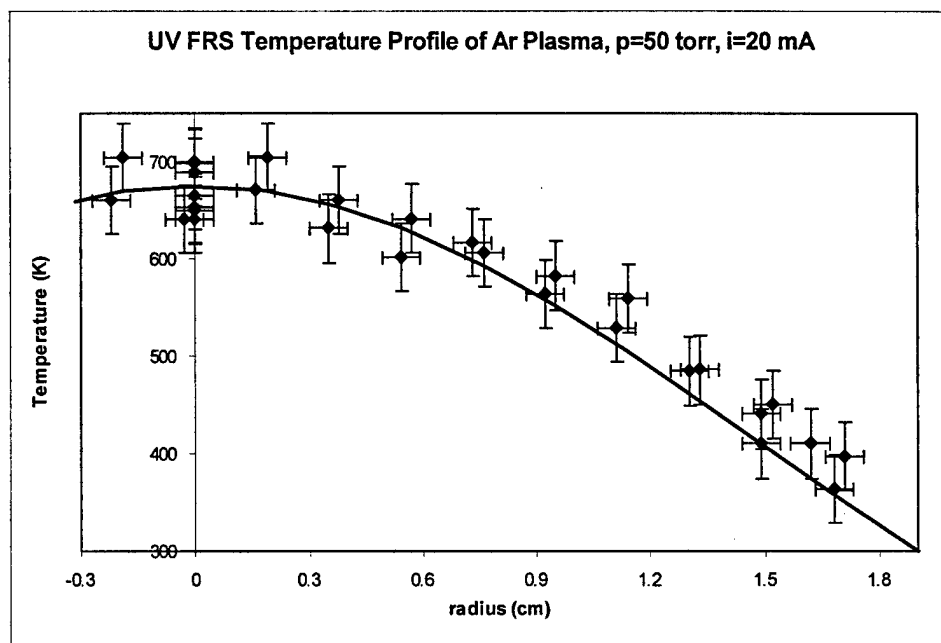


Fig. 5.
Macheret et. al., *Phys. Fluids*

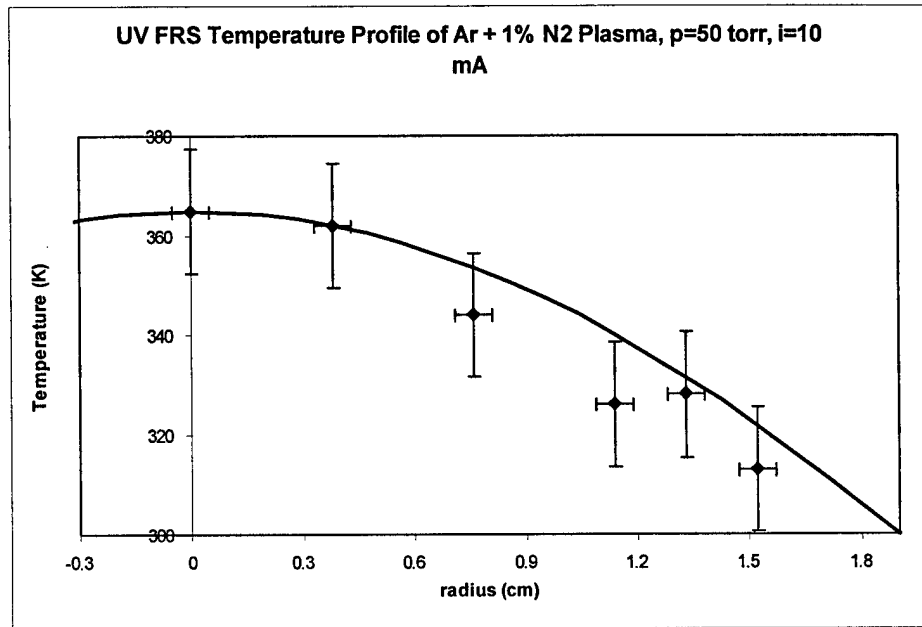


Fig. 6.
Macheret et. al., *Phys. Fluids*

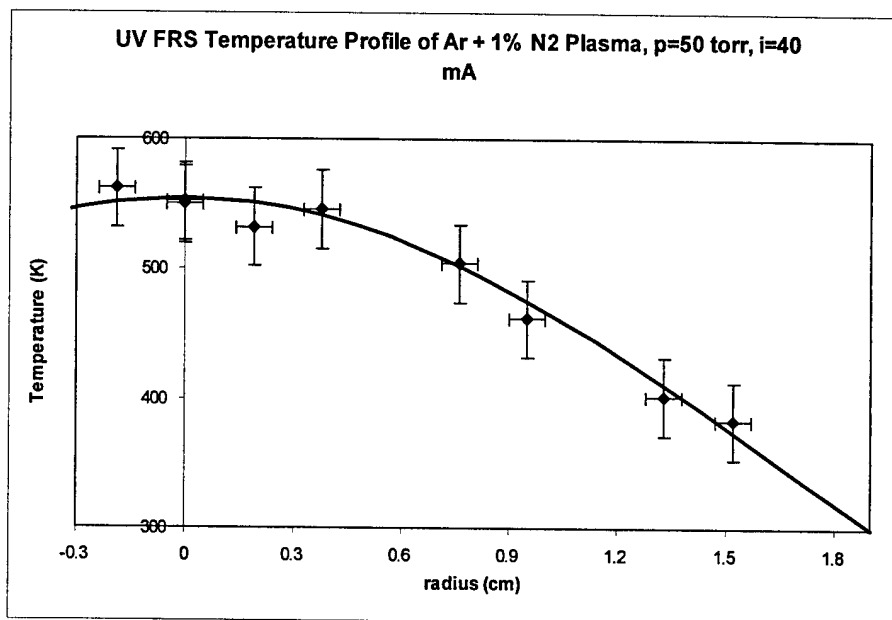


Fig. 7.
Macheret et. al., *Phys. Fluids*

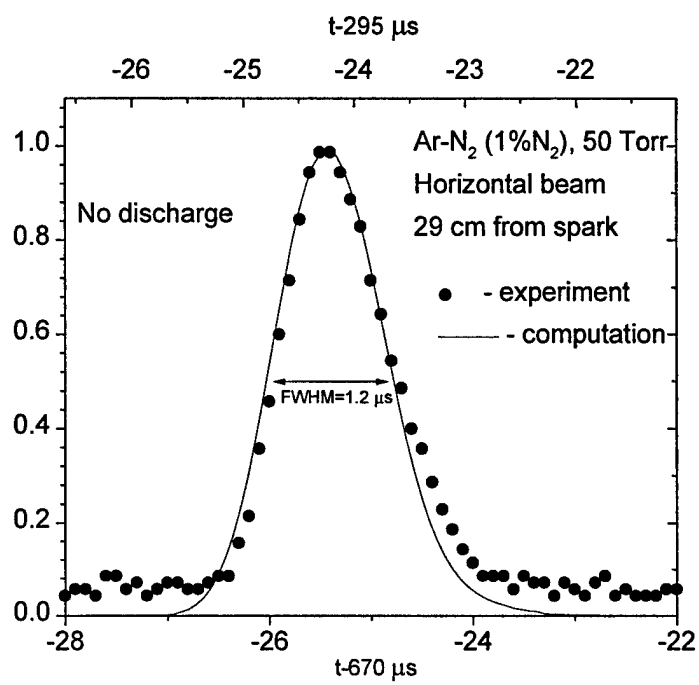


Fig. 8.
 Macheret et. al., *Phys. Fluids*

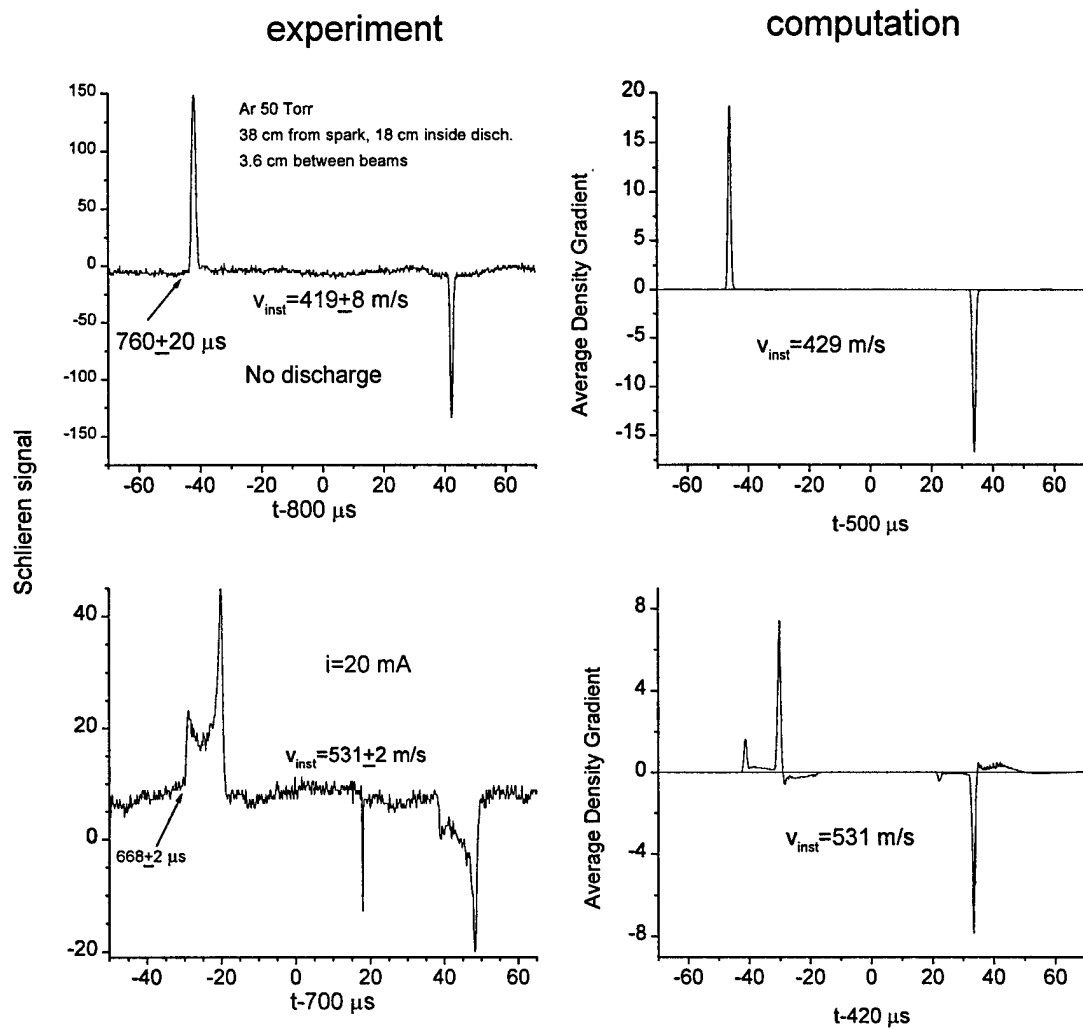


Fig. 9.
 Macheret et. al., *Phys. Fluids*

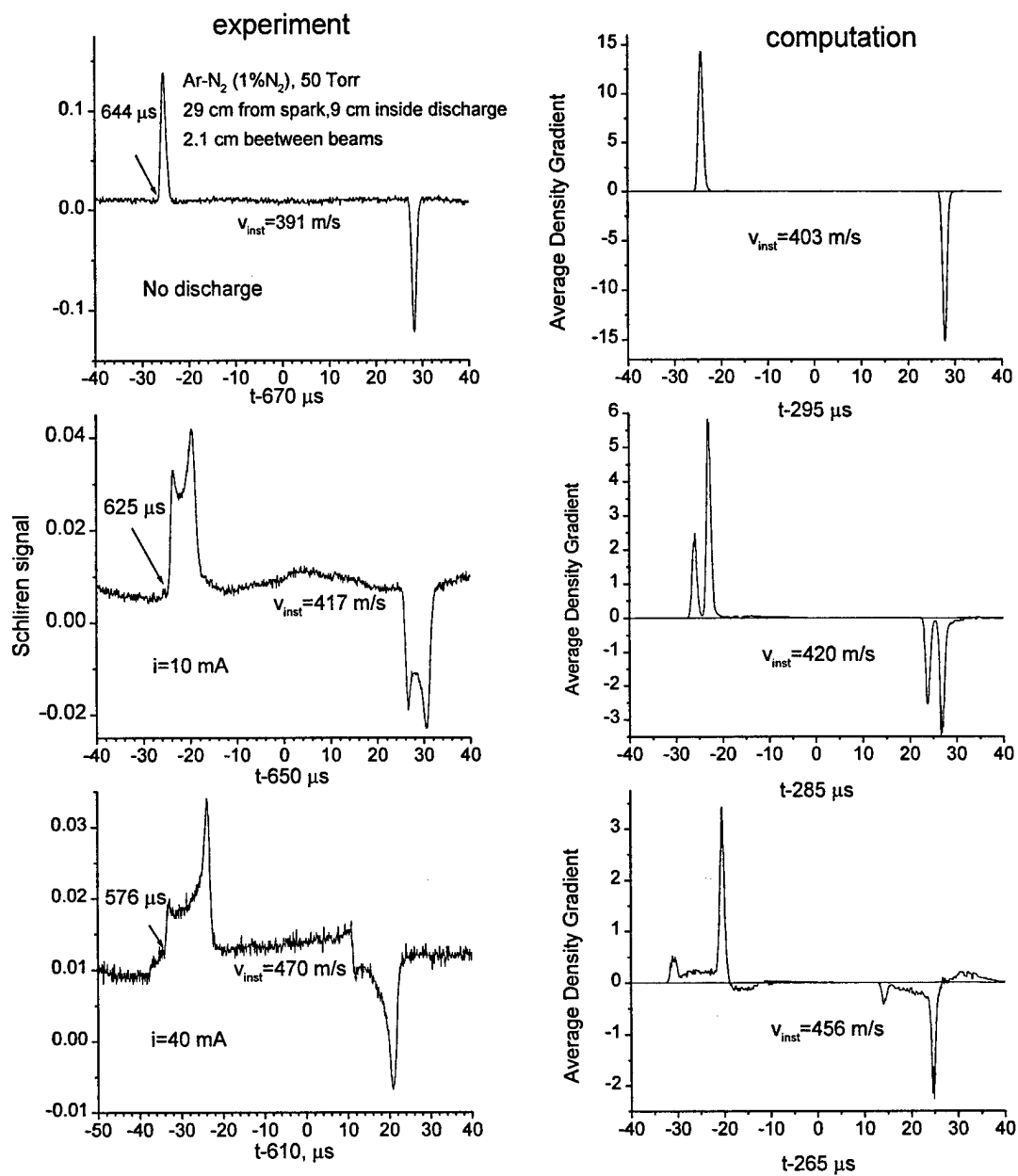


Fig. 10.
Macheret et. al., *Phys. Fluids*

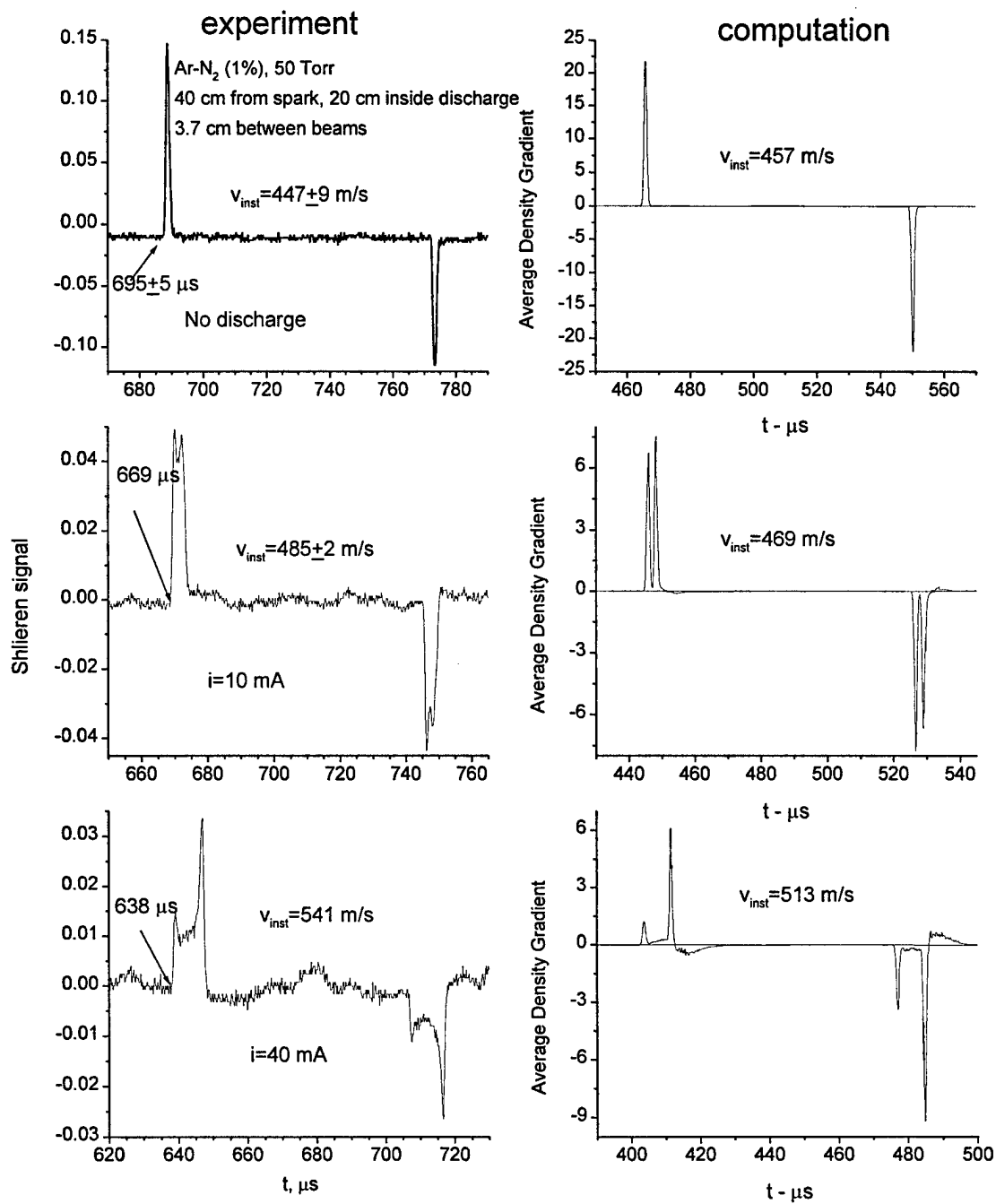
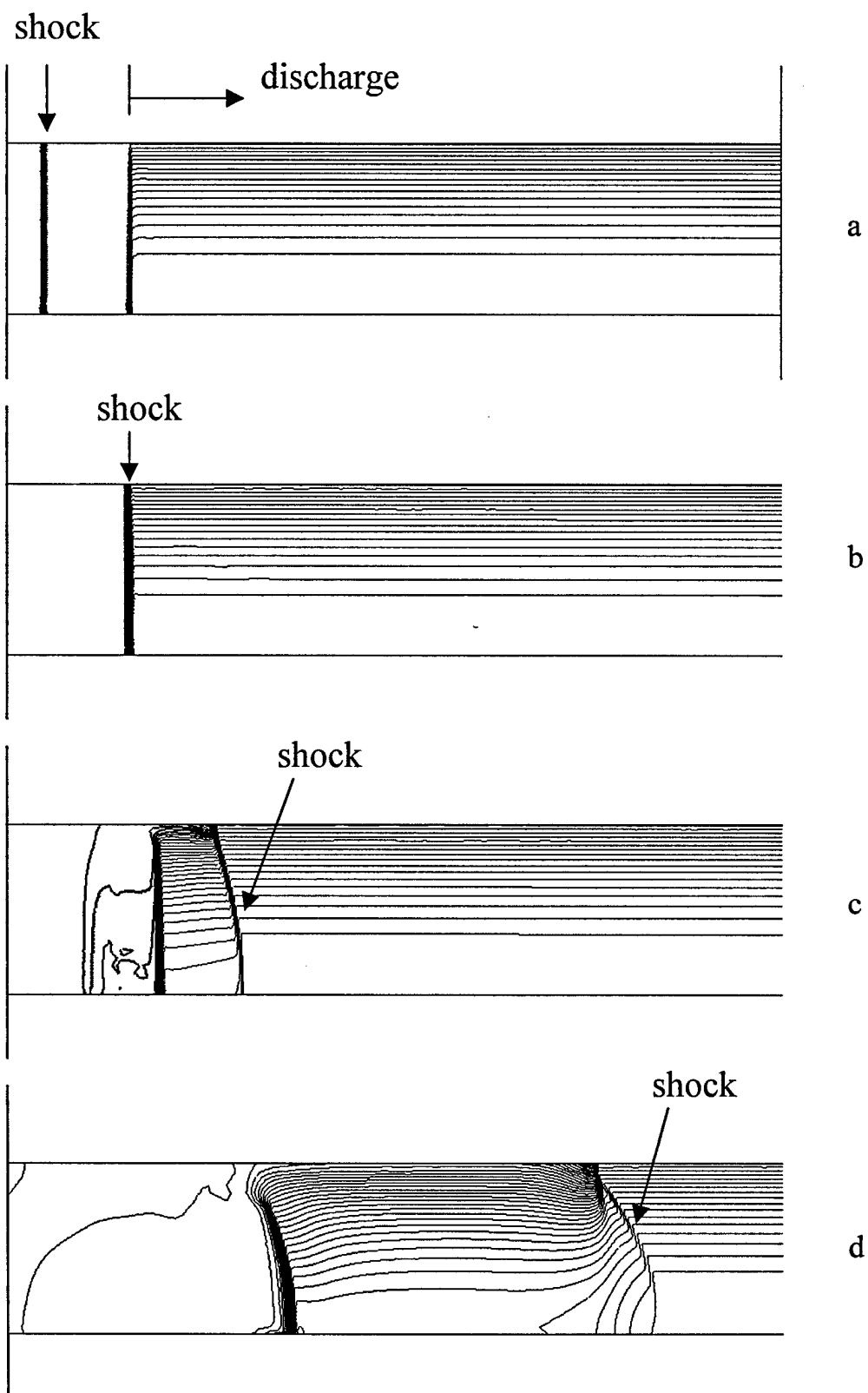


Fig. 11.
Macheret et. al., *Phys. Fluids*



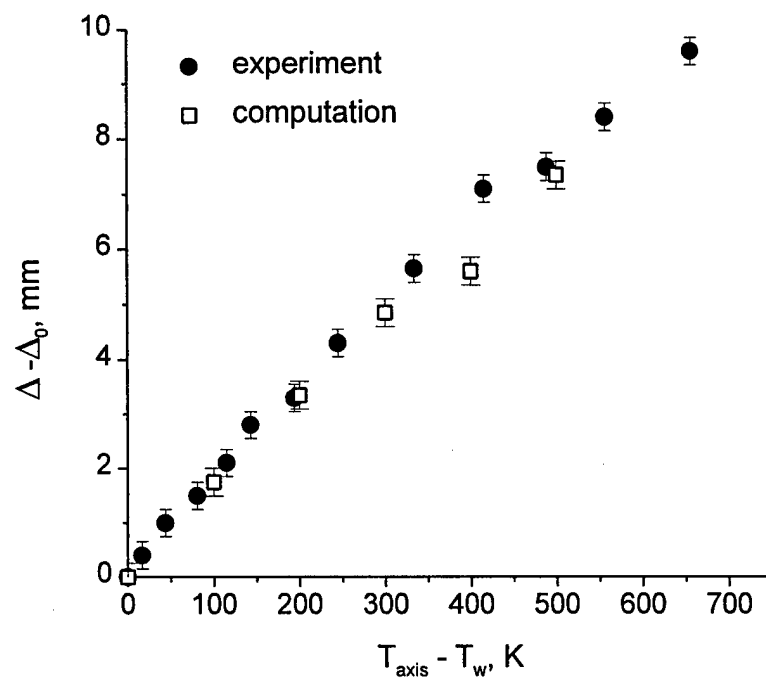


Fig. 13.
Macheret et. al., *Phys. Fluids*

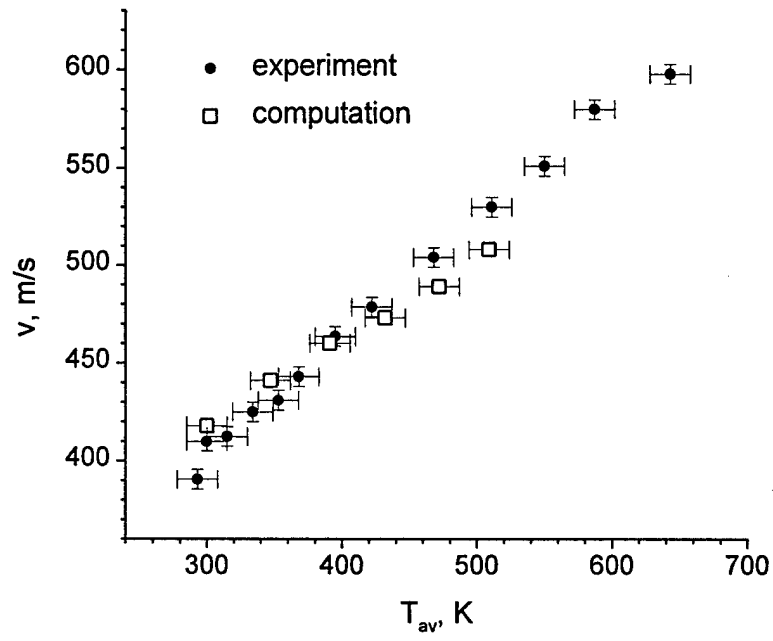


Fig. 14.
Macheret et. al., *Phys. Fluids*

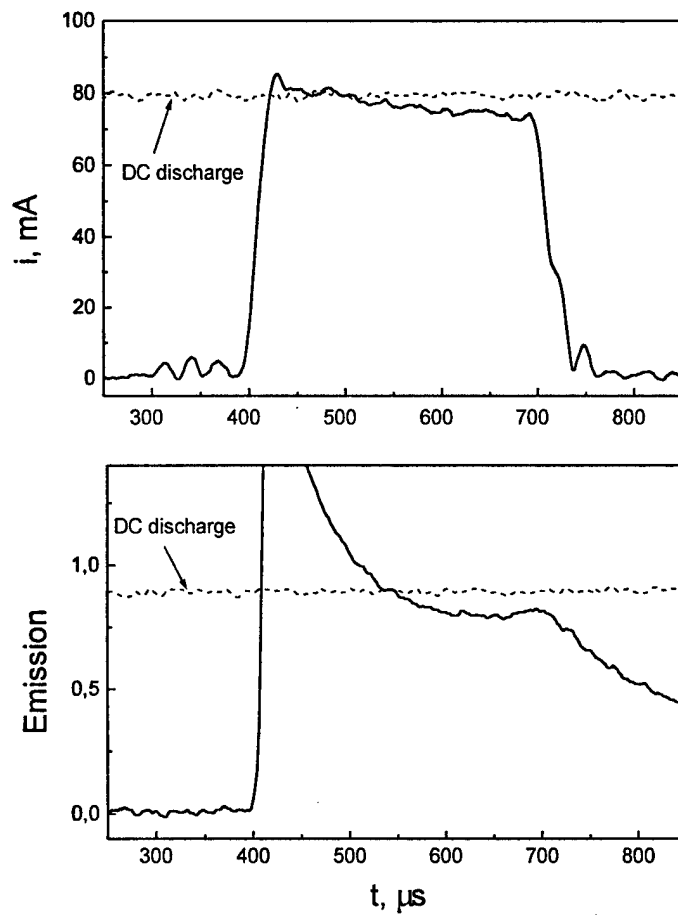


Fig. 15.
Macheret et. al., *Phys. Fluids*

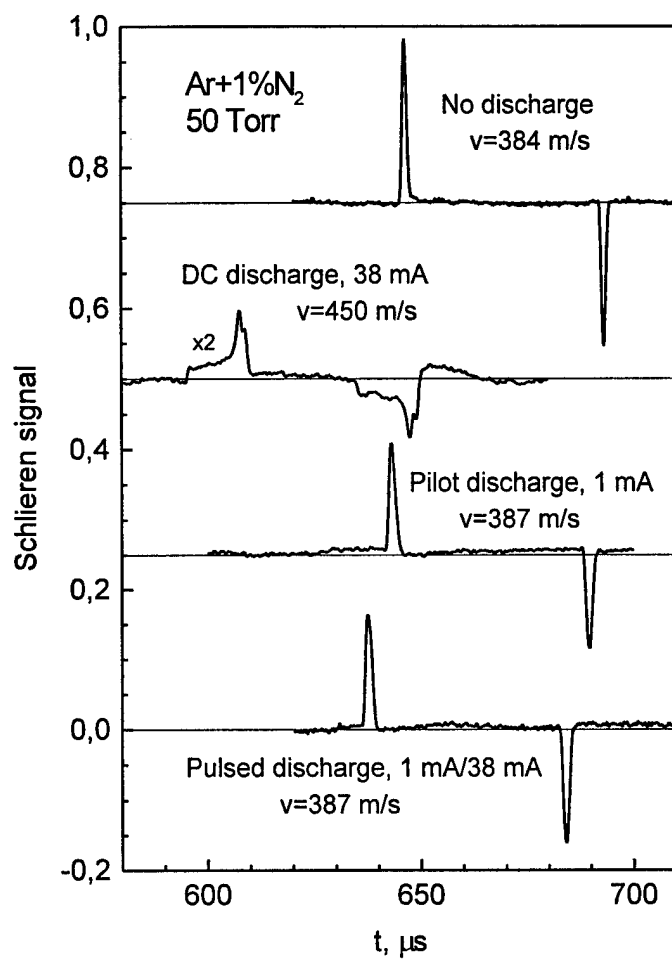


Fig. 16.
Macheret et. al., *Phys. Fluids*

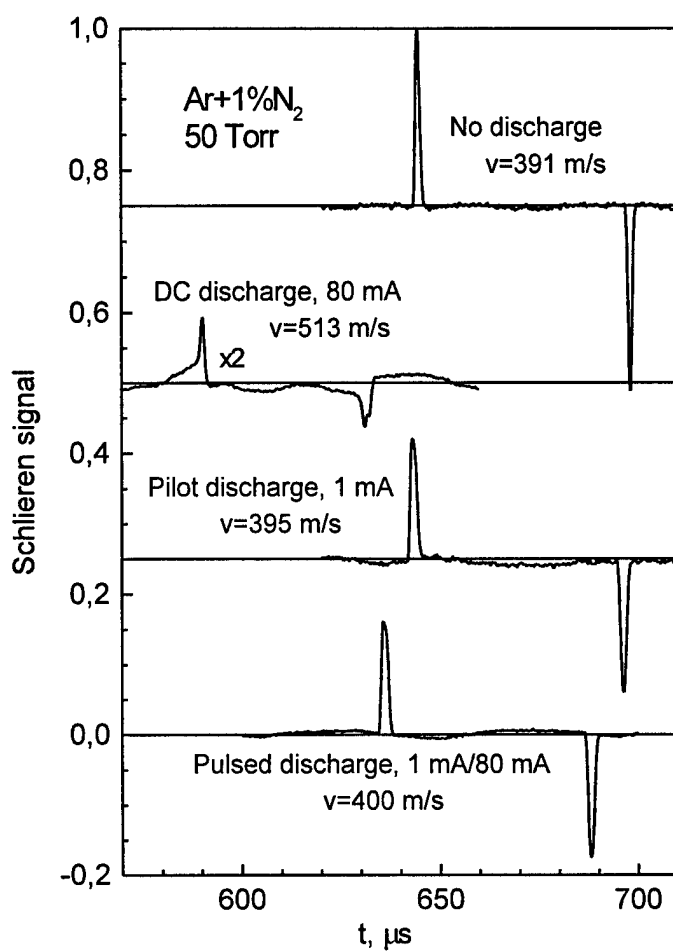


Fig. 17.
Macheret et. al., *Phys. Fluids*

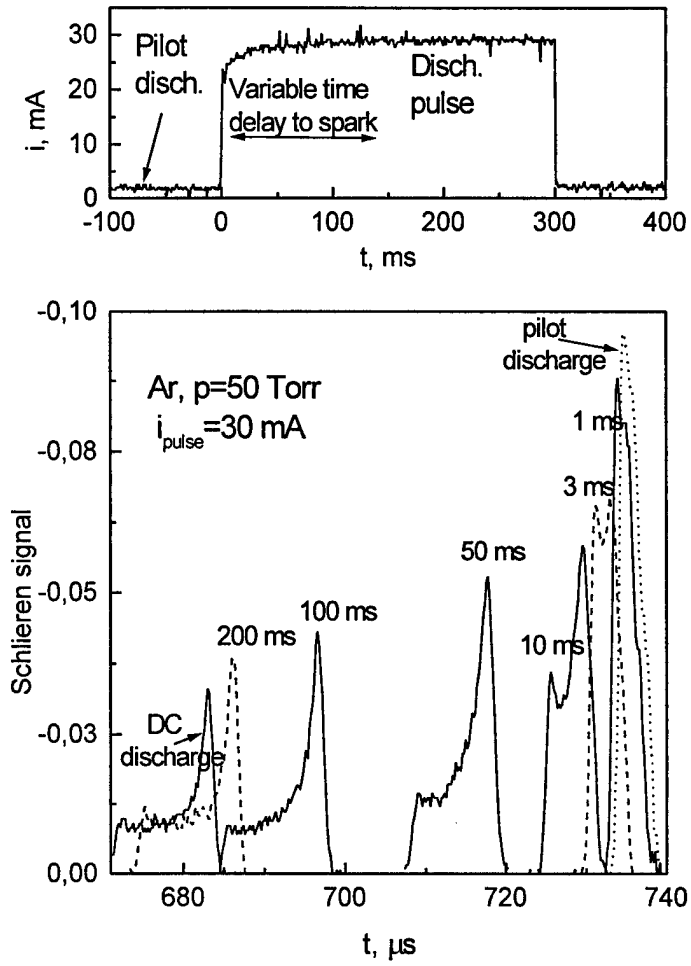


Fig. 18.
Macheret et. al., *Phys. Fluids*

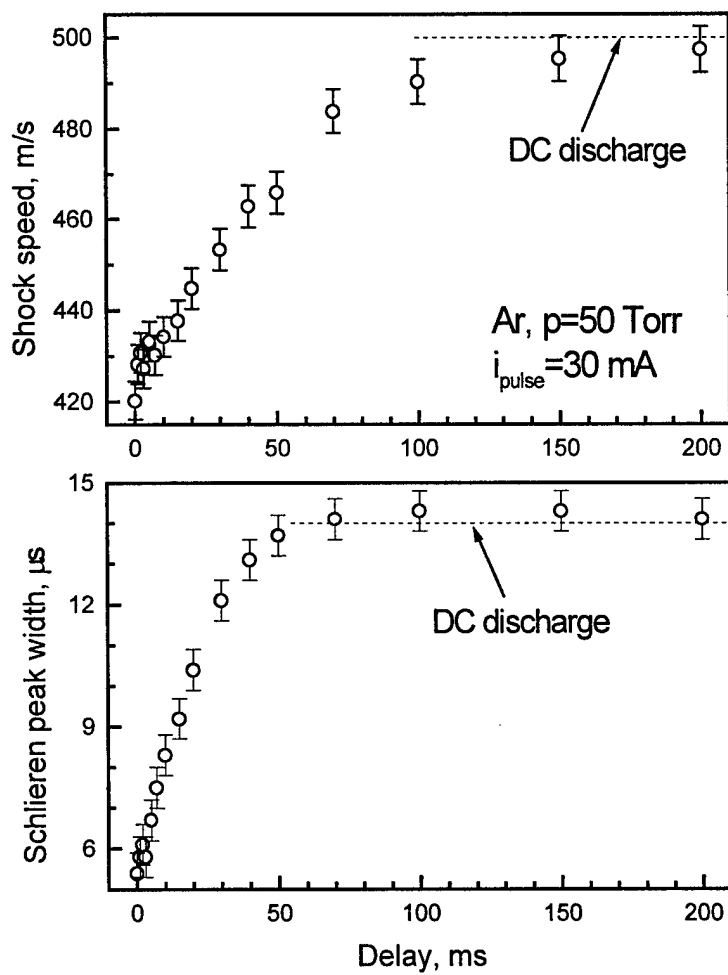


Fig. 19.
Macheret et. al., *Phys. Fluids*

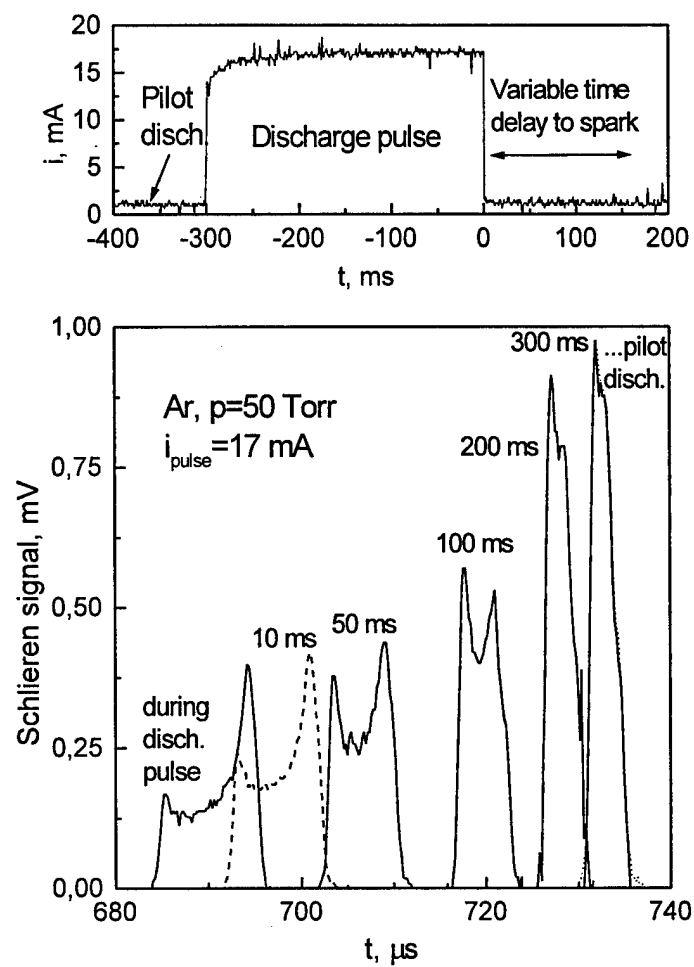


Fig. 20.
Macheret et. al., *Phys. Fluids*

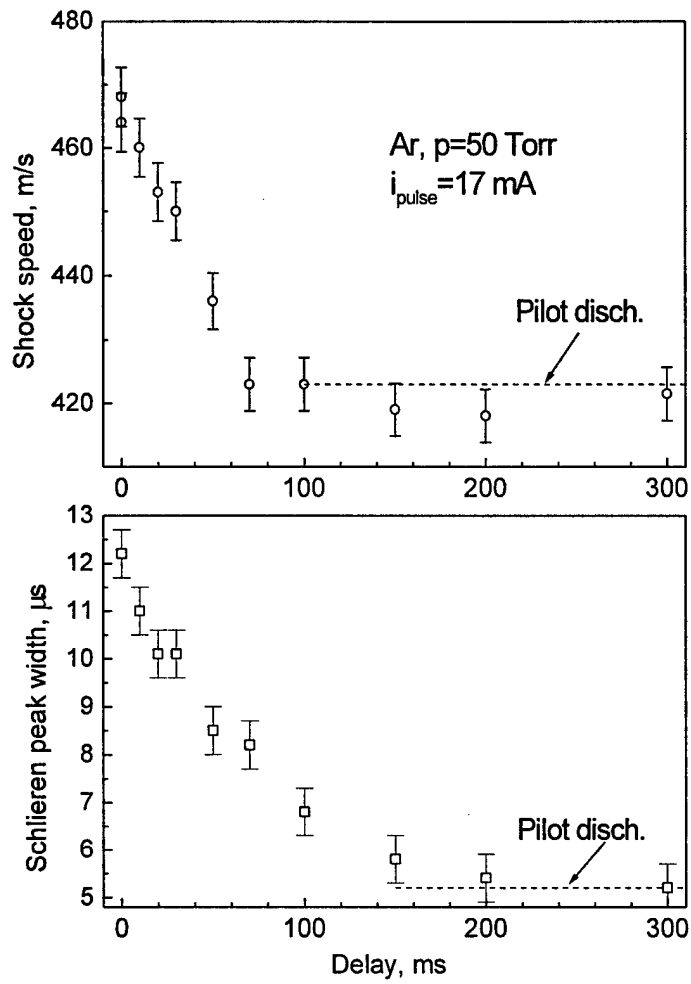


Fig. 21.
Macheret et. al., *Phys. Fluids*

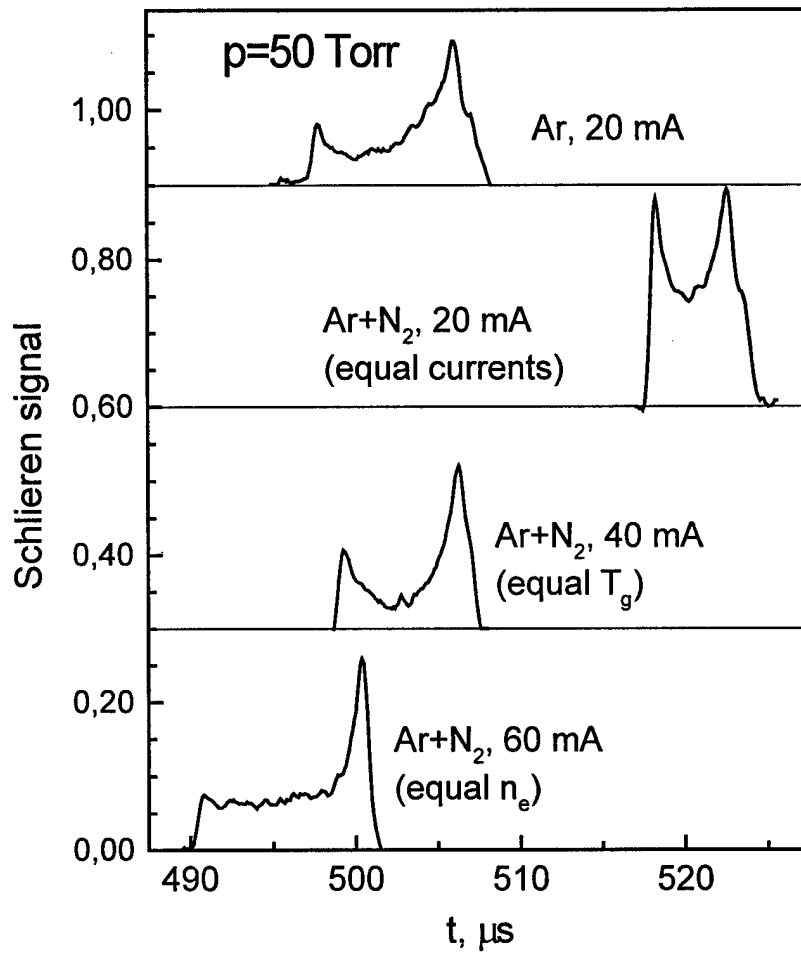


Fig. 22.
Macheret et. al., *Phys. Fluids*

APPENDIX B

1. **A.P. Yalin and R.B. Miles**, "Ultraviolet Filtered Rayleigh Scattering Temperature Measurements with a Mercury Filter," Optics Letters, 24, May 1, 1999, pp. 590-592.
2. **A.P. Yalin**, Y. Ionikh, A. Meshchanov, and **R.B. Miles**, "2-D Temperature Fields in Glow Discharges Measured with Ultraviolet Filtered Rayleigh Scattering," AIAA 2000-0375, 38th Aerospace Sciences Meeting and Exhibit, Jan. 10-13, 2000, Reno, NV.
3. **A.P. Yalin and R.B. Miles**, "Temperature Measurements by Ultraviolet Filtered Rayleigh Scattering Using a Mercury Filter," J. of Thermophysics and Heat Transfer 14, April-June 2000, pp. 210-215.

Ultraviolet filtered Rayleigh scattering temperature measurements with a mercury filter

Azer P. Yalin and Richard B. Miles

Department of Mechanical & Aerospace Engineering, Princeton University, Princeton, New Jersey 08544

Received January 4, 1999

We report the development of ultraviolet filtered Rayleigh scattering as a diagnostic tool for measurements of gas properties. A frequency-tripled narrow-linewidth Ti:sapphire laser illuminates a sample, and Rayleigh scattered light is imaged through a mercury-vapor absorption filter. Working in the ultraviolet improves the signal-to-noise ratio compared with that previously obtained in the visible as the result of an enhanced scattering cross section as well as the nearly ideal properties of the mercury filter. Tuning the laser through the absorption notch of the filter is a means of probing the scattering line shape, which contains temperature information. Temperature measurements of air are shown to have uncertainties of less than 3%. © 1999

Optical Society of America

OCIS codes: 350.2450, 280.2490, 290.5870, 290.3700.

Over the past several years, filtered Rayleigh scattering (FRS) has been employed as a diagnostic in a variety of fluid environments for nonintrusive flow visualization as well as for quantitative measurements of fluid properties. Solving the problem of performing nonintrusive temperature measurements is important for improved understanding of many areas of physics, for example, supersonic flows, weakly ionized plasmas, combustion processes, and even the atmosphere. Depending on the nature of the problem under investigation, a wide array of optical methods is available. FRS is attractive because, by focusing the laser to a sheet, it has the potential to provide a full two-dimensional, quantitative map of the flow field.¹ Typically, spectral measurements, such as absorption and fluorescence, are path integrated. Coherent anti-Stokes Raman spectroscopy and laser-induced thermal acoustics² can be used for point measurements, but they are inherently not well suited for two-dimensional imaging. Raman techniques are species specific and do permit imaging but suffer from low signal levels. Laser-induced methods are amenable to imaging; however, in many cases fluorescence quenching and saturation complicate quantitative analysis. FRS can be used to capture quantitative planar measurements of gas temperature, pressure, density, and velocity; it is nonresonant and thus is unaffected by quenching and saturation, and a high signal-to-noise ratio can be obtained because of the strong background suppression provided by the filter.

In the visible region the FRS technique has already shown its utility in a variety of environments, for example, for temperature measurement in combustion³ and for velocimetry and flow visualization in high-speed flows.^{1,4} Those earlier experiments used primarily frequency-doubled Nd:YAG sources paired with molecular-iodine filters (532 nm); see e.g., Refs. 1, 3, and 4. FRS has also been used in the ultraviolet with an excimer laser with an atomic iron filter (248 nm),⁵ but only modest success has been achieved because of limitations of the laser. Related research by workers in the lidar and other communities have paired narrow-linewidth lasers and filters in the

visible-infrared regions, for example, an alexandrite laser with a potassium filter (770 nm) (Ref. 6) and a dye laser with a cesium filter (389 nm).⁷

The focus of this study is the extension of the FRS technique from the visible to the ultraviolet portion of the spectrum, where the scattering is stronger and the more ideal mercury-vapor filter can be used. Preliminary research characterizing the mercury filter was performed in our laboratory by Finkelstein.⁸ To perform temperature measurements, one images Rayleigh scattering from a gas sample through a mercury filter, and a model is used to fit for gas properties. Because of the frequency dependence of the scattering cross section as well as favorable properties of the filter, higher signal-to-noise ratios are possible in the ultraviolet than in the visible or the infrared.

The FRS concept was described earlier,¹ so only a brief summary is given here. A narrow-linewidth laser is used to illuminate a sample volume, and the scattered light is imaged through a narrow-band atomic- or molecular-vapor absorption filter onto a detector. The amount of scattered light that arrives at the detector depends on the spectral overlap of the scattered light and the filter absorption profile. The scattered light consists of an elastic background component from window scattering and stray reflections as well as of Rayleigh light scattered from the sample volume. The light scattered by the molecules in the sample volume has a Rayleigh-Brillouin line shape that depends primarily on temperature, with a weaker dependence on pressure. One can determine temperature by measuring the scattering line shape with an absorption filter. Tuning the laser causes the Rayleigh-Brillouin line shape to sweep across the absorption filter profile, causing the transmitted light to vary in intensity. Because the absorption profile of the filter is known, the transmitted intensity profile can be deconvolved to yield the Rayleigh-Brillouin line shape, from which the temperature can be determined. This concept is shown schematically in Fig. 1. Note that when an appreciable background is present one may either perform a background subtraction or alternatively take data only in a smaller spectral

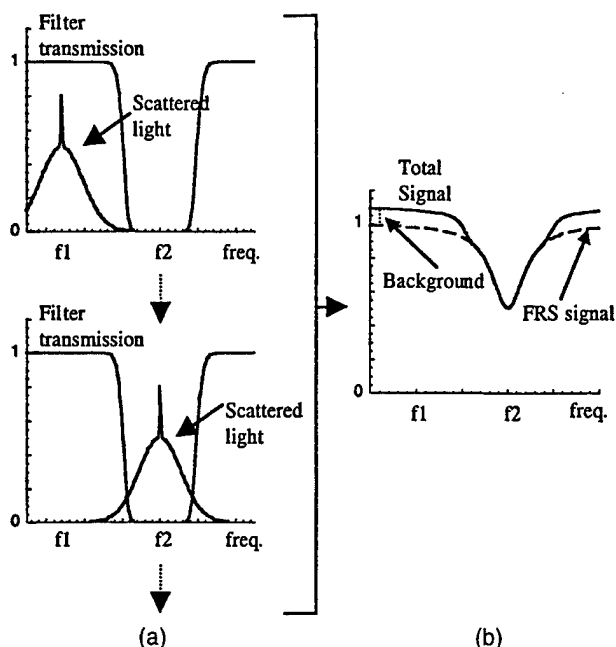


Fig. 1. (a) Spectral overlap of the scattered light with the filter transmission profile at two laser frequencies, f_1 and f_2 . The scattered light has two components, a broadband Rayleigh-Brillouin component and a narrow-band background component. (b) Tuning the laser through the absorption notch yields the FRS signal as a function of frequency. A model is used to fit the FRS data for gas properties.

region about the absorption line center where all background is strongly absorbed. The total Rayleigh scattering signal is proportional to density, so when the gas is in pressure equilibrium and the pressure is known, the temperature can also be determined from the density by use of the ideal gas law.

In FRS, the absorption filter serves two critical purposes: background suppression and probing of spectral information. Desirable filter properties are high out-of-band transmission, high in-band absorption, steeply sloping walls, and flexibility in selection of the absorption width. Mercury has an optically accessible strong ground-state transition at 253.7 nm and is well suited as a filter material. A model for mercury absorption has been developed earlier.⁸ Unlike iron and lead, mercury has a high vapor pressure (e.g., ~ 0.001 Torr at $\sim 20^\circ\text{C}$), so useful vapor number densities can be attained at manageable temperatures. In a 5-cm cell at low vapor pressure (of the order of 0.01 Torr), lines from each of mercury's six naturally occurring isotopes form separate notches with widths up to several gigahertz and filter walls that rise from 10% to 90% transmission over hundreds of megahertz. At a higher vapor pressure (of the order of 1 Torr), the isotopic lines blend together and form a notch with a width of tens of gigahertz. The out-of-band transmission is close to 100% (when filter window losses are neglected), and the in-band optical suppression is predicted to be ten orders of magnitude or more. We control the vapor pressure by setting the temperature of a side arm that contains a small amount (several grams) of liquid mer-

cury. The sidearm is immersed in a temperature-controlled liquid bath (water or mineral oil). The main body of the filter is a quartz tube of 5-cm diameter and 5-cm depth. To prevent any condensation in the main tube we heat the body of the tube to a temperature slightly higher than that of the sidearm.

A custom-built Ti:sapphire laser system⁸ is used as the illumination source for the ultraviolet FRS measurements. The laser is injection seeded and operates with a novel cavity-locking scheme, which ensures almost transform-limited narrow-linewidth single-mode output. The laser runs at 10 Hz and yields as much as 40 mJ of energy per pulse in the ultraviolet (third harmonic). The third-harmonic output from the laser system is delivered along the axes of a cylindrical cell with antireflection-coated windows that houses the sample gas. A 50-cm focal-length lens is used to focus the beam to a waist of $\sim 100\ \mu\text{m}$. To minimize any background light we pass the beam through several irises. A half-wave plate is used to ensure the correct orientation of the linearly polarized beam, and a quarter-wave plate compensates for any elliptical polarization introduced at the window. All the beam-shaping optics are antireflection coated. An antireflection-coated 5-cm focal-length lens is placed 8 cm from the beam and is used to image the Rayleigh scattered light at an observation angle perpendicular to the beam and cell axes. An iris of ~ 1 -mm diameter is placed between the lens and the cell and serves to define the sample region as well as further to reduce background light. The scattered light is passed through the mercury-vapor filter and then passed through a ISA H20 monochromator set to 254 nm, which acts as a broad passband filter. Finally, the scattered light is detected with an R-960 Hamamatsu photomultiplier tube (PMT). A quartz flat is used to pick off a fraction of the beam, after it has passed through the cell, to serve as a power and frequency reference. The picked-off beam is incident upon a diffuser, and elastically scattered light from the diffuser is measured with a photodiode for power normalization as well as passed through a second mercury-vapor absorption filter and measured with a second PMT to serve as a frequency reference. Thin-film interference filters (Corion G25-254-F) are placed in front of the reference photodiode and the PMT such that only the 254-nm light will be detected. The signals from both PMT's and the photodiode are collected with a Stanford Research Systems boxcar unit and a personal computer. A Stanford Research Systems Model 330 preamplifier unit is used at $5\times$ magnification to amplify the signals from the FRS PMT as well as the photodiode. Great care is taken to ensure linearity of the entire detection scheme.

To demonstrate the technique we performed temperature measurements of air. The basic procedure was to scan the laser across the filter absorption and collect the FRS signal as a function of frequency. We normalized the FRS signal, using the reference photodiode, and the frequency axis was established with the reference PMT. A thermocouple inside the sample cell was used as a reference measure of temperature. Data obtained from a typical scan, in this case of air at 50 Torr and $295 \pm 2\ \text{K}$, are shown in

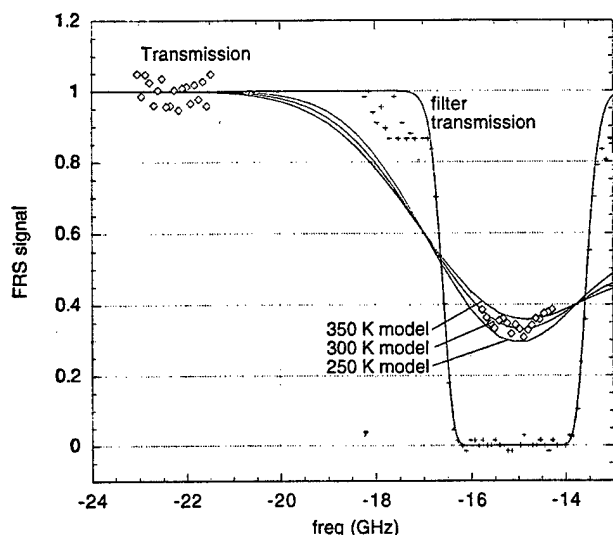


Fig. 2. Ultraviolet FRS data from air at $T = 295 \pm 2$ K and $P = 50$ Torr (open diamonds). The reference frequency axis data (crosses) are also shown, as well as model fits for air at $T = 250, 300, 350$ K and $P = 50$ Torr. The fitting program returned $T = 304 \pm 10$ K.

Fig. 2. The data shown are 100-shot averages. Using the mercury absorption model as well as a fitting routine originally developed for visible FRS,¹ we extracted temperatures from the data. For example, the fit to the data in Fig. 2 returned a temperature of 304 ± 10 K. The data shown in Fig. 2 are after background subtraction. We determined the background by bringing the test cell to vacuum. Preliminary measurements were made at three conditions: $T = 295 \pm 2$ K, $P = 1$ atm; $T = 295 \pm 2$ K, $P = 50$ Torr; $T = 330 \pm 3$ K, $P = 1$ atm. In all cases the fitting routine returned temperatures within 3% of the actual temperature. The model-and-data fitting procedure contains no free parameters or calibration points and does account for the laser line width as well as geometric effects. Uncertainties are determined by the fitting routine from noise in the data. An integral part of the fitting routine is the S6 model created by Tenti *et al.*⁹ for the Rayleigh-Brillouin line shape. The S6 model is designed for a single species of polyatomic atoms and neglects the presence of all branches of rotational Raman scattering. This model has been successfully used by several other researchers.^{1,4,7}

Comparing the signals obtainable with a frequency-doubled Nd:YAG system with those from a frequency-tripled Ti:sapphire system shows the benefit of working in the ultraviolet. The total scattering cross section can be given as¹

$$\sigma = [32\pi^3(n-1)^2/3\lambda^4N^2](6 + 3\rho_0/6 - 7\rho_0),$$

where n is the index of refraction, N is the number density of scatterers, λ is the excitation wavelength, and ρ_0 is the depolarization. The cross section scales as inverse wavelength to the fourth power, though this scal-

ing is offset by an energy per photon scaling, resulting in a cubic dependence of the number of scattered photons for a given beam energy. Decreasing the wavelength from 532 to 254 nm (a factor of 2.09) yields a gain of 9.19 from the wavelength cubed and a gain of 1.16 owing to the increased index of refraction and depolarization.¹⁰ Thus, for a given beam energy, one has 10.7 times more Rayleigh scattered photons at 532 than at 254 nm. Background absorption for the mercury filter is much stronger (suppression of 10^{10} and greater for a typical 5-cm cell) than for the iodine filter (limited to 10^5 by background continuum absorption), so there is a significant reduction in background noise. This is particularly important in cases in which background scattering is strong compared with the Rayleigh signal, such as when windows or walls are in close proximity to the sample volume or when many particulates are present.

In conclusion, we have used ultraviolet filtered Rayleigh scattering to perform accurate temperature measurements in gases, using a mercury absorption filter paired with a Ti:sapphire laser source. Measurements with uncertainties of approximately 3% were obtained under several conditions. The superior spectral properties of the mercury filter as well as the frequency dependence of the Rayleigh cross section indicate that higher signal-to-noise ratios are attained by shifting from the visible to the ultraviolet.

The authors acknowledge the help of several people that was critical to this research. We thank Joe Forkey for providing the code for the fitting routine and Dick Seasholtz for providing a copy of the Tenti code. We also thank Noah Finkelstein and Yuri Ionich for experimental guidance and Mike Sousa for his expertise in constructing optical cells. This research was supported by the U.S. Air Force Office of Scientific Research. A. Yalin's e-mail address is yalin@phoenix.princeton.edu.

References

1. J. N. Forkey, "Development and demonstration of filtered Rayleigh scattering—a laser based flow diagnostic for planar measurements of velocity, temperature, and pressure," Ph.D. dissertation (Princeton University, Princeton, N.J., 1996).
2. E. B. Cummings, *Opt. Lett.* **19**, 1361 (1994).
3. D. Hoffman, K. U. Munch, and A. Leipertz, *Opt. Lett.* **21**, 525 (1996).
4. G. S. Elliot, M. Samimy, and S. A. Arnette, *Exp. Fluids* **18**, 107 (1994).
5. P. Andresen and P. Golz, *Appl. Opt.* **35**, 6054 (1996).
6. S. H. Bloom, P. A. Searcy, K. Choi, R. Kremer, and E. Korevaar, *Opt. Lett.* **18**, 244 (1993).
7. H. Shimizu, S. A. Lee, and C. Y. She, *Appl. Opt.* **25**, 1460 (1986).
8. N. Finkelstein, "An ultraviolet laser source and spectral filters for non-intrusive laser based diagnostics," Ph.D. dissertation (Princeton University, Princeton, N.J., 1997).
9. G. Tenti, C. D. Boley, and R. C. Desai, *Can. J. Phys.* **52**, 285 (1974).
10. D. R. Bates, *Planet. Space Sci.* **32**, 785 (1984).



AIAA 2000-0375

**2-D Temperature Fields in Glow Discharges
Measured with UltraViolet Filtered Rayleigh
Scattering**

Azer P. Yalin, Yuriy Ionikh, Alexander Meshchanov,
and Richard B. Miles

Department of Mechanical and Aerospace Engineering,
Princeton University, Princeton, NJ, 08544

**38th Aerospace Sciences
Meeting & Exhibit
10-13 January 2000 / Reno, NV**

2-D Temperature Fields in Glow Discharges Measured with UltraViolet Filtered Rayleigh Scattering

Azer P. Yalin[†], Yuriy Ionikh^{*}, Alexander Meshchanov^{*}, Richard B. Miles[‡]

*Department of Mechanical & Aerospace Engineering, Princeton University
Princeton, NJ, 08544*

ABSTRACT

We report Filtered Rayleigh Scattering measurements of two dimensional temperature fields in weakly ionized. A measurement system that pairs the frequency tripled output (254nm) of a titanium sapphire laser with a narrow linewidth atomic mercury filter was used. Temperature measurements were performed in 50 torr glow discharges of argon, argon mixed with 1% nitrogen, and nitrogen. The 50 torr argon discharge was studied in a diffuse mode (20 mA) as well as in a contracted mode (70-130 mA). The data from the diffuse discharges is found to be consistent with prior measurements. Data from both the diffuse and contracted discharges is in agreement with calculation. The measurements have a spatial resolution of better than 1 mm, and uncertainties of approximately 5 percent.

INTRODUCTION

In this paper we report two dimensional measurements of temperatures in glow discharges, performed using ultraviolet Filtered Rayleigh Scattering (FRS). The diagnostic system is based upon a high power tunable titanium sapphire laser paired with a mercury absorption filter. This work is the extension of

previous point measurements [1] obtained used a photomultiplier tube (PMT) as the detector. In the current work the laser is focussed into a sheet and an intensified camera is used to obtain two dimensional images.

A variety of non-intrusive optical diagnostics have been used to perform neutral gas temperature measurements in plasmas. We are particularly interested in developing measurement techniques which may be applied in discharges which may be very non-symmetric in their character, such as contracted (filamentary) discharges, partially contracted discharges, and plasmas containing striations. One of the advantages of FRS is that by using a laser sheet as the illumination source, two dimensional measurements may be performed with excellent spatial resolution. In principle, the spatial resolution is limited to the sheet thickness. Like FRS, Laser Induced Fluorescence (LIF) measurements may be performed with excellent resolution. The challenge with LIF is to obtain accurate quantitative results, due to difficulties associated with modeling quenching cross-sections and absorption and emission lineshape factors. Other optical techniques which have been used in plasma diagnostics are generally not well suited for the non-symmetric plasmas we are interested in. Interferometry and absorption techniques are limited by their path integrated nature. Measurements by plasma emission also tend to be limited in spatial resolution, and are path integrated. Apart from spatial resolution the FRS techniques is attractive for several other reasons. The Rayleigh scattering signal has a simple linear dependence with density and is very amenable to analysis. Moreover, Rayleigh techniques are not resonant with the scatterer, and therefore the same experimental setup may be used to probe a variety of plasmas.

[†] Graduate Student, Student Member AIAA

^{*} Visiting Research Scientist from Institute of Physics, St. Petersburg University

^{*} Visiting Graduate Student from Institute of Physics, St. Petersburg University

[‡] Professor, Senior Member AIAA

Copyright © 2000 by Princeton University. Published by the American Institute of Aeronautics and Astronautics, Inc., with permission.

Unlike LIF, which typically yields a rotational temperature, FRS gives the true translational temperature of the gas or plasma. The limiting factor in Rayleigh measurements is often background suppression, and therefore the filter is a powerful addition. The strong suppression of the mercury filter allows the Rayleigh signal to be measured while the background is strongly rejected.

In the current work we focus on measuring the temperatures of diffuse and contracted discharges at fairly low pressures (50 torr) and currents (20-130 mA). The discharges examined were in argon, argon plus 1% nitrogen mixture, and nitrogen. The temperature fields in such discharges are of interest from the viewpoint of both basic plasma research [2], as well as their connection to several specific engineering problems. One of these engineering problems is the interpretation of shock wave propagation experiments [3], [4] in diffuse plasmas. Accurate knowledge of the plasma temperature has enabled us to properly model the thermal effects [5], and interpret these results. Temperature fields in contracted (or filamentary) plasmas are characteristic of discharges in the atmosphere, and may have applications in vehicle control, shock wave suppression, ignition in high speed engines, and aero-optics.

MEASUREMENT APPROACH

Over the past several years, Filtered Rayleigh Scattering has been employed as a diagnostic for both flow visualization as well as quantitative measurements of fluid properties such as density, temperature, and velocity. Filtered measurements, by FRS or related techniques, have been demonstrated in a variety of fluid dynamic environments, e.g. supersonic flows [6], and boundary layers [7], as well as combustion environments [8]. These techniques are based on Rayleigh (or sometimes Mie) scattering from molecules within the flow and are driven by a tunable, narrow linewidth laser source. An atomic or molecular filter may be used to suppress elastically scattered background light. Knowledge of the temperature

dependence of the scattering lineshape allows a temperature measurement via such an approach.

Working in the ultraviolet gives larger signals with lower laser pulse energies due to the frequency to the fourth power dependence of the scattering cross section [6]. In addition, the mercury filter offers greater background suppression, simpler spectroscopy, and more flexibility in its operating conditions than are available with iodine filters in the visible. Recent work has involved the application of UV FRS to point measurements in diffuse plasmas, and now we aim to extend the technique to 2-D measurements in a variety of plasmas.

The Filtered Rayleigh Scattering concept has been thoroughly described in earlier work, [9,10] so that here we will emphasize elements particular to these measurements. A narrow linewidth laser is used to illuminate the sample gas and the scattered light is imaged through a narrow band absorption filter onto a detector, as shown in Fig.1. The laser should be tuneable so that it may be tuned within an absorption notch, and narrow linewidth so that the elastic background (due to windows, particulates etc.) is narrow compared to an absorption notch. The amount of scattered light measured by the detector depends on the spectral overlap of the scattered light and the filter absorption profile. The filter offers very nearly 100% transmission in its passband, yet is extremely optical thick (suppression modeled as 10^5 and higher) within the absorption notches. The light scattered by the atoms and/or molecules in the flow is thermally and collisionally broadened, and is therefore spectrally wider than the laser and background. The goal is to suppress the background while transmitting a large fraction of the light scattered from the flow. By appropriate selection of filter conditions, and laser frequency, one may obtain very strong background suppression (greater than 10^5) while transmitting close to half of the scattered light.

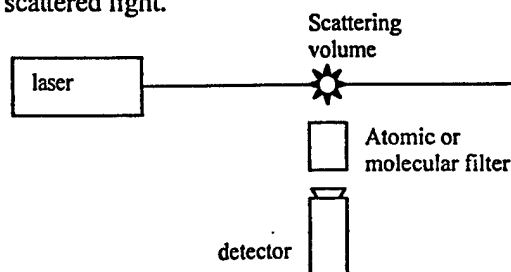


Fig.1 Basic setup for FRS measurements.

Modeled UV FRS signals for Argon, $T=300, \dots, 750$ K

Hg filter: 5 cm, $p=0.0030$ torr, $T=315$ K
signals normalized to 300 K
all 253.7 nm absorption notches shown

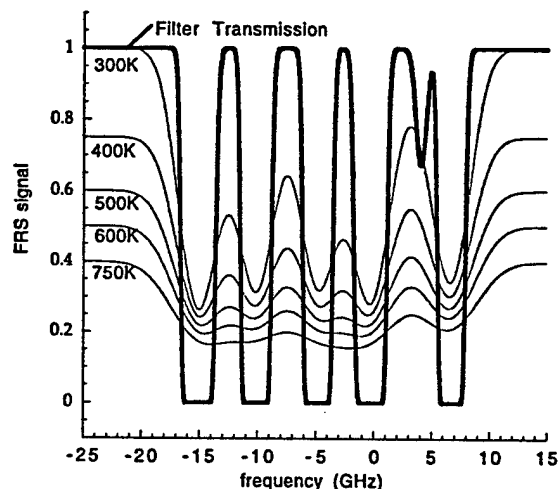


Fig. 2a

Modeled UV FRS signal levels for Argon, $T=300, \dots, 750$ K

Hg filter: 5 cm, $p=0.0030$ torr, $T=315$ K
signals normalized to 300 K
notch used in experiments shown

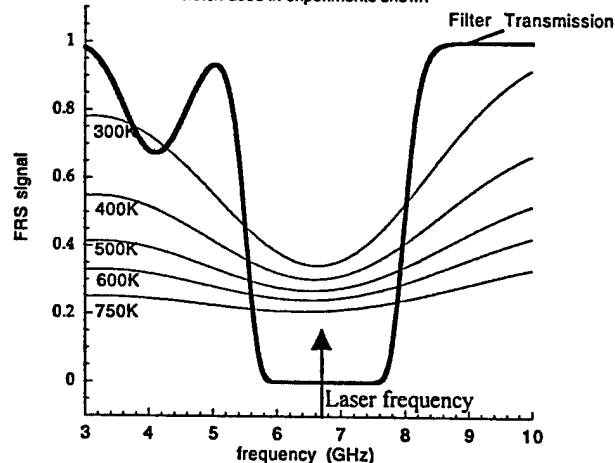


Fig. 2b

Fig. 2a,b Modeled FRS signal levels for Argon at a range of temperatures. Fig. 2a shows all absorption notches in the 253.7 nm vicinity, while Fig. 2b shows the experimentally used (high frequency) notch.

Depending on the application different approaches may be used. Because the pressure is constant (and known) we use a method which does not require background subtraction. The

approach is to ratio the signal at a temperature to be measured, T_M , to the signal at a known temperature, T_{ref} . Both measurements are taken at the same frequency within an absorption notch so that any background is strongly suppressed in both cases. At constant pressure there is a one-to-one correspondence of temperature and density so that the measured ratio uniquely defines the unknown temperature T_M . The signal ratio is primarily determined by the density ratio, with a smaller opposing contribution from lineshape effects.

Conversion Graph: Signal Ratio - Temperature

Hg filter: 5 cm, $P=0.0030$ torr, $T=315$ K
scatterer: argon 50 torr
normalized to $T_{off} = 308$ K

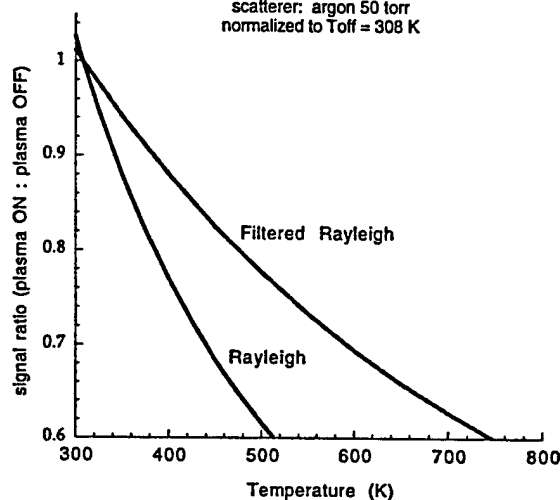


Fig. 3 Look up graph used to convert between signal ratio found with discharge ON/OFF to plasma temperature.

Modeling results for the present measurements are shown in Figs. 2 and 3. Fig. 2a shows the modeled filter transmission profile and FRS signal levels as functions of frequency for argon. The filter has a length of 5 cm, a mercury vapor pressure of 0.0030 torr, and a temperature of 315 K. The six notches are due to hyperfine splitting and different isotopic contributions. The nominal location of the lines is at 253.7 nm. The modeled FRS signal levels are for a scatterer of 50 torr of argon at various temperatures. The Rayleigh scattering cross-section is not affected by the weak ionization and so the curves describe both argon gas and the weakly ionized plasmas used in these experiments. The signals are normalized to

300K (by the ideal gas law) so that their relative magnitudes scale as would be measured by a detector. In the absence of the filter the signal is linear with density (or $1/T$), while within the absorption features there is also a weaker effect from the variation of scattering linewidth with temperature. Fig. 2b is a closer view of the highest frequency absorption notch – the one used in the current work. Again, the modeled FRS signal levels are shown, along with the laser frequency (shown with arrow) used in the experiments. From such modeling one may find the relationship between the experimentally measured FRS signal ratio

$$\text{Ratio} = \text{FRS signal } (T=T_M) / \text{FRS signal } (T=T_{\text{ref}})$$

and the unknown temperature T_M . Fig. 3 is such a curve, plotted for “plasma OFF” temperature $T_{\text{ref}} = 308$ K. The unknown temperature, T_M , corresponds to the “plasma On” temperature.

Of course, in the case of 2-D measurements, each resolution element of the camera should be considered as a separate element. Post processing software has been written to form the signal ratios for each element from the images obtained. Note that this ratioing method automatically normalizes for spatial variations in the laser sheet intensity.

EXPERIMENTAL SETUP

The experimental configuration is illustrated in

Figure 4. A high power, narrow linewidth Titanium Sapphire laser [11] is used as the excitation source. The frequency tripled output is delivered to the plasma tube through several anti-reflection coated beam shaping optics. For these experiments pulse energies of ~ 10 mJ in the ultraviolet (254 nm) were used. The beam passes through a half-wave plate to ensure the correct orientation of the linearly polarized beam, and through a quarter-wave plate to correct for the slight elliptical polarization introduced at the tube windows. Several irises are used to reduce stray light carried with beam. A short focal length (7.5 cm) positive cylindrical lens is arranged confocally with a long focal length (90 cm) positive spherical lens to form a sheet of width roughly 2 cm and a waist of ~ 200 microns. The scattered light is collected at a scattering angle of 90 degrees with an intensified camera after passing through the mercury vapor filter. The filter has length 5 cm and has two temperature controllers yielding a vapor pressure of 0.003 torr, and a filter temperature of 315 K. After the mercury filter, the light passes through a thin film interference filter (CORION G50-254-F), which acts as a broad passband filter, while rejecting plasma luminosity and other colors of light from the laser. The intensified camera is a Princeton Instruments Pentamax system. It is gated to a width of 50 ns and the pixels are binned to form super pixels corresponding to $0.9 \text{ mm} \times 0.9 \text{ mm}$ in the discharge. A picked off portion of the beam is used for power normalization as well as a

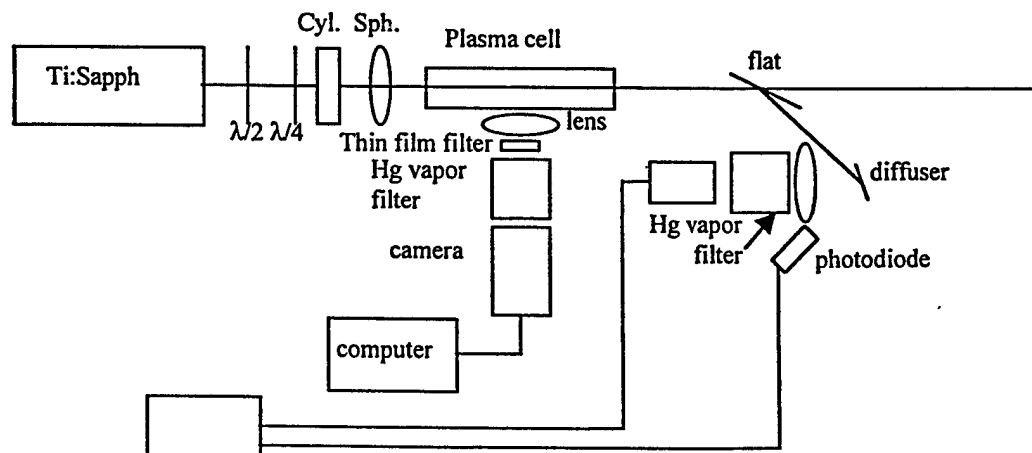


Figure 4 Schematic diagram of apparatus.

frequency reference. The picked off beam illuminates a diffuser, and the elastically scattered light is detected through a second mercury filter (frequency reference), as well as measured by a photodiode (power reference). The latter two measurements use thin film interference filters (CORION G25-254-F) for spectral filtering. The reference signals are collected with a boxcar unit (Stanford Research System).

A small-scale plasma facility has been developed in our laboratory to investigate plasmas and develop diagnostics. A 20kV DC power supply is used to sustain glow discharges in a discharge tube of diameter 38 mm (1.5"). The electrode separation may be selected to be 20, 40, or 60 cm, and the different separations may be used to measure the electric field in the plasma. A flow regulating system allows control of the gas mixture and flowrate. A thermocouple was used to measure the plasma wall temperature. In order to reduce the effects of buoyancy (observed in some cases) the plasma tube was mounted with its axis vertical.

A typical measurement sequence is performed as follows. The laser is scanned down in frequency, from the high frequency transmission side, to within the absorption notch, to approximately the center of the notch. When the center of the notch is reached, the laser frequency is parked and data is collected. The camera is triggered and collects a series of images with the plasma turned on, and then the plasma is extinguished and a further series of images are collected (with the plasma off at the reference temperature T_{ref}). Generally, 256 frames (about 30 seconds) are accumulated in a measurement. The reference temperature is measured with a thermocouple.

In order to perform the data analysis it is necessary to measure, and subtract, the camera dark counts as well as any background signal. The background is measured by bringing the cell to vacuum with the laser tuned to the filter absorption. A small but appreciable background is present. The background is due to the combination of very high camera gain as well as a significant amount of stray reflected light. The geometry of our sheet and tube make it impossible to suppress all of the window back

reflections. It is important to note that this background signal is due to broadband (unseeded) light within the laser pulse (measured as $\sim 1/500$ of total pulse energy [12]) and not due to a lack of filter suppression.

We have written post-processing software to aid in the data analysis. The background and dark count contributions are appropriately subtracted, and at each resolution element the ratio of signal with discharge ON:OFF is formed. The plasma OFF temperature, as well as a look up table are used to determine the plasma temperature at each resolution element.

DATA ANALYSIS

Diffuse Discharges

Diffuse discharges were studied in argon, argon plus 1% nitrogen mixture, and nitrogen, all at a pressure of 50 torr. A digital photograph of a diffuse argon discharge is shown in Plate 1. Apparent structure in the axial direction is likely due to the spatial mode of the laser sheet and not structure within the plasma. The emission appears relatively uniform and fills the tube (between electrodes). The argon discharge was measured at a current of 20 mA. A color plot of the resulting temperature is shown in Plate 2. Fig. 5 shows the result of averaging the temperature along each radial value. Also shown in Fig. 5 with a solid curve is the result of previous temperature point measurements and computation of the same plasma [1]. Clearly, the current data is in good agreement with previous results.

Plate 3 and Fig. 6 show the results of temperature measurements of a 50 torr argon plus 1% nitrogen discharge, at a current of 40 mA. Again, the solid curve in Fig. 6 represents the results of prior measurement and computation and is agreement with the current measurements. Comparing Plate 2 and Plate 3 (or Fig. 5 and Fig. 6) shows that the addition of a small amount of nitrogen to the argon causes a decrease in temperature,

even though the mixture is at higher current. The difference in temperature of the two discharges is likely indicative of differences in their ionization mechanisms.

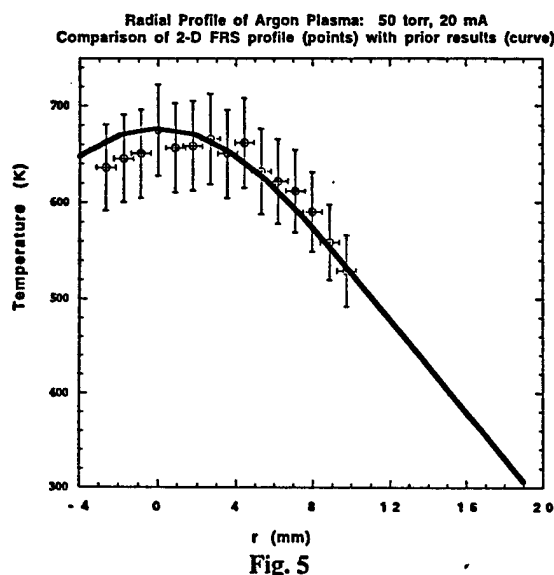


Fig. 5

Figure 5 Temperature profiles of argon plasma. The figure shows the results from Plate 2 radially averaged and plotted with results of previous measurements.

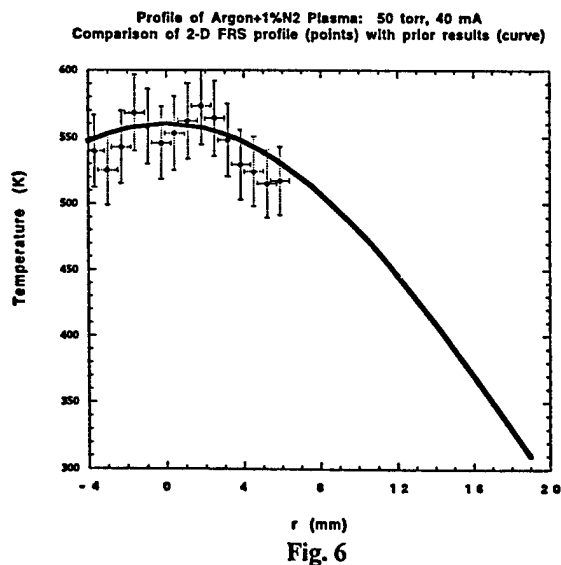


Fig. 6

Figure 6 Temperature profiles of argon plus 1% nitrogen plasma. The figure shows the results from Plate 3 radially averaged and plotted with results of previous measurements.

The temperature profile of a nitrogen discharge was also measured. The nitrogen discharge had a pressure of 50 torr and a current of 50 mA. Results of these measurements are shown in Plate 4 and Fig. 7. In this case we do not have a profile to compare with, but the axial temperature is in accord with that measured previously.

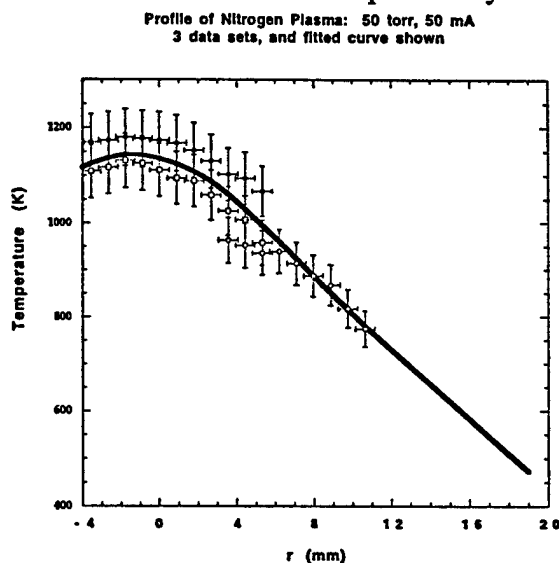


Fig. 7

Figure 7 Temperature profiles of nitrogen plasma. The figure shows the results from Plate 4 radially averaged and plotted with a fitted curve.

Contracted Discharges

Contracted discharges were studied in a 50 torr argon plasma at a range of currents (70 mA, 100 mA, and 130 mA). A photograph of the contracted discharge for the 70 mA case is shown in Plate 5.

Note that while the filament is very close to the center of the tube though most of the filament, it deviates significantly near the electrodes due to their geometry. Such lack of symmetry would pose difficulty in path integrated measurements where the length of the filament must be known, or corrected for.

Plate 6 shows the 2-D temperature maps obtained in the argond discharges at 70 mA, 100 mA, and 130 mA. Apparent

structure in the axial direction is likely due to the spatial mode of the laser sheet and not structure within the plasma.

By using the two electrode pairs it is possible to measure both the current and electric field within the discharge. Using the current, and field, and assuming a current distribution it is possible to compute temperature profiles using the heat equation. These results are then averaged over the dimension of our resolution elements (0.9 mm). It turns out that the width of the current distribution assumed, significantly affects the computation near the axis ($r=0$), while it has little effect on the computation near the tube wall. We define a current width W as the radius of the current distribution at half the peak current value. Therefore, without knowledge of the current distribution it is still possible to compute the temperature within the plasma except for in a small region near the discharge axis. Such computations are shown with curves in Fig.8, and are in good agreement with the radially averaged data. Note that in the case of 100 mA, and 130 mA, the calculations are similar near the wall since the power dissipated in the plasma is very comparable in the two cases. The temperature on the axis is related to the width of the current profile. The curves used here were selected to fit the experimental data near the axis. Calculations indicate that the axial temperature measured for the 70 mA case corresponds to $w=3.3$ mm, while for the 100 mA case corresponds to $w=2.9$ mm, and for the 130 mA case corresponds to $w=1.6$ mm. Calculations for the diffuse argon discharge yield a half width of 7 mm. The tube radius is 19 mm. As expected, for higher currents, the current distribution profile narrows and the axial temperature increases. It is noteworthy that the neutral gas temperature profile does not change dramatically in shifting from the diffuse to contracted regime.

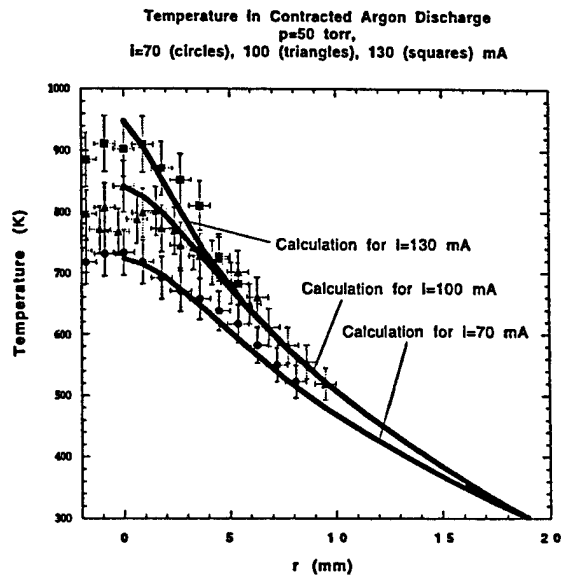


Figure 8 Temperature profiles of contracted argon plasma at several currents. Computed curve is also shown.

CONCLUSIONS

The UV FRS technique has been extended from a zero-D (point) measurement to a 2-D field measurement. The technique was used to measure gas temperature profiles in diffuse as well as contracted discharges. Measurements of the diffuse discharges are in good agreement with previous results. Measurements of the contracted argon discharge indicate that the peak temperature increases with current, while the shape of the profile narrows. The temperature profiles may be used to infer current distributions, and these results indicate that the current distribution is narrower in the contracted than diffuse discharge. Measurements had spatial resolution of better than 1mm, and uncertainties on the order of 5%.

ACKNOWLEDGEMENTS

This work is being supported by the Air Force Plasma Ramparts MURI and the Air Force New World Vista program. The authors would also like to thank Vincent Chiravalle for his aid in writing data analysis software.

REFERENCES

- [1] Yalin, A.P., et al., "Temperature Measurements in Glow Discharges with UltraViolet Filtered Rayleigh Scattering," 30th Plasmadynamics and Lasers Conference, Norfolk, VA, June, 1999. AIAA-99-3431
- [2] Zel'dovich, Y.B., and Raizer, Y.P., "Physics of Shock Waves and High-Temperature Hydrodynamic Phenomena, Vols. 1 and 2, Academic Press, New York, 1966.
- [3] Voinovich, P.A., Ershov, A.P., Ponomareva, S.E., Shibkov, V.M., "Propagation of Weak Shock Waves in Plasma of Longitudinal Flow Discharge in Air," High Temp. 29 (1990) 468.
- [4] Ganguly, B.N., Bletzinger, P., Garscadden, A., "Shock wave damping and dispersion in nonequilibrium low pressure argon plasmas," Physics Letters A, 230 (1997).
- [5] Ioikh, Y.Z., et al., "Shock Wave Propagation Through Glow Discharge Plasmas: Evidence of Thermal Mechanism of Shock Dispersion," 38th Aerospace Sciences Meeting, Reno, NV, Jan. 2000, AIAA-2000-0714
- [6] Smith, M.W., Northam, G.B., "Application of absorption filter planar Doppler velocimetry to sonic and supersonic jets," AIAA J. 34(3), 434-441 (1996).
- [7] Erbland, P.J., et al., "Optical Refraction from High Mach Number Turbulent Boundary Layer Structures," 36th Aerospace Sciences Meeting, Reno, NV, Jan. 1998. AIAA-98-0399
- [8] Elliot, G., Glumac, N., Carter, C., "Molecular Filtered Rayleigh Scattering Applied to Combustion and Turbulence," 37th Aerospace Sciences Meeting, Reno, NV, Jan. 1999. AIAA-99-0644
- [9] Yalin, A.P., Miles, R.B., "Ultraviolet filtered Rayleigh scattering temperature measurements with a mercury filter," Optics Letters, Vol. 24, No. 9, 1999
- [10] Forkey, J.N., "Development and Demonstration of Filtered Rayleigh Scattering - A Laser Based Flow Diagnostic for Planar Measurements of Velocity, Temperature, and Pressure," doctoral thesis #2067-T, Princeton University, Princeton NJ (1996).
- [11] Finkelstein, N.D., Lempert, W.R., and Miles, R.B., "Mercury Vapor Filter Technology and Ultraviolet Laser Source for Flowfield Imaging," 35th Aerospace Sciences Meeting, Reno, NV, Jan. 1997. AIAA-97-0157
- [12] Yalin, A.P., Barker, P., Miles, R.B., "Characterization of Laser Seeding using Group Velocity Dispersion in an Atomic Filter", accepted for publication in Optics Letters



Plate 1 Photograph of diffuse discharge in argon.

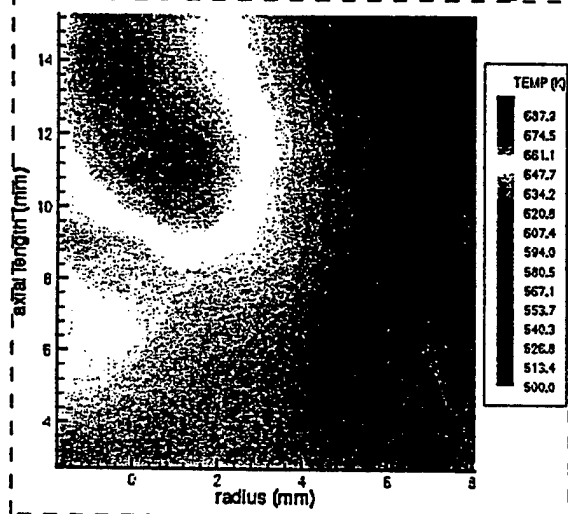


Plate 2

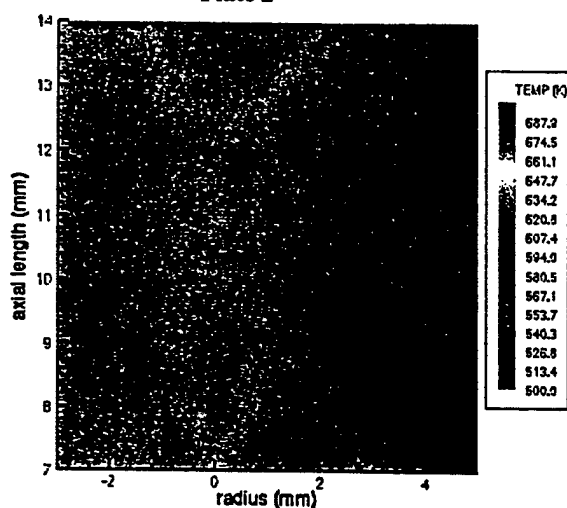


Plate 3

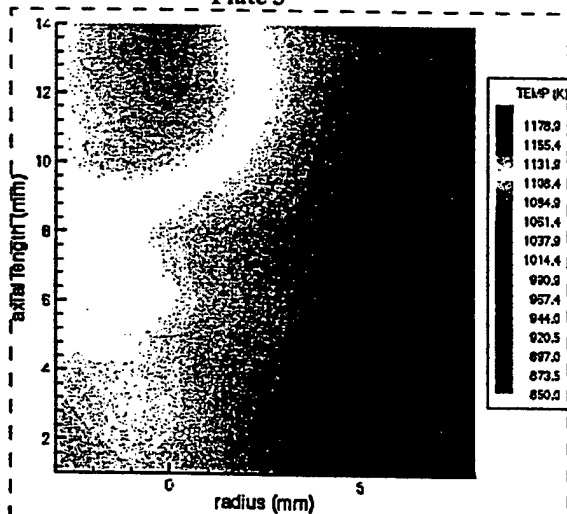


Plate 4

Plates 2,3,4 Two-dimensional temperature maps of several diffuse discharges, all at 50 torr. Plate 2, argon, Plate 3, argon + 1% nitrogen, Plate 4, nitrogen



Plate 5 Photograph of contracted discharge in argon.

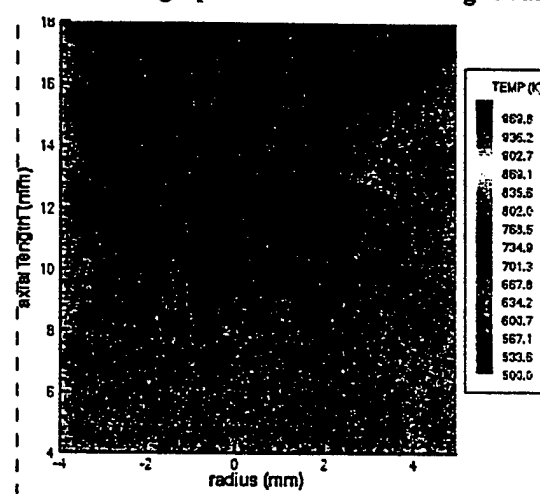


Plate 6a

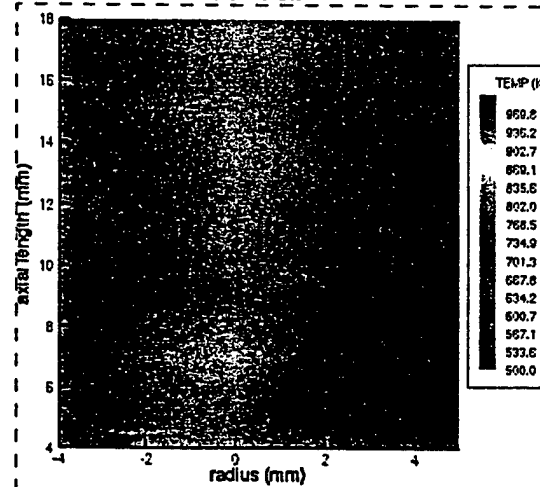


Plate 6b

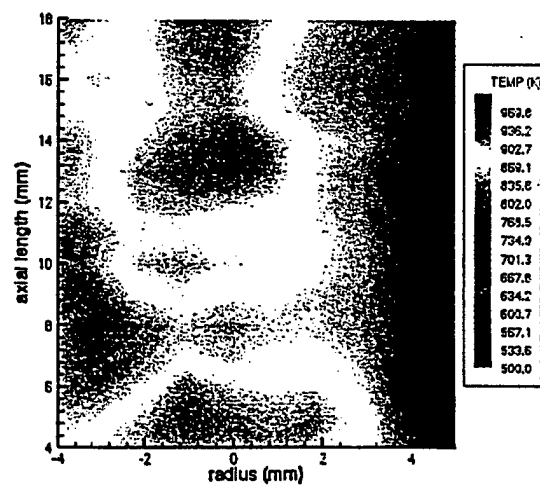


Plate 6c

Plate 6 Two-dimensional temperature maps at a range of currents. Plate 6a, $i=70$ mA, Plate 6b, $i=100$ mA, Plate 6c, $i=130$ mA.

Temperature Measurements by Ultraviolet Filtered Rayleigh Scattering Using a Mercury Filter

Azer P. Yalin* and Richard B. Miles†
Princeton University, Princeton, New Jersey 08544

We report the development of Ultraviolet Filtered Rayleigh Scattering (UV FRS) as a diagnostic tool for measurements of gas properties. A frequency tripled, narrow linewidth, Ti:sapphire laser illuminates a sample, and Rayleigh scattered light is imaged through a mercury vapor absorption filter. The strong absorption of the filter may be used to suppress elastic background. Tuning the laser through the absorption notch of the filter is a means of probing the scattering line shape, which contains temperature information. Temperature measurements of air are shown to have uncertainties of less than 3%, whereas measurements of a weakly ionized discharge have uncertainties of less than 4%. An enhanced scattering cross section as well as nearly ideal filter properties lead to temperature sensitivities for the mercury filter in the ultraviolet which are comparable to those available with an iodine filter in the visible. The absorption for the mercury filter is modeled to be at least 5 orders of magnitude higher than for the iodine filter, meaning that stronger background suppression may be achieved.

Nomenclature

K	= magnitude of the scattering wave vector
k	= Boltzmann's constant
m	= molecular mass
N	= number density of the scattering molecules
n	= index of refraction
P	= gas pressure
S	= filtered Rayleigh scattering signal level at the point of maximum sensitivity, with the signal in the filter transmission normalized to unity
T	= scattering gas temperature
v_0	= thermal velocity
Y	= nondimensional parameter that defines the character of the scattering lineshape
η	= shear viscosity
θ	= scattering angle
λ	= excitation wavelength
ν	= laser frequency
ρ_0	= depolarization factor
σ	= total scattering cross section
$()_{\text{ideal}}$	= indicates that the bracketed quantity is evaluated for an ideal filter

Introduction

OVER the past several years filtered Rayleigh scattering (FRS) has been employed as a diagnostic in a variety of gaseous environments for nonintrusive flow visualization as well as quantitative measurements of fluid properties including temperature. Nonintrusive temperature measurements are very important for improved understanding of many areas of physics, such as supersonic flows, weakly ionized plasmas, combustion processes, and the atmosphere. Our primary motivation for the work reported here is to develop the technique for plasma diagnostics. In particular, we are studying methods for producing low-temperature plasmas with electron number densities of $<10^{13}/\text{cm}^3$ (ionization fractions $<10^{-5}$). We are also interested in the propagation of shock waves through low-density plasmas. The ability to obtain one- or two-dimensional temperature and density maps of these plasmas is critical for this work.

A wide array of optical methods is available depending on the nature of the problem under investigation. FRS is attractive because, by focusing the laser to a sheet, it has the potential to provide a full two-dimensional, quantitative map of the flowfield.^{1,2} Typically, spectral measurements, such as absorption and fluorescence, are path-integrated coherent anti-Stokes Raman scattering (CARS) and laser-induced thermal anemometry (LITA)³ may be used to perform point measurements, but are inherently not well-suited for two-dimensional imaging. Raman techniques are species-specific and could possibly allow imaging, but suffer from very low signal levels. Laser-induced fluorescence (LIF) methods are amenable to imaging; however, in many cases fluorescence quenching and saturation complicate quantitative analysis. For example, one group doing point LIF measurements in an inductively coupled argon plasma found an accuracy of $\pm 80\text{ K}$ ($\sim \pm 10\%$) (Ref. 4). FRS can be used to capture quantitative planar measurements of gas temperature, pressure, density, and velocity. Rayleigh scattering is a nonresonant process and thus unaffected by quenching and saturation. Furthermore, it is linear with scatterer density. Filtering the Rayleigh signal with a narrow linewidth atomic or molecular filter gives an additional temperature dependence to the signal because of the temperature dependence of the scattering line shape. In addition, the filter provides very strong suppression (modeled to be greater than 10^5) of elastic background. Because Rayleigh scattering is an elastic process, it is often difficult to decouple the Rayleigh signal from any spurious elastic background without the use of a filter. Suppression of any nonelastic background (caused by, for example, pump lasers or sample luminosity) may be performed with conventional interference filter technologies.

In the visible region the FRS technique has already shown its utility in a variety of environments, such as for temperature measurement in combustion⁵ and for velocimetry and flow visualization in high-speed flows.^{1,6} This work has primarily used frequency doubled Nd:YAG sources paired with molecular iodine filters (532 nm). Some FRS work has also been done in the ultraviolet, using an excimer laser with an atomic iron filter (248 nm)⁷ but with modest success because of the limitations of the seeding of the laser. Related work in the light detection and ranging (LIDAR) and other communities has paired narrow linewidth lasers and filters in the visible to infrared region, for example, an Alexandrite laser and potassium filter (770 nm)⁸ or a dye laser and cesium filter (389 nm).^{9,10} Additionally, rubidium (780 nm),⁹ barium (554 nm),⁹ magnesium (516–518 nm),^{10,11} calcium (423 nm),¹⁰ and lead (283 nm)⁹ have all been considered or used as atomic filters.

The focus of this work is the extension of the FRS technique from the visible to the UV portion of the spectrum, where the scattering

Received 12 March 1999; revision received 15 September 1999; accepted for publication 1 October 1999. Copyright © 1999 by the American Institute of Aeronautics and Astronautics, Inc. All rights reserved.

*Graduate Student, Department of Mechanical and Aerospace Engineering, Student Member AIAA.

†Professor, Department of Mechanical and Aerospace Engineering, Associate Fellow AIAA.

is stronger and the more ideal mercury vapor filter can be used. Preliminary work characterizing the mercury filter was performed in our laboratory by Finkelstein.¹² To perform temperature measurements, Rayleigh scattering from a gas sample is imaged through a mercury filter, and a model is used to fit for gas properties. The frequency dependence of the scattering cross section, as well as the absorption profile of the filter, lead to comparable temperature sensitivities in the UV than in the visible. However, the much stronger absorption of the mercury filter, compared to iodine, means that superior background suppression may be attained. In this paper the technique is explained, the mercury filter and relevant models are discussed, the experimental setup and results of temperature measurements are presented, and finally a comparison between visible and UV FRS is given. The latter comparison, as well as the discussion of the mercury filter, serve to motivate the selection of mercury as the filter material.

FRS Technique

Overview

A narrow linewidth laser is used to illuminate a sample volume, and the scattered light is imaged through a narrowband atomic or molecular vapor absorption filter onto a detector (Fig. 1). The amount of scattered light arriving at the detector depends on the spectral overlap of the scattered light with the filter absorption profile. The scattered light consists of an elastic background component from window scattering and stray reflections, as well as the Rayleigh light scattered from the flow. The spectral profile of the scattering intensity is termed the scattering line shape. Temperature can be determined by measuring the Rayleigh scattering line shape using the mercury vapor absorption filter. By tuning the laser, the scattering line shape is swept across the absorption filter profile causing the transmitted light to vary in intensity. Because the absorption profile of the filter is known, the transmitted intensity profile can be deconvolved to yield the Rayleigh-Brillouin line shape, from which the temperature may be determined.

Scattering Line Shape

The light scattered by the flow has a Rayleigh-Brillouin line shape generated by the Doppler shifts associated with the thermal motion of the molecules in the sample volume. The line shape is dependent on scattering angle, temperature, pressure, and excitation frequency. The character of the line shape depends on a nondimensional quantity called the Y parameter, defined by Tenti et al.¹³ as

$$Y = NkT/2^{1/2}Kv_0\eta \quad (1)$$

$$[K = 4\pi/\lambda \sin(\theta/2)]$$

where v_0 is a thermal velocity, related to gas temperature and molecular mass:

$$v_0 = (kT/m)^{1/2} \quad (2)$$

One may manipulate this expression and use the Sutherland formula for viscosity to yield an expression for Y in terms of the flow parameters appropriate for scattering from air²:

$$Y = 0.230[(T + 111)/T^2][P\lambda/\sin(\theta/2)] \quad (3)$$

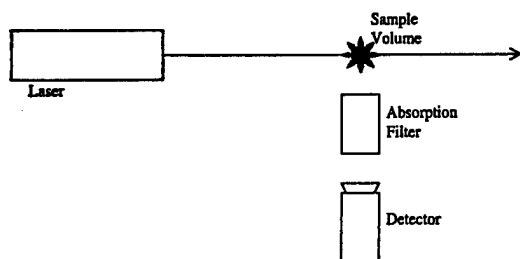


Fig. 1 Basic setup for FRS.

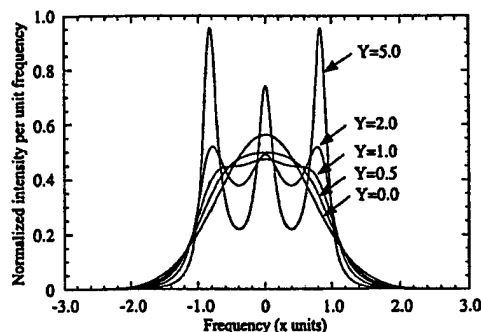


Fig. 2 Rayleigh-Brillouin scattering profiles for various Y values. Frequency is given in normalized units: $x = 2\pi v/2^{1/2}Kv_0$.

where T is in Kelvin, P is in atmosphere, and λ is in nm. For Y values much less than unity, the thermal motion of the gas may be represented by a Maxwellian velocity distribution, leading to a purely Gaussian scattering profile centered at the frequency associated with the average gas motion. In such cases, entitled the Knudsen regime, the line shape is independent of pressure. The opposite extreme, corresponding to high Y values, is known as the hydrodynamic regime. In this case the molecular motion is correlated, and thermally induced sound waves scatter the light. In such cases the line shape has a central Lorentzian component, caused by thermal diffusion, as well as a pair of Lorentzian sidebands, shifted out by a frequency associated with the speed of sound. In this regime the line shape has a weak pressure dependence. We are primarily interested in plasmas with subatmospheric pressures and moderate to high temperatures. Such plasmas have small values of the Y parameter; however, the complete Tenti model¹³ is used. Line shapes for various Y parameters are shown in Fig. 2. In this work we make use of the S6 model, created by Tenti, for the Rayleigh-Brillouin line shape. This model has been successfully used by several other researchers.^{1,6,9} However, even this model is not exact. The S6 model is designed for a single species of polyatomic atom while air contains a number of species. Also, the model neglects the presence of all branches of rotational Raman scattering.

Mercury Vapor Filter

In FRS the absorption filter serves two critical purposes: background suppression and probing of spectral information. Desired filter properties are high out-of-band transmission, high in-band absorption, steeply sloping walls, and flexibility in selecting the absorption width. Mercury has an optically accessible strong ground-state transition at 253.7 nm and is well suited as a filter material. Unlike some other materials with transitions in the UV, such as iron, lead, and cesium, mercury has a low boiling point and high molar mass. The low boiling point means useful vapor number densities may be attained at relatively low temperatures. This low operating temperature together with the high atomic weight of the mercury atom (200.6 amu) reduces thermal broadening and leads to very steep filter walls if the mercury vapor pressure is kept low enough to avoid collisional broadening. In a 5-cm cell, at low vapor pressure (order 0.01 torr) lines from each of mercury's six naturally occurring isotopes form separate notches with widths up to several gigahertz and filter walls that rise from 10 to 90% transmission over hundreds of megahertz. At a higher vapor pressure (order 1 torr) the isotopic lines blend together and form a notch with a width of tens of gigahertz. In this case the filter walls are not very steep because collisional broadening is significant. Figure 3 shows absorption profiles for a 5-cm length mercury vapor cell at three different vapor pressures. The out-of-band transmission is close to 100% (neglecting filter window losses), and the in-band optical suppression is predicted to be five orders of magnitude or more. The vapor pressure is controlled by setting the temperature of a sidearm, which contains a small amount (several grams) of liquid mercury. The sidearm is immersed in a temperature-controlled liquid bath (water or mineral oil). The main body of the filter is a quartz tube of diameter 5 cm and length 5 cm. To prevent any condensation in the main

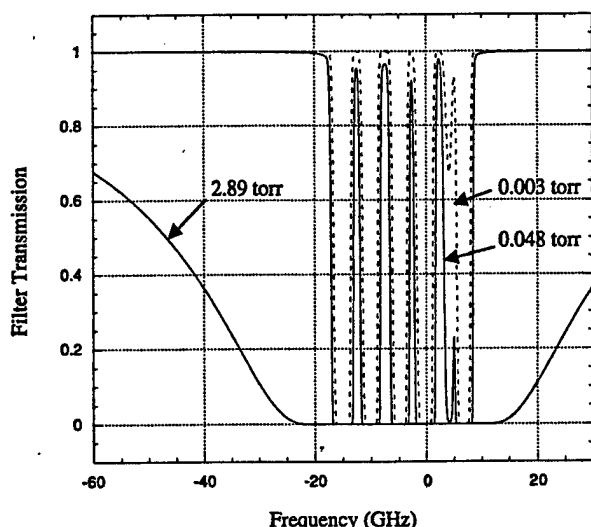


Fig. 3 Absorption profiles for three different 5-cm-length mercury vapor filters. The three filters correspond to vapor pressures of 0.003, 0.048, and 2.89 torr, respectively.

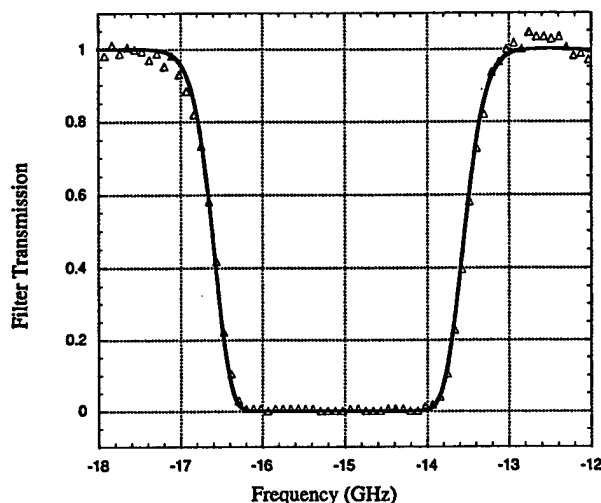


Fig. 4 Absorption scan of the mercury vapor filter. The vapor filter has length 5 cm and a vapor pressure of 0.003 torr. The notch shown corresponds to the Hg 202 isotope and is the notch used for the presented temperature measurements.

tube, the body of the tube is heated to a temperature slightly higher than the sidearm. By varying the sidearm temperature from ~ 20 to ~ 200 C, vapor pressures from ~ 0.001 to ~ 20 torr may be achieved. For the measurements presented in this work, a vapor pressure of 0.0030 torr was used. A model for mercury absorption has been developed in earlier work.¹² Absorption scans were performed for additional validation of the absorption model and the detection system. Figure 4 shows an experimental scan and modeled values for one of the isotopic notches.

FRS Signal and Temperature Measurement

The FRS technique makes use of the temperature dependence of the scattering line shape in order to measure temperature. Depending on the measurement conditions, different variants of the technique may be used. At each laser frequency the amount of scattered light arriving at the detector depends on the spectral overlap of the scattered line shape (centered at the laser frequency) and the filter absorption profile. Figure 5a shows the spectral overlap of the scattered light with the filter transmission at two laser frequencies, f_1 and f_2 . The scattered light has two components: a broad-band Rayleigh-Brillouin component and a narrowband background

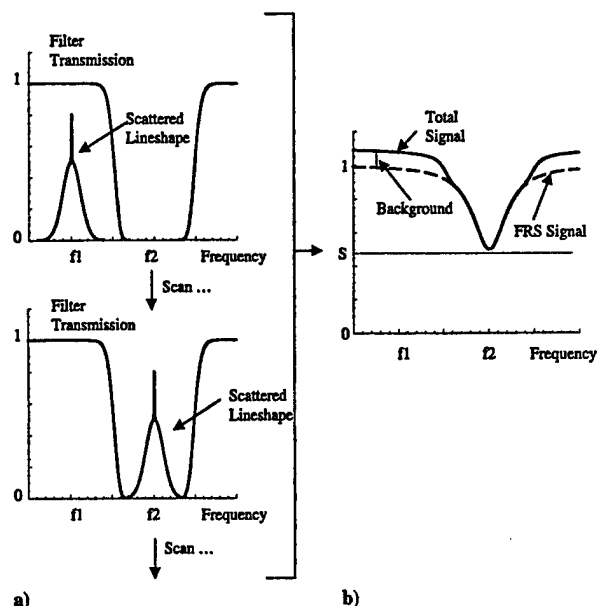


Fig. 5 FRS signal as function of laser tuning: a) spectral overlap of the scattered light with the filter transmission at two laser frequencies, f_1 and f_2 ; b) by tuning the laser through the absorption notch the FRS signal is obtained as a function of frequency. The point in the FRS data with the maximum sensitivity to temperature is the FRS minimum, labeled S.

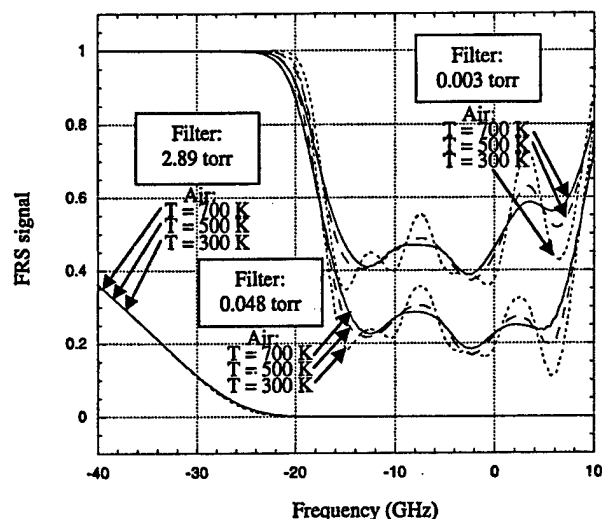


Fig. 6 Modeled FRS signals for three different mercury vapor filter configurations for atmospheric pressure air at temperatures of 300, 500, and 700 K. The three filters correspond to those shown in Fig. 3 and are 5 cm in length with vapor pressures of 0.003, 0.048, and 2.89 torr.

component from windows and stray reflections (shown as a sharp peak). In the most general case, by scanning the laser frequency the Rayleigh-Brillouin line shape is swept across the absorption filter profile causing the transmitted light to vary in intensity. In this manner one obtains the FRS signal as a function of frequency (see Fig. 5b). A model is used to fit the FRS data for gas properties. Of course, a laser with linewidth narrow compared to the width of the filter is required. The FRS signal is a convolution of the scattering line shape (and laser linewidth) with the filter absorption profile. Because the filter absorption profile is known, a fitting routine may be used to extract temperature from the FRS data. In this work we use a code developed by Forkey¹ for visible FRS.

Along with the fitting routine, a program to model the FRS signal has been created.¹ The program requires the filter absorption profile as one of its inputs. Figure 6 shows the modeled FRS signal as a

function of frequency for various filters and temperatures. In each case the FRS signal is normalized to unity in the filter transmission. Here it is clear that sharp filter walls are required to get significant temperature sensitivity.

A variant of the preceding technique may be used in cases where the gas is in pressure equilibrium and the pressure is known. In such cases, there is a one-to-one correspondence between temperature and density so that a single measurement may be used to determine the temperature and density simultaneously. The most practicable measurement is to take the ratio of the FRS signal at a known (reference) condition to the FRS signal at an unknown (to be measured) condition. The FRS signal model may then be used to convert the measured ratio to temperature. This method has the distinct advantage that all data are taken at a single laser frequency, meaning that by selecting the frequency to be within an absorption notch one may suppress elastic background throughout the entire measurement. This method is similar to measuring the temperature with Rayleigh scattering; however, using a filter gives the significant advantage of strong elastic background suppression.

As mentioned, by varying the filter parameters different filter absorption profiles may be obtained. In this manner an absorption filter may be tailored for a specific set of measurements.

Experimental Setup

A schematic diagram of the experimental setup is shown in Fig. 7. A custom-built titanium sapphire laser system¹² is used as the illumination source for the UV FRS measurements. The laser is injection seeded and operates with a novel cavity locking scheme, which ensures almost transform limited, narrow linewidth single mode output. The linewidth of the third harmonic output is approximately 200 MHz, which is narrow compared to the scattering linewidth and filter absorption width, both of which are about 2 GHz. Pulse energies (in the UV) on the order of 10 mJ per pulse were used.

The third harmonic output from the laser system is delivered along the axes of a cylindrical cell, with antireflection (AR) coated windows, which houses the sample gas. A 50-cm focal length lens is used to focus the beam to a waist of $\sim 100\mu$. To minimize any background light, the beam is passed through several irises. A half-wave plate is used to ensure the correct orientation of the linearly polarized beam, and a quarter-wave plate compensates for any elliptical polarization introduced at the window. All of the beam shaping optics are AR coated. An AR coated 5-cm focal length lens is placed 8 cm from the beam and is used to image the Rayleigh scattered light at an observation angle perpendicular to the beam and cell axes. An iris of diameter ~ 1 mm is placed between the lens and cell and serves to define the sample region as well as to further reduce background light. The scattered light is imaged through the mercury vapor filter and then passed through an ISA H20 monochromator set to 254 nm, which acts as a broad (>1 nm) pass band filter. The monochromator rejects other colors of light caused by the pump laser or any non-Rayleigh light from the scattering volume. Finally, the scattered light is detected with an R-960 Hamamatsu photomultiplier tube (PMT).

A quartz flat is used to pick-off a fraction of the laser beam after it has passed through the cell in order to serve as a power and frequency reference. The pick-off beam is incident on a diffuser, and elastically scattered light from the diffuser is measured with a photodiode for power normalization, as well as passed through a second mercury vapor absorption filter and measured with a sec-

ond PMT in order to serve as a frequency reference. The frequency axis may be established using the second mercury vapor filter by fitting the measured transmission to the modeled results. The reference vapor mercury filter was 13 cm in length and ran at room temperature. Thin-film interference filters (Corion G25-254-F) are placed in front of the reference photodiode and PMT in order to detect only the 254 nm light. These interference filters have a width of several nanometers and have a flat response over the spectral region of interest. The signals from both PMTs and the photodiode are collected using a Stanford Research Systems (SRS) boxcar unit and a personal computer. An SRS 330 preamplifier unit is used at $\times 5$ to amplify the signals from the FRS PMT as well as the photodiode. Great care was taken to ensure the linearity of the entire detection scheme.

Results

To demonstrate the technique, we initially performed temperature measurements of air. The basic procedure was to scan the laser across the filter absorption and collect the FRS signal as a function of frequency. The FRS signal was normalized using the reference photodiode, and the frequency axis was established with the reference PMT. A thermocouple inside the sample cell was used as a reference measure of temperature. Data obtained from typical scans, in this case atmospheric pressure air at 295 ± 2 and 330 ± 3 K, are shown in Fig. 8. Both data sets are normalized to one in the filter transmission. Data shown are 100 shot averages. The laser was scanned over a frequency range of ~ 15 GHz with a step size of approximately 40 MHz. Using the mercury absorption model and fitting routine, temperatures are extracted from the data. For example, the fits to the data in Fig. 8 returned a temperature of 304 ± 8 and 330 ± 8 K. The data shown in Fig. 8 are after background subtraction. The background signal was caused by stray elastic scatter from windows and other optics and was measured by bringing the sample cell to vacuum with the laser tuned away from the filter absorption. A test to confirm filter suppression was performed by tuning the laser to within the absorption notch and measuring the PMT signal with the cell at vacuum. In this case no signal could be measured within the dynamic range of our detection system. Air measurements have been made at three conditions: $T = 295 \pm 2$ K, $P = 1$ atm; $T = 295 \pm 2$ K, $P = 50$ torr; and $T = 330 \pm 3$ K, $P = 1$ atm. These three conditions correspond to Y values of 0.39, 0.03, and 0.33, respectively. In all cases the fitting routine returned temperatures within 3% of the actual temperature. The model and data fitting procedure contains no free parameters or calibration points and does account for the laser line width as well as geometric effects.

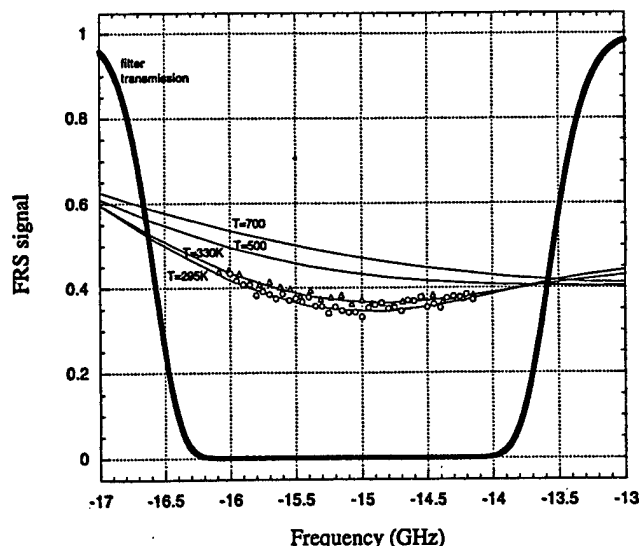


Fig. 8 UV FRS data from air at $T = 295 \pm 2$ K, $P = 1$ atm (O) as well as data from air at $T = 330 \pm 3$ K, $P = 1$ atm (Δ). The modeled filter transmission profile (thick line) is shown, as well as the model fit for atmospheric pressure air at $T = 295, 330, 500$, and 700 K.

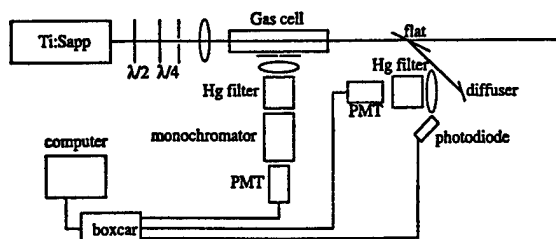


Fig. 7 Schematic diagram of experimental setup.

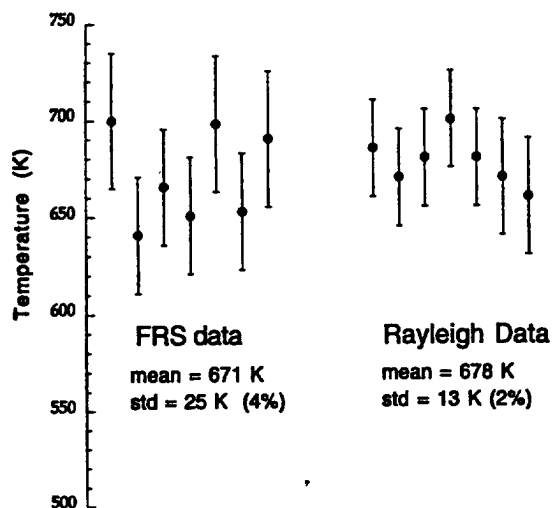


Fig. 9 Comparison of FRS and Rayleigh scattering measurements of the axial temperature of a 50 torr, 20 mA, argon plasma.

Uncertainties are determined by the fitting routine from noise in the data. Some error is introduced when fitting the frequency axis caused by thermal drift in the seed laser (estimated as several megahertz per minute). To remedy this, external locking schemes are being considered, for example, Ref. 14. Also, the background subtraction introduces some error, particularly at low pressure. As mentioned, background caused by stray light and window scatter was subtracted from the FRS signal. The background level may be described in terms of the pressure of a room temperature air sample that would give an equivalent Rayleigh signal in the absence of the filter. Using the AR-coated cell and the optics just described, a background equivalent to approximately 1 torr of Rayleigh scattering from air was detected.

Another series of measurements were performed at more elevated temperatures. Elevated temperatures were obtained by running a weakly ionized (ionization fraction $<10^{-6}$) glow discharge within the sample cell. Figure 9 shows the results of FRS as well as Rayleigh measurements of the centerline temperature of a 50 torr, 20 mA argon discharge. These measurements were obtained using the constant pressure variant of the FRS approach (described in "FRS Signal and Temperature Measurement" section). The monochromator served to suppress any plasma luminosity. The laser was operated at a single frequency within the absorption notch, and the FRS signal with the discharge on was ratioed to the FRS signal at a reference temperature with the discharge off. Because the pressure is fixed, there is now a one-to-one correspondence of temperature and density so that this ratio uniquely defines the unknown temperature. Measurements with and without the filter are within experimental uncertainty. The measurements validate the UV FRS technique in this more elevated temperature range. Standard deviations of the filtered measurements are higher (4% vs 2%) caused primarily by the drift of the seed laser. Measurements by this approach, with the laser at a single frequency in the absorption notch, may also be performed in cases with a high elastic background. Because of the low ionization fraction, the change in scattering cross section caused by excited atoms, changes in scattering line shape, and any Thompson scattering can be neglected. At higher plasma temperatures, with low ionization fractions, a real-gas equation of state may be used. Measurements at higher ionization fractions will be challenging, primarily because of the dramatic variation of scattering cross section for excited atoms.

UV vs Visible FRS

Comparing the signals obtainable with a frequency doubled Nd:YAG system to a frequency tripled Ti:sapphire system shows the benefit of working in the UV. The total scattering cross section may be given as¹

$$\sigma = [32\pi^3(n-1)^2/3\lambda^4 N^2](6+3\rho_0)/(6-7\rho_0) \quad (4)$$

For air at 254 nm, the cross section has a value on the order of 10^{-25} cm^2 (value found by scaling data from Ref. 15). The cross section scales as inverse wavelength to the fourth power, although this is offset by the linear dependence of photon energy with frequency, resulting in a cubic dependence of the number of scattered photons for a given beam energy. Decreasing the wavelength from 532 to 254 nm (a factor of 2.09) yields a gain of 9.19 from the wavelength cubed and a gain of 1.16 caused by the increased index of refraction and depolarization.¹⁶ Thus, for a given beam energy one has 10.7 times more Rayleigh scattered photons in going from 532 to 254 nm. Standard PMTs have comparable quantum efficiencies at 254 and 532 nm (about 25%), yielding an increase in counts by a factor of approximately 10, for a given beam energy. In practice, if one uses a UV source with 10 times lower energy per pulse than is available in the visible (e.g., 30 mJ/pulse from the third harmonic of a Ti:Sapphire system vs 300 mJ/pulse from the second harmonic of a Nd:YAG system), then the number of counts (or signal to noise) in both cases is comparable.

Another important element in comparing filters is an examination of their temperature sensitivities. An ideal absorption filter would consist of a single absorption notch with infinitely steep walls. The width of such a filter would then be adjusted for maximum temperature sensitivity for given scattering conditions. In this ideal case the point of maximum temperature sensitivity of the FRS data is the transmission minimum, which occurs when the laser is in the middle of the absorption filter (see Fig. 5). If one normalizes the FRS signal in the filter transmission to unity and labels the maximum sensitivity point as S , then one may compare the temperature sensitivities of two filters (assuming equal signal to noise) by looking at the nondimensional quantity $T dS/dT$. Using expressions from Ref. 1, one finds that an ideal filter, having infinitely steep walls, optimized for a given scatterer temperature, and assuming $Y \ll 1$, would have

$$T(dS/dT)_{\text{ideal}} = 0.242 \quad (5)$$

The value of $T dS/dT$ for an actual filter may be viewed as a measure of the ideality of the filter. The closer the value is to 0.242, the more ideal the filter. The primary factors in determining the temperature sensitivity of an actual filter are the slope of the filter walls, as well as the presence of other nearby absorption features. It is convenient to parameterize the problem with a nondimensional steepness, where the steepness is defined as the Doppler width (FWHM) of the scattering line shape divided by the frequency interval over which the walls turn on (e.g., the 10–90% width). Analysis shows that for steepness $> \sim 10$ one comes asymptotically close to the maximum sensitivity. Increasing the steepness beyond this value yields very little enhancement of the temperature sensitivity. Mercury and iodine filters both have steep walls (steepness $> \sim 5$) for most measurement conditions because of their high molar masses and low boiling points. Modeled values of $T dS/dT$ for mercury and iodine filters, for scattering from 50 torr air at temperatures of 400 and 800 K, are shown in Table 1. The modeled filters are 5 cm in length, and the filter temperatures (and vapor pressures) are optimized for each measuring condition.

The temperature sensitivities of iodine and mercury filters are very comparable, differing by at most 15%. The temperature sensitivity of the mercury filter is compromised by the presence of isotopes (giving a series of absorption notches), whereas for iodine the sensitivity is limited by the presence of many absorption lines as well as a background continuum absorption. For low air temperatures both filters are nearly ideal, whereas at high temperatures the presence of multiple absorption features reduces the temperature sensitivity. The

Table 1 Comparison of modeled temperature sensitivity for mercury and iodine filters

Air temperature, K	Mercury cell: $T dS/dT$	Iodine cell: $T dS/dT$
400	0.18	0.21
800	0.15	0.16

idea of using an isotopically enhanced mercury filter is attractive but likely not viable. Because we are using very optically thick filters, the degree of isotopic enhancement required would in general be prohibitively expensive. Some additional gain in sensitivity may also be achieved by using longer cells.

Background absorption for the mercury filter is much stronger (suppression modeled to be much greater than 10^5 for a typical 5-cm cell) than for the iodine filter (limited to 10^5 by background continuum absorption) so that there is a significant reduction in background noise. This is particularly important in cases where background scattering is strong compared to the Rayleigh signal, such as when windows or walls are in close proximity to the sample volume, or many particulates are present.

Conclusion

In conclusion, we have used ultraviolet FRS to perform accurate temperature measurements in gases, using a mercury absorption filter paired with a titanium sapphire laser source. Measurements with uncertainties of 3–4% were obtained under several conditions. The absorption profile of the mercury filter, as well as the frequency dependence of the Rayleigh cross section, indicate that comparable temperature sensitivities are attained by shifting from the visible to the ultraviolet. The absorption for the mercury filter is modeled to be several orders of magnitude higher than for the iodine filter, meaning that stronger background suppression may be achieved. We are currently working to extend the diagnostic to perform spatially resolved measurements. Also, we plan to further apply the technique to temperature measurements in plasmas.

Acknowledgments

This work was supported by the Air Force Office of Scientific Research. The authors would like to acknowledge several people whose help was critical to this work. We thank Joe Forkey for providing the code for the fitting routine and Dick Seasholtz for providing a copy of the Tenti code. The authors also thank Noah Finkelstein and Yury Ionikh for experimental guidance and Mike Sousa for his expertise in constructing optical cells.

References

¹Forkey, J. N., "Development and Demonstration of Filtered Rayleigh Scattering—A Laser Based Flow Diagnostic for Planar Measurements of Velocity, Temperature, and Pressure," Ph.D. Dissertation, # 2067-T, Dept. of Mechanical and Aerospace Engineering, Princeton Univ., Princeton, NJ,

April 1996.

²Forkey, J. N., Lempert, W. R., and Miles, R. B., "Accuracy Limits for Planar Measurement of Flow Field Velocity, Temperature and Pressure Using Filtered Rayleigh Scattering," *Experiments in Fluids*, Vol. 24, No. 2, 1998, pp. 151–162.

³Cummings, E. B., "Laser-Induced Thermal Acoustics: Simple Accurate Gas Measurements," *Optics Letters*, Vol. 19, No. 17, 1994, pp. 1361–1364.

⁴Hebner, G. A., "Spatially Resolved, Excited State Densities and Neutral and Ion Temperatures in Inductively Coupled Argon Plasmas," *Journal of Applied Physics*, Vol. 80, No. 5, 1996, pp. 2624–2636.

⁵Hoffman, D., Munch, K. U., and Leipertz, A., "Two-Dimensional Temperature Determination in Sooting Flames by Filtered Rayleigh Scattering," *Optics Letters*, Vol. 21, No. 7, 1996, pp. 525–527.

⁶Elliot, G. S., Samimy, M., and Arnette, S. A., "A Molecular Based Velocimetry Technique for High Speed Flows," *Experiments in Fluids*, Vol. 18, No. 1–2, 1994, pp. 107–118.

⁷Andresen, P., and Golz, P., "Atomic Vapor Filter for Two-Dimensional Rayleigh Imaging Experiments with a Narrow-Band KrF Excimer Laser," *Applied Optics*, Vol. 35, No. 30, 1996, pp. 6054–6061.

⁸Bloom, S. H., Searcy, P. A., Choi, K., Kremer, R., and Korevaar, E., "Helicopter Plume Detection by Using an Ultranarrow Band Noncoherent Laser Doppler Velocimeter," *Optics Letters*, Vol. 18, No. 3, 1993, pp. 244–246.

⁹Shimizu, H., Noguchi, K., and She, C. Y., "Atmospheric Temperature Measurements by a High Spectral Resolution Lidar," *Applied Optics*, Vol. 25, No. 9, 1986, pp. 1460–1466.

¹⁰Gelbwachs, J. A., "422.7-nm Atomic Filter with Superior Solar Background Rejection," *Optics Letters*, Vol. 15, No. 4, 1990, pp. 236–238.

¹¹Chan, Y. C., Tabat, M. D., and Gelbwachs, J. A., "Experimental Demonstration of Internal Wavelength Conversion in the Magnesium Atomic Filter," *Optics Letters*, Vol. 41, No. 14, 1996, pp. 722–724.

¹²Finkelstein, N., "An Ultraviolet Laser Source and Spectral Filters for Non-Intrusive Laser Based Diagnostics," Ph.D. Dissertation, #3015-T, Dept. of Mechanical and Aerospace Engineering, Princeton Univ., Princeton, NJ, Jan. 1997.

¹³Tenti, G., Boley, C. D., and Desai, R. C., "On the Kinetic Model Description of Rayleigh–Brillouin Scattering from Molecular Gases," *Canadian Journal of Physics*, Vol. 52, No. 2, 1974, pp. 285–297.

¹⁴Tsuchida, H., Ohtsu, M., and Tako, T., "Frequency Stabilization of AlGaAs Semiconductor Laser to the Absorption Line of Water Vapor," *Japanese Journal of Applied Physics*, Vol. 21, No. 1, 1982, pp. L1–L3.

¹⁵Shardanand, and Rao, A. D. P., "Absolute Rayleigh Scattering Cross Sections of Gases and Freons of Stratospheric Interest in the Visible and Ultraviolet Regions," NASA TN D-8442, March 1977, URL: <http://techreports.larc.nasa.gov/ntrs/hget.cgi?recon?1897/3=/raid5/index/star/70%25802138%201897%20N19770012747recon1> [cited 20 March 2000].

¹⁶Bates, D. R., "Rayleigh Scattering by Air," *Planetary Space Science*, Vol. 32, No. 6, 1984, pp. 785–797.

APPENDIX C

1. **B. McAndrew, P. Barker, and R.B. Miles**, "Development of a Supersonic Plasma Wind Tunnel," AIAA 2000-0533, 38th Aerospace Sciences Meeting and Exhibit, Jan. 10-13, 2000, Reno, NV.



AIAA 2000-0533

**DEVELOPMENT OF A SUPERSONIC
PLASMA WIND TUNNEL**

B.McAndrew, P.Barker, and R.B.Miles

Princeton University

**38th Aerospace Sciences
Meeting & Exhibit
10-13 January 2000 / Reno, NV**

DEVELOPMENT OF A SUPERSONIC PLASMA WIND TUNNEL

B. McAndrew*, P. Barker[†], and R. Miles[‡]

ABSTRACT

The study of controlled plasma discharges in supersonic air has become an area of increasing interest. These discharges may be used for flow control, drag reduction, combustion initiation and stabilization, as well as for power extraction and plasma shielding applications. In order to study the formation of such discharges and their impact on the flow, proper testing facilities are required. This paper details the work done in the design, construction, and testing of a supersonic plasma wind tunnel.

INTRODUCTION

Over the past decade, research into the interaction of plasma with a gas flow has yielded some results which have not yet been fully explained¹⁻⁵. For example, changes in shock wave strength and shock standoff distance caused by the presence of plasma have been observed experimentally, but cannot be fully explained with present theoretical models. A better understanding of these interactions, as well as the potential applications for the controlled modification of shock structure, motivates the present work.

WIND TUNNEL DESIGN

The basic configuration of the wind tunnel is controlled by the need to create a plasma in the region of supersonic flow. A schematic of the facility is shown in Figure 1 below.

A Plasma is created with a 50 kW, 1 ms pulse of microwave radiation at 2.45 GHz, which induces electric breakdown of the air in the region of supersonic flow. Microwaves are introduced into the plenum through an EM window mounted over a port on one wall. The direction of propagation is then turned 90° by an aluminum reflector, so the microwaves travel coaxially with the flow through the plenum chamber

and nozzle section. The aluminum reflector is made with a dense array of 1/4" holes in it to allow passage of air while simultaneously reflecting the microwaves. The breakdown location is controlled by two factors; a reduced static pressure in the high speed section, and an increased field intensity downstream of the throat.

Microwave discharges occur more easily at low pressure due to the reduced collision frequency. Thus, introducing microwaves through the plenum where the air is at high pressure avoids the risk of parasitic breakdown near the window housing and window surface.

As shown in Figure 1, the waveguide walls are tapered to create an enhancement of the electric field as the microwaves propagate downstream. The nozzle contours within the taper are made of dielectric material so as to transmit the microwave radiation. The taper continues down to and slightly beyond the cutoff dimensions for radiation at 2.45 GHz. This generates a reflection, reversing the propagation direction as the microwaves reach the cutoff point. This taper is used as one end of a microwave resonator. The other end of the resonator is formed by a triple stub tuner on the generator side of the entrance window. This arrangement allows for the build up of a standing wave in the wind tunnel. In order to provide a further field enhancement at the intended breakdown location, and to provide for spatial localization of the plasma, two 1 cm long metal pins are mounted opposite each other on the inside walls of the wind tunnel. The magnetron is protected from spurious reflections by a circulator and dummy load.

The flow of air proceeds from the plenum, through the nozzle, and into the 2"x2" test section. The air is then discharged into a vacuum tank. The nozzles are contoured to achieve Mach 3 flow in the test section. Flow conditions in the test section are 20 Torr static pressure, 110 K static temperature, and a Mach number of 3.

MICROWAVE FIELD DISTRIBUTION

The microwave field distribution was measured along the centerline of the wind tunnel from the reflector plate to the wind tunnel exit plane. For these measurements, the microwave field was generated

* Graduate Student

[†] Research Staff Member, Member AIAA

[‡] Professor, Associate Fellow AIAA

Copyright © 2000 Princeton University. Published by the American Institute of Aeronautics and Astronautics, Inc. with permission.

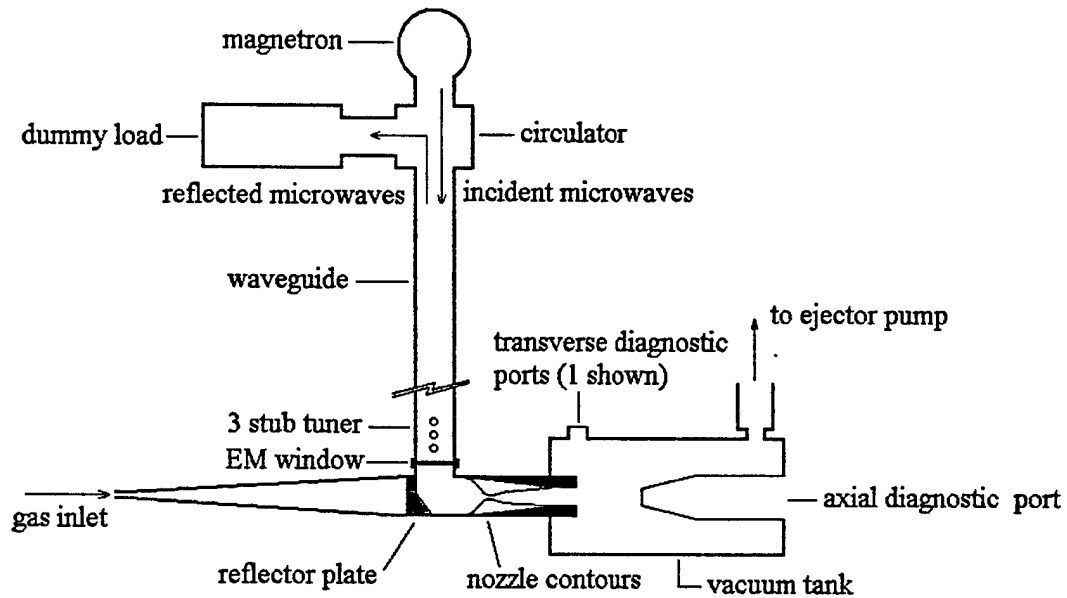


FIGURE 1: FACILITY SCHEMATIC

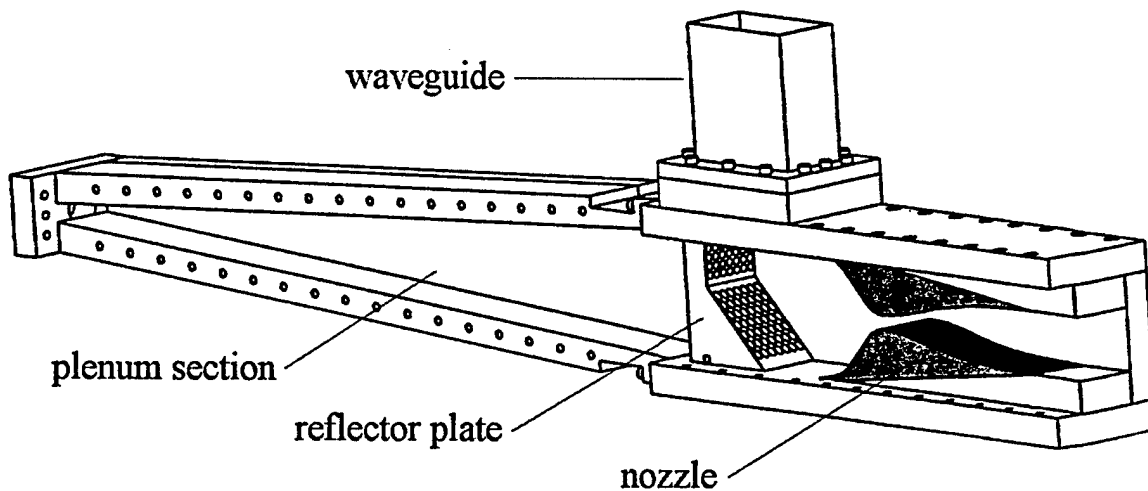


FIGURE 2: PLENUM AND NOZZLE CUTAWAY DRAWING

using a 100 mw source operating in a continuous mode at 2.45 GHz. This source was coupled into the wind tunnel with the same triple stub tuner and window arrangement used for the 50 kW, 1 ms pulse breakdown experiments. The measurements were made with a probe consisting of a 1 cm antenna protruding from a length of semi-rigid coaxial cable. This probe was introduced into the wind tunnel from the downstream end and traversed through the wind tunnel in increments. The 2.45 GHz signal obtained with the probe was attenuated and rectified with a crystal diode before being recorded on a digital oscilloscope. An average of several such traverse measurements is shown in Figure 3.

NUMERICAL SIMULATIONS

To complement the measurements described above, as well as to permit parametric studies of the effect of changes in the electrical properties of the wind tunnel, a commercial finite element code was used to simulate the electric field standing wave pattern.

The code used was the High Frequency Structure Simulator package from Hewlett Packard, which was run on a UNIX based workstation. The results of several case studies, including a comparison with the measurements described above, are presented in Figures 4 through 8.

In the above simulations, incident wave phase is chosen to show the standing wave pattern at its maximum intensity. For the cases shown in Figures 4 and 5 the region of highest field intensity remains localized at the same point throughout each cycle of the incident wave propagation. For the cases shown in Figures 6 and 7, due to the lossy dielectric, deviations from a perfect standing wave pattern occur. In particular, the region of highest field intensity changes dramatically as the incident wave goes through one cycle. The field can be seen to be strongly dependent on dielectric material properties, which has important implications for the generation of plasma inside the wind tunnel.

BREAKDOWN MEASUREMENTS

Using the G-10 nozzle breakdown can occur in either of two locations, depending upon conditions. Under static conditions below about 30 Torr, breakdown occurs upstream of the throat, slightly below the centerline of the wind tunnel. Above 30 Torr under static conditions breakdown occurs downstream of the throat at the intended location. These two positions correspond with the two peaks in field

intensity in the simulation. Note that under flow conditions, with higher pressure upstream of the throat than downstream, the breakdown will also occur in the downstream location.

Breakdown in the wind tunnel was recorded with photodiodes and high speed photographic equipment. The pressure was chosen for the static case so as to match gas density with the flow conditions. Measurements of the plasma luminosity were made both with flow and under static conditions. In all cases the tests were performed in air with a microwave pulse duration of 1 ms. The results indicate the initiation of the plasma within 10 μ s after the start of the microwave pulse without flow, and within 20 μ s after the start of the pulse with flow. A brighter plasma was observed with flow than without flow, as shown in Figures 9 and 10.

The photographs shown in Figure 11 were made with a gated, intensified CCD camera. The view is through the axial diagnostic port shown in Figure 1, looking upstream into the wind tunnel. Images were taken of the plasma both with the wind tunnel running and under static conditions at 60 Torr and room temperature. The pressure was chosen for static conditions to match the density with the Mach 3 flow for comparison. In all cases the camera gate was maintained at 3 μ s. The images show the plasma generated while the wind tunnel was running to be brighter and more contracted than the plasma generated under static conditions. The location of the plasma within the tunnel appears to be stable for the duration of the 1 ms pulse. Note that each image represents a separate instance of plasma generation.

CONCLUSIONS

A Mach 3 wind tunnel with integrated microwave plasma generating capability has been designed and tested. The importance of the electrical properties of the wind tunnel for microwave propagation and breakdown has been shown. Self induced plasma generation has been achieved with a microwave pulse length of 1 ms. A stable, well localized plasma has been maintained in the wind tunnel with flow. Measurements of the plasma indicate a brighter and more filamentary discharge with flow than without flow.

ACKNOWLEDGEMENTS

Funding for this work has been provided by an AFOSR grant.

REFERENCES

1. W. Beaulieu, V. Bytyrin, A. Klimov, S. Leonov, A. Pashina, and B. Timofeev, "Plasma Aerodynamic Wind Tunnel Tests with 1/6 Scale Model of Nose Part of F-15," 3rd Weakly Ionized Gases Workshop, Norfolk, VA, November 1-5, 1999.
2. A. Klimov, S. Leonov, A. Pashina, V. Skvortsov, T. Cain, and B. Timofeev, "Influence of a Corona Discharge on the Supersonic Drag of an Axisymmetric Body," 3rd Weakly Ionized Gases Workshop, Norfolk, VA, November 1-5, 1999.
3. S. Merriman, I. Adamovich, and J.W. Rich, "Studies of Oblique Shock Waves in Weakly Ionized Nonequilibrium Plasmas," 3rd Weakly Ionized Gases Workshop, Norfolk, VA, November 1-5, 1999.
4. R. Yano, V. Contini, E. Ploenjes, P. Palm, S. Merriman, I. Adamovich, W. Lempert, V. Subramaniam, and J.W. Rich, "Flow Visualization in a Supersonic Nonequilibrium Plasma Wind Tunnel," 30th Plasmadynamics and Lasers Conference, Norfolk, VA, June, 1999.
5. V. Soloviev, V. Krivstov, A. Konchakov, N.D. Malmuth, "Mechanisms of Shock Wave Dispersion and Attenuation in Weakly Ionized Cold Discharge Plasmas," IVTAN Perspectives of MHD and Plasma Technologies in Aerospace Applications Conference, Moscow, Russia, March 24-25, 1999.
6. S. Macheret, L. Martinelli, and R. Miles, "Shock Wave Propagation in Non-Uniform Gases and Plasmas," 37th AIAA Aerospace Sciences Meeting and Exhibit, Reno, NV, January 11-14, 1999.
7. A. Yalin, Y. Ionikh, R. Miles, "Temperature Measurements in Glow Discharges with Ultraviolet Filtered Rayleigh Scattering," 30th AIAA Plasmadynamics and Lasers Conference, Norfolk, VA, June 28-July 1, 1999.
8. P. Harsha and E. Gurjanov, "AJAX: New Directions in Hypersonic Technology," 8th Aerospace Planes and Hypersonic Technologies Meeting, Norfolk, VA, April, 1996.
9. A.D. MacDonald, *Microwave Breakdown in Gases*, Wiley, 1966.
10. R. Collin, *Foundations for Microwave Engineering*, McGraw-Hill, 1966.
11. G. Matthaei, L. Young, E. Jones, *Microwave Filters, Impedance Matching Networks, and Coupling Structures*, McGraw-Hill, 1964.

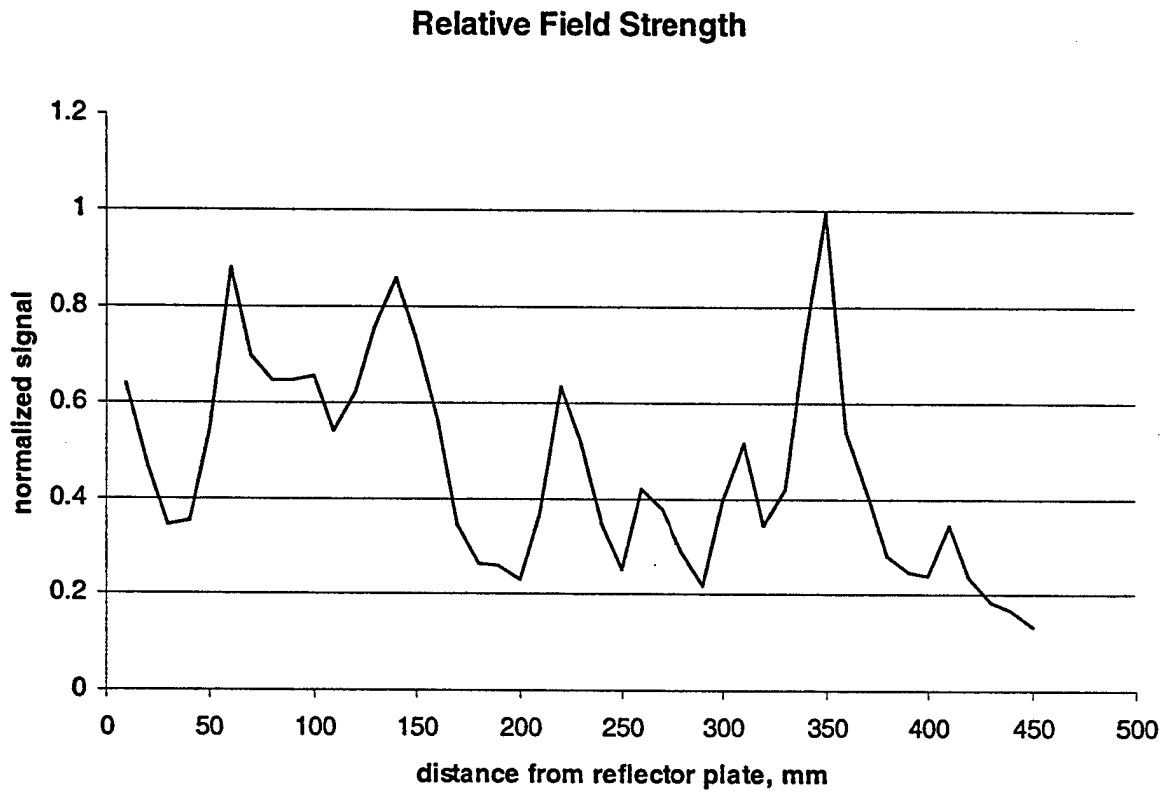


FIGURE 3: MEASURED ELECTRIC FIELD ALONG WIND TUNNEL CENTERLINE

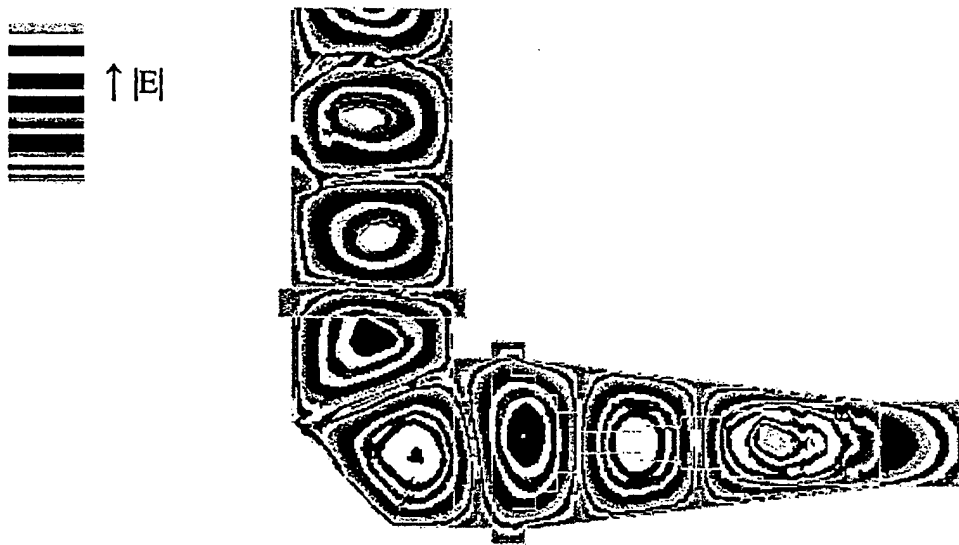


FIGURE 4: ELECTRIC FIELD MAGNITUDE WITH AIR FILLED WAVEGUIDE (NO DIELECTRIC)

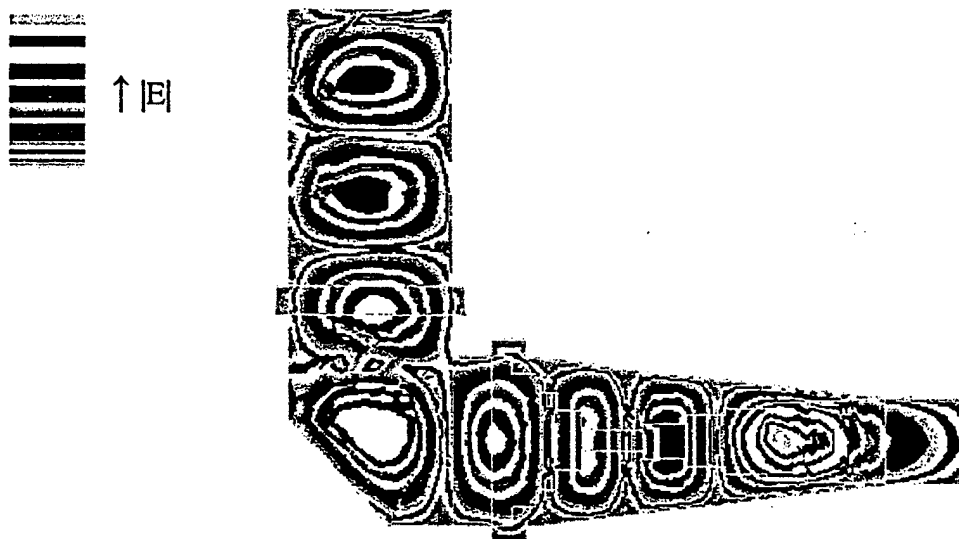


FIGURE 5: ELECTRIC FIELD MAGNITUDE WITH TEFLON NOZZLE
Relative permittivity = 2.08 Dielectric loss tangent = 0.00037

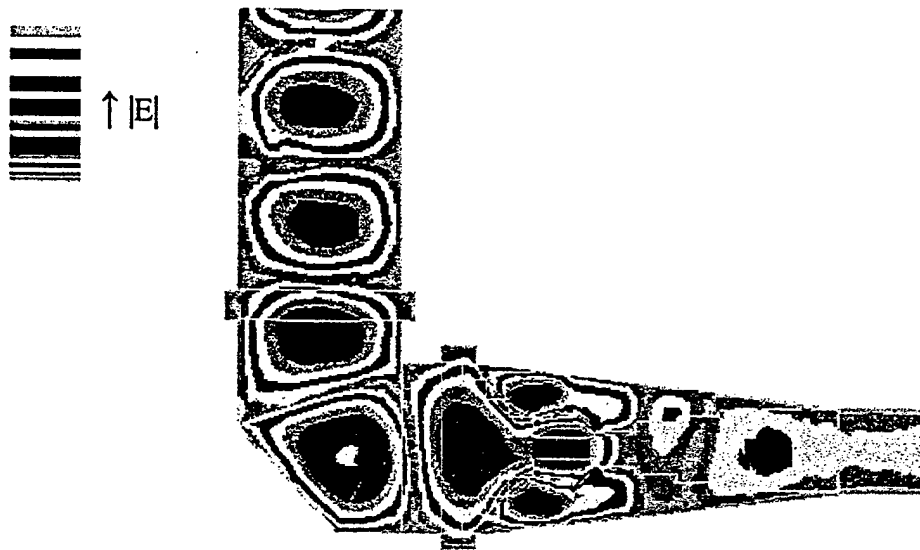


FIGURE 6: ELECTRIC FIELD MAGNITUDE WITH G-10 NOZZLES
 Relative permittivity = 5.0 Dielectric loss tangent = 0.019
 Incident wave phase = 157°

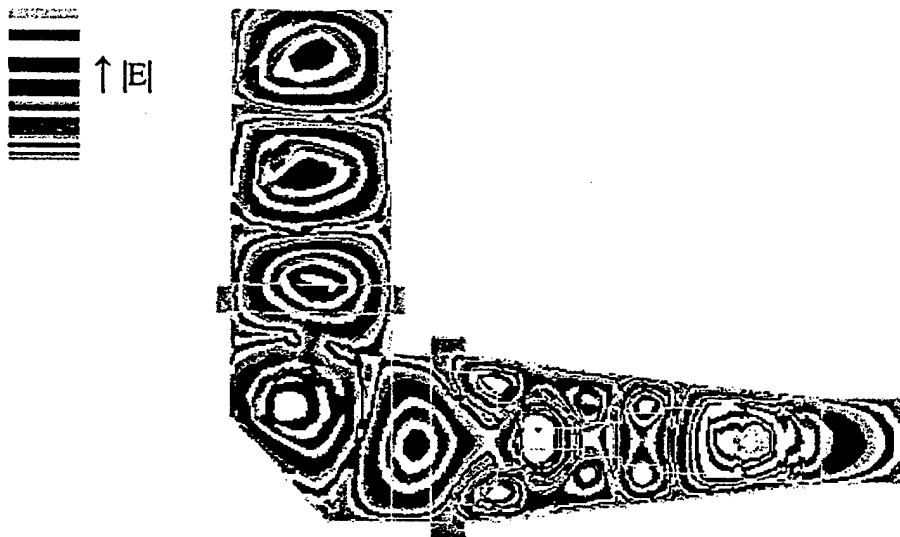


FIGURE 7: ELECTRIC FIELD MAGNITUDE WITH G-10 NOZZLES
 Relative permittivity = 5.0 Dielectric loss tangent = 0.019
 Incident wave phase = 70°

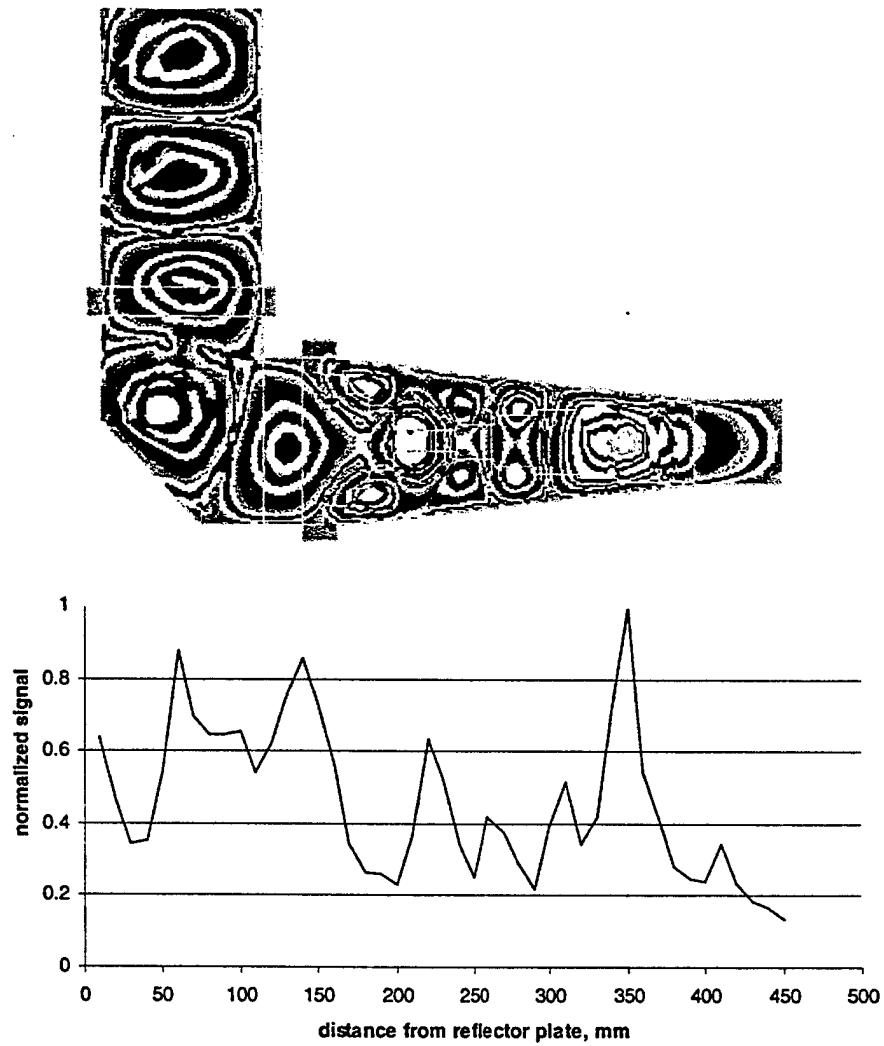


FIGURE 8: COMPARISON BETWEEN SIMULATION AND MEASUREMENT USING G-10 NOZZLES

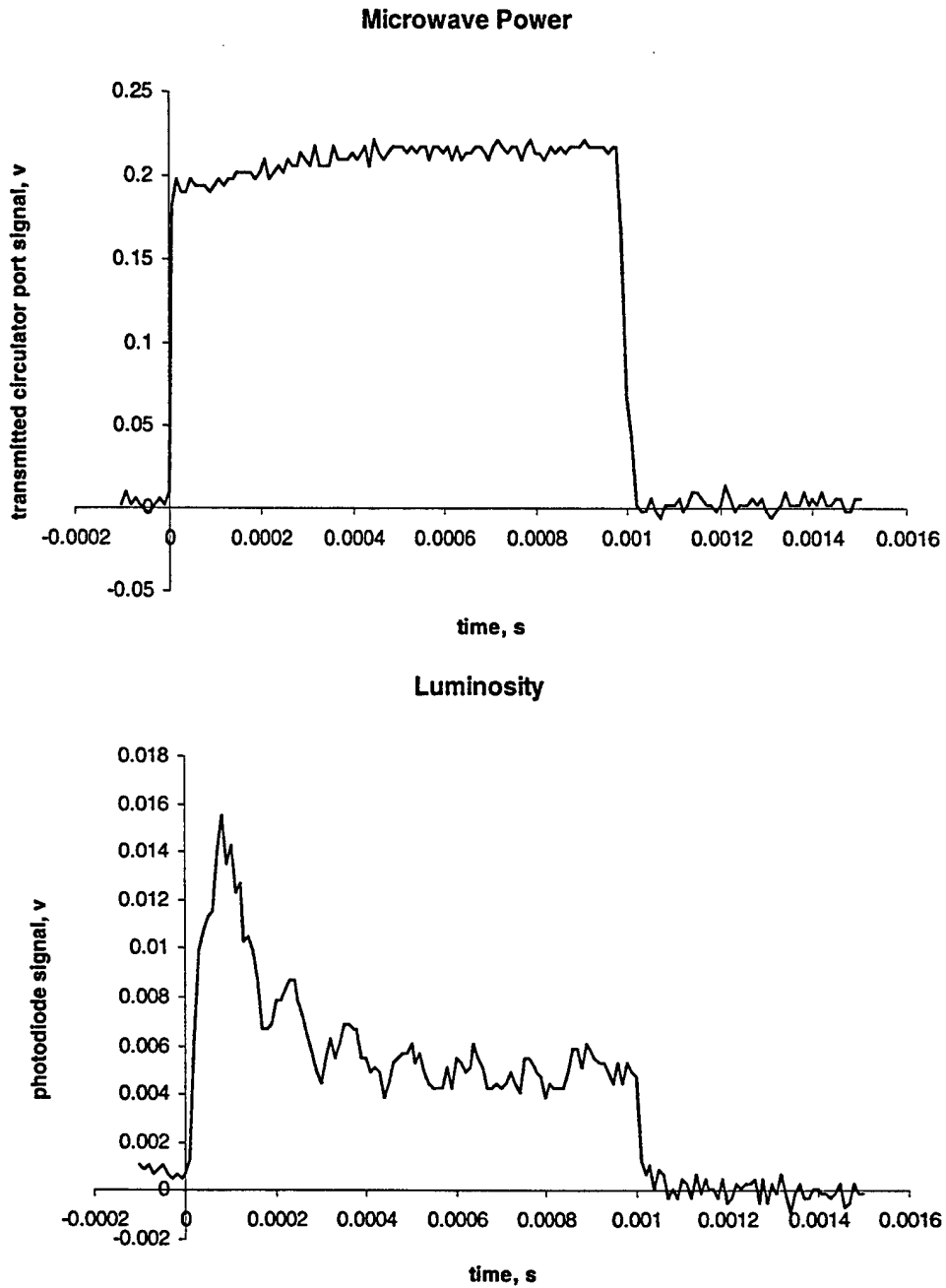


FIGURE 9: PLASMA LUMINOSITY WITHOUT FLOW (60 TORR, 300 K)

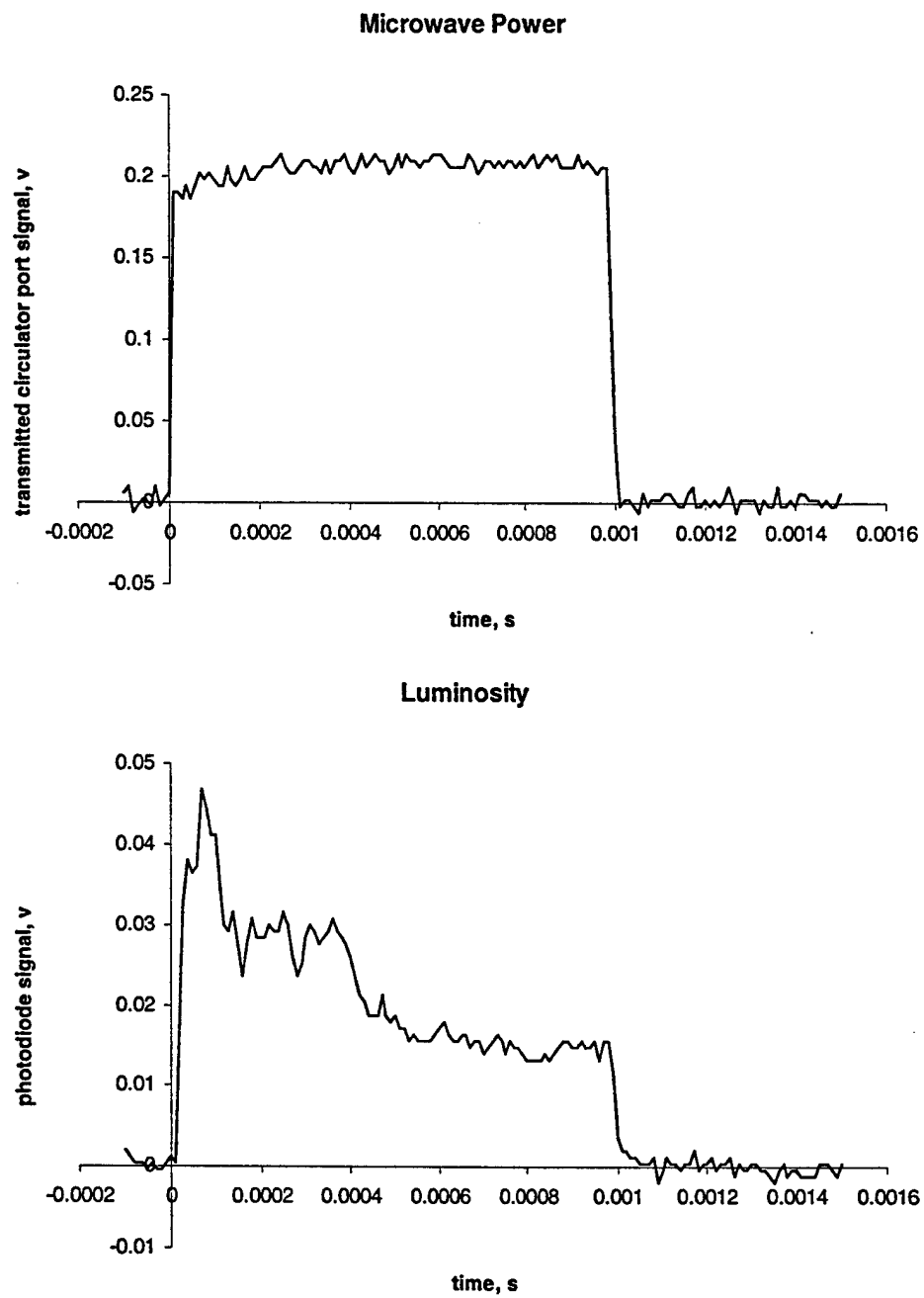


FIGURE 10: PLASMA LUMINOSITY WITH FLOW

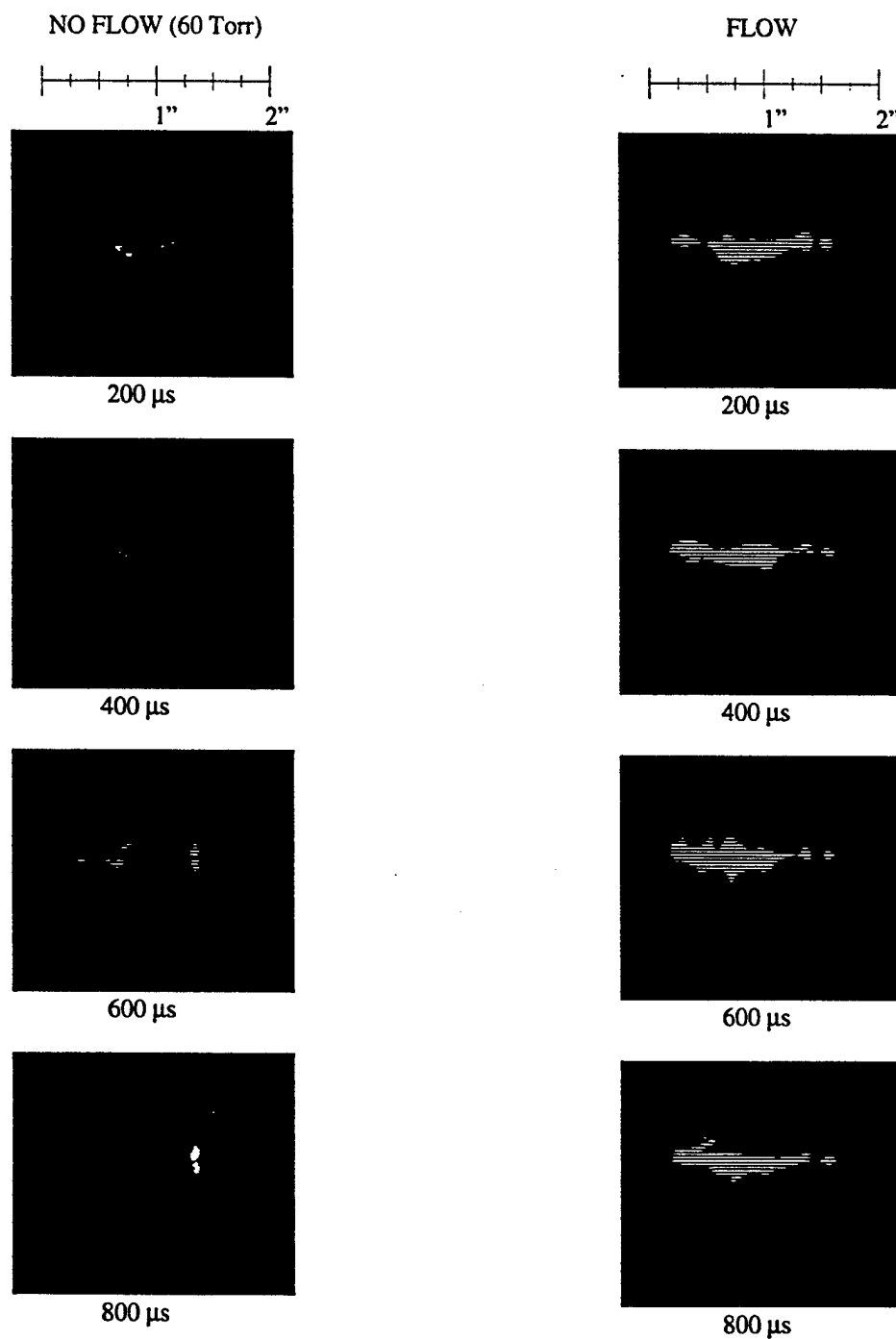


FIGURE 11: COMPARISON OF PLASMA WITH AND WITHOUT FLOW

APPENDIX D

1. **R.B. Miles**, Z. Tang, S.H. Zaidi, **A. Yalin**, and N. Finkelstein, "High Signal-to-Noise Detection of Rotational Raman Scattering Through Refluorescent and Dispersive Atomic Filters," J. Raman Spectroscopy 31, 2000, pp. 843-849.
2. **A.P. Yalin**, P. F. Barker, and **R.B. Miles**, "Characterization of Laser Seeding by Use of Group-Velocity Dispersion in an Atomic Vapor Filter," Optics Letters 25, April 1, 2000, pp. 502-507.
3. **P. Wu**, **W.R. Lempert**, and **R.B. Miles**, "Megahertz Pulse-Burst Laser and Visualization of Shock-Wave/Boundary Layer Interaction," AIAA Journal 38, April 2000, pp. 672-679.

High signal-to-noise detection of rotational Raman scattering through refluorescent and dispersive atomic filters

Richard B. Miles,^{1*} Zhen Tang,¹ Sohail H. Zaidi,¹ Azer Yalin¹ and Noah Finkelstein²

¹ Department of Mechanical and Aerospace Engineering, Princeton University, Olden Street, Princeton, New Jersey 08544, USA

² University of California at San Diego, 9500 Gilman Drive, La Jolla, California 92093-0092, USA

We introduce new methods for capturing rotational Raman scattering that simultaneously suppress background scattering and have exceedingly high spectral dispersion at low wavenumbers. These methods are based on resonant absorption and refractive index dispersion of atomic vapor, and take advantage of the availability of tunable lasers. Three different configurations are presented. The first is an atomic notch transmission filter which is based on refluorescence from an optically thick atomic vapor cell. This configuration is demonstrated in air using mercury vapor at 254 nm. The second configuration is an atomic resonance prism cell which is demonstrated in CO₂ using mercury vapor, again at 254 nm. The third configuration is a density gradient atomic vapor cell which uses rubidium vapor at 780 nm. In the last two configurations, the atomic cell simultaneously blocks the elastic scattering while spatially dispersing the rotational Raman lines. In each case, a tunable Ti:sapphire laser was employed as an illuminating source. Copyright © 2000 John Wiley & Sons, Ltd.

INTRODUCTION

Raman scattering is an important tool for gas-phase diagnostics, since it allows one to measure species concentrations and also rotational and vibrational temperatures through the association of line strengths with population fractions. However, many applications of Raman scattering have been limited by both the low scattering cross-section and the presence of strong background scattering. These limitations have kept Raman scattering from becoming a practical tool for combustion or flow field diagnostics. Only through heroic experiments have multi-dimensional data been recorded.^{1–4}

In virtually all cases, the Raman spectrum that has been recorded is the vibrational Raman spectrum, corresponding to transitions between the ground vibrational state and the first excited vibrational state. It is important to recognize that, for most molecules, the rotational Raman cross-section is one to two orders of magnitude larger than the vibrational cross-section. The rotational Raman spectrum is not typically used for diagnostics because the rotational lines of the various species are interspersed with each other. Furthermore, the rotational Raman spectrum is very close to the Rayleigh line and other background scattering that often obscures it.

The availability of narrow linewidth lasers that can be tuned in the vicinity of atomic resonances offers a new approach to Raman spectroscopy. In this case, atomic filters can be used to provide very strong suppression of

background light while simultaneously providing spectral dispersion with high throughput. Three approaches are outlined in this paper. The first involves using refluorescence from an optically thick atomic mercury vapor cell.⁵ The second and third approaches rely on the dispersion of the atomic vapor near resonance. The second approach achieves this with an atomic mercury vapor prism,⁶ and the third with an atomic rubidium vapor density gradient cell (Z. Tang, S. H. Zaidi and R. B. Miles, Paper AIAA-2000-0644 presented at the 38th Aerospace Sciences Meeting and Exhibition January 10–13, 2000, Reno, NV). In the refluorescence case, the narrow linewidth of the atomic resonance, together with time gating, provides strong suppression of background light, and two-dimensional images can be taken. In the prism and density gradient cell cases, the resonant absorption of the atomic vapor provides the background suppression, and the refractive index variation of the atomic vapor disperses the Raman spectrum. In these cases, one-dimensional images are achievable.

MERCURY VAPOR REFLUORESCENCE FILTER

Recent work has established the utility of an optically thick, atomic blocking, notch filter for the acquisition of Rayleigh scattering data in air.⁷ The filter serves two major functions. By tuning the laser to the center of the filter resonance, the filter serves to suppress strongly elastic background scattering that often arises from particles and from the windows and walls of the experimental chamber. The second function is to permit the spectrum of the Rayleigh scattering to be resolved by tuning the laser frequency relative to the atomic resonance and recording the scattering transmitted through the cell as a function of that

* Correspondence to: R. B. Miles, Department of Mechanical and Aerospace Engineering, Princeton University, Olden Street, Princeton, New Jersey 08544, USA; e-mail: miles@princeton.edu
Contract/grant sponsor: Air Force Office of Scientific Research.
Contract/grant sponsor: M. L. Energia, Inc.

laser frequency. By deconvolving the spectral shape of the atomic transmission from the recorded transmission signal, the spectrum of the Rayleigh scattering is retrieved.⁸

Extending this approach to Raman scattering requires that the strong Rayleigh scattering be suppressed at all times, since that can be more than three orders of magnitude greater than the Raman signal. Since the Rayleigh signal is offset in frequency from the Raman signal, a notch passband rather than a notch blocking filter is required. If such a filter can be designed, then the laser is tuned so the frequency of the Raman light overlaps the passband, and all other scattering is blocked. It is also important to maintain an imaging capability through such a filter and to have a large acceptance angle for good field-of-view and efficient light collection. Background suppression needs to be great enough to allow the Raman scattering to be uncontaminated by other light scattering, whether that be Rayleigh, particle, fluorescence or background from windows and walls.

The two approaches that have been previously proposed for this type of notch passband filter are a double resonance atomic fluorescence cell and atomic Faraday and Voigt filters. The double resonance cell is a device that uses either a local laser,^{9,10} or collisions with a rare gas¹¹ to transfer atoms from a state which has been driven by the incident light to a second state which fluoresces at a different wavelength. Fluorescence is then collected by a sensitive detector. Since the fluorescence is at a very different frequency than either the local laser or the scattered light, standard Schott glass or interference filters can be used to reject the incident and local laser light and pass the fluorescence. Generally, this device has no imaging capability and there may be significant light loss in the system through the 4π refluorescence solid angle and the transfer efficiency of the laser or rare gas collision process.

The Faraday and Voigt filters rely on the polarization rotation that occurs in an atomic vapor near resonance in the presence of a magnetic field.¹² This leads to optical rotation of light propagating through the cell. If polarizers are placed at the entrance and at the exit of the cell, then off-resonance light will not pass, but light which falls close to the atomic resonance can pass through. The Faraday and Voigt approaches have good throughput, but the background rejection is very sensitive to the optical quality of the polarizers and the light propagation angle. Rejection of on axis light is rarely better than two orders of magnitude. The small acceptance angle precludes imaging applications, and the rejection is probably too small to permit Raman spectroscopy.

These limitations are overcome by using an optically thick atomic vapor refluorescence cell as a narrow band, notch transmission filter.⁵ If the atomic transition is to the ground state and there are no other allowed transitions down from the upper state, then light which is absorbed by that transition is re-radiated at the same frequency. This leads to the well-known phenomenon of optical trapping. In an optically thick cell, the on-resonance light entering the cell is absorbed within the first few tens of microns. When this light is re-radiated, the light emitted back toward the entrance window exits the cell, whereas the light which is re-radiated toward the interior of the cell is immediately reabsorbed. When that light is again re-radiated, the portion which is re-radiated back toward the entrance window escapes, and the portion headed farther into the cell is again absorbed. Through

this iterative process, in the absence of quenching, all the light is finally re-radiated back out of the entrance window, with an effective radiation lifetime several times longer than the isolated atom radiation lifetime. If the cell has sufficient optical thickness, this whole process remains very well localized, so the re-radiated light exits the cell at approximately the same location it entered. Light which is not at the atomic resonance frequency passes through the cell. Hence this type of cell can serve as a notch transmission filter by detecting only the re-radiated light. This re-radiated light can be collected through a narrow linewidth interference filter, if necessary, for further background rejection. Even greater rejection of out-of-band light can be achieved by using a pulsed laser to generate the Raman scattering, time-gating the detector to be off during the laser pulse, and then immediately turned on so that only the refluorescence is seen. Any light reflected off the surface of the cell is then rejected since that light will only be present during the laser pulse. Since the absorption length is so small and the refluorescence remains localized, this cell can be used for imaging.¹³

Various factors must be weighed in the selection of an appropriate atomic vapor. The atomic vapor must have a strong, optically thick transition from the ground state and needs to overlap some available narrow linewidth, tunable laser frequency. In order to have good discrimination, the spectral profile of the optically thick filter should be as close to a notch as possible. The ideal notch filter would have no 'transmission' out of band, so the absorption of the atomic vapor in the optically thick regime should quickly go to zero. If the atomic vapor is naturally or collision broadened, then the lineshape of the absorption constant is Lorentzian and falls off from line center as $1/(1 + (\delta\omega)^2)$, where $\delta\omega$ is the frequency offset from line center normalized by the linewidth. If, on the other hand, the atomic vapor line is thermally broadened, then the lineshape is Gaussian and the absorption constant falls off as $e^{-(\delta\omega)^2}$. The exponential fall off leads to orders of magnitude less out of band absorption, particularly in the optically thick regime, so it is important to operate the atomic filter at low enough pressure that the lineshape is dominated by thermal broadening. The sharpness of the thermally broadened filter is determined by the ratio of the temperature to the mass, so the sharpest filters use an atomic vapor with a high atomic mass and high vapor pressure (low boiling point). The best candidates for atomic refluorescence filters are mercury, rubidium and cesium vapor. For Raman scattering, the scattering cross-section increases as the fourth power of the scattering frequency. The mercury transition is in the ultraviolet region where this enhancement is substantial, whereas cesium and rubidium are in the infrared region at frequencies where strong narrow linewidth solid-state and diode lasers are available, but where Raman scattering is weak. For the refluorescence experiments reported here, mercury vapor was used and illumination was provided by a tunable, injection locked, frequency-tripled Ti:sapphire laser.

Figure 1 shows a diagram of the setup. The frequency-tripled Ti:sapphire laser was focused into air. The Raman scattering was collected at 90° and imaged on to an optically thick mercury vapor cell. The light that was refluoresced was collected and imaged with a camera that views the front surface of that cell.

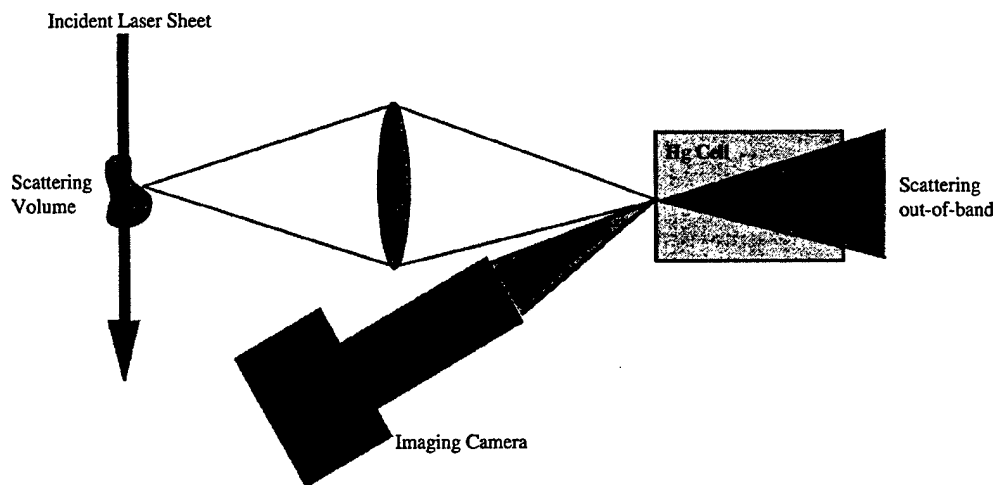


Figure 1. Narrow passband imaging filter layout. Scattering from an interrogation volume is imaged on to the inside surface of a mercury vapor cell. Light coincident with the ground-state transition at 253.7 nm is fluoresced and imaged by a camera.

Figure 2 shows the absorption and refluorescence spectra of the mercury vapor cell. The mercury side-arm was maintained at a temperature of approximately 25 °C, and the cell was heated to avoid mercury condensation on the windows. This temperature corresponds to a vapor pressure of 0.002 Torr (1 Torr = 133.3 Pa). The spectral features of the absorption bands are due to the various isotopic species and hyperfine states. Note that the absorption and refluorescence spectra are nearly the inverse of one another, demonstrating that the refluorescence cell can be operated as an effective bandpass filter.

Figure 3 shows the refluorescence signal collected as a function of time for a factor of 20 range of mercury vapor pressures. Note that there is very little change and that the refluorescence time is 450 ns, which is slightly less than four times the 120 ns natural lifetime of mercury vapor. For Fig. 2, the detector was gated 60 ns after the laser pulse and integrated the signal for 4 μ s. The spatial resolution of the cell is determined by the penetration depth of the resonant light, and improves at higher vapor pressures. At 0.05 Torr (70 °C side-arm temperature), the penetration depth at the mercury-202 line frequency is 35 μ m. Under these conditions a resolution of approximately 100 μ m

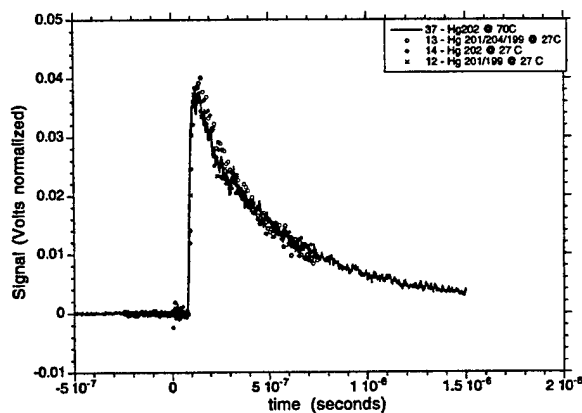


Figure 3. Narrow passband filter: temporal response for varying number density. Number density varies by a factor of 20 for Hg-202 and a factor of two between isotopes.

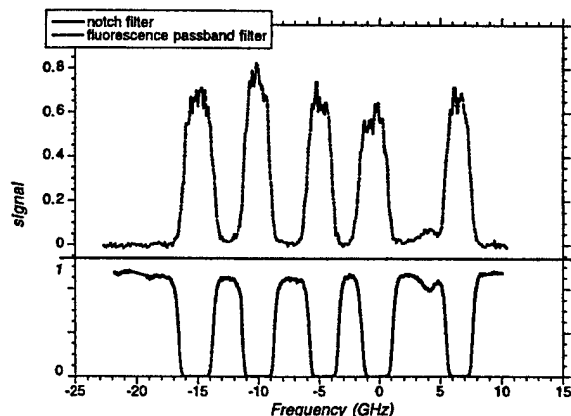


Figure 2. Narrow passband filter and notch absorption filter: spectral profiles. Simultaneous spectral scans of the Hg cell operating in two modes. Above, narrow passband; below, notch absorption. The bands arise from naturally occurring isotopes.

is achievable for short imaging delay times. At longer delays the resolution degrades due to photon and particle diffusion inside the cell.

As the laser is tuned, the rotational Raman lines from the air are sequentially scanned through the atomic mercury vapor resonance. The refluorescence from the entrance face of the cell is collected by a lens and directed on to a photomultiplier tube through a narrow line interference filter centered at 254 nm, the mercury vapor resonance frequency. Only the light that is close to the mercury resonance frequency passes through the filter. This rejects laser-induced fluorescence and other light that is far from the mercury resonance line. The signal from the photomultiplier tube is time gated to exclude the time interval when the Ti:sapphire laser is on, so Rayleigh and background scattering from the laser that might be reflected off the surface of the mercury cell is further rejected. With this configuration, a rotational Raman spectrum of the air can be taken with virtually no background noise.

Figure 4 shows a portion of the rotational Raman spectrum of both oxygen and nitrogen in the air taken with a mercury cell vapor pressure of 0.1 Torr (100 °C side-arm temperature). The laser pulse length is approximately 10 ns, and the linewidth is close to the transform limit.

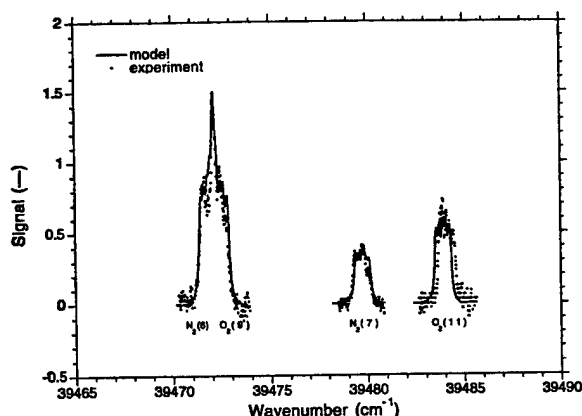


Figure 4. Rotational Raman scattering from room air. Experiment and model predictions. Model includes rotational Raman broadened lineshape convolved with Monte Carlo model for the passband filter. Three different spectral scans cover four individual rotational Raman lines.

The laser is frequency tripled to yield 10 mJ pulses tunable in the vicinity of 253.7 nm. The lines are identified in the figure, and the structure associated with each line represents the isotopic and hyperfine structure of the filter itself. It is interesting to note that the oxygen lines are stronger than the nitrogen lines, even though the mole fraction of oxygen is one quarter that of nitrogen. This occurs because the oxygen Raman polarizability is resonantly enhanced by the UV Schumann Runge band. The spectra in Fig. 4 were taken with three different laser scans and represent 30 shot averages. The refluorescence efficiency is estimated to be 80%, with the loss primarily due to quenching and optical trapping. In addition, some loss (6–8% per surface) occurs at the windows. The major inefficiency in this experiment occurs from the losses associated with the recollection of the fluorescent light re-radiated as Lambertian surface emission from the front of the cell. The collection efficiency, η , is

$$\eta = \frac{1}{4(f^*)^2 \left[1 + \frac{1}{m} \right]^2 + 1}$$

where f^* is the f number of the collection lens ($f^* = \text{focal length/lens diameter}$) and m is the magnification.

An $f/1$ lens only collects 20% of that light. In the experimental setup used for the data shown above, an $f/4.5$ lens was used with a magnification of 1.5, so only

0.44% of the refluorescent light was collected. For non-imaging applications, better efficiency can be achieved, for example, by using a compound parabolic concentrator simultaneously to focus on the cell and collect the refluorescence.¹⁴

ATOMIC MERCURY VAPOR PRISM

The second and third approaches to Raman imaging with an atomic filter take advantage of the resonant dispersion of the atomic vapor in the vicinity of the atomic transition. In these cases, the entire spectrum can be simultaneously observed, and the cell throughput is high. If desired, the scattering along a line can be imaged in the direction orthogonal to the spectral dispersion of the filter. The dispersion can be achieved either using a prism configuration or a density gradient. A mercury prism cell is discussed here, and a gradient rubidium dispersion cell is presented in the next section.

A diagram of the mercury vapor cell is shown in Fig. 5. The cell is configured like a prism, with the windows at Brewster's angle for the 253.7 nm resonance light. When the Raman light passes through the cell, the strong variation in the refractive index causes the light to be bent at the interface in accord with Snell's law. In this configuration, the dispersion of the mercury vapor can be measured by recording the displacement of the laser as a function of laser frequency. The mercury prism cell was run with a side-arm temperature of 170°C. A 300 μm slit was back-illuminated by diffuse laser scattering, and the light passing through the slit was collimated through the prism cell with an $f/10$ lens and then re-imaged at 0.895 m on to the microchannel plate of an intensified camera. The laser was tuned, and the wavenumber was monitored by a Burleigh wavemeter ($\pm 0.3 \text{ cm}^{-1}$). The measured displacement as a function of laser wavenumber is shown in Fig. 6 and compared with a Voigt model for the same geometry. The fit is best at a temperature of 168°C, although the fit at 170°C is within the data error bars.

The rotational Raman spectrum is recorded by tuning the laser to the center of the mercury vapor absorption manifold. For most molecules of interest, the rotational Raman lines are shifted by more than 10 GHz and fall out of the absorption band of the mercury. They are, however, very close to that band and fall within the highly refractive portion of the refractive index curve. The lines which fall at lower frequency than the mercury absorption lines encounter an index which is > 1 and the light is

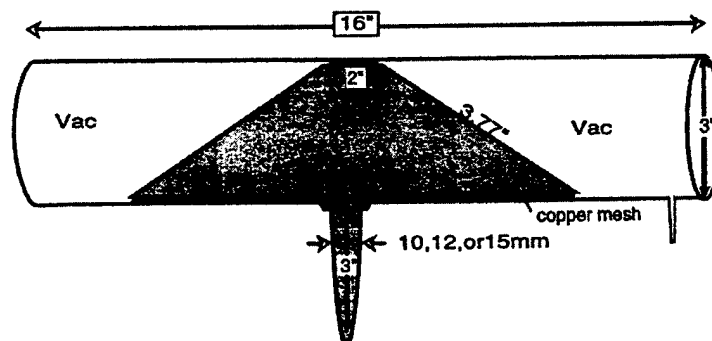


Figure 5. Schematic diagram of the Hg vapor prism. Concentric quartz cylinders allow for heating of the inner Brewster cut windows, while keeping the outer flat windows cool.

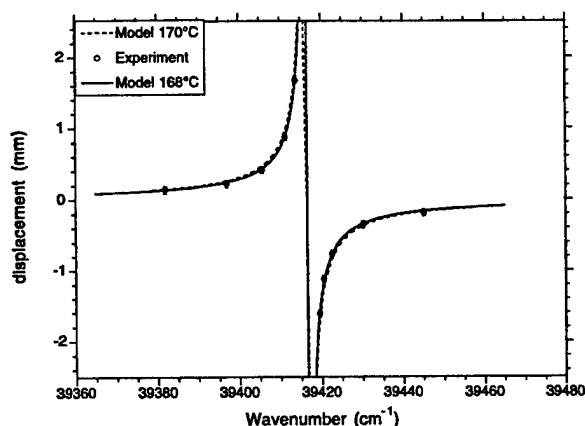


Figure 6. Vapor prism: measured and predicted deviation as a function of incident wavenumber.

refracted down. Those lines which fall above the mercury absorption encounter a refractive index <1 , and they are refracted up. The magnitude of the refraction increases as the frequency of the scattering approaches the mercury resonance. Those lines which are shifted from the laser frequency by the least amount are associated with transitions between the lowest lying rotational levels, and they are the most dispersed. Lines associated with higher lying rotational states are less dispersed, until light scattered far from the laser frequency and, thus, far from the mercury vapor frequency is essentially undeflected. Usually this includes the vibrational Raman lines, which fall one to three orders of magnitude further away from the driving laser frequency. In the vicinity of the mercury resonance, where the lower rotational lines fall, the dispersion of this Raman spectrometer is much higher than that of grating spectrometers. This suggests that this filter will more easily be able to resolve lines from individual molecular species, which are most easily distinguished at low rotational levels. Shifts associated with heavier molecules are smaller, so more complex molecules such as hydrocarbons will have more dispersed spectra. Tuning the laser with respect to the resonance can also increase the dispersion of particular spectral regions.

In the proof-of-concept experiment, CO_2 was used because it has a rotational B coefficient which is five times smaller than nitrogen ($B = 0.39 \text{ cm}^{-1}$ compared with 2 cm^{-1} for N_2), so the rotational lines are much closer to the driving laser frequency. The rotational Raman scattering cross-section of CO_2 is also about 6.5 times larger than N_2 . A comparison of the model predictions for both CO_2 and N_2 is shown in Fig. 7. For these measurements, the vapor pressure of the mercury is increased until absorption of the lowest rotational states is observed, so the cell dispersion is as large as possible. That corresponds to a vapor pressure of 12 Torr. Note that the $J = 0$ and $J = 2$ lines of CO_2 are strongly deflected, but also have significant absorption. On-line center attenuation of the cell was predicted to exceed 10^4 per cm. The experiment was conducted with the laser tuned slightly off the center of the line (7.7 cm^{-1}) so that attenuated Rayleigh scattering could be simultaneously collected. Since the Rayleigh scattering was closest to the mercury vapor line center, it was the most deflected. Figure 8 shows the collected spectrum from pure CO_2 . The image shows the dispersion in the vertical direction and is resolved along the $100 \mu\text{m}$

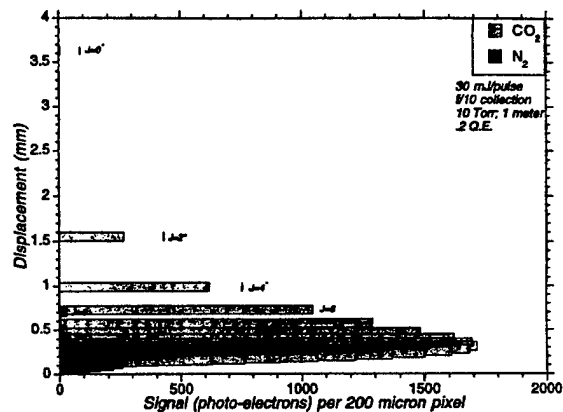


Figure 7. Model predictions for signal level and deviation of CO_2 and N_2 rotational Raman Lines. The asterisks indicate absorption of some fraction of incident radiation.

diameter laser line in the horizontal direction. The laser was operated at 30 mJ per pulse and the data in the figure represent a 50 shot average. The scattering was collected with an $f/5.8$ lens, collimated through the mercury cell, and imaged with a 0.895 m imaging lens on to a Princeton Instruments Pentamax CCD camera.

DENSITY GRADIENT RUBIDIUM CELL

The third approach again uses refractive index dispersion in the vicinity of an atomic resonance for Raman spectroscopy, but in this case the deflection arises from a density gradient across the cell rather than from refraction at the windows.⁷ The density gradient bends the light, just as light is bent in the thermally induced density gradient associated with a mirage. Therefore, by appropriate selection of filter length, the density gradient cell offers much stronger dispersion than its prism counterpart. It is important to note that for the rubidium cell, the maximum refractive index is limited by the temperature at which the rubidium reacts with the windows. In an atomic prism cell, contact with the windows is unavoidable, whereas in a gradient refractive index cell, windows can be removed from the atomic vapor, shielded by a buffer gas and cooled to temperatures far below the atomic vapor temperature. For this work, the main body of the cell was 10 in long, with a 5 in² cross-section. A reservoir at the bottom of the cell was filled with 10 g of high-purity (99.99%) rubidium. The cell was filled with a helium buffer gas at a pressure low enough to avoid thermally induced convective effects. As the bottom of the cell was heated, rubidium vapor diffused through the helium and condensed at the top, which was cooled. A narrow linewidth (1 GHz), tunable Ti:sapphire laser was used to measure the dispersion characteristics of the cell, which are shown plotted in Fig. 9, along with model predictions for bottom plate temperatures of 310, 292 and 212°C, and a constant top plate temperature of 60°C. A similar set of absorption curves for 287, 258 and 208°C with a constant 60°C top plate temperature are shown with model predictions in Fig. 10. The experimental configuration for the Raman measurement is shown in Fig. 11. The Ti:sapphire laser was tuned to overlap the center of the rubidium cell absorption, and the rotational Raman scattering from a CO_2 jet was collected through a slit, passed through the cell and imaged

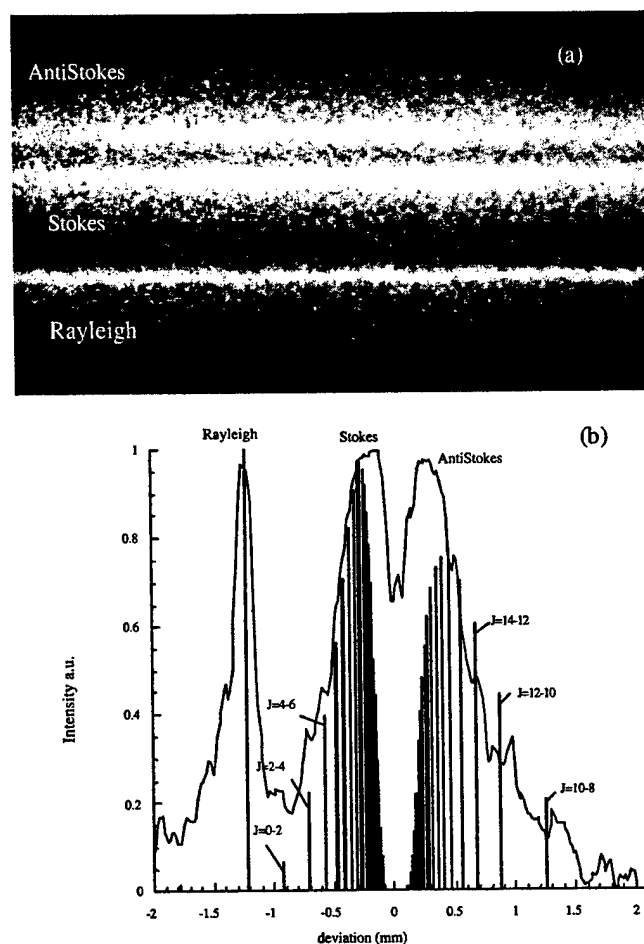


Figure 8. CO₂ rotational Raman scattering imaged with the mercury-vapor prism. (a) Raman scattering images of CO₂. (b) Intensity versus location for vertical cut through (a).

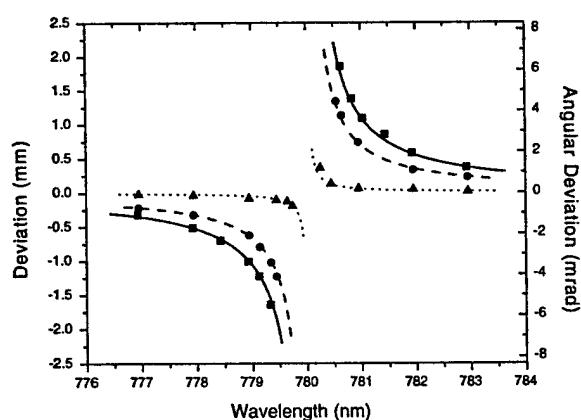


Figure 9. Measured and modeled deviation of light through the density gradient dispersive absorption filter as a function of incident wavelength. Measurements taken with (■) 310 to 60 °C, (●) 292 to 60 °C and (▲) 212 to 60 °C temperature gradients along with the modeled prediction. The right-hand vertical axis labels the angular deviation through the filter.

on to a second slit in front of a photomultiplier tube. The second slit was scanned in position, and the spectrum that was recorded is shown in Fig. 12. The locations of individual rotation lines are shown in the diagram. The lowest lying rotational states are not visible since they fall within

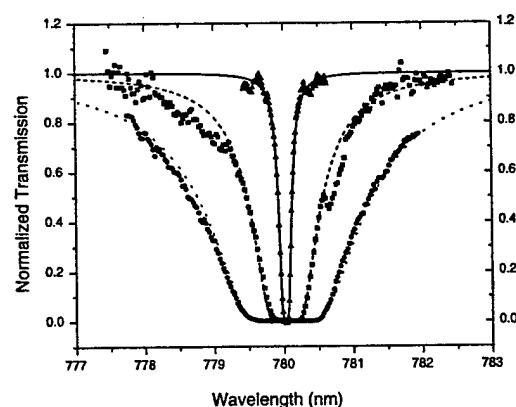


Figure 10. Measured and modeled predictions of the transmission profiles under various operating conditions. Data taken for temperature gradients of (●) 287 to 60 °C, (■) 258 to 60 °C and (▲) 208 to 60 °C. Also shown are the respective model predictions.

the absorption profile for the particular experimental conditions in this example.

CONCLUSION

The three examples presented in this paper indicate that the use of tunable lasers, together with atomic spectral

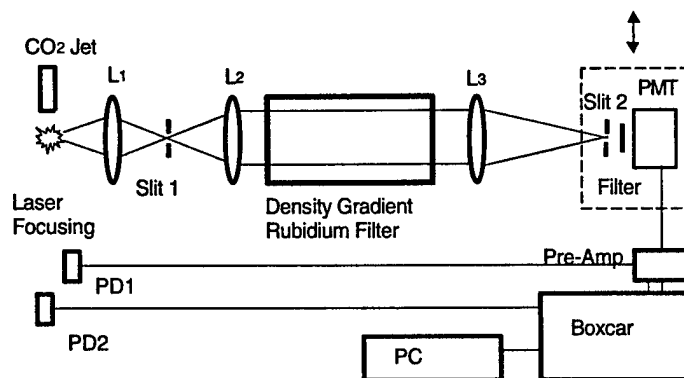


Figure 11. Schematic diagram for experimental setup. PD1 and PD2, photodiodes 1 and 2; L1, focal length 50 mm lens; L2, focal length 250 mm lens; L3, focal length 300 mm lens. The interference filter used in this experiment was a 10 nm bandwidth passband filter.

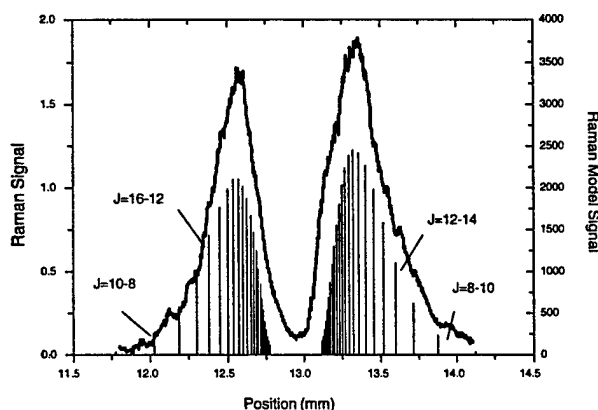


Figure 12. The 1-D carbon dioxide rotational Raman spectroscopic profile taken through the density gradient rubidium cell. Also shown are the numerical model predictions of the positions of each individual rotational line and its strength. The first few rotational Raman scattering lines are attenuated.

filters, is an attractive new way to perform rotational Raman spectroscopy. The refluorescence cell provides the capability of generating two-dimensional images of single Raman line scattering which may be useful for species

identification, species location and temperature measurements in fluid dynamic and combustion environments. With time gating and GHz-resolution spectral selectivity, the refluorescence filter strongly suppresses background noise. The refluorescence process, however, does contribute to additional signal loss, particularly for imaging applications. The dispersive filters have significantly higher efficiency and can be used to image the entire rotational Raman spectrum along a line. Two versions of these filters have been explored, a vapor prism and a gradient dispersion cell. The vapor prism has the advantage of simplicity and is demonstrated in the UV region using mercury vapor at 253.7 nm. The dispersive filter requires a density gradient and, therefore, introduces additional complexity, but has higher dispersive powers than the prism. This approach was demonstrated using rubidium vapor near 780 nm in the near-infrared region. For both dispersive cells, rotational Raman spectra from gas-phase CO₂ at atmospheric pressure were observed.

Acknowledgements

This work was supported by the Air Force Office of Scientific Research through the New World Vistas Program, the Air Plasma Ramparts MURI, and through a Small Business Innovative Research program with M. L. Energia, Inc.

REFERENCES

- Long MB, Fourquette DC, Escoda MC. *Opt. Lett.* 1983; **8**: 244.
- Nandula SP, Brown TM, Pitz RW. *Combust. Flame* 1994; **99**: 775.
- Brockhinke A, KohseHoinghaus K, Andresen P. *Opt. Lett.* 1996; **21**: 2029.
- Rothe EW, Andresen P. *Appl. Opt.* 1997; **36**: 3971.
- Finkelstein ND, Lempert WR, Miles RB. *Opt. Lett.* 1997; **22**: 537.
- Finkelstein ND, Yalin AP, Lempert WR, Miles RB. *Opt. Lett.* 1998; **23**: 1615.
- Miles RB, Lempert WR. *Annu. Rev. Fluid Mech.* 1997; **29**: 285.
- Forkey JN, Lempert WR, Miles RB. *Exp. Fluids* 1998; **24**: 151.
- Shay TM, Chung YC. *Opt. Lett.* 1988; **13**: 443.
- Gelbwachs JA. *IEEE J. Quantum Electron.* 1988; **14**: 1266.
- Gelbwachs JA, Chan YC. *IEEE J. Quantum Electron.* 1992; **28**: 2577.
- Menders J, Searcy P, Roff K, Korevaar E. *Opt. Lett.* 1992; **17**: 1388.
- Langberg E, Naylor M, Heckscher H. *Proceedings of Conference on Optical Instruments and Techniques*, Habell KJ (ed). Chapman and Hall: London, 1962; 229–237.
- Rabl A, Goodman NB, Winston R. *Solar Energy* 1979; **22**: 373.

Characterization of laser seeding by use of group-velocity dispersion in an atomic-vapor filter

Azer P. Yalin, Peter F. Barker, and Richard B. Miles

Department of Mechanical and Aerospace Engineering, Princeton University, Princeton, New Jersey 08544

Received October 1, 1999

A method for measuring laser seeding efficiencies by use of group-velocity dispersion has been developed. By tuning the laser near a resonance in an atomic-vapor filter it is possible to temporally decouple the seeded (narrow-band) light from the unseeded (broadband) light. We measured a seeding efficiency of 99.8% of the third harmonic of an injection-seeded Ti:sapphire laser. A model for the observed dispersion has been developed and tested. The group-velocity dispersion in the filter may also be used to chirp pulses for spectral analysis in the time domain. © 2000 Optical Society of America

OCIS codes: 300.6500, 190.5530, 140.3590.

A novel method for discriminating between the seeded narrow-band and the unseeded broadband components of a seeded laser has been developed and can be used to measure laser seeding efficiencies. Often laser seeding efficiencies are high, quoted as greater than 99%, making it a challenging problem to measure the small fraction of broadband light present in the beam. However, in many spectroscopic applications it is important to have accurate knowledge of the seeding efficiency, or spectral purity. For example, in measurements of laser-induced fluorescence the broadband light will interact with nonresonant transitions, and in filtered Rayleigh scattering measurements the elastic background suppression may be compromised.¹ To measure the small fraction of broadband light, techniques that measure the light transmission near optically thick transitions have been developed.² These methods require accurate spectral knowledge of the transition in use, of the laser frequency, and of the narrow-band linewidth. In contrast, our method uses group-velocity dispersion (GVD) to decouple the narrow-band and broadband components to permit a direct determination of the laser seeding efficiency. Seeding efficiency can be measured on a shot-to-shot basis, and precise knowledge of the laser characteristics or of the vapor characteristics is not required. To demonstrate the technique we measured the seeding efficiency of the third-harmonic output of an injection-seeded Ti:sapphire laser to be ~99.8%.

Our method uses the strong variation in group velocity near an atomic resonance to temporally separate frequency components within a pulse of width ~20 ns. Tuning the laser near a resonant transition of the vapor filter causes the seeded (narrow-band) portion of the light to propagate through the filter with a group velocity that is significantly less (of the order of 100 times) than the speed of light. The unseeded light is broad in frequency compared with the absorption bandwidth and therefore travels through the filter at close to the speed of light. Its slower group velocity means that the seeded light is delayed relative to the unseeded light, permitting temporal discrimination between the two components. Delayed pulses in rubidium vapor were observed previously³; furthermore, GVD in atomic vapors has been used to measure

Lorentzian linewidths⁴ and to determine electric transition dipole moments.⁵

The GVD is due to the variation in the real part of the index of refraction⁶:

$$V_g(\omega) = \frac{c}{\left(n + \omega \frac{dn}{d\omega}\right)}, \quad (1)$$

where V_g is the group velocity, c is the speed of light, n is the index of refraction, ω is the radial frequency, and $dn/d\omega$ is the derivative of real index with respect to radial frequency. The real index of refraction near a transition is given as⁶

$$n = 1 - \left(\frac{e^2}{2M_e}\right) N f \frac{1}{\epsilon_0} \left[\frac{(\omega^2 - \omega_0^2)}{(\omega^2 - \omega_0^2)^2 + \omega^2 \gamma^2} \right], \quad (2)$$

where e is the electron charge, M_e is the electron mass, N is the number density, f is the oscillator strength, ϵ_0 is the electric permittivity, γ is the linewidth, ω is the radial frequency, and ω_0 is the resonant frequency. The authors' research group has developed a model for the real index of mercury vapor, including isotopes and hyperfine structure.⁷ Variations in the derivative of the real index with respect to frequency cause variations in group velocity, or temporal dispersion. Narrow-band light of frequency ω propagates through the vapor with a group velocity given by Eq. (1), whereas light much broader than the transition width propagates with nearly the unperturbed speed of light. The propagation delay time through a vapor cell for a seeded narrow-band pulse relative to an unseeded broadband pulse is then simply

$$T_{\text{delay}}(\omega) = \frac{L}{V_g(\omega)} - \frac{L}{c}, \quad (3)$$

where T_{delay} is the delay time and L is the cell length.

Figure 1(a) shows the modeled delay time of narrow-band light relative to broadband light as a function of frequency through a 5-cm-length mercury-vapor cell. Also shown is the modeled filter transmission, found from Beer's law. The complex structure is due to isotopic contributions as well as to hyperfine splitting. The frequency axis shown is relative to

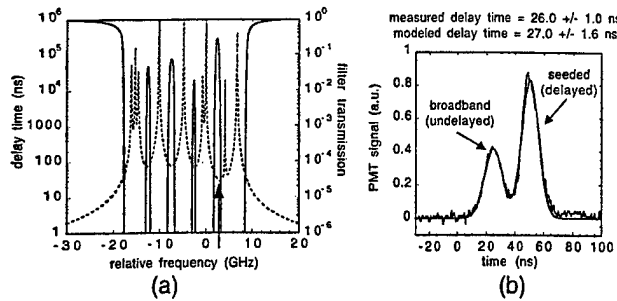


Fig. 1. (a) Modeled delay time (dashed curve) and modeled transmission (solid curve) for the 5-cm mercury-vapor filter near 253.7 nm. The multiple peaks are due to both isotopic abundance and hyperfine splitting. (b) Oscilloscope trace showing the narrow-band light delayed relative to the broadband light as well as a sum of two Gaussians fitted to the data. The laser frequency in (b) is marked by an arrow in (a).

39412.4 cm^{-1} (253.7 nm). The cell is modeled as having a vapor pressure of 0.445 Torr and a temperature of 403 K. The cell is an evacuated quartz tube of diameter 5 cm and length 5 cm. The vapor pressure is regulated by immersion of a cold tip containing liquid mercury into a temperature-regulated bath.

Figure 1(b) shows an oscilloscope trace that illustrates the GVD through the mercury filter. The early peak is due to the unseeded light; the delayed peak is due to the seeded pulse. The filter was operated as described above, and the laser was tuned as indicated in Fig. 1(a). Such traces were taken at a range of filter conditions and served to verify the GVD model; for example, in this case the modeled and measured delay times were 27.0 ± 1.6 and 26.0 ± 1.0 ns, respectively.

Separating the seeded and the unseeded pulses allowed us to measure the seeding efficiency of the third harmonic of our pulsed Ti:sapphire laser. The laser was injection seeded from a continuous-wave Ti:sapphire laser and operated with a ramp-and-lock feedback system to ensure single-mode output.⁸ The output from the laser was attenuated significantly and then imaged through a mercury-vapor cell and collected with a photomultiplier tube (PMT; Hamamatsu Model R-960). The mercury-vapor filter was operated at conditions similar to those modeled in Fig. 1. A monochromator (ISA Model H20) was placed between the mercury filter and the PMT and was used to reject other colors of light from the pump beams and the first and second harmonics. We used boxcar integrators (Stanford Research Systems) to measure separately the integrated intensity of the unseeded (undelayed) light and the seeded (delayed) light. The unseeded light was measured with one channel, and a wider delayed gate from a second channel was used to measure the seeded light. The firing of the laser has some jitter, and care was taken to ensure that the unseeded signal did not overlap the delayed gate. Such a configuration ensured that all broadband light would appear in the first gate and that all light delayed by greater than ~ 25 ns would appear in the second gate. Of course, for laser tunings for which the delays are less than ~ 25 ns, the seeded light leaks into the first gate. Note that to see both the delayed

light and the undelayed light pulses simultaneously one must tune the laser to near the edge of the filter transmission, such that the filter absorption is comparable with the seeding efficiency ($\sim 99\%$). In this case the seeded pulse is attenuated to a level comparable with that of the unseeded pulse, and the two pulses can be viewed at the same time.

Figure 2 shows the results of a frequency scan of the broadband and narrow-band signal amplitudes starting in the filter absorption and moving to the filter transmission. Also shown is the modeled narrow-band signal level. We established the frequency axis for the model by using data from a second, optically thinner, mercury-vapor filter, which acted as a frequency reference. The seeded signal is strongly absorbed within the notch and then becomes apparent as one moves toward the edge of the filter ($I/I_0 \sim 0.01$). Meanwhile, the signal from the broadband light remains quite uniform, even in the spectral region where the seeded light is moving into the transmission, indicating that the linewidth of the broadband light is much wider than the filter ($\sim 0.3 \text{ cm}^{-1}$). Tuning the monochromator indicates that the broadband light is narrow compared with the 3-nm passband of the monochromator, which allows us to bracket the linewidth of the broadband light by 0.3 and 300 wave numbers. In the filter transmission the seeded signal is undelayed, so both the seeded and the broadband signals appear in the first gate. To collect the signal in the filter transmission we inserted a neutral-density filter (transmission, 0.0056) into the beam path.

From such data it is straightforward to extract the seeding efficiency (or spectral purity), which we define as the fraction of seeded energy in the pulse. The signal measured with the laser tuned to the

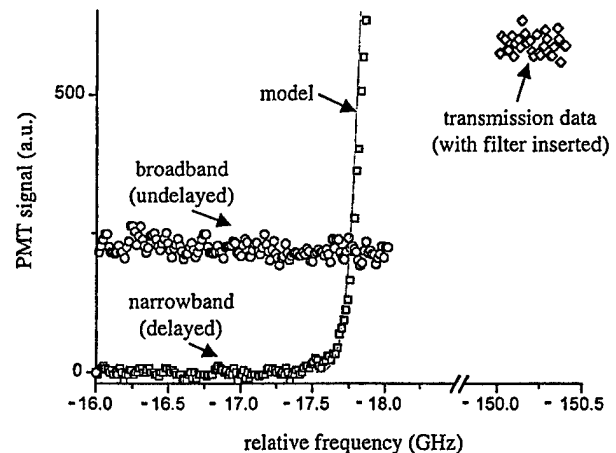


Fig. 2. Narrow-band (delayed) and broadband (undelayed) light intensities as the laser frequency is tuned from -16 GHz (within the absorption notch) to -150 GHz (far from the absorption). Within the absorption notch, the narrow-band component is strongly attenuated, and only the broadband component can be detected. The narrow-band (delayed) intensity agrees with the model (shown as a solid curve). Far from resonance, both components propagate through the filter with approximately the same speed and with no attenuation. The ratio of the broadband signal to the transmission signal measured far from resonance gives the seeding efficiency.

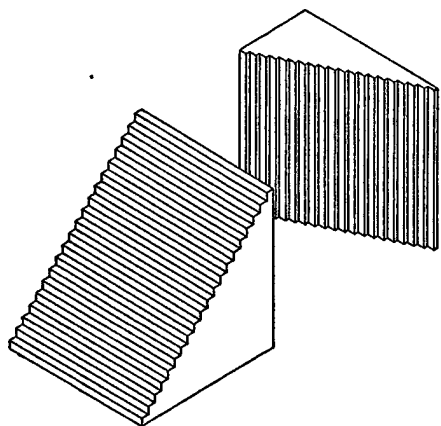


Fig. 2. Schematic of the echelon optics. The two echelons have step thicknesses of 300 and 15 μm , leading to optical delays of 500 and 25 fs, respectively. Each echelon has 20 steps, giving a total temporal range of 10 ps.

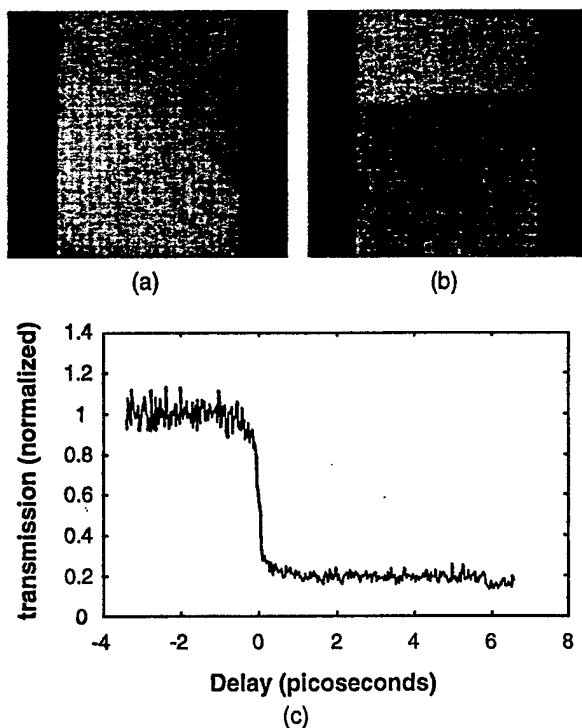


Fig. 3. Data recorded from a glass coverslip sample. (a) Image of the transmission of the probe light through the sample without any excitation pulse present. (b) Image of the transmission of the probe light through the sample with an excitation pulse whose intensity exceeds the dielectric breakdown threshold. (c) Plot of the temporal response obtained from the image in (b), normalized by the image in (a), averaged over ten such measurements. Data points from pixels on the CCD horizontal edges have been corrected as described in the text.

The 400 separate probe beams are clearly visible. Each step to the right increases the temporal delay by 25 fs; each step down, by 500 fs. Figure 3(b) shows the image when a 40-fs, 600- μJ , 800-nm excitation pulse is used. The intensity of the pump pulse at the sample is approximately 67 TW/cm², which is well above the dielectric breakdown intensity for

the glass. The transmitted probe-light intensity decreases over the temporal range covered by several echelon steps following the arrival of the excitation pulse. We expect that the damage and reduction in optical quality of the sample will occur on the time scale of the excitation pulse duration,⁶ and the observed response reflects the apparatus response time. This result was limited by the probe-pulse duration of 300 fs, owing to group-velocity dispersion in the optics. Figure 3(c) shows the time-dependent probe transmission, derived from the data shown in Fig. 3(b) and averaged over ten such measurements. The change in absorption after the initial response is negligible over the time range of the experiment. Repetition of the experiment with different delays between the pump pulse and the set of probe pulses resulted in shifting of the CCD pixels that showed a response near $t = 0$ but no change in the response itself. An experimental artifact observed in the 40 probe beams at the horizontal edges of the CCD images was corrected through this procedure. For these 40 beams, distortion in the focusing optics led to reduced overlap with the pump light and correspondingly reduced changes in transmission following $t = 0$. Based on the repeated experiments with different overall delays, these periodic differences were corrected for in the plot shown in Fig. 3(c) and in the analysis of data from other materials.

Figure 4 shows similar results for a highly reactive organic molecular crystal, 1,3,3-trinitroazetidine, that is used as an explosive. In this case, excitation with high-intensity light leads to a violent reaction and complete decomposition after a limited number of shots.

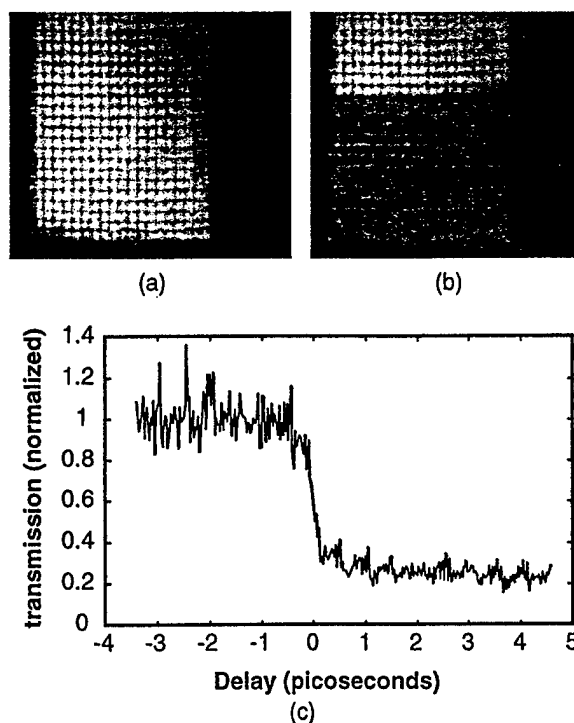


Fig. 4. Data recorded from a single crystal of the explosive 1,3,3-trinitroazetidine. (a), (b), and (c) are the same as in Fig. 3, except that the plot in (c) is from only one measurement.

Nevertheless, single-shot data can be collected. The data in Fig. 4(c) are from a single laser shot, not averaged as in Fig. 3(c). The data show a rapid decline in transmitted probe-light intensity. Coherent excitation of lattice vibrations might be expected through impulsive stimulated Raman scattering, as has been observed in our lab at lower excitation intensities³ or through the effect on the lattice of suddenly released electrons or photofragments.⁷ Unfortunately the probe-pulse duration is too long to permit clear observation of coherent phonon oscillations. The experiment will be repeated with shorter probe-pulse duration in the near future.

The standard deviation of the signal intensity for a single pump-probe measurement is 9% of the signal level. Future modifications to the apparatus will substantially improve the signal/noise ratio. Specifically, normalization of the signal image will be conducted through the use of an image of the probe beams from the same pulse that is used in the actual measurement, rather than the current method of normalization by use of two different probe pulses. This approach will reduce the noise that is due to shot-to-shot variations in the probe beam's transverse profile.

The results presented here demonstrate that real-time, single-shot femtosecond spectroscopy with ultrafast time resolution, limited only by the excitation and probe-pulse duration, is possible and practical. Other experimental observables, including transient birefringence (optical Kerr effect) and transient probe spectral shifting,⁸ have been measured on a single-shot basis by insertion of the proper polarization or spectral filtering optics into the setup described above. Several experimental improvements are under way that will further facilitate these measurements. These improvements include the use of shorter probe pulses and improvements in the probe imaging system to eliminate the need for corrections of data from 40 of the 400 probe pulses as a result of varying excitation and

probe-pulse overlap. The method demonstrated here could be extended to include more points or different time steps. Once this method becomes sufficiently routine, its use may prove advantageous even in measurements with many laser shots on samples that can be flowed or that are not permanently changed by the excitation light. The multiplex advantage of acquiring data at many temporal delays for each shot could substantially improve data-collection times and signal/noise ratios, especially in cases in which excitation laser intensity fluctuations contribute significantly to noise. Finally, the approach demonstrated here offers a simple real-time readout method that may find applications in ultrafast, high-bandwidth signal processing.

This work was supported in part by U.S. Office of Naval Research Grant N00014-96-1-1038. K. A. Nelson's e-mail address is kanelson@mit.edu.

References

1. L. Dhar, J. T. Fourkas, and K. A. Nelson, *Opt. Lett.* **19**, 643 (1994).
2. Z. P. Jiang and X. C. Zhang, *Appl. Phys. Lett.* **72**, 1945 (1998).
3. D. D. Chung, "Femtosecond pump-probe spectroscopy of chemical reactions in liquids and crystals," Ph.D. dissertation (Department of Chemistry, Massachusetts Institute of Technology, Cambridge, Mass., 1998).
4. M. R. Topp, P. M. Rentzepis, and R. P. Jones, *J. Appl. Phys.* **42**, 3415 (1971).
5. M. C. Nuss, D. H. Auston, and F. Capasso, *Phys. Rev. Lett.* **58**, 2355 (1987).
6. A. C. Tien, S. Backus, H. C. Kapteyn, M. M. Murnane, and G. Mourou, *Phys. Rev. Lett.* **82**, 3883 (1999).
7. V. A. Apkarian and N. Schwentner, *Chem. Rev.* **99**, 1481 (1999).
8. Y. X. Yan and K. A. Nelson, *J. Chem. Phys.* **87**, 6240 (1987).

Megahertz Pulse-Burst Laser and Visualization of Shock-Wave/Boundary-Layer Interaction

Pingfan Wu,* Walter R. Lempert,[†] and Richard B. Miles[‡]
Princeton University, Princeton, New Jersey 08544

The development and application of a Nd:YAG pulse-burst laser system, which is capable of operating at up to 1-MHz pulse repetition rate with high pulse energy and narrow spectral linewidth, is presented. The laser system can generate a burst of from 1 to 99 pulses over a maximum time interval of 100 μ s. The average single pulse energy at 1.064 μ m is 10 mJ. This laser is paired with a new megahertz-rate charge-coupled device framing camera to obtain images of a Mach 2.5 flow over a 14-deg angle wedge at a 500-kHz repetition rate. The sequential images clearly show the dynamic interaction between the incoming turbulent boundary layer and the unsteady oblique shock wave.

I. Introduction

IN recent years there has been enormous progress in the development and application of diagnostic imaging techniques, such as planar laser-induced fluorescence (PLIF),¹ Rayleigh scattering,² and Raman scattering.³ However, the ability to capture time-evolving information has been severely constrained by the limitations of laser technology. For example, the pulse repetition rates of commercially available high-energy solid-state lasers are limited up to 30 Hz. Nd:YAG lasers combining continuous pumping with repetitive Q switching at up to 50 kHz have been built.⁴ However, the pulse energy at these rates is only about 100 μ J. Also available are 20-kHz repetition-rate metal vapor lasers,⁵ with single pulse energy a few millijoules. Newly developed, repetitively Q-switched ruby lasers have pushed the repetition rate up to 500 kHz.^{6,7} After amplification the individual pulse energy can get hundreds of millijoules.⁷ However, when the repetition rate extends to 1 MHz, repetitive Q-switched operation becomes very unreliable.⁶

Our objective has been to develop a laser imaging system to capture high-speed and unsteady flow phenomena, such as turbulent structure and shock-wave/boundary-layer interactions. The dynamics of the highly unsteady shock-wave/boundary-layer interaction is very important in the stability and control of supersonic vehicle. Because the particular characteristics of the turbulence are still unknown, the dynamic visualization of shock wave and boundary-layer structure becomes very important. The characteristic small-scale eddy turnover time is on the order of microseconds, and so a megahertz repetition-rate laser source and imaging system become critical for this application.

The pulse burst concept is chosen for megahertz rate imaging diagnostics systems because the product of repetition rate and energy per pulse is constrained by the thermal loading that the solid-state lasing elements can tolerate. The current maximum power for a commercially available pulsed Nd:YAG system is approximately 15 W at 1.06 μ m (1.5 J/pulse at 10 Hz). This means that, for example, if the megahertz pulse laser were to be run as a continuous duty cycle system, thermal considerations alone would limit the output energy to approximately 150 μ J per pulse. This is approximately 100 times too low to be generally useful for flow imaging experiments. The key to the burst concept is the reduction of the duty cycle in order

to achieve high energies in each individual pulse. A typical pulse-burst can be seen in Fig. 1a: every 0.1 s a burst of about 30 pulses is generated (in this figure only 5 pulses are shown).

In this paper we present the design of a Nd:YAG-based, high-power, narrow-linewidth, pulse-burst laser source that can generate a burst of from 1 to 99 laser pulses with an interpulse period as short as 1 μ s and a pulsewidth from 10 to 100 ns. The spectral width of these pulses is comparable to the Fourier transform of their temporal profiles, which makes this pulse-burst laser an ideal source for narrow-linewidth, long coherence length applications such as holographic interferometry and filtered Rayleigh scattering (FRS).^{8,9} In particular, the FRS is useful for the imaging of high-speed flows because it can be used to suppress background scattering from windows and walls as well as to highlight particular velocity components.

This pulse-burst laser system has been paired with a Princeton Scientific Instruments' fast-framing charge-coupled-device (CCD) camera that can capture up to 30 images at a rate of up to 1 μ s a frame. The laser and the camera were set up to visualize the Mach 2.5 flow over a 14-deg wedge from streamwise view and planform view at a 0.5-MHz rate. The optically thick iodine vapor filter was placed in front of the camera and used to highlight different velocity components of the flow by selectively passing different Doppler-shifted frequencies. The images that were acquired clearly illustrate the unsteadiness of the oblique shock wave and show that the unsteady shock motion is closely coupled to the incoming boundary-layer structure.

II. General Description of the Laser

The challenge is to create a controllable pulse-burst system, which produces a uniform set of high-energy pulses with very low background. The background is primarily caused by amplified spontaneous emission that occurs naturally through the amplifier chain. Incidental feedback must also be carefully controlled so that the system does not develop parasitic lasing. In addition, the gain seen by each pulse in the pulse burst is slightly different because of the gain saturation from the previous pulse. In the design of this system, it was decided not to use a regenerative amplifier configuration because of the limited versatility of such a system and concerns regarding gain depletion and Q-switch leakage. The design of the pulse-burst laser system is, therefore, based on a master oscillator power amplifier (MOPA) configuration, as shown in Fig. 2. The laser system consists of six principle parts: 1) monolithic, single-frequency, diode-pumped, CW Nd:YAG laser; 2) four-pass preamplifier 1; 3) pulse slicer (a pair of Pockels cells); 4) two-pass preamplifier 2; 5) three-stage high-energy amplifier chain; and 6) second harmonic crystal.

A continuous wave (CW) Nd:YAG ring laser serves as the master oscillator. The laser can be frequency tuned and has a single mode output. Because this laser is amplified through the amplifier chain,

Received 1 April 1999; revision received 16 August 1999; accepted for publication 18 August 1999. Copyright © 1999 by the American Institute of Aeronautics and Astronautics, Inc. All rights reserved.

*Graduate Student, Department of Mechanical and Aerospace Engineering, Student Member AIAA.

[†]Senior Research Scientist, Department of Mechanical and Aerospace Engineering; currently Associate Professor, Department of Mechanical Engineering, Ohio State University, Columbus, OH 43210.

[‡]Professor, Department of Mechanical and Aerospace Engineering. Associate Fellow AIAA.

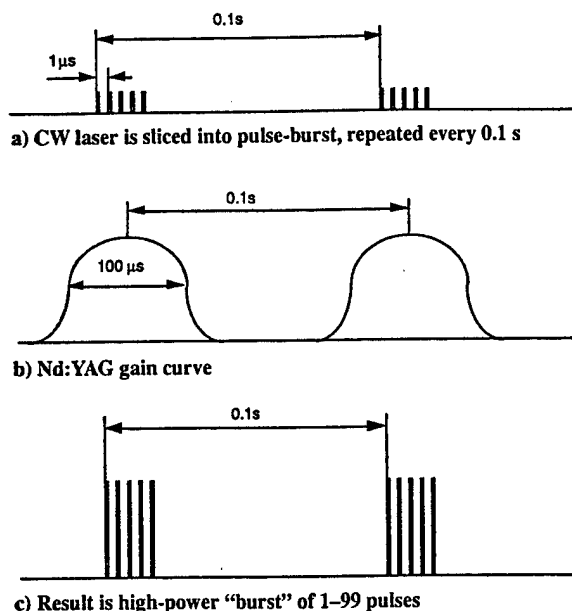


Fig. 1 Concept of pulse-burst laser system.

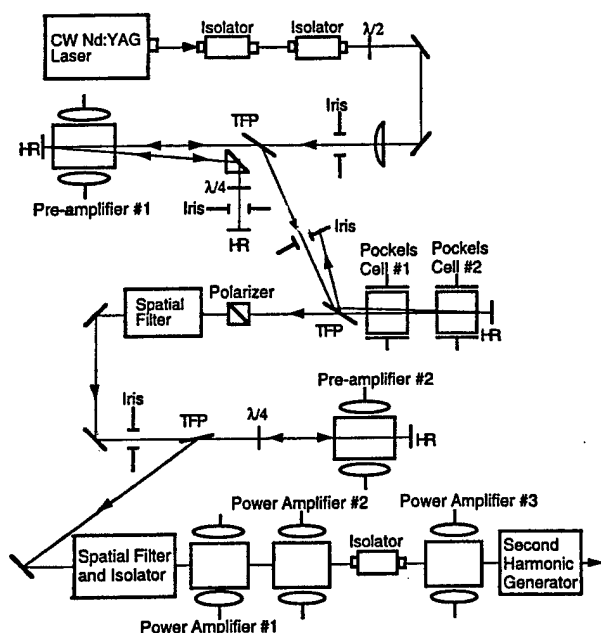


Fig. 2 Schematic diagram of pulse-burst laser system.

its frequency determines the output frequency of the pulse-burst laser system. To minimize amplified spontaneous emission (ASE), the four-pass preamplifier 1 amplifies this CW laser light over the 100- μ s-or-so gain window of the flashlamp-pumped Nd:YAG laser rods. The power remains below saturation, and so there is no loss in gain associated with amplifying a CW laser as compared to a pulsed laser in this stage. This CW preamplification suppresses the ASE that would otherwise be present between pulses had the pulse slicing been done before preamplifier 1. ASE occurs continuously during the flashlamp pumping time so that if the light were chopped with a $\frac{1}{100}$ duty cycle the ASE generated in preamplifier 1 would be stronger than the amplified laser signal. This is avoided by putting the pulse slicer after preamplifier 1. The slicer not only chops the pulse but also blocks the cross-talk between preamplifier 1 and preamplifier 2 and, therefore, serves as an isolation stage in the amplifier chain.

III. System Performance

A. Master Oscillator

The master oscillator is a commercially available monolithic Nd:YAG ring laser with output power about 20 mW (Lightwave

120-03A). The frequency of this laser can be voltage-tuned over a range of approximately 1 cm^{-1} at $1.06 \text{ }\mu\text{m}$. The CW laser beam has a very good spectral and spatial profile. The linewidth is about 5 kHz (in 1 ms), and the frequency drift is about 50 MHz/h.

B. Preamplifier 1

Preamplifier 1 is a four-pass, 10-Hz repetition-rate, flashlamp-pumped, 6.5 mm diam \times 110 mm long Nd:YAG rod. A long-focal-length (1-m) lens reduces the beam diameter to approximately 2 mm to accommodate the multiple passes. The overall gain of the four-pass system, taking optical losses into account, is approximately 2500 times. Preamplifier 1 is currently operated at much lower level than its maximum gain in order to prevent spontaneous lasing.

C. Pulse Slicer

The pulse slicer, custom built by Medox, Inc. (Ann Arbor, Michigan), consists of a pair of electro-optic Pockels cells, similar to those used as Q switches for standard solid-state laser systems. By applying a suitable voltage, a $\lambda/4$ polarization retardation is imposed upon the laser beam by each Pockels cell for each pass. Consequently, when either one of the cells is on, the resulting polarization is rotated 90 deg (from vertical to horizontal) and is, therefore, transmitted through the thin-film polarizer (TFP). When both (or neither) of the Pockels cells are on, the polarization of the beam is unchanged, and it is reflected by the TFP and blocked by an iris diaphragm.

Figure 3 shows a timing diagram for the pair of Pockels cells. Each individual Pockels cell has a minimum rise time of approximately 4 ns and an on time duration (t_2) of approximately 150 ns. The delay between the rising edges t_1 is variable from 5 to 100 ns. The slicer is on, during the interval t_1 when Pockels cell 1 is high and Pockels cell 2 is low. From the diagram it is apparent that the falling edge is much slower than the rising edge, which is the reason two Pockels cells are used instead of one. For this system the timing of the laser pulses solely depends on the rising edge of the high voltage, which is applied to the Pockels cells. The high-voltage timing is determined by a 500-MHz precision clock that controls the Pockels cells' power supply unit, resulting the timing jitter for the laser pulses that is less than 2 ns. The timing of pulses here is much more precise than the repetitively Q-switched laser,⁷ in which even the Q-switched pulse buildup time will cause time uncertainty 10 ns.

D. Preamplifier 2

After the pulse slicer the output pulse train is spatially filtered and then double-passed through preamplifier 2. The spatial filter has two functions: 1) decrease the ASE and 2) clean the spatial profile of the laser.

Preamplifier 2 is an 8 mm diam \times 110 mm long Nd:YAG rod. The peak double-pass gain of preamplifier 2 is approximately 13 times. The output peak pulse power is about 650 W, corresponding to an average 13 μ J for a single, 20-ns-duration pulse. Again to prevent

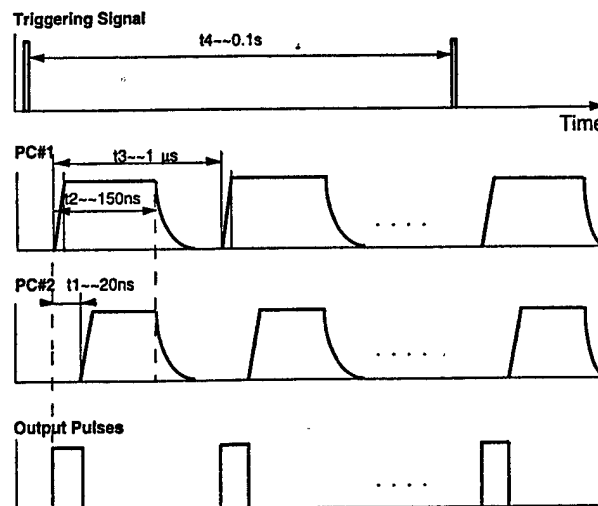


Fig. 3 Timing diagram for the work of the pair of Pockels cells.

spontaneous lasing, preamplifier 2 is operated at a gain level lower than maximum power.

E. Power Amplifier Chain and Second Harmonic Generation

The power amplifier chain consists of three additional Nd:YAG rods, taken from a commercial (Continuum Model YG-592) laser system. The rods are 6.5, 6.5, and 9.5 mm diam, respectively. Between power amplifiers 2 and 3, there are a telescope beam expansion system (not shown in the figure) and a 10-mm-diam optical isolator (Electro-optics Technology, Inc., Traverse City, Michigan). The peak gain of the individual stage has been measured to be 10, 10, and 8 times, respectively, resulting in an overall peak system gain of approximately 2.5×10^7 (including preamplifiers). The corresponding energy is approximately 10 mJ for a single 20-ns duration pulse at 30 pulses per burst.

An important aspect of the system is the saturation of the final power amplifier. For the amplification of a single pulse, Frantz and Nodvik¹⁰ and Lowdermilk and Murry¹¹ have given the relation

$$E_{out} = I_{sat} \times A \times l_n \left\{ 1 + \left[\exp\left(\frac{E_{in}}{I_{sat} \times A}\right) - 1 \right] \times G_0 \right\} \quad (1)$$

where E_{in} and E_{out} are, respectively, the input and output energy of the pulse through the amplifier. I_{sat} is called the saturation flux of the amplifier, which is 440 mJ/cm² for a Nd:YAG amplifier. A is the area of the cross section of the amplifier. G_0 is the small signal gain of the amplifier, which is defined as

$$G_0 = \exp(g_0 L) = \exp(n\sigma L) \quad (2)$$

where n is the inverted population density and σ is the cross section of the stimulated radiation. L is the length of the rod. We can relate the small signal gain G_0 to the stored energy E_{store} :

$$E_{store} = nh\nu LA = A \times (h\nu/\sigma) \times l_n G_0 \quad (3)$$

where h is the Planck constant and ν is the frequency of the laser. For a specific laser amplifier the cross section A and $h\nu/\sigma$ are constant. The small signal gain G_0 is exponentially related to the stored energy E_{store} . In the pulse-burst laser system, as a pulse is being amplified, it depletes the stored energy from the amplifier, and G_0 decreases. From Eq. (1) the pulse amplification ratios decrease from pulse to pulse in the same burst. We have found the overall stored energy in the power amplifiers is about 800 mJ. For a pulse burst with 30 pulses, the first 29 pulses and other losses will take more than 300 mJ from the rods. The gain of the 30th pulse is only about $\frac{1}{8}$ of the gain of the first pulse in the burst. To compensate for this depletion, the preamplifiers are run on the rising edge of the temporal gain curve. This gives an increasing energy per pulse after preamplifier 2 (Fig. 4a), which leads to a more uniform pulse burst after the final amplifier (Fig. 4b). The oscilloscope (Tektronix Model TDS 360)

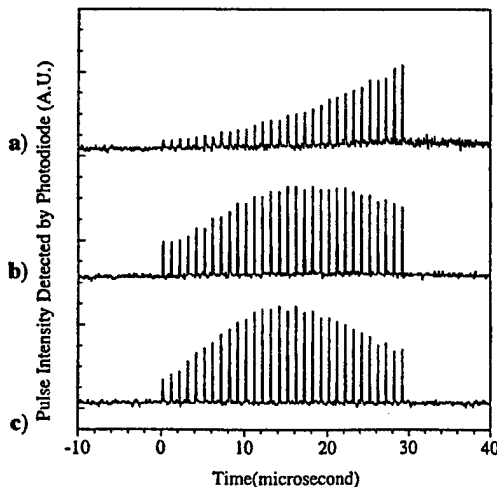


Fig. 4 Single-pulse burst a) before and b) after the final three stages of amplifier train; c) is the second harmonic of the pulse burst. There are 30 pulses per burst, with interpulse separation of 1 μ s and single-pulse duration of about 20 ns.

trace was detected by photodiode with 1-ns response time (Thorlabs Model DET210).

Because of gain depletion, the pulse-to-pulse energy is still far from constant. Especially after doubling, the lowest pulse energy is only about one-third of the highest pulse energy in the same burst. For this reason the dynamic range of the imaging system will decrease by a factor of three, which is still tolerable in our system. With further engineering the nonuniform pulse energy problem can be overcome by using a diode laser to replace the CW Nd:YAG laser as the master oscillator. The diode laser power is easily controlled through the driving current. In that case the input energy of each pulse can be tailored to get a uniform output after the final amplifier.

The final part of the laser system is the second harmonic generator. A telescope system (not shown in the picture) reduces the laser beam diameter to 4 mm before it passes through the doubling crystal. The peak intensity of fundamental light into the doubling crystal is about 4.5 MW/cm². The variation in pulse energy is accentuated by the second harmonic process as shown in Fig. 4c. The shape of a single pulse of second harmonic light closely follows that of the fundamental because both are rectangular in time. In contrast to a Gaussian pulse, the temporal profile of the second harmonic of a perfectly rectangular pulse, assuming a simple intensity squared law for conversion efficiency, is identical to that of the fundamental. The full width at half-maximum (FWHM) of the second harmonic is about 14 ns as compared to 16 ns primarily because of the rise time of fundamental pulse. With this system we only get average 0.4 mJ per pulse of second harmonic 0.532 μ m. The reason for the low conversion ratio is the low 1.06- μ m input intensity. Follow-on work indicates that pulse energy on the order of 25 mJ per pulse at 0.532 μ m are achievable with greater amplitude of 1.06- μ m light.

IV. Laser Spectral Profile

For many diagnostics applications, narrow spectral linewidth and frequency tunability over a limited range are important. Because the narrow-linewidth CW laser serves as a master oscillator and there is no resonator cavity in the amplification stage, the configuration of the pulse-burst laser system gives a very good spectral profile.

Each individual second harmonic pulse is predicted to have a time-average linewidth on the order of 63 MHz, based on the Fourier transform of a 14-ns rectangular temporal profile ($\delta\nu \times \delta t = 0.88$ for a sinc²/rectangular Fourier transform pair).

As shown in Fig. 5, a 2-GHz free spectral range, confocal Fabry-Perot spectrum analyzer (Burleigh Model RC-46) was used to directly measure the spectral profile of the second harmonic output of the pulse-burst laser. For these measurements the laser was operated at full gain, and the output was attenuated by reflection from an uncoated quartz flat (not shown in Fig. 5). The internal photodiode/mount assembly was removed from the etalon and replaced with a fast response photodiode. The pulsed output from the photodiode was integrated by a boxcar averager (Stanford Research Systems Model SRS 250) and sent to a PC computer. For the data presented next, the boxcar averaged the photodiode voltage over 30 laser shots. Simultaneously, the wavelength of the CW master oscillator was slowly scanned (on the order 1 MHz/s) by applying a computer generated voltage "staircase" (2.5 mV a step) to the input of the laser voltage controller, while holding the voltage to the etalon mirrors constant. The laser, rather than the etalon, was tuned

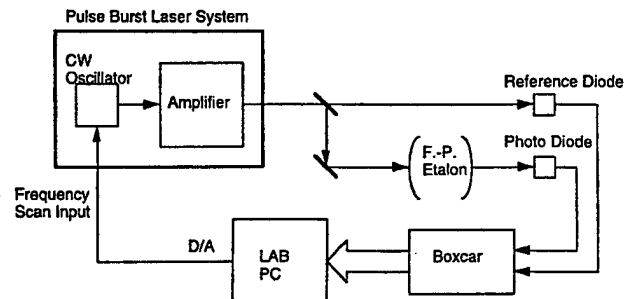


Fig. 5 Schematic diagram for measuring the spectral profile of the pulse-burst laser.

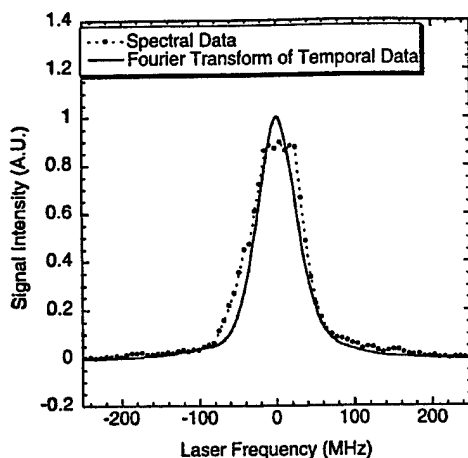


Fig. 6 Time-averaged spectral profile (....) of second harmonic output of pulse-burst laser and the convolution (—) between the etalon equipment function and Fourier transform of the temporal single-pulse profile.

because the etalon could not be scanned slowly enough to capture the profile of the pulsed laser smoothly. The frequency tuning rate of the laser was calibrated with the Fabry-Perot free spectral range. The observed scanning rate was 3 GHz/V and was assumed to be constant over the duration of the scan. The effective finesse of the etalon is measured by passing the CW laser (very narrow linewidth) through the etalon with exactly the same beam path. The measured finesse is about 70, corresponding to spectral resolution of 28 MHz.

Figure 6 (dotted line) shows the measured time-averaged spectral profile of the second harmonic output of the laser, operating nominally with 14-ns duration pulses. Also shown is the convolution between the instrumental function of the etalon and the Fourier transform of a real 14-ns FWHM pulse. It is clear that the spectral profile is approximately the Fourier transform limit of the laser pulse. The Fourier transform of the pulse burst with 30 pulses would be modulated by a high-frequency comb function, but because of the finesse of the etalon, this high frequency cannot be detected.

V. Attenuation of Transmission Through Molecular Iodine Vapor Cell

FRS⁸ has the abilities of extracting a weak signal by suppressing background scattering, as well as obtaining quantitative measurements of velocity, temperature, and density of flow simultaneously. The key component of FRS is an optically thick, well-characterized molecular iodine vapor filter that has a very sharp absorption line. The iodine filter, which has been described in detail previously,⁹ is 9.98 cm long with cell temperature of 80°C and side-arm temperature at 40°C. The side-arm temperature is maintained to within ± 0.1 K with a circulating hot-water bath. In the Rayleigh-scattering experiment, if the frequency of laser source is tuned to the center of the absorption line, the background scattering will be absorbed by the iodine cell while the flowfield signal will pass through the cell because of the Doppler frequency shift. If we tune the laser frequency through the absorption line when measuring the scattered intensity through iodine cell, we can get the spectral shift and the spectral profile of the scattered flow signal and obtain the velocity and temperature of the flow.⁸

Before doing a FRS experiment, it is important to characterize the attenuation of transmission through the iodine cell and the laser spectral purity by scanning the frequency of the laser source through the absorption band. The actual experimental apparatus is similar to Fig. 5, except the Fabry-Perot etalon is replaced by an iodine cell. The second harmonic (0.532- μ m) output of the pulse-burst laser hit an aluminum post, and scattered light was collected and passed through the iodine cell. The signal was observed by a photodetector and transferred to the boxcar integrator, as described earlier. At the same time the frequency of the laser was tuned through the absorption lines of iodine. A reference detector was used to monitor the laser output intensity fluctuations as the frequency was tuned. A series of calibrated neutral density filters was used to attenuate the beam prior to tuning into the resonance feature of the iodine

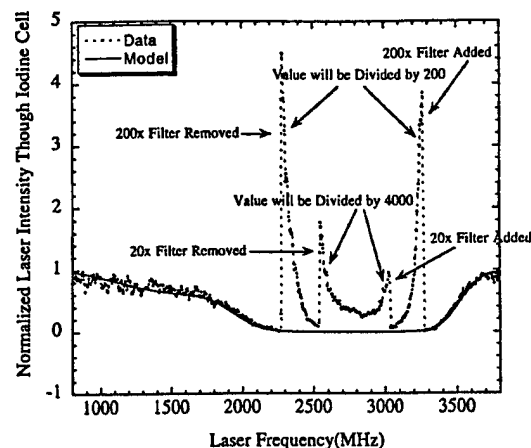


Fig. 7 Experimental attenuation of pulse-burst laser intensity through the iodine cell (....). Convolution of modeled transmission and laser spectral profile from Fig. 6 (—).

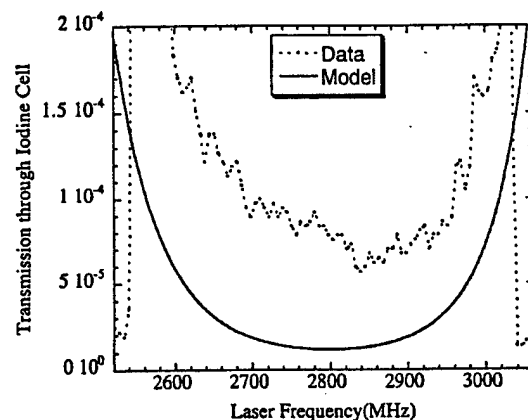


Fig. 8 Blowup of central portion of Fig. 7, illustrating absolute transmission near center iodine absorption line.

vapor. As the laser was tuned into the absorption band, the filters were sequentially removed, boosting the light level reaching the detector. Thus the dynamic range of the attenuation measurement was increased beyond the limitations imposed by the linear operating range of the photodiode.

The dotted line in Fig. 7 shows the experimental result as the frequency was slowly tuned across the absorption line A (around frequency 18788.5 cm^{-1})⁹ of the iodine cell. The detected signal has been normalized in such a way as to set the apparent transmission equal to approximately 1 at the endpoints of the scan. When the laser scan passed approximately the 2200-MHz point, a 200-times neutral density filter (Schott Glass Technology, Inc., NG10) was removed from the beam path, resulting in a large increase in signal reaching the detector. Then a second 20-times neutral density filter (Schott NG9) was removed. The neutral density filters were put back as the laser frequency was tuned out of the resonance of iodine. The solid line in Fig. 7 is the convolution between the pulse-burst laser linewidth and the theoretically predicted transmission across the absorption line A. Figure 8 is a blowup of the central 500 MHz of the experimental data (dotted line) and the theoretically predicted transmission (solid line). In this case the experimental data have been converted to absolute transmission by accounting for the attenuation of the neutral density filters. The experimental line center transmission is 5×10^{-5} , as compared to the modeled value of approximately 1.5×10^{-5} . The experimental curve fits well to the theoretical model with a correction for residual transmission. This residual transmission is presumed to arise from the nonideal wings of the laser spectrum and residual ASE. The experiment results not only mean that the pulse-burst laser has very good attenuation when passing through the resonance of the iodine, but the spectral profile of the laser is very good. The laser clearly operates with single mode. These results should be compared to a commercial injection seeded Nd:YAG laser

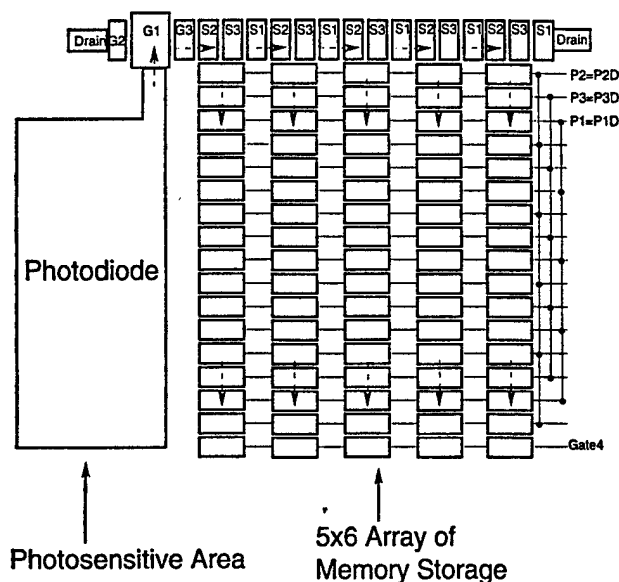


Fig. 9 Architecture of one pixel of megahertz-rate CCD camera. The CCD chip is developed by John Lowrance from Princeton Scientific Instruments, Inc., and Walter Kosonochy from the New Jersey Institute of Technology.

for which the attenuation through iodine resonance only reaches a factor of the order of 300 (Ref. 12), and locking is intermittent.

VI. Fast-Framing Megahertz CCD Camera

A new fast-framing CCD camera¹³ developed by Princeton Scientific Instruments, Inc., is used to collect images formed by the pulse-burst laser. The CCD camera chip (U.S. Patent 5355165) has a 30-image storage buffer built into each pixel of the image sensor chip itself and can frame at a rate up to 1 MHz. The pixel format is 360×360 , divided into four quadrants of 180×180 each. A simplified diagram of the architecture of 1 pixel is shown in Fig. 9. Each pixel consists of a photoactive region and a 5×6 array of memory elements. The charge is sequentially shifted across the top row of five storage elements at an interval as fast as $1 \mu\text{s}$. Subsequently, the charge in each row of memory elements is shifted down in parallel. Upon receipt of a master trigger, the camera operates continuously until a stop trigger is issued. At this point the last 30 images are read out to a standard PC computer.

By coupling the megahertz CCD camera with the pulse-burst laser, a megahertz high-speed flow diagnostic system has been built. This system can capture up to 30 sequential images of rapidly fluctuating phenomena. In the case of high-speed flow, 30 images are usually sufficient to follow the evolution of a structure all the way through the field of view.

VII. Visualization of Shock-Wave/Boundary-Layer Interaction in Mach 2.5 Wind Tunnel

To capture the dynamics of shock-wave/boundary-layer interaction, the pulse-burst laser system has been used to get 0.5-MHz repetition-rate sequential planar images of a turbulent Mach 2.5 boundary flow over a 14-deg wedge.

Figure 10 illustrates the experimental setup to obtain the streamwise view of the dynamics of the turbulent boundary-layer flow. The Mach 2.5 wind tunnel has a cross section of 1×0.5 in. The observation region is 16 in. downstream of the throat so that the boundary layer grows to a thickness of about 2 mm. The direction of the flow in the figure is from right to left. To get the streamwise view, a 0.8-mm-wide slit was cut in the centerline of the wedge to let the laser sheet pass through. The size of the slit is small enough to have almost no influence on the overall dynamic process. The second harmonic output of the pulse-burst laser was formed into an approximately 1.5 cm high \times 100 μm thick sheet and directed into the flow at an angle of 45 deg with respect to the freestream motion. The angle of 45 deg was chosen to generate enough of a Doppler frequency shift for FRS background suppression. The camera had

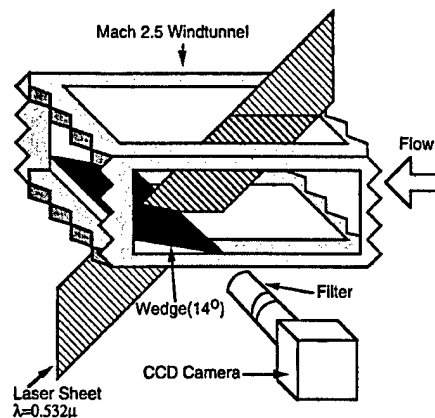


Fig. 10 Experimental setup of side-view visualization of shock-wave/boundary-layer interaction by shooting Mach 2.5 turbulent flow over a 14-deg wedge.

its optical axis perpendicular to the plane of the laser sheet. The flow was run with a stagnation pressure of 120 psig and a stagnation temperature of 258 K. As the Mach 2.5 flow passes by the wedge, an oblique shock forms.

To enhance the scattering signal, gaseous CO_2 was seeded into the flow at a level less than 1% (wt). After the nozzle, because of the temperature decrease of the flow, CO_2 condensed into a finely dispersed fog. We have measured the scattered signal while changing the polarization of incoming laser light. We found the scattering is in the Rayleigh-scattering region so that the condensed CO_2 cluster size is much smaller than the laser wavelength (532 nm). The CO_2 was seeded far upstream in the plenum and was chosen for its ease of handling and because it mixed homogeneously with the air. CO_2 causes less disturbance to the flow than using water vapor as seeder.¹⁴ In the warmer thermal boundary layer the CO_2 is in vapor form, resulting in very high image contrast. The boundary layer is visualized owing to the combined effects of density changes within the boundary layer and CO_2 cluster evaporation. These two effects are related because both result from temperature recovery within the boundary layer. Smith and Smits¹⁵ found the condensed cluster scattering intensity profile in the outer part of a supersonic boundary layer showed good agreement with those obtained using a probe survey.

Figure 11 shows a typical sequence of 25 streamwise view images with an image size of 0.5×0.5 in. The time interval between images is $2 \mu\text{s}$. The bright straight line at the left bottom corner is the wedge. In particular, comparing images 9 to 15, we can see the curvature of the shock wave has been changed. The unsteady shock-wave motion is coupled with the incoming boundary-layer structure shown in the upstream of shock wave in image 9. The images are conveniently formed into a loop movie to give a dynamic view of the interaction.⁸

The shock-wave/boundary-layer interaction is usually three-dimensional, and so the experiment was also set up to obtain planform view images of the shock-wave/boundary-layer interaction. The layout was similar to that illustrated in Fig. 10 except the laser sheet was parallel to the wall of wind tunnel and grazed the surface of wedge. Figure 12 shows six sequential planform view images each separated by $2 \mu\text{s}$. The shock wave now turns into a wavy line, and the boundary-layer structure is seen as the dark region in the flow. From these images it is particularly apparent how the shape of the shock wave changes as the boundary-layer structure passes. A discontinuity in the boundary layer can also be seen as it crosses the shock because the oblique shock changes the direction of the flow, forcing it out toward laser sheet plane.

As the flow crosses the shock, its speed decreases, and the scattered light has a smaller Doppler frequency shift. To highlight the different parts of the flow, we put the molecular iodine vapor cell in front of the camera and tuned the frequency of the laser. With the laser frequency tuned near the center of the iodine absorption, scattering from lower-speed flow and nonmoving elements such as

⁸This movie can be seen on the Web at <http://www.princeton.edu/~milesgrp/Movie/PBL1.html>.

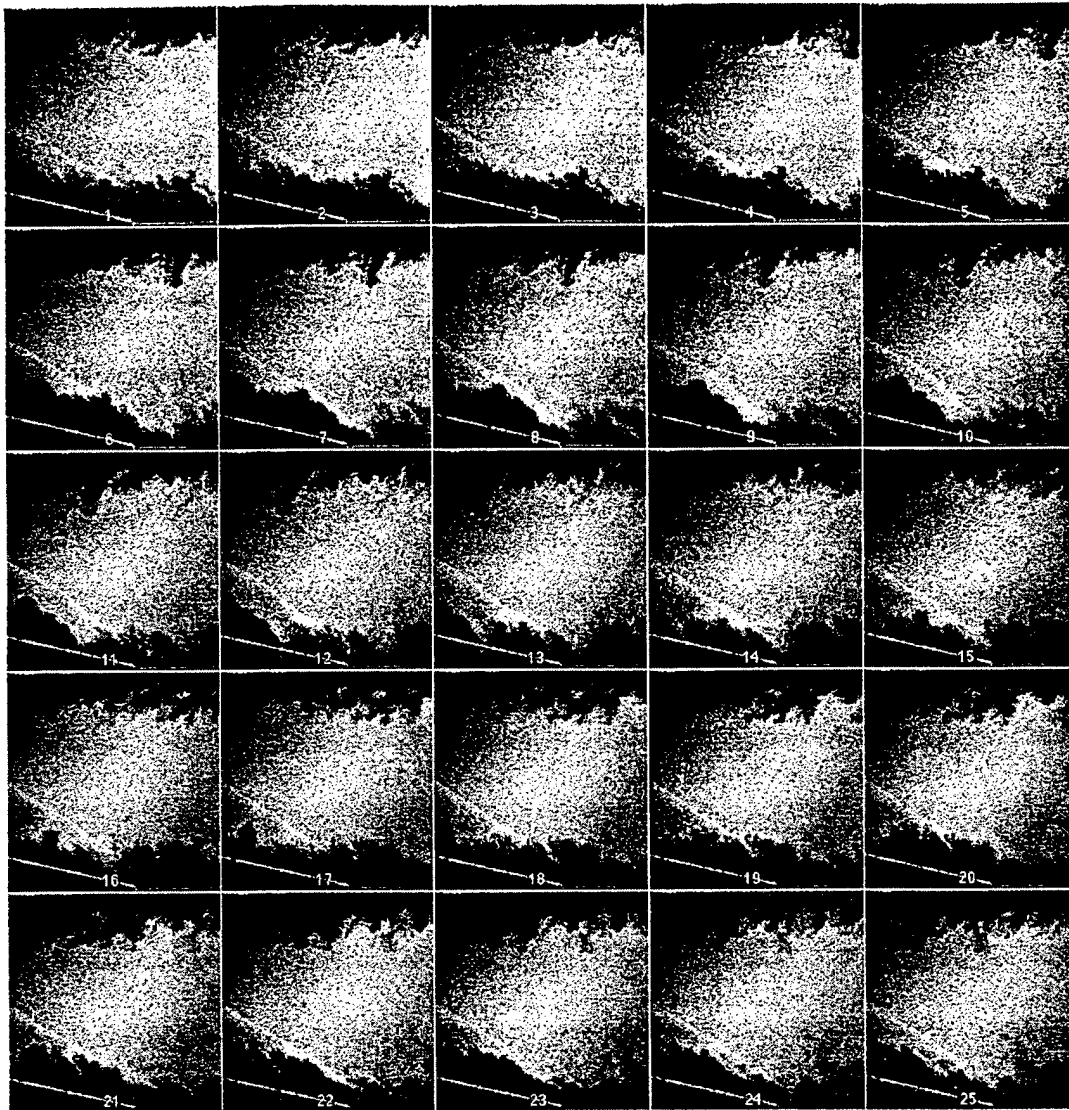


Fig. 11 Sequence of 25 streamwise view images of Mach 2.5 flow over 14-deg wedge. Flow is from right to left with $2 \mu\text{s}$ between images.

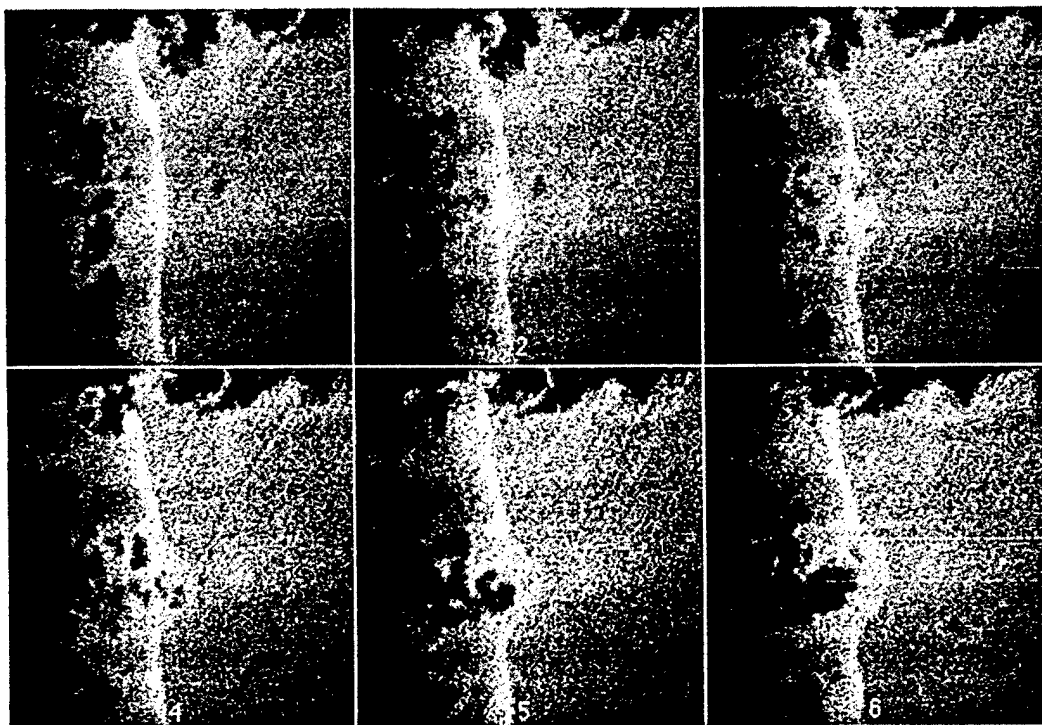


Fig. 12 Sequence of six planform view images of Mach 2.5 flow over 14-deg wedge. Flow is from right to left with $2 \mu\text{s}$ between images.

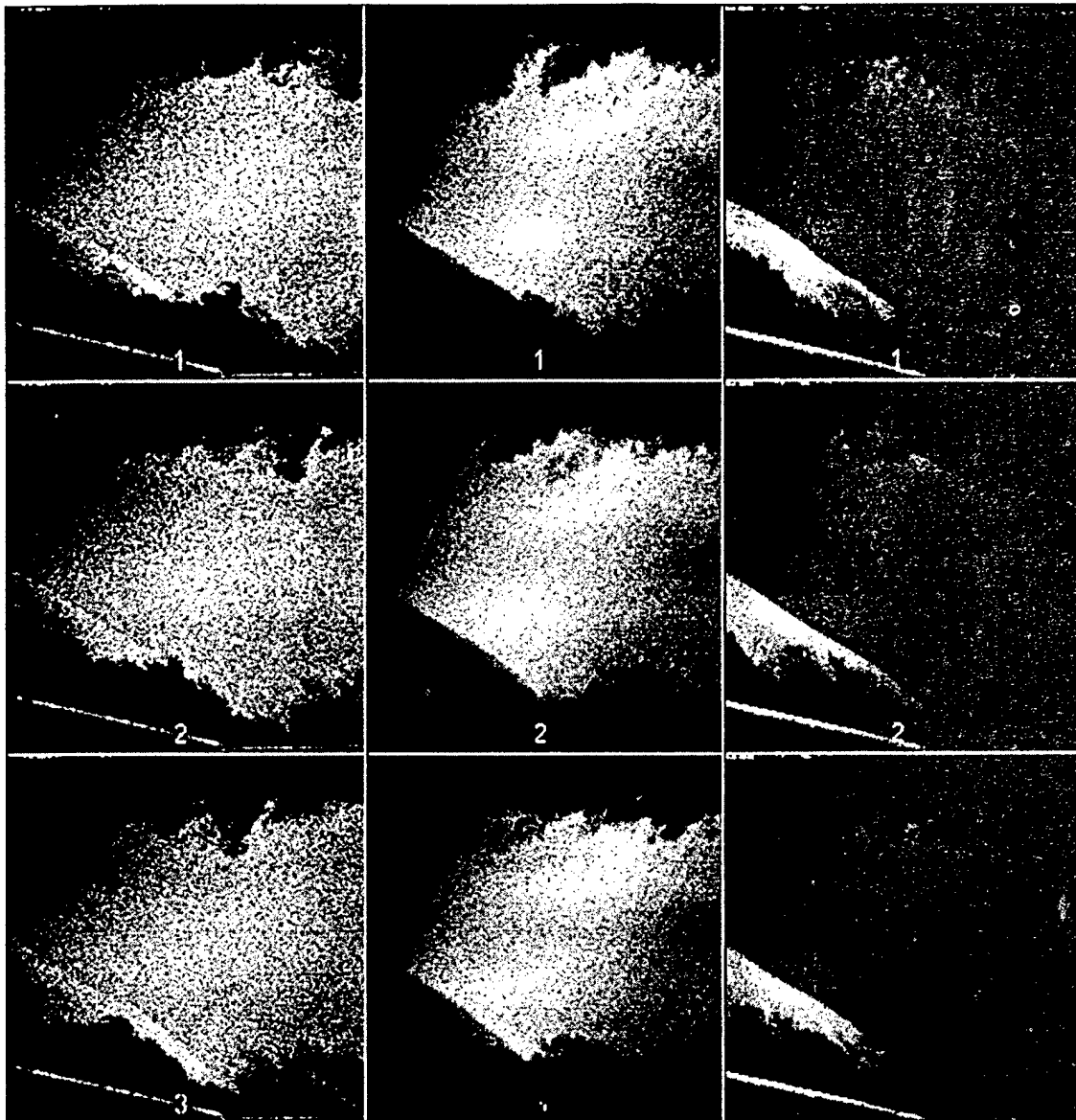


Fig. 13 Comparison of filtered and unfiltered side-view images. Flow from right to left with 4- μ s time interval between images: left column, unfiltered images; middle column, filtered to highlight high-speed flow; and right column, filtered to highlight low-speed flow.

the surface of the wedge is selectively attenuated, as illustrated in the middle column of Fig. 13. Alternatively, as shown in right column of Fig. 13, the scattering from the high-speed flow can also be suppressed by tuning the laser so that the Doppler-shifted-scattering coincides with the absorption line of iodine. The sequence of images in the right column also shows another weak oblique shock at the upper right corner. Without the filter the signal from the mean stream flow is so strong that it completely masks that shock-wave structure.

VIII. Conclusion and Future Work

A megahertz pulse-burst laser system has been developed and has been used for the visualization of shock-wave/boundary-layer interactions in a Mach 2.5 wind tunnel at a 0.5-MHz repetition rate.

The pulse-burst laser is capable of producing a programmable burst of from 1 to 99 pulses, with individual pulse duration from 10 to 100 ns and interpulse separation from 1 to 10 μ s. A fundamental output energy (at 1.06 μ m) of approximately 10 mJ has been achieved in each of 30 individual, 20-ns duration pulses. The second harmonic output was about 400 μ J per individual pulse.

Experimental results have shown that the laser has a narrow linewidth. The range of frequency tunability is about 1 cm^{-1} at 1.06 μ m. The transmission through a 9.98-cm-long molecular iodine vapor filter (40°C side band, 80°C cell temperature) was mea-

sured to be 5×10^{-5} , which conforms well with model prediction. Consequently, the system can be used for FRS and other frequency or long coherence-length-related laser diagnostics, such as holography.

As an application of the megahertz pulse-burst laser system, the visualization of a Mach 2.5 flow over a 14-deg wedge shows the unsteadiness of a shock wave and its coupling to the structure of the incoming boundary layer.

We are now building a second-generation high-power pulse-burst laser system. Average single-pulse fundamental and second harmonic energy on the order of 100 and 25 mJ have been achieved, respectively. The new pulse-burst imaging system will be used for imaging in the plasma propulsion facility in the Electric Propulsion and Plasma Diagnostics Laboratory.

Acknowledgments

The authors wish to acknowledge Jay H. Grinstead and Philip Howard for their assistance in the Mach 2.5 imaging measurement. We would also like to thank A. J. Smits for the helpful discussion in the shock-wave/boundary-layer interaction and Princeton Scientific Instruments, Inc., for providing the megahertz-framing-rate CCD camera. The pulse-burst laser system has been developed with support from two grants from the U.S. Air Force Office of Scientific Research, Julian Tishkoff (University Research Initiative)

and Leonidas Sakell (External Aerodynamics), Technical Monitors. Money was also provided by NASA Phase I Project Grant NASA-97090 and the state-sponsored New Jersey Center for Opto-Electronics. The second-generation pulse-burst laser is supported by the Air Force Office of Scientific Research (Grant F49620-97-1-0373) as part of a joint Department of Defense University Research Initiative Program with the Princeton Electric Propulsion group. The CCD framing camera has been developed by Princeton Scientific Instruments, Inc., under Small Business Innovative Research grants from U.S. Office of Naval Research with Edwin Rood as Technical Monitor and the U.S. Air Force, Wright Laboratories, with Charles Tyler as Technical Monitor.

References

- ¹Kyachoff, G., Seitzman, J., and Hanson, R. K., "Instantaneous Temperature Field Measurements Using Planar Laser-Induced Fluorescence," *Optics Letters*, Vol. 10, No. 9, 1985, pp. 439-441.
- ²Miles, R. B., and Lempert, W. R., "Two-Dimensional Measurement of Density, Velocity, and Temperature in Turbulent High-Speed Air Flows by UV Rayleigh Scattering," *Applied Physics*, Vol. B51, No. 1, 1990, pp. 1-7.
- ³Cheng, T. S., Wehrmeyer, J. A., and Pitz, R. W., "Simultaneous Temperature and Multispecies Measurement in a Lifted Hydrogen Diffusion Flame," *Combustion and Flame*, Vol. 91, No. 3/4, 1992, pp. 323-345.
- ⁴Wagner, J. W., Deaton, J. B., and Spicer, J. B., "Generation of Ultrasound by Repetitively Q-Switching a Pulsed Nd:YAG Laser," *Applied Optics*, Vol. 27, No. 22, 1988, pp. 4696-4700.
- ⁵Ruff, G. A., Bernal, L. P., and Faeth, G. M., "High Speed In-Line Holographicematography for Dispersed-Phase Dynamics," *Applied Optics*, Vol. 29, No. 31, 1990, pp. 4544-4546.
- ⁶Huntley, J. M., "High-Speed Laser Speckle Photography. Part 1: Repetitively Q-Switched Ruby Laser Light Source," *Optical Engineering*, Vol. 33, No. 5, 1994, pp. 1692-1699.
- ⁷Grace, J. M., Nebolsine, P. E., and Goldey, C. L., "Repetitively Pulsed Ruby Lasers as Light Sources for High-Speed Photography," *Optical Engineering*, Vol. 37, No. 8, 1998, pp. 2205-2212.
- ⁸Forkey, J. N., Finkelstein, N. D., Lempert, W. R., and Miles, R. B., "Demonstration and Characterization of Filtered Rayleigh Scattering for Planar Velocity Measurements," *AIAA Journal*, Vol. 34, No. 3, 1996, pp. 442-448.
- ⁹Forkey, J. N., Lempert, W. R., and Miles, R. B., "Corrected and Calibrated I₂ Absorption Model at Frequency Doubled Nd:YAG Laser Wavelengths," *Applied Optics*, Vol. 36, No. 27, 1997, pp. 6729-6738.
- ¹⁰Frantz, L. M., and Nodvik, J. S., "Theory of Pulse Propagation in a Laser Amplifier," *Journal of Applied Physics*, Vol. 34, No. 8, 1963, pp. 2346-2349.
- ¹¹Lowdermilk, W. H., and Murry, J. E., "The Multipass Amplifier: Theory and Numerical Analysis," *Journal of Applied Physics*, Vol. 51, No. 5, 1980, pp. 2436-2444.
- ¹²Forkey, J. N., Lempert, W. R., and Miles, R. B., "Observation of a 100-MHz Frequency Variation Across the Output of a Frequency-Doubled Injection-Seeded Unstable-Resonator Q-Switched Nd:YAG Lasers," *Optics Letters*, Vol. 22, No. 4, 1997, pp. 230-232.
- ¹³Kosonocky, W. F., Yang, G., Ye, C., Kabra, R. K., Lowrance, J. L., Mastrocola, V., Shallcross, F. V., and Patel, V., "360°360 Element, Very High Framing Rate, Burst Image Sensor," 1996 IEEE International Solid-State Circuits Conf., San Francisco, Feb. 1996.
- ¹⁴Erbland, P. J., Baumgartner, M. L., Etz, M. R., Yalin, A., and Miles, R. B., "Development of Planar Diagnostics for Imaging Mach 8 Flowfields Using Carbon Dioxide and Sodium Seeding," AIAA Paper 97-0154, 1997.
- ¹⁵Smith, M. W., and Smits, A. J., "Visualization of the Structure of Supersonic Turbulent Boundary Layers," *Experiments in Fluids*, Vol. 18, No. 4, 1995, pp. 288-302.

R. P. Lucht
Associate Editor